ELECTRONIC PROPERTIES AND DEVICE APPLICATIONS OF $GaAs/Al_xGa_{1-x}As$ QUANTUM BARRIER AND QUANTUM WELL HETEROSTRUCTURES

Thesis by

Alice Renée Bonnefoi

In Partial Fulfillment of the Requirements

for the Degree of

Doctor of Philosophy

California Institute of Technology

Pasadena, California

1987

(Submitted November 24, 1986)

A ma mère

Acknowledgments

I wish to express my deepest gratitude to Professor T. C. McGill for the privilege of having been a member of his research group. This group is unique, not only for the high quality of research which is performed, but also for the friendly and cooperative environment which always exists among its members. I owe a great deal to Professor McGill for his stimulating advice, encouragement and support. I have also benefited greatly from the valuable discussions I have had with him and from his great physical intuition. I would also like to thank him for reading my papers as well as this thesis and for making useful suggestions to improve them. I wish to express my deepest appreciation to Vere Snell for providing the daily ray of sun which keeps the group running in harmony. Special thanks to Carol McCollum for her help in many ways.

I am grateful to Drs. R. S. Bauer and R. D. Burnham of Xerox Palo Alto Research Center, who provided the MOCVD samples used in this work.

I am indebted to Professors P. G. de Gennes of E. S. P. C. I., Paris, and R. Orbach of U. C. L. A., for encouraging and supporting me in applying to Caltech.

I wish to thank Professors N. R. Corngold, W. L. Johnson, D. Psaltis, and T. A. Tombrello for agreeing to serve on my thesis defense committee.

I am most grateful to Dr. R. T. Collins for his time and guidance in helping me start my research project. I also wish to acknowledge Drs. C. Mailhiot, A. Prabhakar, T. E. Schlesinger, and A. Zur for valuable discussions. I have also profitted from fruitful interactions with D. H. Chow and T. K. Woodward and from discussions with R. J. Hauenstein, M. K. Jackson, M. B. Johnson, R. H. Miles, and G. Y. Wu.

Finally, my deepest gratitude is extended to my family for their constant support and encouragement.

Abstract

This thesis presents an experimental and theoretical study of some of the electronic properties and device applications of GaAs/$Al_xGa_{1-x}As$ single and double barrier tunnel structures. In Chapter 2, energy band diagrams are calculated for heterostuctures in which tunneling occurs between two degenerately doped electrodes separated by a single quantum barrier. When a bias voltage is applied to a structure, the energy band profile gives the voltage drop distribution in the cladding layers as well as in the barrier. This distribution may differ significantly from that based on the commonly made assumption that the entire applied voltage drops linearly across the barrier layer. It is shown that band bending effects become more important for larger applied voltages, thicker barriers, smaller electrode doping densities and larger barrier doping concentrations. Energy band diagrams are found to be useful for calculating tunneling currents and determining what the dominant low temperature current transport mechanisms occurring in these structures are. In some cases, they reveal that these mechanisms are different from those predicted when band bending is neglected.

In Chapter 3, elastic and inelastic tunneling processes are investigated in GaAs–AlAs–GaAs single barrier heterostructures grown on [100]–oriented substrates. The GaAs electrodes are degenerately doped n–type with Se, and the AlAs quantum barriers are doped either p–type with Mg or n–type with Se. In p–type barrier structures, low temperature current transport is found to be dominated by elastic and inelastic electron tunneling through the AlAs band gap at the Γ–point *and* at the X–point. Anomalous zero–bias conductances obtained from several of the samples are also discussed. A theoretical model, which treats trap levels in the AlAs barrier as intermediate states for two–step tunneling processes shows that impurity–assisted tunneling becomes more important as the tunnel barrier is made thicker. In heterostructures in which the n–type barrier

layers are thick enough and/or sufficiently doped, the AlAs conduction band at the X–point is not totally depleted of electrons. The dominant low temperature current transport mechanism is then tunneling through two reduced AlAs X–point barriers separated by a bulk region of AlAs. When the n–type AlAs barrier layer is sufficiently thin, the AlAs conduction band remains fully depleted of carriers. As a result, electrons tunnel through the AlAs band gap at the X–point and/or at the Γ–point in a one–step process. In these structures, it is found that plasmons located near the GaAs/AlAs interfaces interact with GaAs and AlAs longitudinal optical (LO) phonons when the doping density in the n–type GaAs electrodes is such that the plasma frequency becomes comparable to the LO phonon frequencies.

Chapter 4 presents a study of resonant tunneling in GaAs/$Al_xGa_{1-x}As$ double barrier heterostructures grown epitaxially in the [100]–direction. In these structures, electrons tunnel through two $Al_xGa_{1-x}As$ quantum barriers separated by a thin GaAs layer forming a quantum well. The resonant energy levels in the GaAs well which produce negative differential resistances in the experimental I–V characteristics are identified by calculating the energy band diagrams of the structures. In samples having pure AlAs barrier layers, tunneling via resonant states confined in the well by the AlAs Γ–point potential energy barriers is often inconsistent with experimental results. However, the experimental data can usually be explained by tunneling via quasi–stationary levels confined in the well by the AlAs X–point potential energy barriers as well as the AlAs Γ–point barriers. The relative contributions of tunneling via resonant Γ– and X–states in the well are found to depend upon the samples studied and sometimes upon the sign of the applied bias. Resonant tunneling is also investigated in double barrier heterostructures in which a low doped GaAs buffer layer is grown before the first $Al_xGa_{1-x}As$ barrier. As a result of this structural asymmetry, the peaks in

current corresponding to a given resonant state in the quantum well may be observed in the experimental I–V characteristics at very different applied voltages in reverse bias than in forward bias.

In Chapter 5, we propose and analyze two types of three–terminal devices based upon resonant tunneling through quantum well and quantum barrier heterostructures. The first type includes two configurations in which a base voltage controls the emitter–collector tunneling current by shifting the resonances in a quantum well. In the proposed devices, the relative positions of the base and collector are interchanged with respect to the conventional emitter–base–collector sequence as a means for obtaining negligible base currents and large current transfer ratios. The second type of three–terminal devices includes three configurations in which the current through a double barrier structure is modulated by a Schottky barrier gate placed along the path of the electrons. These devices feature, in their output current–voltage (I_D–V_D) curves, negative differential resistances controlled by a gate voltage.

Chapter 6 presents a growth uniformity study performed on several of the heterostructures discussed in the thesis. First, the reproducibility and uniformity of the electrical characteristics of GaAs/AlAs tunnel structures are used to show that the doping concentrations and layer thicknesses are uniform across the samples under test. Secondly, discrete fluctuations in layer thicknesses are discussed in GaAs/$Al_{0.35}Ga_{0.65}As$ double barrier heterostructures. These fluctuations are manifested by non–uniform experimental results and by sequences of negative differential resistances in the I–V characteristics of many devices.

Parts of this thesis have been or will be published under the following titles:

Chapter 2:

Energy Band Diagrams and Current–Voltage Characteristics of Single Barrier Tunnel Structures,

A. R. Bonnefoi, D. H. Chow, and T. C. McGill, (to be published).

Chapter 3:

Inelastic and Resonant Tunneling in GaAs/AlAs Heterostructures,

R. T. Collins, A. R. Bonnefoi, J. Lambe, T. C. McGill, and R. D. Burnham, in *Proceedings of the 17th International Conference on the Physics of Semiconductors*, San Francisco, August 6–10, 1984.

Inelastic and Resonant Tunneling in GaAs/AlAs Heterostructures,

R. T. Collins, A. R. Bonnefoi, J. Lambe, T. C. McGill, and R. D. Burnham, in *Proceedings of the International Conference on Superlattices, Microstructures and Microdevices*, Champaign–Urbana, Illinois, August 13–16, 1984.

Current Transport Mechanisms in GaAs/AlAs Tunnel Structures Grown by Metalorganic Chemical Vapor Deposition,

A. R. Bonnefoi, D. H. Chow, T. C. McGill, R. D. Burnham, and F. A. Ponce , J. Vac. Sci. Techn. B **4**, 988 (1986).

Tunneling in MOCVD Grown GaAs–AlAs–GaAs Heterostructures,
A. R. Bonnefoi, D. H. Chow, T. C. McGill, R. D. Burnham, and F. A. Ponce , Bul. Am. Phys. Soc. **31**, 395 (1986).

Interactions Between Interface Plasmons and Longitudinal Optical Phonons in GaAs–AlAs–GaAs Tunnel Structures,
A. R. Bonnefoi, T. C. McGill, and R. D. Burnham, (to be published).

Chapter 4:

Inelastic and Resonant Tunneling in GaAs/AlAs Heterostructures,
R. T. Collins, A. R. Bonnefoi, J. Lambe, T. C. McGill, and R. D. Burnham, in *Proceedings of the 17th International Conference on the Physics of Semiconductors*, San Francisco, August 6–10, 1984.

Inelastic and Resonant Tunneling in GaAs/AlAs Heterostructures,
R. T. Collins, A. R. Bonnefoi, J. Lambe, T. C. McGill, and R. D. Burnham, in *Proceedings of the International Conference on Superlattices, Microstructures and Microdevices*, Champaign–Urbana, Illinois, August 13–16, 1984.

Resonant Tunneling in GaAs/AlAs Heterostructures Grown by Metalorganic Chemical Vapor Deposition,
A. R. Bonnefoi, R. T. Collins, T. C. McGill, R. D. Burnham, and F. A. Ponce, Appl. Phys. Lett. **46**, 285 (1985).

Observation of Resonant Tunneling Through GaAs Quantum Well States Confined by AlAs X–Point Barriers,

A. R. Bonnefoi, T. C. McGill, R. D. Burnham, and G. B. Anderson, (to be published).

Resonant Tunneling Through GaAs Quantum well Energy Levels Confined by $Al_xGa_{1-x}As$ Γ– and X–Point Barriers,

A. R. Bonnefoi, T. C. McGill, and R. D. Burnham, (to be published).

The Role of Barrier Phonons in the Tunneling I–V Characteristics of Double Barrier Heterostructures,

G. Y. Wu, A. R. Bonnefoi, and T. C. McGill, (to be published).

Chapter 5:

Inverted Base–Collector Tunnel Transistors,

A. R. Bonnefoi, D. H. Chow, and T. C. McGill, Appl. Phys. Lett. **47**, 888 (1985).

Resonant Tunneling Transistors with Controllable Negative Differential Resistances,

A. R. Bonnefoi, T. C. McGill, and R. D. Burnham, Elect. Dev. Lett. **EDL-6**, 636 (1985).

Chapter 6:

Uniformity in the Electrical Characteristics of GaAs/AlAs Tunnel Structures Grown by Metalorganic Chemical Vapor Deposition,

A. R. Bonnefoi, T. C. McGill, and R. D. Burnham, Appl. Phys. Lett. **47**, 307 (1985).

Contents

Acknowledgments iii

Abstract iv

List of Publications vii

1 Fundamental Properties and Device Applications of GaAs/$Al_xGa_{1-x}As$ Tunnel Structures 1

1.1 Introduction 1

1.2 Current Transport in Single and Double Barrier Tunnel Structures 3

1.3 Importance of the Study 5

1.4 Summary of Thesis 7

2 Energy Band Diagrams and Current–Voltage Characteristics of Single Barrier Tunnel Structures 16

2.1 Introduction 16

2.2 Theoretical Basis 19

2.2.1 Energy Band Diagrams 19

2.2.2 J–V Characteristics 23

2.3 p–Type Barrier Structures 24

2.4 Undoped Barrier Structures 49

2.5 n–Type Barrier Structures 56

2.6 Other Structures 68

2.7 Summary 74

3 Elastic and Inelastic Tunneling Processes in GaAs–AlAs–GaAs Heterostructures Grown by Metalorganic Chemical Vapor Deposition 79

3.1 Introduction 79

3.2 Experimental Procedures 82

3.3 Samples with p–Type AlAs Barrier Layers 84

3.3.1 Tunneling Through AlAs Γ– and X–Point Barriers 84

3.3.2 Impurity–Assisted Tunneling 94

3.3.3 Inelastic Tunneling Processes 99

3.3.4 Zero–Bias Anomalies 108

3.4 Samples with n–Type AlAs Barrier Layers 116

3.4.1 Current Transport Through Thick n–Type AlAs Layers . 116

3.4.2 Current Transport Through Thin n–Type AlAs Layers . . 125

3.5 Summary 140

4 Resonant Tunneling in GaAs/$Al_xGa_{1-x}As$ Double Barrier Heterostructures 147

4.1 Introduction 147

4.2 Theoretical Model 155

4.3 Resonant Tunneling in Structures with Direct Band Gap $Al_xGa_{1-x}As$ Barrier Layers 157

4.4 Resonant Tunneling in Structures with Indirect Band Gap $Al_xGa_{1-x}As$ Barrier Layers 171

4.5 Relative Importance of Tunneling via Resonant Γ– and X–states 181

4.6 Resonant Tunneling in Asymmetrically Doped Structures 192

4.7 Summary 204

5 Resonant Tunneling Transistors **214**

5.1 Introduction 214

5.2 Inverted Base–Collector Tunnel Transistors 215

5.3 Resonant Tunneling Transistors with Controllable Negative Differential Resistances 222

5.4 Summary 232

6 Growth Characterization of GaAs/Al$_x$Ga$_{1-x}$As Tunnel Structures Grown by Metalorganic Chemical Vapor Deposition **237**

6.1 Introduction 237

6.2 Uniformity in the Electrical Characteristics of GaAs/AlAs Tunnel Structures 238

6.3 Layer Thickness Fluctuations in GaAs/Al$_x$ Ga$_{1-x}$As Double Barrier Heterostructures 245

Chapter 1

Fundamental Properties and Device Applications of GaAs/$Al_xGa_{1-x}As$ Tunnel Structures

1.1 Introduction

Semiconductor quantum well and quantum barrier heterostructures are a topic of great current interest. They are frequently fabricated by molecular beam epitaxy (MBE) or metalorganic chemical vapor deposition (MOCVD). These techniques make it possible to grow epitaxial layers of one semiconductor on top of another as thin as 10 to 20 Å with interfaces as abrupt as a few atomic layers.

The properties of these structures result from quantum effects produced by their small characteristic dimensions and from the band offsets at the heterojunction interfaces. Band offsets are potential energy discontinuities which characterize the relative positions of the energy bands of two different semiconductors

brought into contact at an interface. These new aspects have no counterparts in conventional semiconductor devices exploiting the bulk properties of the materials. In particular, tunneling becomes an important current transport mechanism in structures having thin quantum barriers. The associated tunneling effects yield novel electronic properties, some of which remain to be fully understood.

Although other materials are being investigated,[1–5] the III–V compound semiconductors GaAs and $Al_xGa_{1-x}As$ continue to be used extensively in experimental and theoretical studies of semiconductor heterojunctions.[6–16] The band offsets between both materials cause $Al_xGa_{1-x}As$ layers to act as potential energy barriers to charge carriers in GaAs. A major advantage in using these two semiconductors is that they are lattice matched. As a result, negligible strain is introduced into the crystals when they are grown on top of each other. Futhermore, GaAs is important to both solid state physics in general, and device physics in particular. Because it is characterized by a high electron mobility and a large saturated drift velocity, GaAs can be used in reliable semiconductor devices operating at very high frequencies. Another important property of GaAs is that it is a direct energy gap semiconductor having its conduction band minimum at the Brillouin zone center (Γ–point). $Al_xGa_{1-x}As$ is also a direct band gap material for small Al compositions. However, it becomes indirect for Al contents greater than 0.40–0.45, with the conduction band minima occuring in the $< 100 >$–directions, at the X–point. Local minima also exist in the $< 111 >$–directions, at the L–point. These are higher in energy than the X–point minima, but lower than the Γ–point minimum.[17]

In this thesis, electronic transport perpendicular to the heterojunction interfaces is investigated in $GaAs/Al_xGa_{1-x}As$ layered heterostructures. In the simplest structure, electron transport occurs between two GaAs electrodes separated by a single $Al_xGa_{1-x}As$ quantum barrier. In double barrier heterostructures, the

charge carriers tunnel through two $Al_xGa_{1-x}As$ quantum barriers separated by a thin GaAs layer forming a quantum well. Both types of structures are studied, and some of their electronic properties and device applications are discussed. It is also shown that electrical characteristics provide information about the properties of the materials and the heterojunction interfaces, and may be used to probe the growth uniformity of the samples under test.

1.2 Current Transport in Single and Double Barrier Tunnel Structures

Electronic tunneling has been investigated in a number of structures, including tunnel diodes, metal–insulator–metal and metal–semiconductor tunnel junctions.[18] A tunnel junction usually consists of two conducting layers of material forming the electrodes, separated by a thin layer of material acting as a potential energy barrier to the charge carriers in the electrodes. Upon applying a bias to the junction, charge carriers flow from one electrode to the other by tunneling through the quantum barrier. This one must be sufficiently thin to make the tunneling probability large enough. Barrier thicknesses are usually on the order of 50–100 Å. Elastic tunneling occurs when charge carriers go through the barrier without energy loss, from occupied states in one electrode into unoccupied states in the other electrode. Elastic tunneling provides information not only about the barrier penetration probability, but also about the band offsets, the coherence length of the electron wave functions, and the complex band structure in the barrier layers. As they tunnel through the structure, the charge carriers may also be scattered or excite fundamental excitations such as vibrational modes of local impurities, lattice vibrations, plasmons, etc. In such processes, energy is not conserved; this is inelastic tunneling. If a funda-

mental excitation is created in an inelastic tunneling process, a charge carrier loses a quantum of energy ($\hbar\omega_0$) to some mode as it tunnels. By the exclusion principle, a tunneling transition can only occur from an initially occupied state to an initially unoccupied state. As a result, the potential difference between the Fermi levels in the electrodes determines which transitions are possible at low temperatures. For carriers tunneling from left to right, an inelastic process can only occur when there is an empty state in the right electrode at an energy ($\hbar\omega_0$) below a filled state in the left electrode. The inelastic channel thus opens up at a threshold voltage $V_0 = \hbar\omega_0/e$. This produces a change in the slope of the junction I–V curve at the applied bias V_0. Such effects are usually too small to be easily detected in experimental I–V characteristics. However, sensitive measurements of the first, $(dI/dV)(V)$, and second, $(d^2I/dV^2)(V)$, derivatives of the I–V curves generally make it possible to detect inelastic tunneling processes. This is because a change in the slope of an I–V curve at a particular threshold voltage leads to a step discontinuity in the first derivative spectrum and to a peak in the second derivative curve at the same voltage. If several modes can be excited, each one contributes a peak in the second derivative at the corresponding threshold voltage, so that the $(d^2I/dV^2)(V)$ curve is a direct representation of their spectrum. The peak positions may thus be used to identify the scattering processes and the fundamental excitations which can couple to the tunneling charge carriers. In addition, the peak amplitudes provide information about the strength of the interactions. Inelastic tunneling measurements are usually made at low temperatures. This is because the amplitude of a second derivative peak is proportional to 1/kT and its resolution (full width at half height) is 5.4 kT.[19] At 4.2 K, the resolution of inelastic tunneling spectroscopy is thus limited to about 2 meV. The usual technique for obtaining first and second derivative curves is to superpose a small oscillatory component on the voltage ramp applied to the

junction, and to detect the signals generated at the first and second harmonics of the modulation frequency, respectively.[20] This modulation introduces an instrumental broadening of the second derivative peaks which is proportional to V_m, the RMS amplitude of the oscillatory component of the applied voltage.[19] The resolution can thus be increased by decreasing the modulation amplitude. Unfortunately, the time for measurement increases rapidly as V_m is decreased.

The tunnel junctions discussed in this thesis consist of two degenerately doped n–type GaAs electrodes separated by one or two $Al_xGa_{1-x}As$ quantum barriers. Electron transport perpendicular to the layers is studied as a function of temperature, doping densities and layer thicknesses. This is achieved by performing I–V, as well as $(dI/dV)(V)$ and $(d^2I/dV^2)(V)$ measurements on the samples. The derivative spectra are obtained using modulation frequencies of 5 and 50 kHz, respectively.[20] Typical modulation voltages range between a fraction of millivolt and 5 mV peak–to–peak. In single barrier heterostructures, the dominant current transport mechanisms are thermionic emission at high temperatures, and elastic and inelastic tunneling at low temperatures. In double barrier heterostructures, resonant electronic states exist in the GaAs quantum well due to the confinement of the electron wave functions by the $Al_xGa_{1-x}As$ quantum barriers. These resonant states have the property of producing negative differential resistances in the structure I–V characteristics.

1.3 Importance of the Study

The purpose of the experimental and theoretical study presented in this thesis was to gain a basic understanding of $GaAs/Al_xGa_{1-x}As$ single and double barrier tunnel structures. This was achieved by examining a few aspects of each of three major topics of interest in the field of small–scale semiconductor heterostructures.

(*i*) We have investigated a number of fundamental electronic properties of the structures. Emphasis has been placed on determining the dominant low temperature current transport mechanisms, identifying scattering processes, and showing the importance of realistic energy band diagrams in interpreting experimental results. (*ii*) We have studied some device applications of resonant tunneling through quantum well and quantum barrier heterostructures by proposing two types of novel three–terminal devices. Such devices are a source of considerable interest because they exhibit negative differential resistances in their current–voltage characteristics and are expected to operate at very high frequencies. As a result, they have potential applications in millimeter–wave oscillators,[21] fast switches, frequency multipliers, multistate memories and high–speed analog–to–digital converters.[22] (*iii*) We have investigated some growth properties of the samples by attempting to characterize the quality of the constituent materials and the heterojunction interfaces, and also by studying the uniformity of the electrical characteristics and the effects of fluctuations in layer thicknesses.

The present study differs from other investigations of $GaAs/Al_xGa_{1-x}As$ tunnel structures on a number of grounds. (*i*) While other studies have usually been either experimental or theoretical, this thesis develops several theoretical models which are used to interpret experimental results. (*ii*) Whereas MBE is the most widely used technique for growing small–scale heterostructures, the majority of the samples discussed in the following chapters were grown by MOCVD. (*iii*) For simplicity, tunnel barriers are generally made of direct band gap $Al_xGa_{1-x}As$,$(x < 0.40 - 0.45)$.[10–16] The conduction band edge minimum in the barrier layers then occurs at the Γ–point. Only a few studies of heterostructures having indirect band gap $Al_xGa_{1-x}As$[8,9] or pure AlAs[6,7] barrier layers have been reported. In most of the samples presented here, the quantum barriers consist of indirect band gap $Al_xGa_{1-x}As$ or pure AlAs. Current transport in these

structures is more complex because tunneling through the $Al_xGa_{1-x}As$ band gap at the Γ–point usually fails to explain the experimental data. This indicates that other transport mechanisms must contribute to the total current. In particular, there must be contributions from tunneling through the $Al_xGa_{1-x}As$ band gap at symmetry points other than the Γ–point, which is actually higher in energy than both the X– and L–points. Until recently, such effects have been totally overlooked.[23,24] (*iv*) Most studies of semiconductor tunnel structures have only been concerned with elastic tunneling mechanisms. We also investigate inelastic processes and effects related to anomalous zero–bias conductances. (*v*) The existing theoretical models for calculating quantum barrier tunneling probabilities and tunnel structure I–V characteristics all assume that the entire applied voltage drops linearly across the barrier layers. We have performed the first realistic calculations of energy band diagrams, making it possible to account for the actual shapes of the tunnel barriers and the voltage drop distribution in the electrodes as well as in the barrier layers. This is critical in calculating tunneling currents and in interpreting certain experimental results which cannot be explained by models in which band bending effects are neglected.

1.4 Summary of Thesis

In Chapter 2, energy band diagrams of single barrier heterostuctures are calculated by solving Poisson's equation self–consistently. The implications of these energy band profiles on the electronic properties of a few structures of current interest are discussed. In these structures, tunneling occurs between two degenerately doped electrodes separated by a single quantum barrier, which may be either undoped, or doped p–type or n–type. When a bias voltage is applied to a heterostructure, the energy band profile gives the voltage drop distribution in

the cladding layers as well as in the barrier. This distribution may differ significantly from that based on the commonly made assumption that the entire applied voltage drops linearly across the barrier layer. The effects of applied bias, barrier thickness, electrode doping density and barrier doping concentration are discussed in the case of GaAs–$Al_xGa_{1-x}As$–GaAs heterostructures. It is found that band bending plays a more important role for larger applied voltages, thicker barriers, smaller electrode doping densities and larger barrier doping concentrations. Energy band profiles are shown to be useful in determining the nature of the dominant low temperature current transport mechanisms taking place in these structures. In some cases, they reveal that these mechanisms should be different from those predicted when band bending is neglected. Calculations of tunneling currents using energy band diagrams are presented for heterostructures in which the barrier layers are totally depleted of free carriers. These currents are extremely sensitive to the actual shape of the barrier through which the charge carriers tunnel. Energy band profiles may thus provide information about certain quantities which are difficult to determine accurately, such as band offsets and barrier doping densities. They may also be useful in studying the novel electronic properties of single barrier tunnel structures from which negative differential resistances are expected. This is illustrated in the case of $Hg_{1-x}Cd_xTe$–CdTe–$Hg_{1-x}Cd_xTe$ double heterojunctions.

In Chapter 2, a simple theoretical model is developed to calculate the energy band diagrams and the current–voltage characteristics of single barrier tunnel structures. In Chapter 3, these concepts are related to a study of elastic and inelastic tunneling processes in GaAs–AlAs–GaAs double heterojunctions grown by MOCVD in the [100]–direction. The GaAs electrodes in the heterostructures studied are degenerately doped n–type with Se. The AlAs quantum barriers are doped either p–type with Mg or n–type with Se. Measurements of

current–voltage, I–V, characteristics, as well as first, $(dI/dV)(V)$, and second, $(d^2I/dV^2)(V)$, derivatives of the I–V curves, are performed at temperatures ranging from 300 to 4.2 K. In structures having thin p–type AlAs barrier layers, the dominant current transport mechanisms at low temperatures are found to be (*i*) elastic electron tunneling through the AlAs Γ–point barrier; (*ii*) inelastic and/or elastic tunneling through the AlAs X–point barrier; and (*iii*) the creation of fundamental excitations such as phonons by electrons tunneling through the AlAs band gap at the Γ–point and at the X–point. The p–type barrier heterostructures are classified into two categories depending upon the inelastic processes which may be identified in the derivative spectra. These results reveal that the dominant current transport mechanisms taking place in single barrier tunnel structures depend upon the samples studied. This seems to be related primarily to the quality of the materials and the heterojunction interfaces. A number of samples also depict anomalous zero–bias conductances. These so–called "zero–bias anomalies" may be due to interface states, or to trap levels located in the AlAs barrier and/or near the heterojunction interfaces. A theoretical model, which treats trap levels in the AlAs barrier as intermediate states for two–step tunneling processes, is developed and discussed in the case of p–type barrier structures. Calculations indicate that this impurity–assisted tunneling current can become important when the AlAs barrier is thick enough. Samples in which the AlAs layers are doped n–type are characterized by high current densities at low temperatures, even when the AlAs layers are very thick (140–730 Å). Furthermore, these samples do not display the proper relationship between current density and barrier thickness expected from tunnel structures. Energy band diagram calculations reveal that when the barrier layers are thick enough and/or sufficiently doped, the AlAs conduction band at the X–point is not fully depleted of electrons. The dominant low temperature current transport mech-

anism is then tunneling through two reduced AlAs X–point barriers separated by a bulk region of n–type AlAs. These results are consistent with the peaks observed in the second derivative spectra of the samples. These peaks may be attributed to the creation, by the tunneling electrons, of single AlAs X–point phonons in the barriers, or to the excitation of two AlAs X–point phonons, one near each heterojunction interface. In samples having sufficiently thin n–type AlAs layers, the AlAs conduction band remains totally depleted of free carriers. As a result, tunneling occurs through the AlAs band gap at the X–point and/or at the Γ–point, in a one–step process. The structure observed in the derivative spectra of these samples is shown to be consistent with the excitation of mixed plasmon–phonon modes by the tunneling electrons. Plasmons located near the GaAs/AlAs interfaces can interact with GaAs and AlAs longitudinal optical (LO) phonons when the doping density in the GaAs electrodes is such that the plasma frequency becomes comparable to the LO phonon frequencies.

Chapter 4 deals with GaAs/$Al_xGa_{1-x}As$ double barrier heterostructures grown epitaxially on [100]–oriented substrates. The resonant energy levels in the GaAs quantum well which produce negative differential resistances in the experimental I–V characteristics are identified. This is achieved by comparing the experimental data to results anticipated from the calculated energy band diagrams of the heterostructures. The validity of this approach is illustrated in the case of samples having direct band gap $Al_xGa_{1-x}As$ barrier layers. The negative differential resistances then arise without ambiguity from resonant tunneling via quasi–stationary states in the GaAs quantum well confined by the $Al_xGa_{1-x}As$ Γ–point potential energy barriers. However, taking into account band bending effects and the fractions of applied voltage dropping in the cladding layers is shown to be critical for obtaining good agreement between the positions of the quasi–stationary levels in the quantum well and the peaks in current observed in the

I–V curves. When the barrier layers are made of pure AlAs, resonant tunneling via quasi–bound Γ–states alone is often inconsistent with the I–V characteristics of the samples. However, the experimental data can usually be explained by tunneling via resonant states in the well confined by the AlAs X–point potential energy barriers as well as the AlAs Γ–point barriers. Furthermore, the quasi–bound X–states are found to be associated with the large longitudinal X–point electron mass in AlAs, and not with the small transverse effective mass. This indicates that tunneling through the AlAs band gap at the X–point arises primarily from the coupling of virtual AlAs X–point states with GaAs Γ–point states due to the breaking of translational symmetry in the direction perpendicular to the heterojunction interfaces. It may thus be anticipated that the dominant low temperature current transport mechanisms in GaAs/$Al_xGa_{1-x}As$ double barrier heterostructures in which the barrier layers are made of indirect band gap alloys are resonant tunneling via quasi–bound Γ– and X–states. However, it is observed that the relative contributions of these two mechanisms differ from sample to sample. In some cases, they also depend upon the sign of the applied bias. Such effects should thus be related to the quality of the materials and the heterojunction interfaces. Resonant tunneling is also investigated in double barrier heterostructures in which a low doped GaAs buffer layer is grown between the degenerately doped GaAs electrode adjacent to the substrate and the first $Al_xGa_{1-x}As$ quantum barrier. As long as the buffer layer is thin compared to the GaAs electrode on top of which it is grown, the structure behaves as if it had a uniformly doped back GaAs cladding layer. The average doping density in this layer decreases as the GaAs buffer layer is made thicker and/or more lightly doped. In these samples, the negative differential resistances corresponding to a given resonant state in the quantum well may be observed in the experimental I–V characteristics at very different applied voltages in reverse bias than in

forward bias. This may be used to determine the degree of asymmetry between the doping density in the top GaAs electrode and the average doping level in the back cladding layer.

In Chapter 5, we propose and analyze three–terminal devices based upon resonant tunneling through quantum well and quantum barrier heterostructures. Although other semiconductors could be used, the devices are presented in the context of GaAs/$Al_xGa_{1-x}As$ heterojunction technology. Since tunneling is the main current transport mechanism, these devices should feature the high–speed capabilities associated with tunnel structures. Two types of resonant tunneling transistors are proposed. The first kind includes two configurations in which the relative positions of the base and collector are interchanged with respect to the conventional emitter–base–collector sequence. This provides a means for obtaining negligible base currents and large current transfer ratios. In the proposed devices, a base voltage controls the emitter–collector tunneling current by shifting the resonances in a quantum well. Calculations indicate that significant variations in the emitter–collector current–voltage characteristics can be obtained for reasonable base–emitter voltages. These two devices are called a "Stark Effect Transistor," and a "Negative Resistance Stark Effect Transistor," respectively. In the second type of three–terminal devices, the current through a double barrier heterostructure is modulated by a Schottky barrier gate placed along the path of the electrons. In fact, these devices can be viewed simply as tunnel structures integrated with Schottky barrier field effect transistors (FET's). Three configurations are proposed and analyzed. All of them feature, in their output current–voltage (I_D–V_D) curves, negative differential resistances controlled by a gate voltage. Because of the high–speed characteristics associated with tunnel structures, these devices could find applications in tunable millimeter–wave oscillators, negative resistance amplifiers and high–speed digital circuits.

Chapter 6 is concerned with a growth characterization of the GaAs/Al_x $Ga_{1-x}As$ single and double barrier heterostructures described throughout the thesis. First, the reproducibility and uniformity of the electrical characteristics of a number of MOCVD grown GaAs/AlAs tunnel structures are investigated. Current–voltage curves, along with their first and second derivatives, are measured for heterostructures having either one or two AlAs tunnel barriers. For each sample studied, sets of 10 to 80 identical devices having specific sizes and taken randomly across the wafer are systematically tested. Reproducible and uniform results are obtained, showing evidence that the doping concentrations and layer thicknesses are uniform across the samples under test. These results suggest further that, in single barrier tunnel structures, the average fluctuations in the thicknesses of ultra–thin layers can be as small as one atomic layer. Secondly, discrete fluctuations in layer thicknesses are reported in MOCVD grown GaAs/$Al_{0.35}Ga_{0.65}As$ double barrier heterostructures. These fluctuations cause the width of the GaAs quantum well to vary by discrete steps and the resonant states in the well to form sets of quasi–stationary levels. These sets of discrete levels are manifested by non–uniform experimental data and by sequences of negative differential resistances in the I–V characteristics of many devices. These results indicate that islands are formed during the growth of certain samples.

References

1. R. J. Hauenstein, L. J. Schowalter, B. D. Hunt, O. J. Marsh, and T. C. McGill, in *Proc. of the Mat. Res. Soc.*, Palo Alto, 1986 (to be published).

2. J. Heremans, D. L. Partin, and P. D. Dresselhaus, Appl. Phys. Lett. **48**, 644 (1986).

3. D. H. Chow, and T. C. McGill, Appl. Phys. Lett. **48**, 1485 (1986).

4. M. A. Reed, R. J. Koestner, and M. W. Goodwin, in *Proc. of the MCT workshop,* Dallas, 1986.

5. H. Toyoshima, Y. Ando, A. Okamoto, and T. Itoh, in *Proc. of the GaAs and Related Compounds Conf.*, Las Vegas, Oct. 1986.

6. R. T. Collins, J. Lambe, T. C. McGill, and R. D. Burnham, Appl. Phys. Lett. **44**, 532 (1984).

7. A. R. Bonnefoi, R. T. Collins, T. C. McGill, R. D. Burnham, and F. A. Ponce, Appl. Phys. Lett. **46**, 285 (1985).

8. I. Hase, H. Kawai, K. Kaneko, N. Watanabe, Electon. Lett. **20**, 491 (1984).

9. L. L. Chang, L. Esaki, and R. Tsu, Appl. Phys. Lett. **24**, 593 (1974).

10. D. Delagebeaudeuf, P. Delescluse, P. Etienne, J. Massies, M. Laviron, J. Chaplart, and N. T. Linh, Electron. Lett. **18**, 85 (1982).

11. P. Guéret, and U. Kaufmann, Electron. Lett. **21**, 344 (1985).

12. T. C. L. G. Sollner, W. D. Goodhue, P. E. Tannenwald, C. D. Parker, and D. D. Peck, Appl. Phys. Lett. **43**, 588 (1983).

13. M. A. Reed, "Excited State Resonant Tunneling in GaAs–$Al_xGa_{1-x}As$ Double Barrier Heterostructures," to be published in *Superlattices and Microstructures*, (Academic Press).

14. R. Tsu, and L. Esaki, Appl. Phys. Lett. **22**, 562 (1973).

15. B. Jogai, and K. L. Wang, Appl. Phys. Lett. **46**, 167 (1985).

16. T. J. Shewchuk, P. C. Chapin, P. D. Coleman, W. Kopp, R. Fischer, and H. Morkoç, Appl. Phys. Lett. **46**, 508 (1985).

17. H. C. Casey, and M. B. Panish, *Heterostructure Lasers. Part A*, (Academic Press, New York, 1978), p.192.

18. C. B. Duke, *Tunneling in Solids*, (Academic Press, New York, 1969).

19. C. J. Adkins, and W. A. Phillips, J. Phys. C **18**, 1313 (1985).

20. R. T. Collins, Ph.D. Thesis, California Institute of Technology, 1985.

21. T. C. L. G. Sollner, P. E. Tannenwald, D. D. Peck, and W. D. Goodhue, Appl. Phys. Lett. **45**, 1319 (1984).

22. F. Capasso, and R. A. Kiehl, J. Appl. Phys. **58**, 1366 (1985).

23. A. R. Bonnefoi, D. H. Chow, T. C. McGill, R. D. Burnham, and F. A. Ponce, J. Vac. Sci. Technol. B **4**, 988 (1986).

24. A. C. Marsh, "Indirect Band Gap Tunneling Through a (100)–GaAs/AlAs/GaAs Heterostructure," to be published in IEEE J. Quantum Electronics.

Chapter 2

Energy Band Diagrams and Current–Voltage Characteristics of Single Barrier Tunnel Structures

2.1 Introduction

Semiconductor quantum well and quantum barrier heterostructures are the object of considerable theoretical and experimental work. The small characteristic dimensions of these structures makes tunneling an important current transport mechanism. Although other materials are being studied,[1–3] GaAs and $Al_xGa_{1-x}As$ continue to be used extensively. For these materials, emphasis is currently being placed on resonant tunneling structures which display negative differential resistances in their I–V characteristics,[4–10] may operate at very high frequencies,[6,11] and are expected to be incorporated in high–speed three–terminal devices.[12–14] However, understanding the current transport mechanisms taking

place in single barrier structures is still of interest. These constitute the basic units of a number of more elaborate heterostructures and make it possible to study some fundamental physical properties of tunnel structures such as inelastic processes, band offsets and band structures. Furthermore, they have recently been the object of a revived interest since it has been proposed that, in some cases, they may produce negative differential resistances.[2,3]

In investigating the possible current transport mechanisms taking place in single barrier structures, experimental current–voltage (I–V) characteristics are usually compared to theoretical I–V curves obtained from simple models.[15–17] These models all assume that the entire applied voltage drops linearly across the barrier layer. However, tunneling currents are extremely sensitive to the actual shape of the barrier through which the charge carriers tunnel and to the voltage drop distribution not only in the barrier but also in the electrodes. Energy band diagram calculations are thus important whether the barrier is doped or not. In addition, energy band profiles reveal that, in some cases, the dominant current transport mechanisms may differ significantly from those expected when band bending is neglected.

In this chapter, we concentrate primarily on the importance of energy band diagrams in calculating tunneling currents through double heterojunctions, and in understanding some of the electronic properties of these structures. In Chapter 3, these concepts will be related to an experimental study of elastic and inelastic tunneling processes in MOCVD grown GaAs–AlAs–GaAs heterostructures.

Although tunnel structures are often grown with nominally undoped barrier layers,[15–17] cases in which barriers are purposely doped may also be important: *(i)* in investigating how electronic properties and scattering mechanisms may vary when dopings are changed from p–type to n–type and from high to low;[18,19] and *(ii)* in tailoring quantum barriers to particular heights and shapes. Further-

more, ultra–thin layer doping levels are still difficult to control and determine accurately. As a result, even when barriers are grown nominally undoped, non–negligible background dopings or dopant memory effects may in fact cause them to be doped to a significant level and modify the experimental data.[20]

Section 2.2 presents the theoretical basis used to calculate the energy band diagrams and current density vs. voltage (J–V) characteristics of single barrier tunnel structures. In section 2.3, n^+–p–n^+ heterostructures are discussed and illustrated for the GaAs/$Al_xGa_{1-x}As$ system. It is found that applying a bias voltage alters the shapes of the band edges not only in the barrier but also in the cladding layers. Furthermore, the voltage drop distributions across the structures are strong functions of barrier thickness, electrode doping densities and barrier doping concentration. This occurs because the amount of band bending increases when the barrier layer is made thicker or more heavily doped, or when the electrode doping is reduced. The calculated J–V curves are found to be very sensitive to the barrier doping density. Tunneling characteristics could thus provide useful information about very thin layer doping levels, which are not directly accessible experimentally. Section 2.4 is devoted to heterostructures having undoped barrier layers. In these structures as well, the voltage drop distributions and the J–V curves may differ significantly from those based on the commonly made assumption that the entire applied voltage drops linearly across the barrier. Results obtained from n^+–n–n^+ heterostructures are discussed in section 2.5. It is found that as long as the barrier layer is thin enough and not too heavily doped, it remains totally depleted of carriers and the energy band profiles bear a number of similarities with those of p–type or undoped barrier structures. However, if the barrier is thick enough and/or sufficiently doped, it may feature a region with bulk–like properties. Energy band diagrams indicate that when this occurs, the dominant current transport mechanisms may be different from

those predicted by the simple linear voltage drop model. This result is illustrated for GaAs–AlAs–GaAs heterostructures. In section 2.6, other cases of interest are presented. In particular, we consider structures in which the electrodes are degenerately doped p–type and current transport occurs via the tunneling of holes. We also consider single barrier tunnel structures from which negative differential resistances may be expected. We show that energy band diagrams are useful in properly choosing the parameters of such heterostructures. Although these concepts are illustrated in the case of $Hg_{1-x}Cd_xTe$–CdTe–$Hg_{1-x}Cd_xTe$ double heterojunctions, other materials could be similarly analyzed. Finally, the results of this study are summarized in section 2.7.

2.2 Theoretical Basis

2.2.1 Energy Band Diagrams

An energy band profile is found most readily by solving Poisson's equation, which relates the space charge density $\rho(\vec{r})$ to the electric displacement $\vec{\mathcal{D}}(\vec{r})$ as

$$\vec{\nabla} \cdot \vec{\mathcal{D}}(\vec{r}) = \rho(\vec{r}). \tag{2.1}$$

Taking a linear relationship between $\vec{\mathcal{D}}$ and the static electric field $\vec{\mathcal{E}}$ as $\vec{\mathcal{D}} = \epsilon\vec{\mathcal{E}}$, Poisson's equation becomes, in one dimension:

$$\frac{d\mathcal{E}(x)}{dx} = \frac{\rho(x)}{\epsilon} \equiv \frac{\rho(x)}{\epsilon_0 \epsilon_r}, \tag{2.2}$$

where ϵ is the dielectric constant of the material and ϵ_0 the vacuum value.

In calculating energy band profiles, it is more convenient to solve directly for the conduction band edge energy $E_c(x)$, or the valence band edge energy $E_v(x)$, which may be related to the electrostatic potential $\psi(x)$ or the electric field $\mathcal{E}(x)$ as

$$\frac{dE_c(x)}{dx} = \frac{dE_v(x)}{dx} = -e\frac{d\psi(x)}{dx} = e\mathcal{E}(x), \tag{2.3}$$

where e is the magnitude of the electronic charge.

Poisson's equation then takes the form

$$\frac{d^2E_c(x)}{dx^2} = \frac{d^2E_v(x)}{dx^2} = \frac{e\rho(x)}{\epsilon_0\epsilon_r}. \tag{2.4}$$

The charge density $\rho(x)$ is the sum of all the charged species present in the material:

$$\rho(x) = -e(n - p + n_A - n_D), \tag{2.5}$$

where n is the electron density in the conduction band, p is the hole density in the valence band, n_A is the density of ionized acceptors, and n_D is the density of ionized donors.

The number of occupied conduction band levels is

$$n = \frac{2}{\sqrt{\pi}} N_c(T)\, \mathcal{F}_{1/2}\Big(\frac{\mu - E_c}{kT}\Big). \tag{2.6}$$

In this equation, μ is the chemical potential; $N_c(T)$ is the effective density of states in the conduction band given by

$$N_c(T) = \frac{1}{4}\left(\frac{2m_e^*kT}{\pi\hbar^2}\right)^{3/2}, \tag{2.7}$$

where m_e^* is the density–of–states effective mass for electrons in the conduction band; and $\mathcal{F}_{1/2}(\varsigma)$ is the Fermi–Dirac integral defined by

$$\mathcal{F}_{1/2}(\varsigma) = \int_0^\infty \frac{\epsilon^{1/2}}{1 + exp(\epsilon - \varsigma)}\, d\epsilon. \tag{2.8}$$

For the Boltzmann statistics case in nondegenerate semiconductors, Eq.(2.6) reduces to the well known form

$$n = N_c(T)\, exp\Big(-\frac{E_c - \mu}{kT}\Big)\,. \tag{2.9}$$

In the case of degenerate semiconductors, the Fermi–Dirac integral form (2.6) must be used to obtain the electron density at finite temperature. However,

simple expressions may be obtained at absolute zero:

$$n = \begin{cases} 0, & E_f < E_c; \\ \frac{1}{3\pi^2}\left(\frac{2m_e^*}{\hbar^2}\right)^{3/2}(E_f - E_c)^{3/2} \equiv A_e(E_f - E_c)^{3/2}, & E_f \geq E_c, \end{cases} \tag{2.10}$$

where E_f is the Fermi energy.

Similarly, the hole density in the valence band at absolute zero is given by

$$p = \begin{cases} 0, & E_f > E_v; \\ \frac{1}{3\pi^2}\left(\frac{2m_h^*}{\hbar^2}\right)^{3/2}(E_v - E_f)^{3/2} \equiv A_h(E_v - E_f)^{3/2}, & E_f \leq E_v. \end{cases} \tag{2.11}$$

In this equation, m_h^* is the density–of–states effective mass for holes in the valence band:

$$m_h^* = \left({m_{lh}^*}^{3/2} + {m_{hh}^*}^{3/2}\right)^{2/3}, \tag{2.12}$$

where m_{lh}^* and m_{hh}^* refer to the light and heavy hole masses, respectively.

Calculating energy band profiles in the direction perpendicular to the layers of double heterojunctions thus involves solving Poisson's equation while satisfying the appropriate boundary conditions and requiring overall charge neutrality across the structure. The boundary conditions are as follows. *(i)* Far enough away from the barrier layer, the semiconductor properties are bulk–like. *(ii)* If there are no charges localized at the interfaces, the electric displacement $\mathcal{D} = \epsilon\mathcal{E}$ must be continuous. For an interface at $x = x_0$, between two regions (I) and (II), we thus have $\epsilon_I \mathcal{E}_I(x_0) = \epsilon_{II}\mathcal{E}_{II}(x_0)$. *(iii)* At each interface between two different semiconductors, the band edges are discontinuous by a given amount equal to the corresponding band offset. *(iv)* Under no applied bias, the Fermi level remains constant throughout the entire structure. Under an applied bias V_a, the Fermi levels in the electrodes must differ by $\pm eV_a$, depending on the polarity.

The expressions necessary for obtaining the energy band diagrams of single barrier heterostructures are developed from the above equations under the following assumptions. *(i)* The interfaces are assumed to be abrupt. This constitutes a fairly good approximation in many structures, for improvements in

growth techniques now allow the fabrication of interfaces as sharp as one atomic layer. *(ii)* The temperature is assumed to be 0 K. The major advantage of this approximation is that Eqs.(2.10) and (2.11) for the carrier densities may be used instead of the corresponding Fermi–Dirac integral forms. As a result, calculations may be greatly simplified and a number of equations can be solved analytically. In fact, the 0 K approximation remains quite good as long as it is used to describe low temperature properties of heterostructures. This is usually the case in tunnel structures, which are frequently studied at liquid nitrogen temperatures and lower. *(iii)* Two–dimensional energy subbands in accumulation layers are neglected. Whenever accumulation regions exist, the corresponding subbands should be solved for self–consistently and the appropriate density of states should be used in the calculations. Although this effect may reduce the current densities obtained from our simple model, it should not alter the results of our calculations qualitatively. *(iv)* The densities of ionized impurities in each layer are assumed to be determined experimentally, either from the flow rates or beam fluxes used during sample growth, or from doping profile or Hall measurement techniques. In nondegenerate semiconductors, free carriers are frozen out at low temperatures. However, in degenerate materials, impurity bands are formed, which extend into the conduction or valence bands and produce large free carrier concentrations even at low temperatures. If band tailing effects are neglected, the Fermi level of a degenerate bulk material at 0 K may be expressed in a very simple form. For an n–type semiconductor having a density of ionized donors n_D, it follows from Eq.(2.10) that

$$E_f - E_c \equiv \delta_e = \frac{\hbar^2}{2m_e^*}(3\pi^2 n_D)^{2/3}. \quad (2.13)$$

Similarly, for a bulk p–type semiconductor having a density of ionized acceptors n_A,

$$E_v - E_f \equiv \delta_h = \frac{\hbar^2}{2m_h^*}(3\pi^2 n_A)^{2/3}. \quad (2.14)$$

2.2.2 J–V Characteristics

In this section, energy band diagrams are used to calculate the J–V characteristics of single barrier heterostructures. These calculations are based upon the model of Tsu and Esaki.[4] In this approach, the electrons in each of the two cladding layers are assumed to form independent Fermi gases. Therefore, if $f(E, E_f)$ is defined to be the Fermi distribution function:

$$f(E, E_f) \equiv \frac{1}{exp[(E - E_f)/kT] + 1}, \tag{2.15}$$

the occupation probabilities for a state of energy E may be written as $f(E, E_f^l)$ and $f(E, E_f^r)$ in the left and right electrodes, respectively. If V_a is the voltage applied to the heterostructure, E_f^l and E_f^r, the Fermi levels in the left and right cladding layers, are related by

$$E_f^l - E_f^r = eV_a. \tag{2.16}$$

The current density in the x–direction, perpendicular to the planes of the layers, is then given by [4]

$$J_x = \frac{e}{4\pi^3 \hbar} \int_{k_x > 0} d^3k \, (f(E, E_f^l) - f(E, E_f^r)) \cdot T \cdot \frac{\partial E}{\partial k_x}, \tag{2.17}$$

where T is the transmission probability for an electron tunneling through the barrier with energy E. In Eq.(2.17), E is measured with respect to the conduction band edge in the left electrode at the first heterojunction interface.

In this paper, the WKB approximation is used to calculate T:

$$T \propto \exp(-2 \int_0^a \kappa \, dx), \tag{2.18}$$

where κ is the imaginary part of the electron wavevector in the barrier of thickness a. κ is evaluated by using the two–band model, $\mathbf{k} \cdot \mathbf{p}$ theory formula described by Kane:[21]

$$\kappa = \left\{ \frac{2m_0}{\hbar^2} \left[\left[E_{g_b}^2 (1 - \frac{m_0}{2m_b^*})^2 + E_{g_b}(E - E_{v_b}(x))(\frac{m_0}{m_b^*} - 1) \right]^{\frac{1}{2}} - E + E_{v_b}(x) - E_{g_b}(\frac{m_0}{2m_b^*} - 1) \right] \right\}^{\frac{1}{2}}, \tag{2.19}$$

where m_b^*, E_{g_b}, and $E_{v_b}(x)$ are the electron effective mass, the energy gap, and the valence band edge in the barrier, respectively.

This one–parameter (effective mass) formula is valid in the forbidden gap of a direct semiconductor such as $Al_xGa_{1-x}As$ with $x < 0.40 - 0.45$. In the case of an indirect band gap semiconductor such as AlAs, it is more appropriate to use the simple "one–band model" formula:

$$\kappa(x) = \left[\frac{2m_b^*(E_{c_b}(x) - E)}{\hbar^2}\right]^{1/2}, \tag{2.20}$$

where $E_{c_b}(x)$ denotes the conduction band edge in the barrier.

2.3 p–Type Barrier Structures

Let us first consider n^+–p–n^+ double heterojunctions featuring a single p–type barrier layer between two degenerately doped n–type electrodes. A schematic diagram of the conduction and valence band edges of such a structure under no applied bias is illustrated in Fig.2.1. The two interfaces at $x = 0$ and $x = a$ define three spatial regions labeled (I), (II) and (III) in Fig.2.1, which correspond to the left electrode, the barrier and the right electrode, respectively. Since the carriers of importance in electronic transport across these structures are conduction band electrons, the energy band diagrams are described in terms of the conduction band edge $E_c(x)$. Since $E_c(x) - E_v(x) = E_g$, the valence band edge $E_v(x)$ in any region follows immediately from the value of the band gap, E_g, in that region.

As shown in Fig.2.1, the p–type doping in the barrier causes the bands to bend upward. As a result, the barrier conduction band remains totally depleted of carriers and space–charge regions are formed in the cladding layers near the interfaces. At the edges of the space–charge regions, taken as c_1 and c_3 in the left and right electrodes, respectively, the bands flatten and the semiconductor

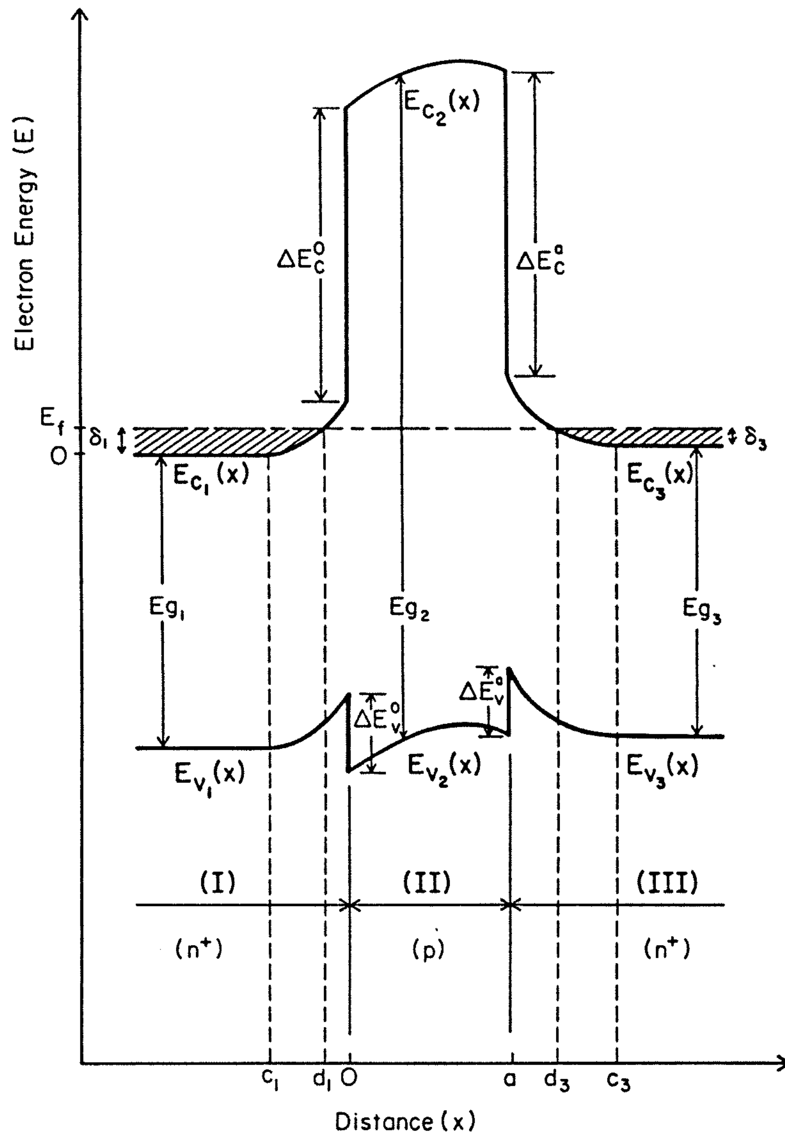

Figure 2.1: Schematic energy band diagram for an arbitrary n^+–p–n^+ single barrier heterostructure under no applied bias. E_f is the Fermi energy. $E_c(x)$ and $E_v(x)$ denote the conduction and valence band edges, respectively. ΔE_c^0 (ΔE_v^0) and ΔE_c^a (ΔE_v^a) are the conduction (valence) band offsets at the heterojunction interfaces. The origin of energy is taken to be the conduction band edge in the left neutral semiconductor.

properties become bulk–like. In the space–charge regions and the barrier, ($c_1 < x < c_3$), an electric field $|\mathcal{E}| > 0$ exists, whereas $\mathcal{E} \equiv 0$ in the bulk semiconductor regions ($x \leq c_1$ and $x \geq c_3$). In the most general case depicted in Fig.2.1, each cladding layer space–charge region may be divided into two subregions: *(i)* one which is fully depleted of carriers and adjacent to the interface, such as regions $d_1 < x \leq 0$ and $a \leq x < d_3$ in semiconductors (I) and (III), respectively; and *(ii)* one which is only partially depleted and extends up to the edge of the space–charge layer, such as regions $c_1 < x \leq d_1$ and $d_3 \leq x < c_3$ in semiconductors (I) and (III), respectively. According to the structure parameters and the bias conditions, the fully depleted layers may or may not exist.

In this chapter, the widths of the entire space–charge regions are referred to as Λ_D^l in the left electrode and Λ_D^r in the right electrode. When fully depleted regions exist in the left and/or the right cladding layers, their respective widths are labeled λ_D^l and λ_D^r. The notations used in Fig.2.1 thus yield $\Lambda_D^l \equiv -c_1$; $\Lambda_D^r \equiv c_3 - a$; $\lambda_D^l \equiv -d_1$; and $\lambda_D^r \equiv d_3 - a$.

Let $y(x) \equiv E_f - E_c(x)$. In terms of this new variable, Poisson's equation (Eq.2.4) becomes

$$\frac{d^2y(x)}{dx^2} \equiv y''(x) = -\frac{e\rho(x)}{\epsilon_0\epsilon_r}. \tag{2.21}$$

Let $\Delta E_c^0(\Delta E_v^0)$ and $\Delta E_c^a(\Delta E_v^a)$ denote the conduction (valence) band offsets at $x = 0$ and $x = a$. The ionized donor concentrations in semiconductors (I) and (III) are n_{D_1} and n_{D_3}, and the density of ionized acceptors in the barrier layer is n_{A_2}. If Poisson's equation is integrated in each region using the boundary conditions described previously, the following relationships, expressed with the notations of Fig.2.1, are obtained.

$x \leq c_1$: Neutral bulk semiconductor in the left electrode

$$\rho_1(x) = 0,$$

$$y_1(x) = \delta_1 \equiv \frac{\hbar^2}{2m_1^*}(3\pi^2 n_{D_1})^{2/3}. \tag{2.22}$$

$c_1 < x \leq d_1$: Partially depleted space–charge region in the left electrode

$$\rho_1(x) \approx -en_1(x) + en_{D_1},$$

$$n_1(x) = \frac{1}{3\pi^2}\left(\frac{2m_1^*}{\hbar^2}\right)^{3/2}[y_1(x)]^{3/2} \equiv A_1[y_1(x)]^{3/2},$$

$$[y'_1(x)]^2 = 2\left(\frac{e^2 n_{D_1}\delta_1}{\epsilon_0\epsilon_{r_1}}\right)\left\{\frac{2}{5}\left[\frac{y_1(x)}{\delta_1}\right]^{5/2} - \left[\frac{y_1(x)}{\delta_1}\right] + \frac{3}{5}\right\}, \tag{2.23}$$

with

$$y_1(c_1) = \delta_1,$$

$$y'_1(c_1) = 0.$$

$d_1 < x \leq 0$: Totally depleted space–charge region in the left electrode

$$\rho_1(x) \approx en_{D_1},$$

$$y_1(x) = -\left(\frac{e^2 n_{D_1}}{\epsilon_0\epsilon_{r_1}}\right)\frac{x^2}{2} + y_1'(0)\,x + y_1(0), \tag{2.24}$$

with

$$y_1(d_1) = 0,$$

$$y'_1(d_1) = -\sqrt{\frac{6}{5}\left(\frac{e^2 n_{D_1}\delta_1}{\epsilon_0\epsilon_{r_1}}\right)},$$

$$y_1'(0) = -\sqrt{2\left(\frac{e^2 n_{D_1}\delta_1}{\epsilon_0\epsilon_{r_1}}\right)\left(\frac{3}{5} - \left[\frac{y_1(0)}{\delta_1}\right]\right)}.$$

$0 \leq x \leq a$: Barrier layer

$$\rho_2(x) \approx -en_{A_2},$$

$$y_2(x) = \left(\frac{e^2 n_{A_2}}{\epsilon_0 \epsilon_{r_2}}\right)\frac{x^2}{2} + y_2'(0)\,x + y_2(0), \tag{2.25}$$

with

$$y_2(0) = y_1(0) - \Delta E_c^0,$$

$$y'_2(0) = \left(\frac{\epsilon_{r_1}}{\epsilon_{r_2}}\right) y_1'(0).$$

$a \leq x < d_3$: Totally depleted space–charge region in the right electrode

$$\rho_3(x) \approx e n_{D_3},$$

$$y_3(x) = -\left(\frac{e^2 n_{D_3}}{\epsilon_0 \epsilon_{r_3}}\right)\frac{(x-a)^2}{2} + y_3'(a)\,(x-a) + y_3(a), \tag{2.26}$$

with

$$y_3(a) = y_2(a) - \Delta E_c^a,$$

$$y'_3(a) = \left(\frac{\epsilon_{r_2}}{\epsilon_{r_3}}\right) y_2'(a).$$

$d_3 \leq x < c_3$: Partially depleted space–charge region in the right electrode

$$\rho_3(x) \approx -e n_3(x) + e n_{D_3},$$

$$n_3(x) = \frac{1}{3\pi^2}\left(\frac{2m_3^*}{\hbar^2}\right)^{3/2} [y_3(x)]^{3/2} \equiv A_3 [y_3(x)]^{3/2},$$

$$[y'_3(x)]^2 = 2\left(\frac{e^2 n_{D_3}\delta_3}{\epsilon_0 \epsilon_{r_3}}\right)\left\{\frac{2}{5}\left[\frac{y_3(x)}{\delta_3}\right]^{5/2} - \left[\frac{y_3(x)}{\delta_3}\right] + \frac{3}{5}\right\}, \tag{2.27}$$

with

$$y_3(d_3) = 0,$$

$$y'_3(d_3) = \sqrt{\frac{6}{5}\left(\frac{e^2 n_{D_3}\delta_3}{\epsilon_0 \epsilon_{r_3}}\right)}.$$

$x \geq c_3$: Neutral bulk semiconductor in the right electrode

$$\rho_3(x) = 0,$$

$$y_3(x) = \delta_3 \equiv \frac{\hbar^2}{2m_3^*}(3\pi^2 n_{D_3})^{2/3}. \tag{2.28}$$

Eqs.(2.23) and (2.27) are then integrated numerically to obtain $y(x)$, and thus $E_c(x)$, in each region. Once a value of the Fermi level with respect to the conduction band edge at $x = 0$ (i.e., $y_1(0)$) is set, Eqs.(2.24), (2.23) and (2.22) are successively used to find $y_1(x)$ in region (I) and determine d_1 and c_1. Then, Eqs.(2.25)–(2.28) yield $y_2(x)$ in layer (II) and $y_3(x)$ in region (III), along with d_3 and c_3. The total charge Q across the structure then takes the form:

$$\frac{Q}{e} = -c_1 n_{D_1} - a n_{A_2} + (c_3 - a) n_{D_3} - A_1 \int_{c_1}^{d_1} [y_1(x)]^{3/2}\, dx - A_3 \int_{d_3}^{c_3} [y_3(x)]^{3/2}\, dx. \tag{2.29}$$

Different values of $y_1(0)$ are chosen until Q is found to be zero. It should be noted that $y_1(0)$ and $y_3(a)$ may be positive or negative, depending on the structure parameters. When $y_1(0)$ remains positive, $d_1 \equiv 0$ and $\lambda_D^l \equiv 0$. Similarly, whenever $y_3(a)$ is positive, $d_3 \equiv a$ and $\lambda_D^r \equiv 0$.

Two examples of these calculations are illustrated in Fig.2.2 in the case of GaAs–$Al_{0.3}Ga_{0.7}As$–GaAs heterostructures. Only the conduction band edges are displayed and the origin of energy is taken to be the conduction band edge in the left neutral semiconductor. Since GaAs and $Al_{0.3}Ga_{0.7}As$ are direct band gap materials, the energy band profiles correspond to the Γ–point conduction band edges. In GaAs ($Al_{0.3}Ga_{0.7}As$), the effective mass is taken to be $0.067\, m_0$ ($0.092\, m_0$), the relative dielectric constant is 13.1 (12.2), and the low temperature band gap is chosen to be 1.52 eV (1.89 eV).[22] A valence band discontinuity of $(0.55 \times x)$ eV is assumed at GaAs/$Al_xGa_{1-x}As$ interfaces,[23] resulting here in a conduction band offset of 210 meV. In Fig.2.2(a), a region which is totally

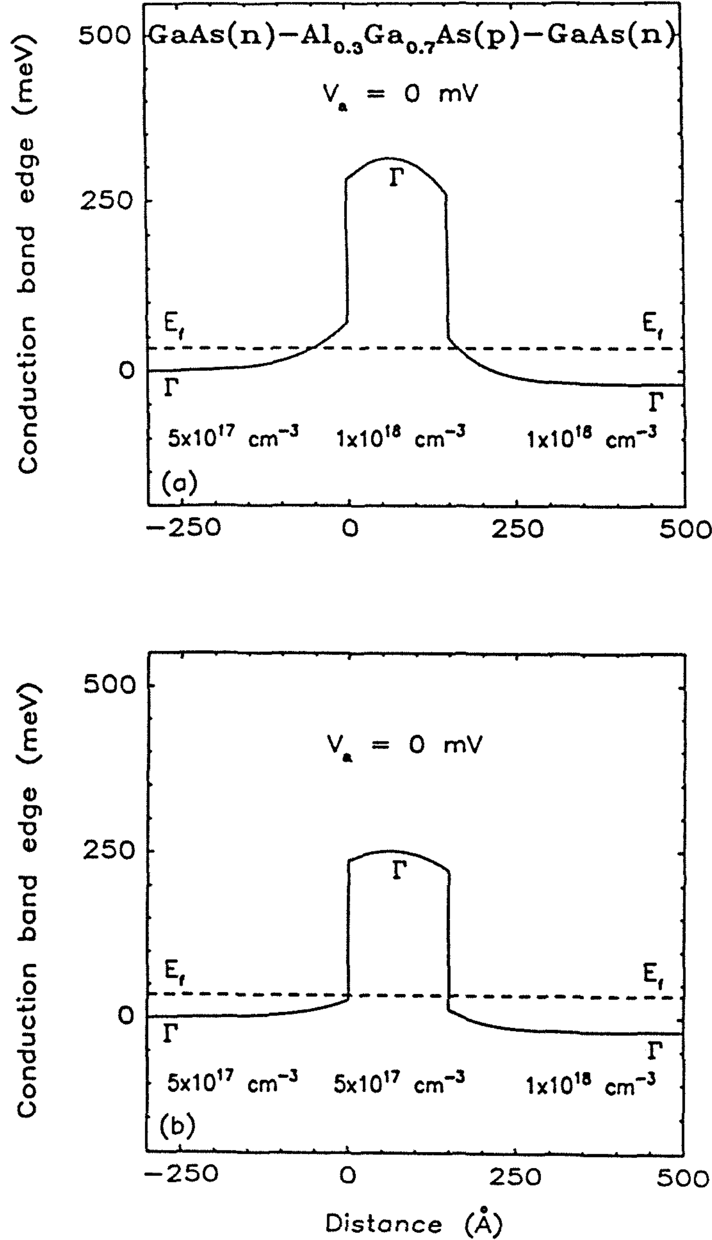

Figure 2.2: Calculated Γ–point conduction band edges, as functions of distance in the direction perpendicular to the planes of the layers, for n^+–p–n^+ GaAs–$Al_{0.3}Ga_{0.7}As$–GaAs heterostructures under no applied bias. Free carrier densities of 5×10^{17} and $1 \times 10^{18} cm^{-3}$ are taken in the left and right GaAs electrodes, respectively. The density of ionized acceptors in the 150 Å thick $Al_{0.3}Ga_{0.7}As$ barrier layer is $1 \times 10^{18} cm^{-3}$ in (a), and $5 \times 10^{17} cm^{-3}$ in (b). The conduction band discontinuity at the heterojunction interfaces is 210 meV.

depleted of carriers exists in each cladding layer, on either side of the barrier. The corresponding structure has a 150 Å thick p–type $Al_{0.3}Ga_{0.7}As$ barrier layer in which the density of ionized acceptors is $1 \times 10^{18} cm^{-3}$. The two n–type GaAs electrodes are asymmetrically doped, with free carrier densities of 5×10^{17} and $1 \times 10^{18} cm^{-3}$ in regions(I) and (III), respectively. This asymmetry causes the fully depleted space–charge region in the left electrode, (λ_D^l = 53 Å), to be broader than in the right electrode, (λ_D^r = 14 Å). For the same reason, the bands become flat a distance Λ_D^l = 396 Å away from the barrier in region (I), while bulk–like properties are encountered a distance Λ_D^r = 343 Å away from the barrier in region (III). In Fig.2.2(b), the structure is the same as in Fig.2.2(a), except that the density of ionized acceptors in the barrier has been reduced to $5 \times 10^{17} cm^{-3}$. As a result, the amount of band bending is decreased and the totally depleted space–charge regions in the GaAs electrodes are suppressed. The bands also become flat closer to the barrier than in Fig.2.2(a), specifically 286 and 265 Å away from the heterojunction interfaces in the left and right cladding layers, respectively.

The examples illustrated in Fig.2.2 indicate that large amounts of band bending may be obtained for values of structure parameters commonly used in growing GaAs/$Al_xGa_{1-x}As$ heterostructures. They indicate further that the presence of ionized acceptors in region(II) may produce significant increases in barrier heights, and that barrier dopings are critical in determining the actual shapes of the barriers through which the GaAs electrons may tunnel. The most drastic effects occur whenever fully depleted space–charge regions exist in the electrodes. In Fig.2.2(a) for example, electrons near the Fermi level lie 280 meV below the barrier conduction band edge maximum and must tunnel through parts of the GaAs cladding layers in addition to the $Al_{0.3}Ga_{0.7}As$ barrier itself.

The energy band profiles of biased heterostructures may also be found using the approach described above once two assumptions are made: *(i)* steady–state

conditions; *(ii)* electrons flowing across the structures do not significantly alter the overall shapes of the band diagrams. When a bias voltage V_a is applied across a double heterojunction, the Fermi energies E_f^l and E_f^r in the bulk semiconductors (I) and (III), respectively, satisfy $E_f^l - E_f^r = eV_a$. Eqs.(2.22)–(2.24) and (2.26)–(2.28) still hold provided $y_1(x)$ and $y_3(x)$ are now defined with respect to the Fermi energy in the corresponding cladding layer:

$$y_1(x) = E_f^l - E_{c1}(x), \tag{2.30}$$

and

$$y_3(x) = E_f^r - E_{c3}(x). \tag{2.31}$$

In the barrier layer, Poisson's equation is integrated in terms of $E_{c2}(x)$, yielding

$$E_{c_2}(x) = -\left(\frac{e^2 n_{A_2}}{\epsilon_0 \epsilon_{r_2}}\right)\frac{x^2}{2} + E'_{c_2}(0)\,x + E_{c_2}(0), \tag{2.32}$$

with, at $x = 0$:

$$E_{c_2}(0) = E_f^l - y_1(0) + \Delta E_c^0,$$

$$E'_{c_2}(0) = -\left(\frac{\epsilon_{r_1}}{\epsilon_{r_2}}\right) y'_1(0);$$

and, at $x = a$:

$$y_3(a) = E_f^l - eV_a - E_{c_3}(a),$$

$$y'_3(a) = -\left(\frac{\epsilon_{r_2}}{\epsilon_{r_3}}\right) E'_{c_2}(a).$$

Two examples of these calculations are illustrated in Fig.2.3, in which 300 mV are applied across the structures depicted in Fig.2.2. They reveal that the applied voltage drops not only in the $Al_{0.3}Ga_{0.7}As$ barrier but also in the electrodes, (i.e., alters the shapes of the band edges in the cladding layers as well as in the barrier). The voltage drops V_1, V_2 and V_3 in regions (I), (II) and (III), respectively, are given by

$$eV_1 = [y_1(0)]_{V_a \neq 0} - [y_1(0)]_{V_a = 0}, \tag{2.33}$$

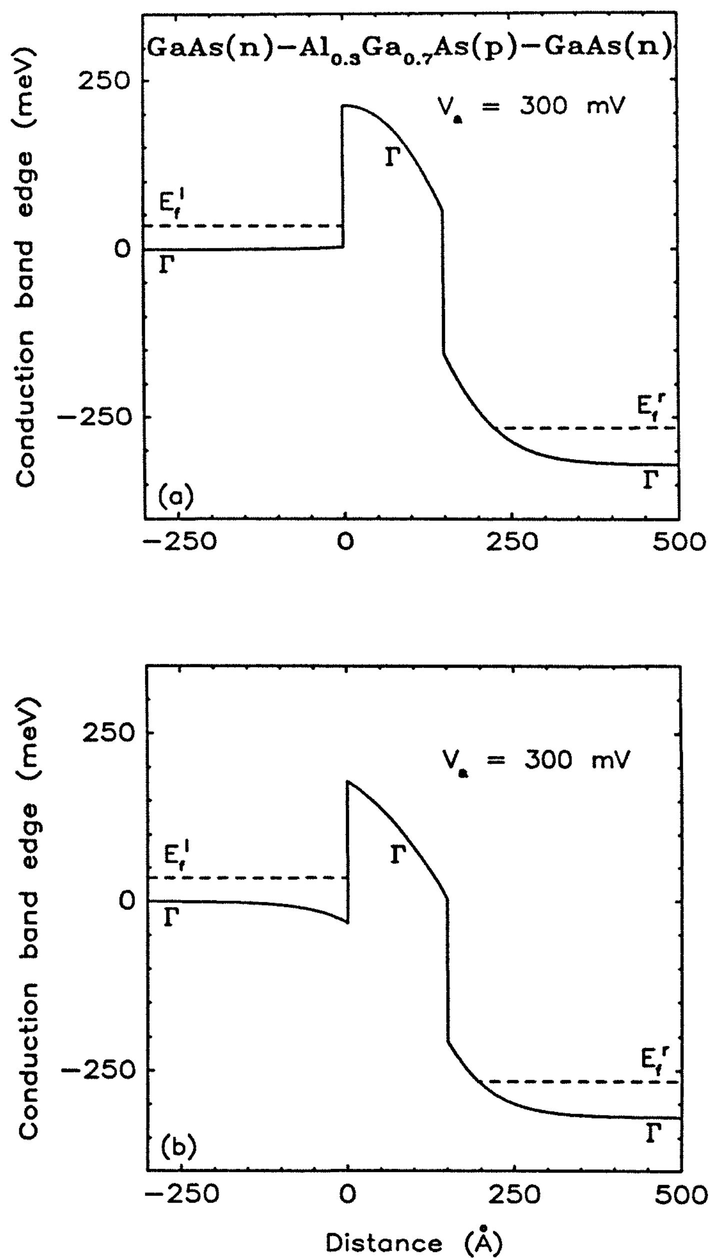

Figure 2.3: Calculated Γ–point conduction band edges for the same heterostructures as in Fig.2.2, under an applied bias of 300 mV. E_f^l (E_f^r) denotes the Fermi level in the left (right) cladding layer.

$$eV_2 = [E_{c_2}(0) - E_{c_2}(a)]_{V_a \neq 0} - [E_{c_2}(0) - E_{c_2}(a)]_{V_a=0}, \tag{2.34}$$

and

$$eV_3 = [y_3(a)]_{V_a=0} - [y_3(a)]_{V_a \neq 0}. \tag{2.35}$$

For the structure shown in Fig.2.3(b), 54% of the total applied bias drops in the barrier, while 19% and 27% drop in the left and right cladding layers, respectively. In the case depicted in Fig.2.3(a), only 45% of the applied voltage is dropped across the barrier, while 23% is dropped in the left electrode, and 32% in the right electrode. This occurs because more voltage drops in the cladding layers of the heterostructure featuring the larger zero–bias electrode space–charge regions, thus reducing the percentage of applied voltage dropping across the barrier.

Fig.2.3 also illustrates the general behavior of the energy band profiles of biased structures. As the negative voltage applied to the left electrode with respect to the right one is increased, the space–charge region in the right cladding layer becomes larger, and the percentage of total applied voltage dropping in region (III) increases. On the other hand, the depletion region in the left electrode is reduced and an accumulation layer appears when the heterostructure is sufficiently biased. As this accumulation layer becomes larger, the percentage of total applied bias dropping in region (I) is reduced, along with the effective conduction band offset, $\Delta E_{eff} \equiv (E_{c_2}(0) - E_f^l)$, for incident electrons near the Fermi level E_f^l. These results are illustrated in Figs.2.4 and 2.5, which correspond to the structure depicted in Figs.2.2(b) and 2.3(b). Fig.2.4 represents plots of the voltage drops $V_1(V_a)$, $V_2(V_a)$ and $V_3(V_a)$, expressed as percentages of the total applied bias, V_a. For this particular structure, the asymmetric electrode doping densities cause V_1 to be greater than V_3 at low voltages and the curves $V_1(V_a)$ and $V_3(V_a)$ to cross at $V_a = 150$ mV. In the case of symmetric structures, $V_1(V_a)$

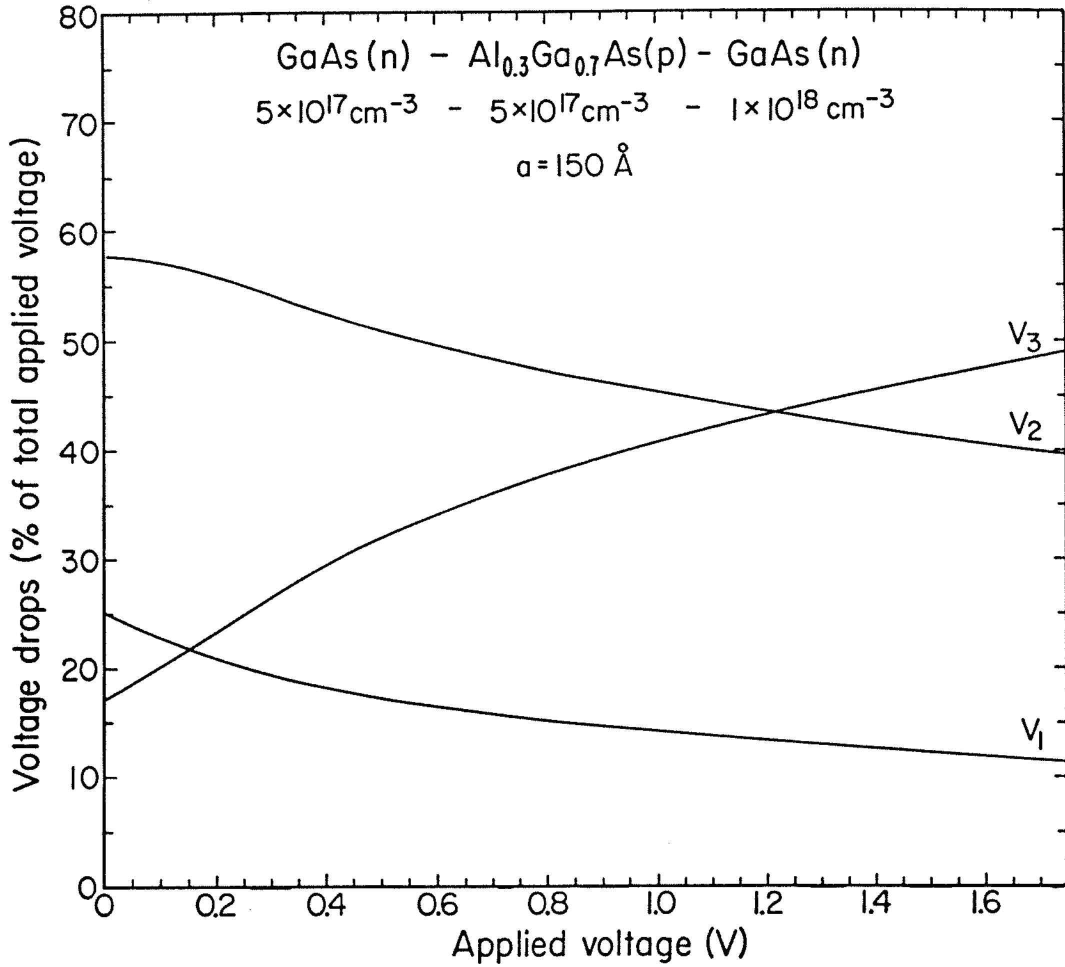

Figure 2.4: Voltage drops $V_1(V_a)$, $V_2(V_a)$ and $V_3(V_a)$ in regions (I), (II) and (III), respectively, for the n^+–p–n^+ structure illustrated in Figs.2.2(b) and 2.3(b). The voltage drops are expressed as percentages of the total applied bias V_a.

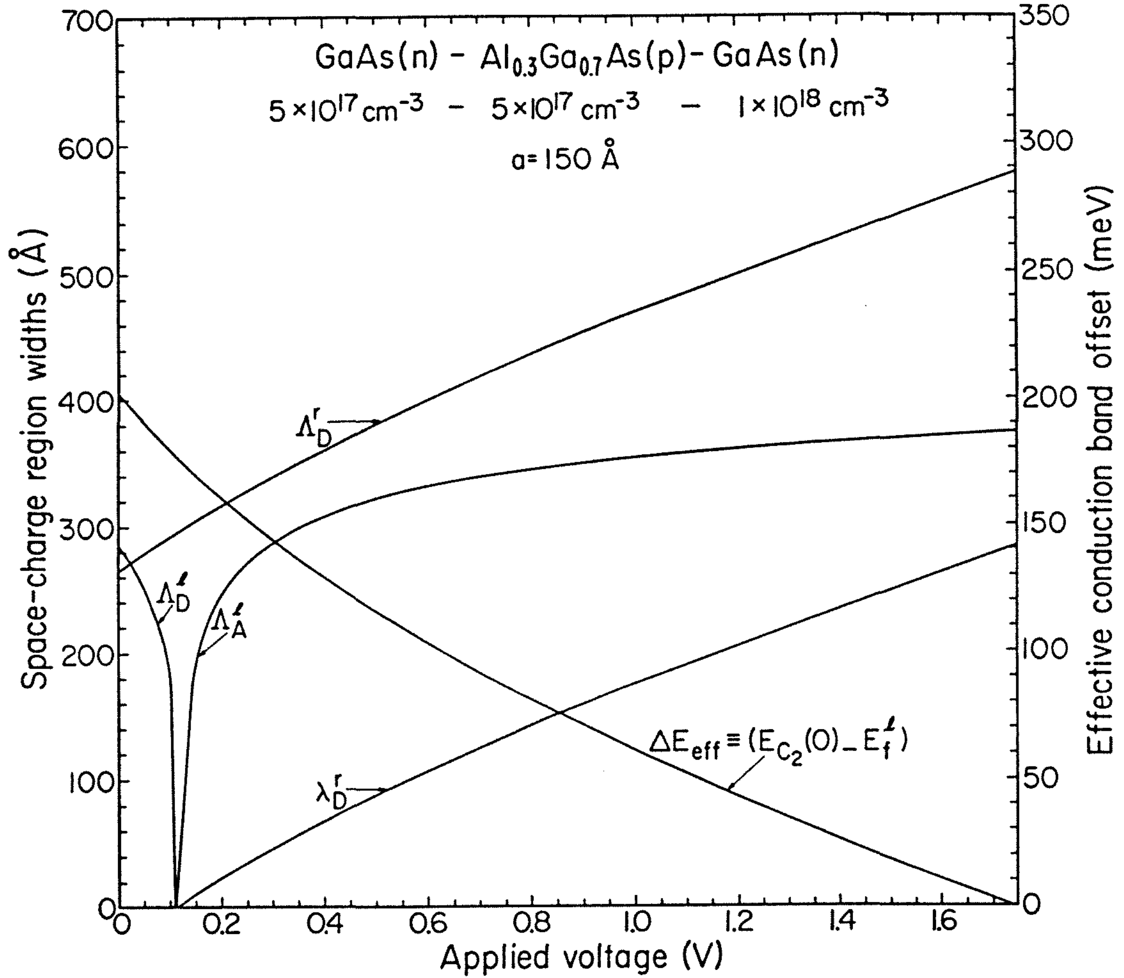

Figure 2.5: Variations with applied bias of the effective conduction band offset for incident electrons near the Fermi level E^l_f, $(\Delta E_{eff} \equiv E_{c_2}(0) - E^l_f)$, and of the widths of the cladding layer space–charge regions, $(\Lambda^l_D, \Lambda^l_A, \Lambda^r_D, \lambda^r_D)$. Λ^l_D (Λ^r_D) corresponds to the entire depletion layer in the left (right) electrode; λ^r_D denotes the width of the fully depleted space–charge region in the right cladding layer; Λ^l_A corresponds to the accumulation layer in the left electrode. The structure is the same as in Figs.2.2(b), 2.3(b) and 2.4.

and $V_3(V_a)$ cross at $V_a = 0$. As indicated in Fig.2.4, the rate at which $V_3(V_a)$ increases in region (III) is larger than the rate at which $V_1(V_a)$ decreases in region (I). It follows that $V_2(V_a)$ is a decaying function, and that V_3 becomes greater than V_2 when the largest fraction of the applied bias drops in the right electrode depletion region. In the case depicted in Fig.2.4, this occurs when $V_a \geq 1.22$ V. For this heterostructure, it should also be noted that the maximum value of V_2 is only $0.58\,V_a$. This is in disagreement with simple models which neglect band bending and assume that the entire applied voltage drops in the barrier.

In Fig.2.5, the widths of the total space–charge regions in the electrodes, Λ^l_D, Λ^l_A and Λ^r_D, are plotted against V_a, along with the depletion length λ^r_D in the right cladding layer and the effective conduction band offset ΔE_{eff}. When $V_a = 110$ mV, a totally depleted region appears in the right electrode. As V_a is further increased, the charge motion occurring in region (III) is manifested through monotonic increases in the band curvature and the length λ^r_D of the fully depleted space–charge layer. The width Λ^r_D of the total space–charge region thus increases by the same amount, and the two curves $\Lambda^r_D(V_a)$ and $\lambda^r_D(V_a)$ remain parallel. Whereas these two functions are monotonic and slowly varying over the entire voltage range, the space–charge region in the left electrode behaves quite differently. As V_a increases from zero, the positive curvature of the band edges in region (I) is reduced, causing Λ^l_D to decrease rapidly and vanish at $V_a = 110$ mV. At larger applied voltages, the band edge curvature in the left cladding layer becomes negative and charges accumulate near the interface at $x = 0$. As shown in Fig.2.5, the accumulation length Λ^l_A first increases very rapidly with V_a. However, the slope of $\Lambda^l_A(V_a)$ gradually decreases and becomes smaller than that of $\Lambda^r_D(V_a)$ at applied voltages greater than 350 mV. This behavior is closely related to the evolution of the band edge curvature with bias in the cladding layers. At low voltages, the curvature of the bands in region (I) is much smaller

than in region (III). As a result, for the same amount of charges accumulating in the left electrode and depleting the right electrode, the variation in accumulation length in region (I) is greater than the variation in depletion length in region (III). As V_a is made larger, the curvature of the bands increases faster in the left cladding layer than in the right one and the slope of $\Lambda^l_A(V_a)$ is reduced. Eventually, when $V_a \geq 350$ mV, the curvature of the bands becomes larger in region (I) than in region (III) and the variation in accumulation length in the left electrode becomes smaller than the variation in depletion length in the right electrode. The effective conduction band offset, $\Delta E_{eff}(\equiv E_{c2}(0) - E^l_f)$, is a measure of the actual barrier height for incident electrons at the Fermi energy E^l_f. This quantity remains constant in models which assume that the entire applied voltage drops linearly across the barrier layer. It is actually a fairly rapidly decaying function of V_a. In Fig.2.5, for instance, ΔE_{eff} is 203 meV at zero bias, but only 116 meV at $V_a = 0.5$ V and 62 meV at $V_a = 1.0$ V. It eventually vanishes for an applied voltage of 1.75 V.

The energy band profiles depicted in Figs.2.2 and 2.3 reveal that the band diagrams and the voltage drops in each region depend strongly upon the structure parameters. The effects of barrier thickness, electrode doping density and barrier doping concentration are illustrated in Figs.2.6–2.9 in the case of symmetric GaAs–$Al_{0.4}Ga_{0.6}As$–GaAs double heterojunctions. The $Al_{0.4}Ga_{0.6}As$ barrier is characterized by a low temperature band gap of 2.02 eV, an electron Γ–point effective mass of $0.100\, m_0$, and a relative dielectric constant of 11.9.[22] Using a valence band discontinuity of $(0.55 \times x)$ eV, the conduction band offset is found to be 280 meV. Fig.2.6 depicts four zero bias energy band profiles. In Figs.2.6(a) and (b), the free electron concentration in both GaAs cladding layers is taken to be $n_D = 1 \times 10^{18} cm^{-3}$, corresponding to a Fermi level of 54 meV. The p–type barriers have a density of ionized acceptors, n_{A_2}, of $5 \times 10^{17} cm^{-3}$, and thicknesses

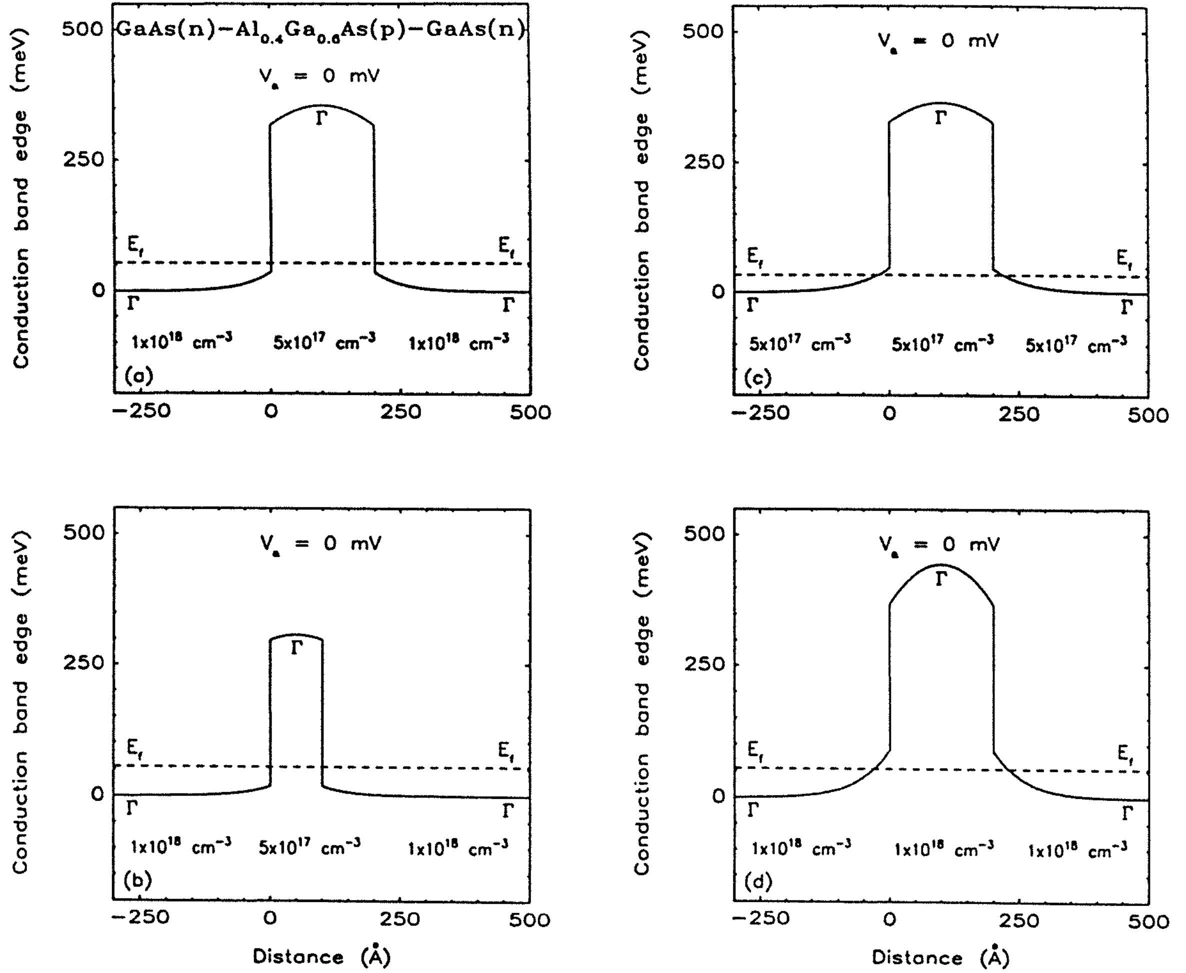

Figure 2.6: Calculated Γ–point conduction band edges for symmetric n^+–p–n^+ GaAs–$Al_{0.4}$ $Ga_{0.6}$As–GaAs heterostructures under no applied bias. In (a), the GaAs electrodes are doped at $1 \times 10^{18} cm^{-3}$ and the density of ionized acceptors in the 200 Å thick barrier layer is $5 \times 10^{17} cm^{-3}$. (a) may be used as a reference for the other three structures: in (b), the barrier thickness has been reduced to 100 Å; in (c), the electrode doping density has been changed to $5 \times 10^{17} cm^{-3}$; in (d), the barrier doping concentration has been increased to $1 \times 10^{18} cm^{-3}$. The conduction band offset at the heterojunction interfaces is taken to be 280 meV.

of 200 and 100 Å in Figs.2.6(a) and (b), respectively. Fig.2.6(c) illustrates the effect of electrode doping by showing a structure which only differs from that depicted in Fig.2.6(a) by the free electron density in the cladding layers. This density has been reduced to $5 \times 10^{17} cm^{-3}$, corresponding to a Fermi energy of 34 meV. The effect of barrier doping is illustrated in Fig.2.6(d), in which the heterostructure is the same as in Fig.2.6(a) except for the density of ionized acceptors in the barrier, which is taken to be $1 \times 10^{18} cm^{-3}$ instead of $5 \times 10^{17} cm^{-3}$.

Figs.2.6(a) and (b) indicate that when region (II) is made thicker, the amount of band bending increases both in the barrier and the cladding layers. This occurs because more ionized acceptors are present in thicker barrier layers, thus requiring more electrons to migrate from the electrodes into the barrier to make the Fermi level constant throughout the entire structure. A meaningful quantity in describing the amount of band bending and characterizing the actual height of the tunnel barrier is the conduction band edge maximum in region (II) in the unbiased structure. For symmetric n^+–p–n^+ double heterojunctions, this maximum is $E_{c2}(a/2)$, given by

$$E_{c_2}(a/2) = -\left(\frac{e^2 n_{A_2}}{\epsilon_0 \epsilon_{r_2}}\right)\frac{a^2}{8} + E'_{c_2}(0)\,\frac{a}{2} + E_{c_2}(0). \qquad (2.36)$$

This quantity is plotted in Fig.2.7(a) as a function of barrier thickness for structures such as those depicted in Figs.2.6(a) and (b). $E_{c2}(a/2)$ is a rapidly increasing function of a. This occurs because both $E_{c2}(0)$ and $E'_{c2}(0)$ increase with barrier thickness in such a way that the last two positive terms in Eq.(2.36) always dominate the first negative term. In Fig.2.7(a) for example, $E_{c2}(a/2)$ is already 355 meV in the case of a 200 Å thick barrier layer, and as large as 580 meV, more than twice the conduction band offset, for a 450 Å thick barrier. Furthermore, as illustrated in Figs.2.6(a) and (b), an increase in barrier height is also accompanied by an increase in the distance Λ_D ($\Lambda_D^l \equiv \Lambda_D^r$ for symmetric structures at zero bias) over which the bands bend in the cladding layers. Con-

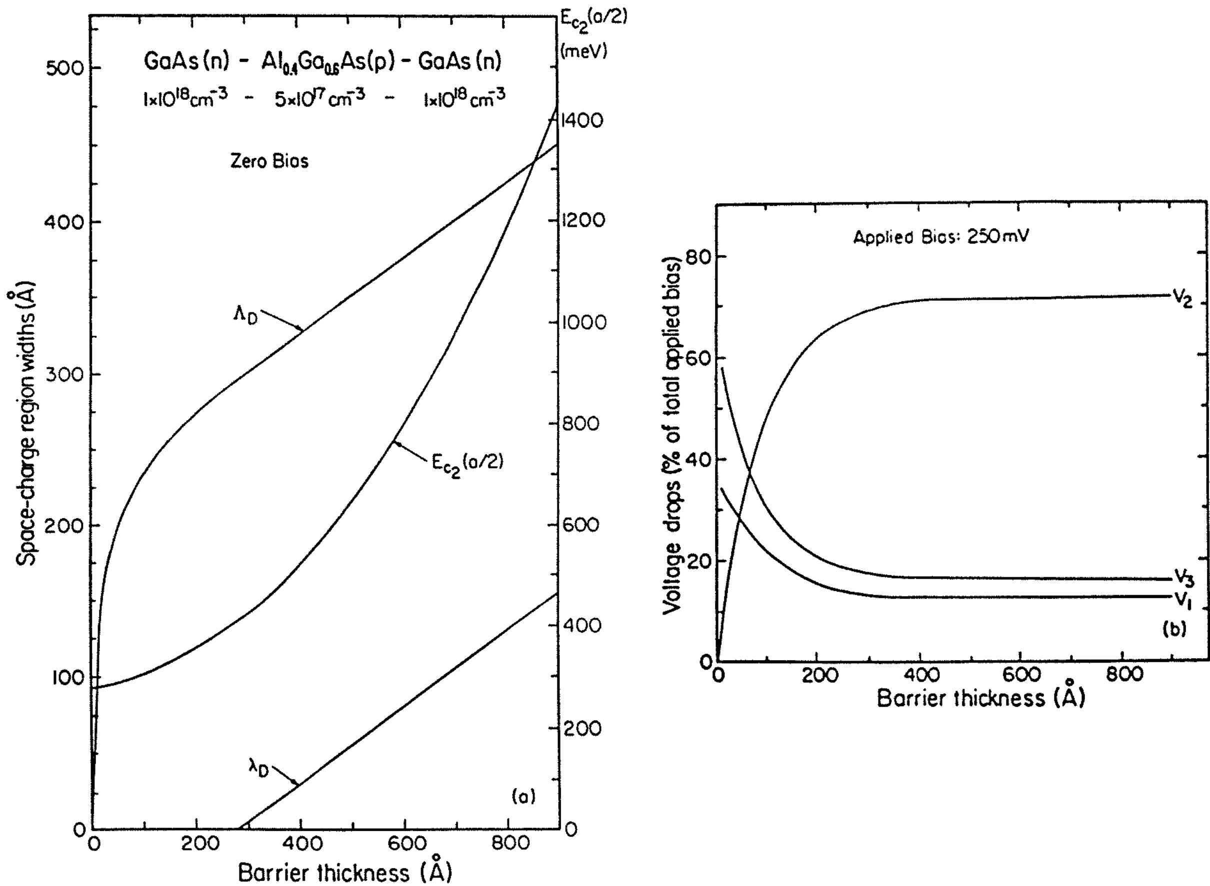

Figure 2.7: Variations with barrier thickness of energy band profile properties of n^+–p–n^+ heterostructures having, as in Figs.2.6(a) and (b), doping densities of $1 \times 10^{18} cm^{-3}$ in the cladding layers and $5 \times 10^{17} cm^{-3}$ in the barrier. (a) illustrates the properties of the unbiased structures: Λ_D is the distance over which the bands bend in the cladding layers, and λ_D is the width of the fully depleted space–charge regions in the electrodes. $E_{c_2}(a/2)$ denotes the barrier conduction band edge maximum. (b) depicts the voltage drops $V_1(a)$, $V_2(a)$ and $V_3(a)$ in regions (I), (II) and (III), respectively, when the structures are under an applied bias of 250 mV.

sequently, for thick enough barriers, ($a \geq 280$ Å in Fig.2.7(a)), fully depleted space–charge regions of width λ_D exist in the electrodes near the heterojunction interfaces. Fig.2.7(a) indicates that $\Lambda_D(a)$ first increases very rapidly, and then becomes linear as soon as $\lambda_D \geq 0$. This occurs because a variation Δa in barrier thickness produces a variation in barrier charge which is proportional to Δa. The subsequent variation ΔQ_e in electrode charges is thus also proportional to Δa. As long as the cladding layer space–charge regions remain partially depleted, their width variation, $\Delta\Lambda_D$, is not proportional to ΔQ_e, and Λ_D is a rapidly increasing function of a. However, when fully depleted space–charge regions exist in the electrodes, ΔQ_e is proportional to $\Delta\lambda_D$, and λ_D increases linearly with a. Furthermore, when this occurs, $\Delta\Lambda_D = \Delta\lambda_D$. As a result, $\Lambda_D(a)$ is also linear with the same slope as $\lambda_D(a)$. This slope varies with electrode and barrier doping densities: it decreases when the electrode dopings become larger or when the barrier doping is made smaller, i.e., when the amount of band bending is reduced.

The evolution of zero–bias band diagrams with barrier thickness may be used further to explain some properties of the energy band profiles of biased heterostructures. In Fig.2.7(b), the voltage drops $V_1(a)$, $V_2(a)$ and $V_3(a)$ in regions (I), (II) and (III), respectively, expressed as percentages of the total applied bias, are plotted for the same heterostructures as those discussed in Fig.2.7(a). The applied voltage, V_a, is taken to be 250 mV. The voltage drop, V_2, across the barrier first increases rapidly with a. For barriers thicker than about 300 Å, $V_2(a)$ becomes a very slowly varying function, going to a maximum asymptotic value of $0.72\,V_a$. Similarly, the voltage drops $V_1(a)$ and $V_3(a)$ in the cladding layers decrease rapidly for thin barriers and become almost constant when region (II) is thicker than approximately 300 Å. As indicated in Fig.2.7(a), the cladding layer space–charge regions are much wider than the barrier itself when a is very small.

As a result, a large fraction of the applied bias is dropped in the electrodes and V_2 is small. As the barrier is made thicker, the ratio Λ_D/a decays rapidly, resulting in a fast decrease of V_1 and V_3, and a rapid increase of V_2. The reason why V_1 and V_3, and thus V_2, become very slowly varying functions of a is due to the fact that when fully depleted space–charge regions exist at zero bias in the cladding layers, they sustain most of the voltage drops occurring in the electrodes. Since their widths increase linearly with a, they drop about the same percentage of total applied voltage regardless of the value of a. As shown in Fig.2.7(b), the maximum asymptotic value of $V_2(a)$, due to the finite voltage drops in the cladding layers, sets an upper limit to the fraction of applied bias which may drop across the barrier. This value may be used to evaluate the smallest error made when band bending is neglected.

Figs.2.6(a) and (c) illustrate the effect of electrode doping concentration on zero–bias energy band diagrams. As n_D, the density of free carriers in regions (I) and (III), is decreased, the bands in the cladding layers bend more and over larger distances. As a result, the barrier height increases, and for small enough values of n_D, fully depleted space–charge regions may appear in the cladding layers. For symmetric structures such as those depicted in Figs.2.6(a) and (c), Fig.2.8 indicates that as long as $n_D \leq 7 \times 10^{17} cm^{-3}$, fully depleted space–charge regions exist in the electrodes. Their width, λ_D, and thus the distance Λ_D over which the bands bend in regions (I) and (III), decays very rapidly when n_D is increased. The same is also true for the barrier conduction band maximum, $E_{c2}(a/2)$. When $n_D > 7 \times 10^{17} cm^{-3}$, the cladding layer space–charge regions are only partially depleted ($\lambda_D = 0$), and further increasing the electrode doping densities does not modify the energy band profiles very much. It follows that Λ_D and $E_{c_2}(a/2)$ become slowly decaying functions of n_D.

The solid line in Fig.2.9 illustrates how the energy band diagrams of biased

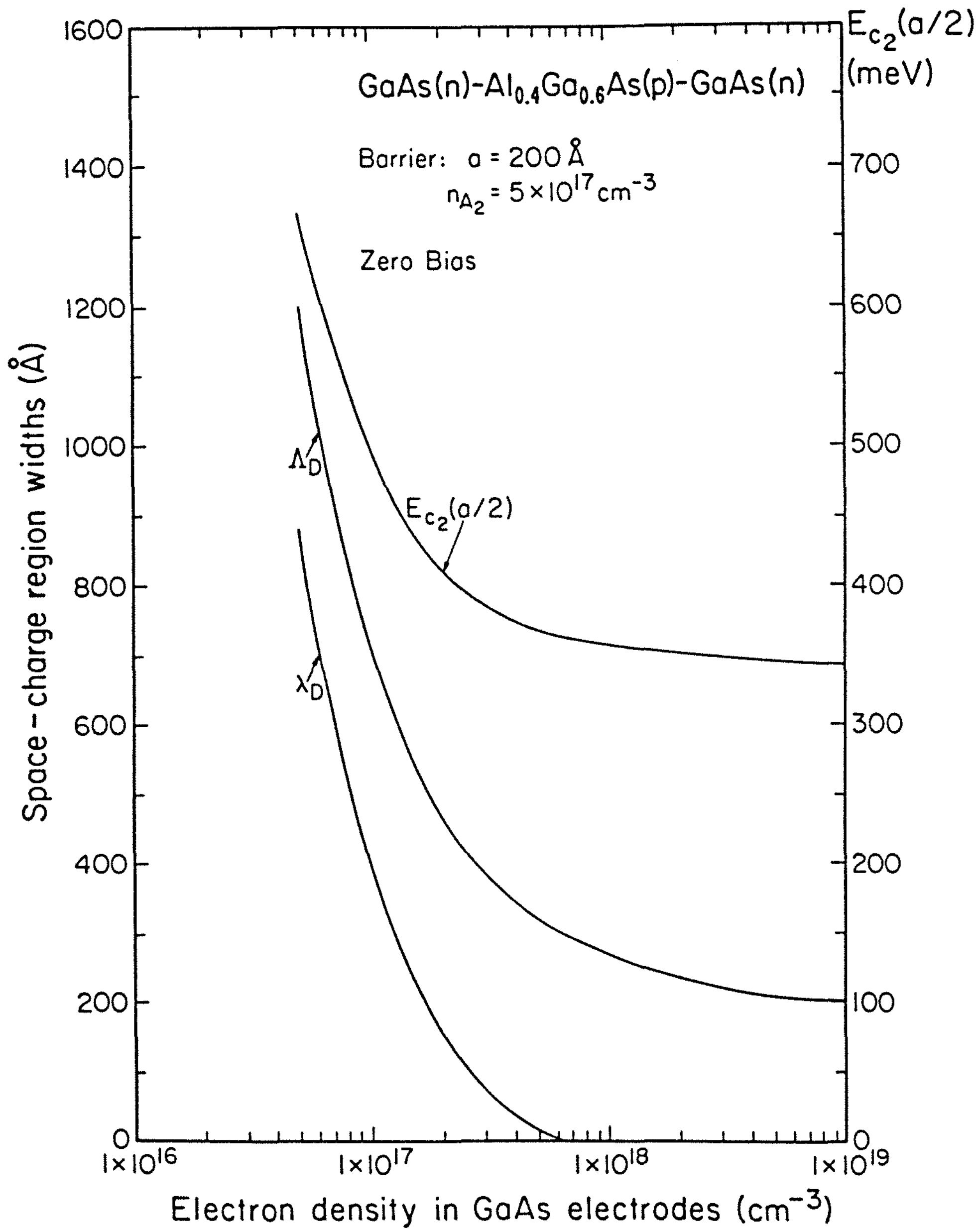

Figure 2.8: Variations with electrode doping of the cladding layer space–charge regions, (Λ_D, λ_D), and of the barrier conduction band edge maximum, $E_{c_2}(a/2)$, for n^+–p–n^+ heterostructures in which, as in Figs.2.6(a) and (c), the 200 Å thick barrier layer has a density of ionized acceptors of $5 \times 10^{17} cm^{-3}$.

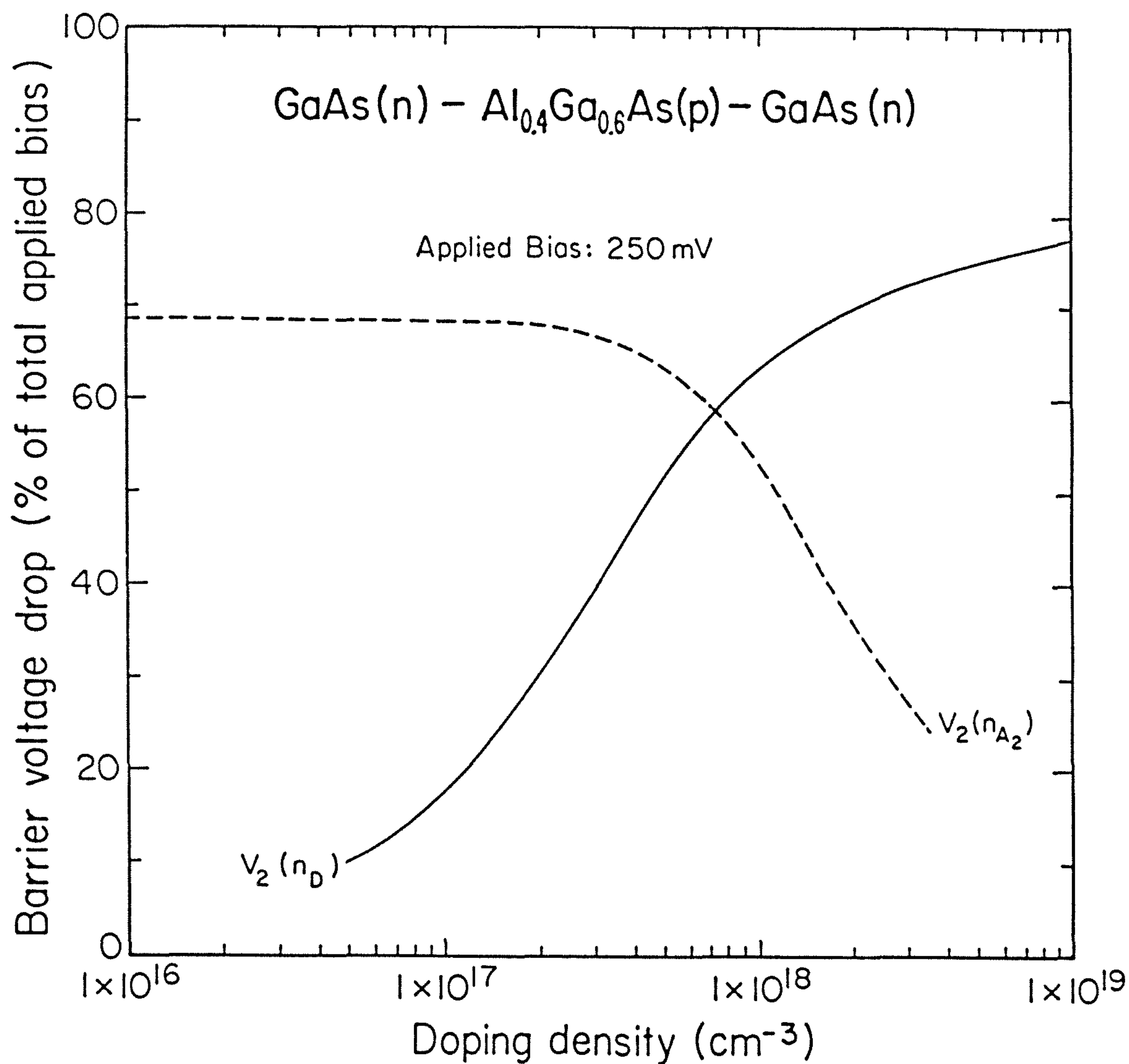

Figure 2.9: Barrier voltage drops in n^{+}–p–n^{+} GaAs–$Al_{0.4}Ga_{0.6}As$–GaAs heterostructures under an applied bias of 250 mV. The solid line represents the variations of V_2 with electrode doping density, $V_2(n_D)$, and the dashed line corresponds to the variations of V_2 with the barrier doping concentration, $V_2(n_{A_2})$.

structures vary with electrode doping. It corresponds to the same heterostructures as those discussed in Fig.2.8. Again, the total applied bias is 250 mV. The variations of $V_1(n_D)$, $V_2(n_D)$, and $V_3(n_D)$ may be understood in terms of the zero–bias band profile properties shown in Fig.2.8: because λ_D and Λ_D are decaying functions of n_D, the voltage drops V_1 and V_3 in the cladding layers are reduced when n_D becomes larger and V_2 increases monotonically with n_D. Furthermore, since the variations of $V_1(n_D)$ and $V_3(n_D)$ are closely related to those of $\lambda_D(n_D)$ and $\Lambda_D(n_D)$, the slope of $V_2(n_D)$ is large whenever totally depleted space–charge regions exist in the electrodes at zero bias. It gradually decreases as n_D increases when $\lambda_D = 0$. As in Fig.2.7(b), the finite voltage drops in the cladding layers set an upper limit to the amount of voltage dropping in the barrier. In the present case, this limit is $0.80\,V_a$ and may be achieved at very high doping densities only. However, in practical cases, V_2 is significantly reduced. For example, V_2 is $0.64\,V_a$ for $n_D = 1 \times 10^{18} cm^{-3}$ and only $0.52\,V_a$ for $n_D = 5 \times 10^{17} cm^{-3}$.

The energy band diagrams depicted in Figs.2.6(a) and (d) indicate that the shapes of the band edges in the barrier and the cladding layers may also be greatly modified by making n_{A_2}, the density of ionized acceptors in region (II), larger. When n_{A_2} is very small, ($n_{A_2} \leq 5 \times 10^{16} cm^{-3}$ for the structures under discussion), the band edges remain almost flat and $E_{c_2}(a/2)$ does not differ significantly from the conduction band offset. As n_{A_2} increases, the amount of band bending, and thus the barrier height and the cladding layer space–charge region widths, Λ_D and λ_D, become larger. As long as these space–charge regions remain partially depleted ($\lambda_D = 0$), the slope of $\Lambda_D(n_{A_2})$ is large. However, it decays with n_{A_2}, and when fully depleted space–charge regions exist near the heterojunction interfaces ($\lambda_D \geq 0$), both $\lambda_D(n_{A_2})$ and $\Lambda_D(n_{A_2})$ become linear. For example, when $n_{A_2} \geq 7 \times 10^{17} cm^{-3}$ in structures such as those illustrated in Figs.2.6(a) and (d), incrementing n_{A_2} by $1 \times 10^{17} cm^{-3}$ causes $\Lambda_D(n_{A_2})$ and $\lambda_D(n_{A_2})$ to increase by

10 Å. This slope would be larger for thicker barriers or smaller electrode doping densities. For the same reasons, the barrier height increases rather slowly with the barrier doping concentration as long as $\lambda_D = 0$, but more and more rapidly when $\lambda_D > 0$. For the heterostructures under discussion, $E_{c_2}(a/2)$ is only 294 meV when $n_{A_2} = 1 \times 10^{17} cm^{-3}$, but 444 meV when $n_{A_2} = 1 \times 10^{18} cm^{-3}$, and 729 meV, 2.6 times the conduction band offset, when $n_{A_2} = 2 \times 10^{18} cm^{-3}$. Because Λ_D and λ_D are increasing functions of the barrier doping density, the same is true for the voltage drops in the cladding layers. As a result, the fraction of applied bias dropping in the barrier is a decaying function of n_{A_2}. This is illustrated by the dashed line in Fig.2.9. It corresponds to structures under an applied voltage of 250 mV having, as in Figs.2.6(a) and (d), a 200 Å thick $Al_{0.4}Ga_{0.6}As$ barrier and electrode free carrier densities of $1 \times 10^{18} cm^{-3}$. For these heterostructures, V_2 reaches a maximum value of $0.69\, V_a$ when $V_a = 250$ mV. As discussed previously, this value could be made larger by increasing the barrier thickness or the electrode doping densities.

The actual shape of the barrier through which electrons in the cladding layers may tunnel depends strongly upon the structure parameters. This dependence is expected to be reflected in the J–V characteristics of the heterostructures. Increasing the barrier thickness or decreasing the electrode doping level will indeed reduce the current density. However, the J–V curves are particularly sensitive to the barrier doping concentration. Fig.2.10 depicts elastic tunneling J–V characteristics calculated for a GaAs–$Al_{0.4}Ga_{0.6}As$–GaAs heterostructure in which $a = 120$ Å and $n_D = 2 \times 10^{18} cm^{-3}$. As anticipated from the above discussion, increasing n_{A_2} causes the current density to be reduced because the amount of band bending and the barrier height become larger. Fig.2.10 also indicates that J increases by more than 1.5 order of magnitude when n_{A_2} is varied from 2×10^{18} to $1 \times 10^{18} cm^{-3}$, but only by half an order of magnitude when n_{A_2} is reduced

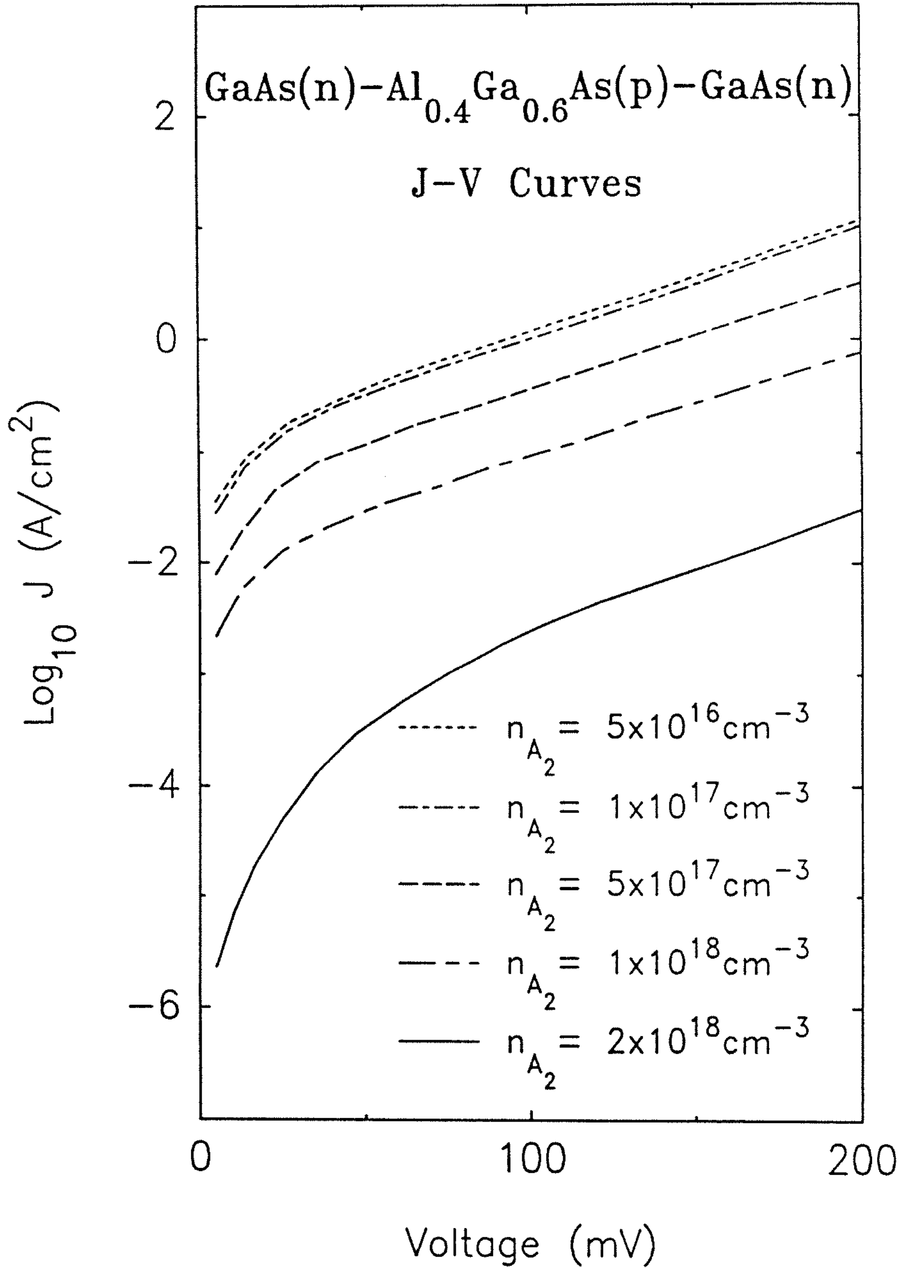

Figure 2.10: Theoretical current density vs. voltage (J–V) characteristics for elastic tunneling through n^+–p–n^+ GaAs–$Al_{0.4}Ga_{0.6}As$–GaAs heterostructures having a 120 Å thick barrier layer and electrode free carrier densities of $2 \times 10^{18} cm^{-3}$. The five J–V curves correspond to densities of ionized acceptors in the $Al_{0.4}Ga_{0.6}As$ barrier ranging between 5×10^{16} and $2 \times 10^{18} cm^{-3}$.

from 1×10^{18} to $5 \times 10^{17} cm^{-3}$. These results suggest that tunneling through single barrier heterostructures could provide useful information about ultra–thin layer doping levels.

2.4 Undoped Barrier Structures

These structures are important since many experimental studies of tunneling processes are performed on heterostructures composed of nominally undoped barriers adjacent to degenerately doped electrodes.

The formalism used to calculate the energy band diagrams of n^+–i–n^+ single barrier structures is the same as that developed for n^+–p–n^+ heterostructures. This is because the barrier is also totally depleted of carriers. Fig.2.11 illustrates the energy band diagrams of two asymmetric n^+–i–n^+ heterostructures at zero bias. Fig.2.11(a) corresponds to a GaAs–$Al_{0.4}Ga_{0.6}As$–GaAs structure having a 100 Å thick barrier layer and free electron densities of 1×10^{17} and $1 \times 10^{18} cm^{-3}$ in the left and right cladding layers, respectively. As a result of the asymmetric electrode dopings, electrons accumulate in the left electrode near the first heterojunction interface, while a partially depleted space–charge region adjacent to the second heterojunction interface exists in the right electrode. Since n_{A_2} vanishes in Eq.(2.25), the band edges remain linear in the barrier. Fig.2.11(b) depicts a GaAs–$Al_{0.4}Ga_{0.6}As$–$Al_{0.1}Ga_{0.9}As$ structure in which the barrier layer is 100 Å thick and the electrodes are doped at $5 \times 10^{17} cm^{-3}$. The conduction band offsets at the interfaces are taken to be $\Delta E_c^0 = 280$ meV and $\Delta E_c^a = 210$ meV. In the $Al_{0.1}Ga_{0.9}As$ cladding layer, the effective mass is $0.075\, m_0$, and the relative dielectric constant is 12.8.[22] Because the electrodes are made of different materials, the Fermi level lies 34 and 31 meV above the conduction band edges in the left and right neutral semiconductors, respectively. As in Fig.2.11(a), the

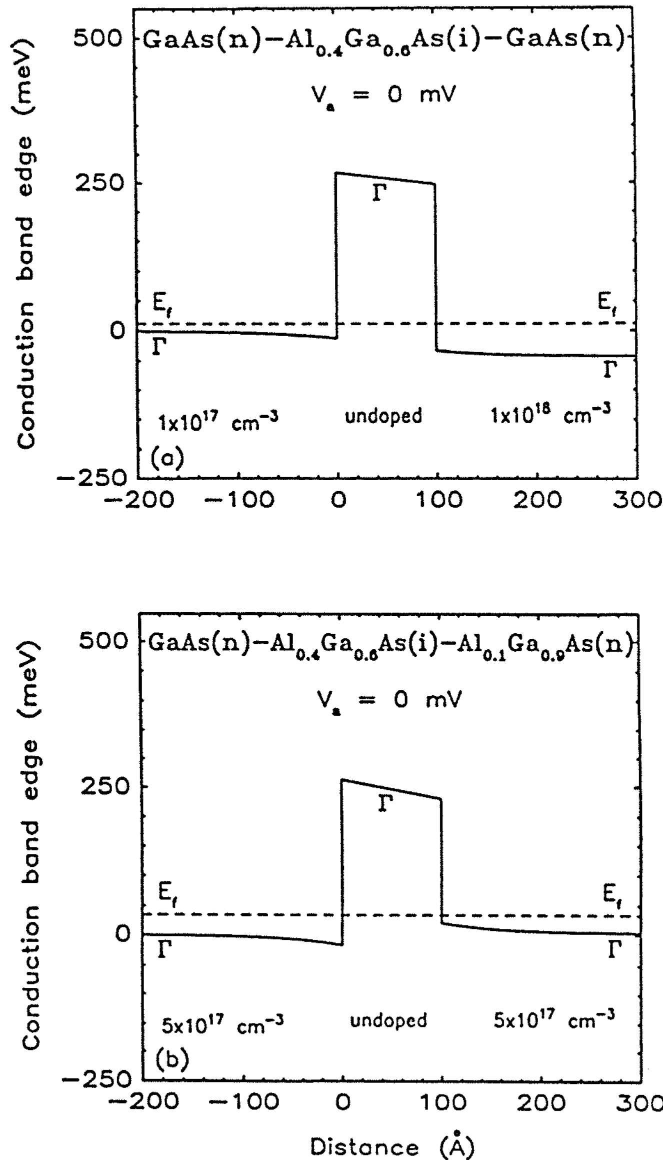

Figure 2.11: Calculated Γ–point conduction band edges for two asymmetric n^+–i–n^+ heterostructures under no applied bias. In both cases, the 100 Å thick barrier layer is made of $Al_{0.4}Ga_{0.6}As$. In (a), the two GaAs electrodes are asymmetrically doped, with free electron densities of $1 \times 10^{17} cm^{-3}$ in region (I) and $1 \times 10^{18} cm^{-3}$ in region (III). In (b), the two cladding layers are doped at $5 \times 10^{17} cm^{-3}$. However, they are made of different materials: GaAs in the left electrode, and $Al_{0.1}Ga_{0.9}As$ in the right electrode. The conduction band discontinuities are taken to be 280 meV at GaAs–$Al_{0.4}Ga_{0.6}As$ interfaces and 210 meV at $Al_{0.1}Ga_{0.9}As$–$Al_{0.4}Ga_{0.6}As$ interfaces.

band edges remain linear in the barrier but bend in the electrodes.

In the case of symmetric heterostructures, all the bands are flat at zero bias. When the structures are biased, setting n_{A_2} equal to zero in Eq.(2.32) causes the band edges to remain linear in the barrier. However, accumulation and depletion regions exist in the cladding layers. Consequently, part of the applied voltage drops in the electrodes and the shapes of the band edges differ from those obtained when band bending is neglected. These results are illustrated in Fig.2.12 for a symmetric GaAs–$Al_{0.4}Ga_{0.6}As$–GaAs heterostructure having a 100 Å thick barrier layer and GaAs free electron densities of $5 \times 10^{17} cm^{-3}$. Figs.2.12(a) and (b) correspond to applied voltages of 100 and 300 mV, respectively. The solid lines represent the actual energy band profiles. The solid–dashed lines depict the conduction band edges obtained when band bending is ignored. Fig.2.12(a) reveals that both diagrams are similar at low biases. However, increasing V_a causes the electrode space–charge regions to become larger and the shapes of the band edges to be further altered, not only in the cladding layers but also in the barrier. As a result, $\Delta E_{eff} (\equiv E_{c2}(0) - E_f^l)$, the effective conduction band offset for incident electrons near the Fermi level in the left electrode, is a decaying function of applied voltage. If band bending is neglected, the band edges remain flat in the cladding layers and ΔE_{eff} is constant regardless of the value of V_a. Such discrepancies between the two models are expected to be manifested most clearly in studies of tunneling processes, which are extremely sensitive to the shape of the barrier through which the charge carriers tunnel. For example, Fig.2.12(b) indicates that when $V_a = 300$ mV, the tunneling length for electrons near the Fermi level in the left electrode is in fact the full barrier thickness, as opposed to only 82 Å if band bending is neglected.

Fig.2.13 illustrates the dependence of the energy band diagrams upon barrier thickness and electrode doping concentration. Fig.2.13(a) gives the voltage drops

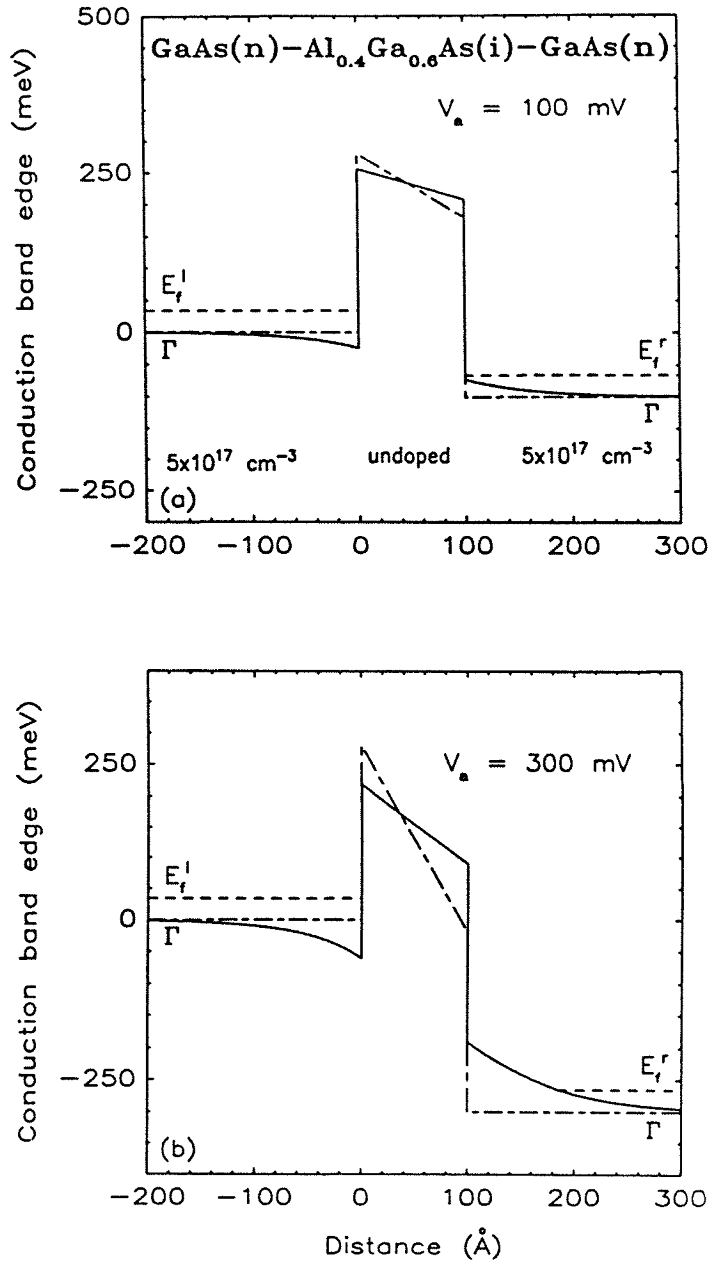

Figure 2.12: Calculated Γ–point conduction band edges (solid lines) for a symmetric n^+–i–n^+ GaAs–$Al_{0.4}Ga_{0.6}As$–GaAs heterostructure having a 100 Å thick barrier layer and electrode doping densities of $5 \times 10^{17} cm^{-3}$. The solid–dashed lines represent the conduction band edges obtained when band bending is neglected. (a) and (b) correspond to applied voltages of 100 and 300 mV, respectively.

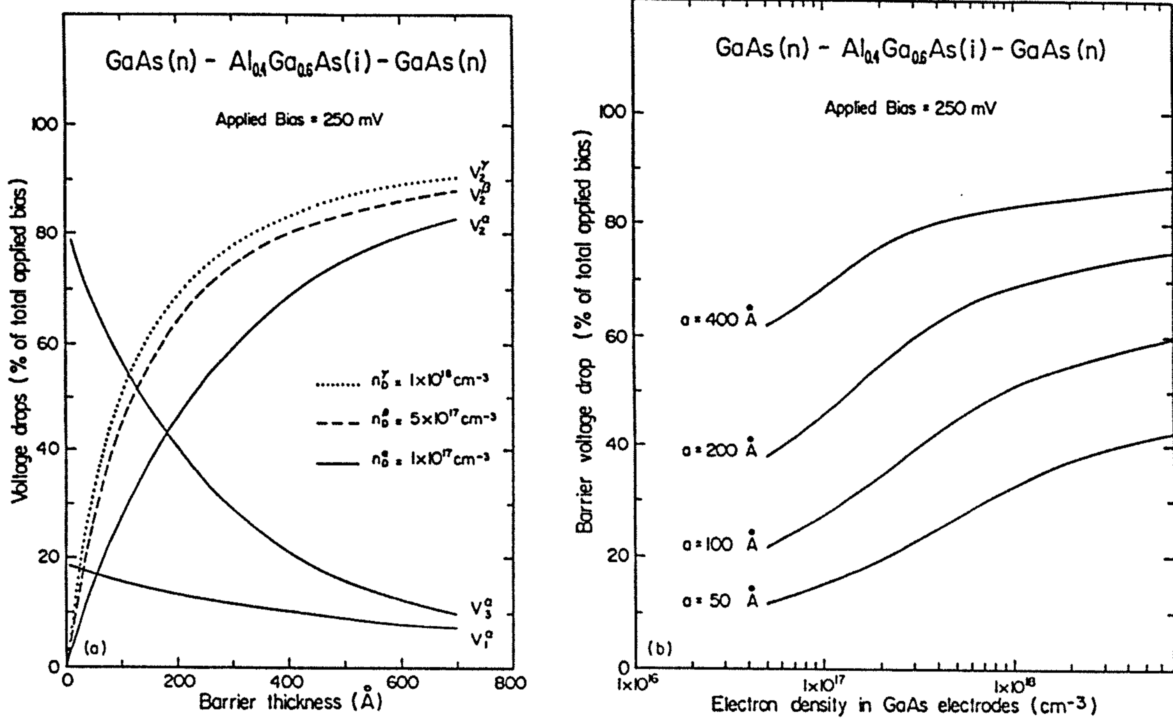

Figure 2.13: Variations with barrier thickness (a), and electrode doping (b), of the voltage drop distributions in n^+–i–n^+ GaAs–$Al_{0.4}Ga_{0.6}As$–GaAs heterostructures. The applied voltage is 250 mV. Three different electrode dopings are depicted in (a). Four barrier thicknesses ranging between 50 and 400 Å are illustrated in (b).

$V_1^\alpha(a)$, $V_2^\alpha(a)$ and $V_3^\alpha(a)$ for structures having electrode free carrier densities, n_D^α, of $1 \times 10^{17} cm^{-3}$. The barrier voltage drop is also plotted in dashed line for $n_D^\beta = 5 \times 10^{17} cm^{-3}$, (V_2^β), and in dotted line for $n_D^\gamma = 1 \times 10^{18} cm^{-3}$, (V_2^γ). Fig.2.13(b) shows plots of $V_2(n_D)$ for different barrier thicknesses. These figures reveal that, as in n^+–p–n^+ structures, V_2 is an increasing function of barrier thickness and electrode doping concentration. Consequently, the error made by neglecting band bending increases when the electrode doping densities are lowered and/or the barrier is made thinner. For example, in a typical GaAs–$Al_{0.4}Ga_{0.6}As$–GaAs tunnel structure having a 100 Å thick barrier and electrode doping densities of $5 \times 10^{17} cm^{-3}$, the voltage drop across the barrier is only $0.45\, V_a$ at $V_a = 250$ mV. This effect is strongly reflected in the structure J–V curves shown in Fig.2.14. The solid line is the characteristic calculated from energy band diagrams, $J_b(V_a)$. The dashed line corresponds to the J–V curve obtained when band bending is ignored, $J_{nb}(V_a)$. As expected from Fig.2.12, both curves are in good agreement at low applied voltages ($V_a < 100$ mV), but deviate more significantly as V_a becomes larger. This illustrates the importance of band bending in calculating tunneling currents, even when the barrier is undoped. Whereas $J_b(V_a)$ increases gradually, $J_{nb}(V_a)$ displays a sharp turn–on corresponding to the voltage at which electrons in the left electrode start tunneling through a triangular barrier. At lower biases, $J_b > J_{nb}$ because the energy band profiles feature an accumulation layer in the left electrode and the effective conduction band offset for the tunneling electrons is a decaying function of V_a. At higher voltages, $J_b < J_{nb}$ because the reduction in the tunneling length when band bending is neglected dominates the competing effects produced by the bending of the energy bands.

Another issue of interest is that of band offsets at heterojunction interfaces. These values are still somewhat a matter of debate in the GaAs/$Al_xGa_{1-x}As$ sys-

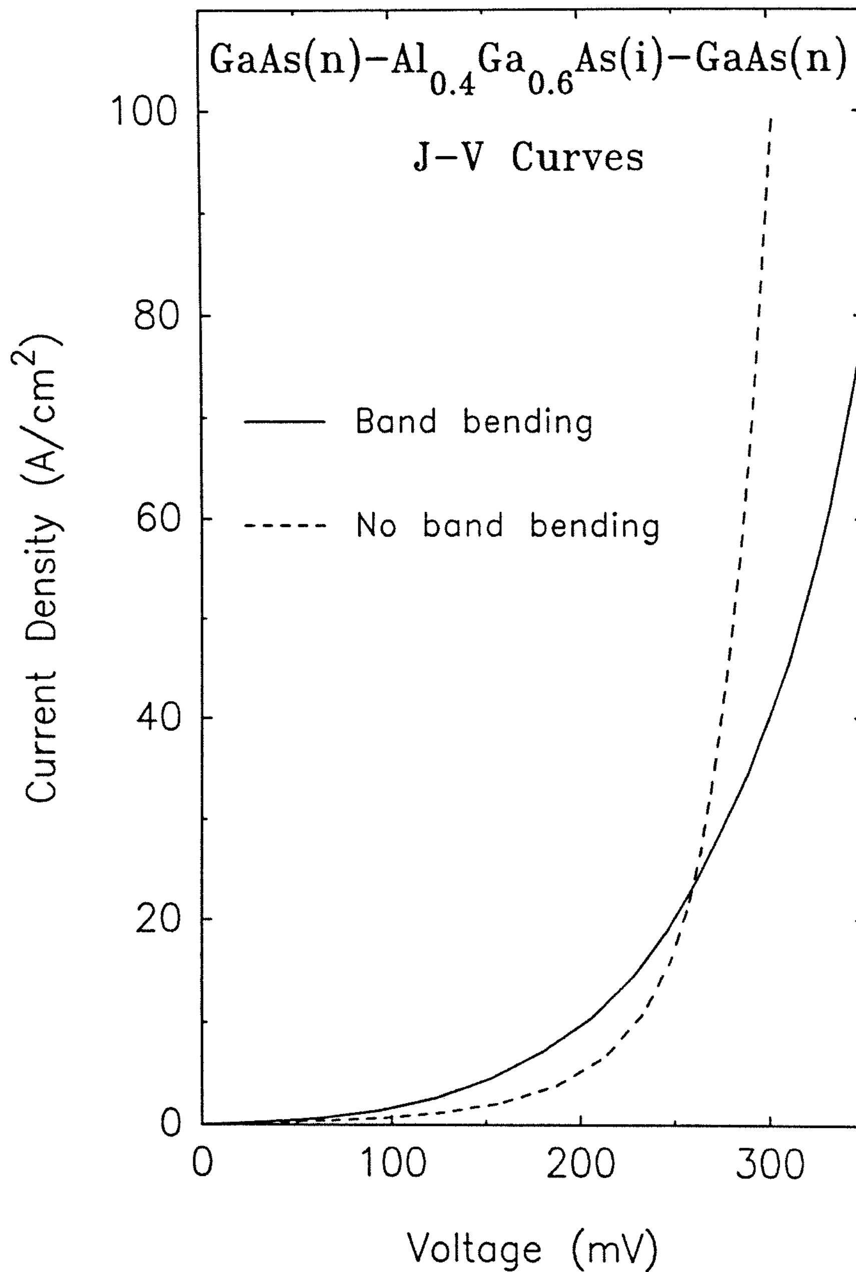

Figure 2.14: Theoretical *J–V* characteristics for elastic tunneling through an n^+–i–n^+ heterostructure in which the GaAs electrodes are doped at $5 \times 10^{17} cm^{-3}$ and the undoped $Al_{0.4}Ga_{0.6}As$ barrier layer is 100 Å thick. The solid line is the *J–V* curve calculated from the energy band profiles. The dashed line is the characteristic obtained when band bending is neglected.

tem. Taking a valence band discontinuity of $(0.55 \times x)$ eV[23] yields a conduction band offset, ΔE_c, which is only about 56% of the direct band gap difference, ΔE_g^Γ, when $x = 0.4$. However, values of ΔE_c as high as $0.75\,\Delta E_g^\Gamma$ are still commonly used.[24] If ΔE_c is taken to be $0.65\,\Delta E_g^\Gamma$, the conduction band offset at $GaAs/Al_{0.4}Ga_{0.6}As$ interfaces is 325 meV, and not 280 meV as assumed throughout this chapter. The J–V curves calculated using these two values display the same general behavior, but differ by as much as half an order of magnitude. Tunneling characteristics could thus provide useful information about the values of band offsets.

Fig.2.15 illustrates how the J–V characteristics may vary with barrier thickness and electrode doping density. Fig.2.15(a), which corresponds to $n_D = 1 \times 10^{18} cm^{-3}$ and four different barrier thicknesses (a = 50, 100, 150, 200 Å), shows that J is a rapidly decaying function of a. In this case, J drops by about 3 orders of magnitude when a is increased by 50 Å. In Fig.2.15(b), the barrier is 100 Å thick and the electrode doping density is varied between 1×10^{17} and $2 \times 10^{18} cm^{-3}$.

2.5 n–Type Barrier Structures

When the barrier layer is doped n–type, the band edges at zero–bias bend downward and not upward as in the case of p–type barrier structures. Depending on doping concentrations and barrier thicknesses, two cases may occur. *(i)* When the barrier layer is thin enough and/or sufficiently lightly doped, its conduction band remains totally depleted of carriers. This case is similar in a number of ways to those discussed previously. *(ii)* When the barrier is thick enough and/or sufficiently doped, its conduction band is no longer fully depleted, and a region with bulk–like properties may exist in the barrier layer. This may greatly modify

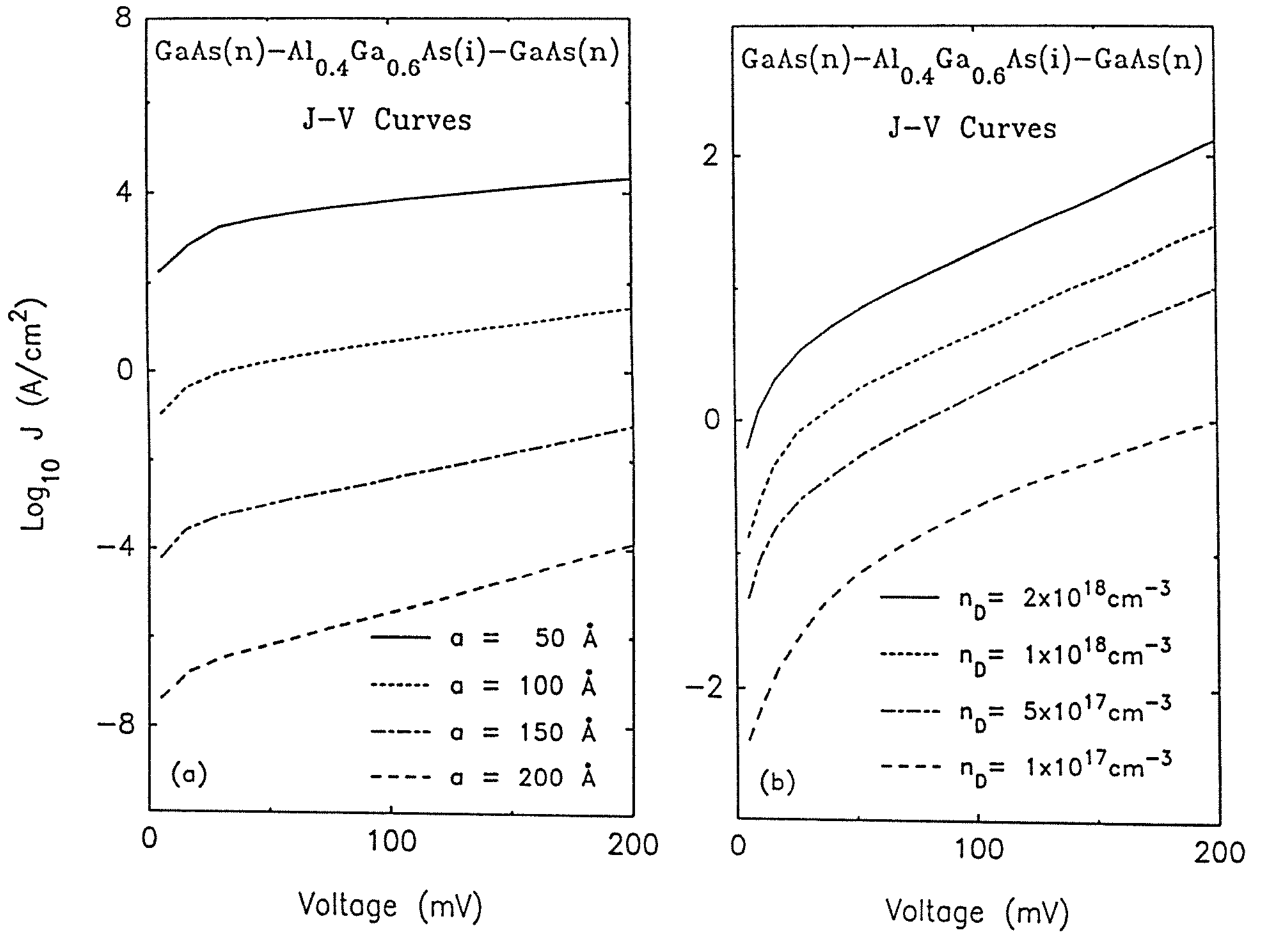

Figure 2.15: Theoretical J–V characteristics for n^+–i–n^+ GaAs–$Al_{0.4}Ga_{0.6}As$–GaAs heterostructures. In (a), the electrode free carrier density is $1 \times 10^{18} cm^{-3}$, and different barrier thicknesses ranging between 50 and 200 Å are depicted. In (b), the barrier is 100 Å thick, and the doping concentration in the cladding layers is varied between 1×10^{17} and $2 \times 10^{18} cm^{-3}$.

the nature of the dominant current transport mechanisms occurring in these structures.

In the case of totally depleted barriers, the energy band diagrams may be found using the same approach as for n^+–p–n^+ heterostructures provided that n_{A_2} is replaced by $(-n_{D2})$, where n_{D2} is the concentration of ionized donors in the barrier. An example of these calculations is illustrated in Fig.2.16, again in the case of a symmetric GaAs–$Al_{0.4}Ga_{0.6}As$–GaAs heterostructure for comparison with n^+–p–n^+ and n^+–i–n^+ structures. The electrode free carrier density is taken to be $1 \times 10^{18} cm^{-3}$. The barrier is 200 Å thick, with $n_{D2} = 5 \times 10^{17} cm^{-3}$. Fig.2.16(a) represents the conduction band edge at zero bias, while Fig.2.16(b) corresponds to an applied voltage of 300 mV. As shown in Fig.2.16(a), the zero–bias space–charge regions in the electrodes now take the form of accumulation layers. This is because all the free carriers in the barrier have migrated into the adjacent cladding layers to make the Fermi level constant throughout the heterostructure. As before, the space–charge regions and the band bending become larger when the electrode doping densities are decreased or when the barrier thickness or doping concentration are increased. As a result, the average barrier height may be significantly reduced. For example, the barrier conduction band edge minimum is only 153 meV above the Fermi level in Fig.2.16(a). It would lie 226 meV above E_f in the case of an undoped barrier. Fig.2.16(b) illustrates the behavior of the energy band profiles of biased structures. As V_a is increased from zero, more electrons accumulate in the left cladding layer near the first heterojunction interface. In the right electrode, the accumulation layer is progressively reduced until the slopes of the band edges become negative and a depletion region is formed, $(\Lambda_D^r \geq 0)$. Eventually, when V_a is sufficiently large, a fully depleted space–charge layer $(\lambda_D^r \geq 0)$ appears in region (III), near the second heterojunction interface. It follows that $V_3(V_a)$ increases more rapidly than

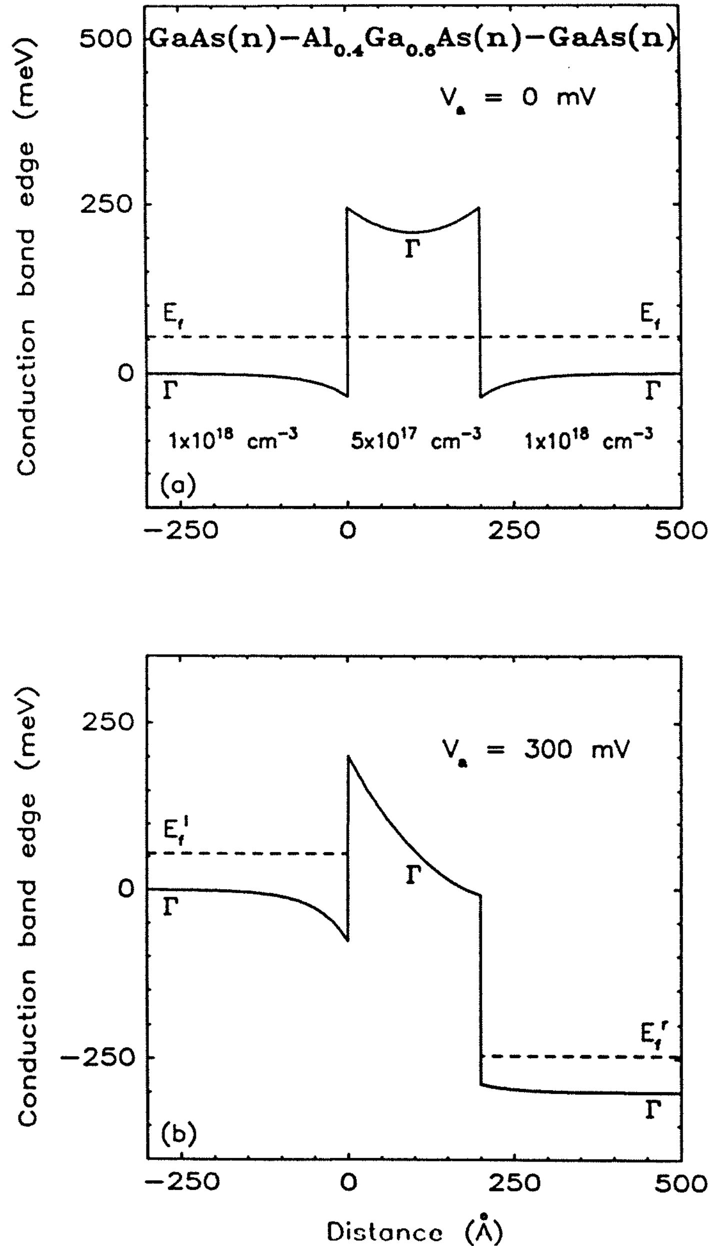

Figure 2.16: Calculated Γ–point conduction band edges for a symmetric n^+–n–n^+ heterostructure in which the barrier remains totally depleted of carriers. The free electron density in the GaAs electrodes is $1 \times 10^{18} cm^{-3}$. The density of ionized donors in the 200 Å thick $Al_{0.4}Ga_{0.6}As$ barrier layer is taken to be $5 \times 10^{17} cm^{-3}$. (a) represents the unbiased structure, and (b) corresponds to an applied voltage of 300 mV.

$V_1(V_a)$ decreases, causing V_2 to be a decaying function of V_a. Furthermore, for a given applied bias, V_2 increases when any one of the parameters, barrier thickness, barrier doping density or electrode doping concentration, is made larger. For a fixed value of V_a, increasing either a or n_{D2} causes more electrons to accumulate in region (I). In region (III), if accumulation layers still exist, they become larger while, if depletion layers are present, they become smaller. As a result, when either a or n_{D2} becomes larger, both V_1 and V_3 are reduced, and V_2 is increased. This result is different from that obtained for n^+–p–n^+ structures, for which V_2 was found to be an increasing function of a but a decaying function of the barrier doping density. This difference is due to the fact that whereas unbiased n^+–p–n^+ heterostructures have depletion regions in their cladding layers, n^+–n–n^+ structures feature accumulation regions. V_2 is also an increasing function of electrode doping concentration because the cladding layers drop smaller fractions of the applied voltage when they become more heavily doped.

Fig.2.17 illustrates how current densities increase with barrier doping. For comparison with Fig.2.10, it depicts elastic tunneling J–V characteristics for a GaAs–$Al_{0.4}Ga_{0.6}As$–GaAs heterostructure having a 120 Å thick barrier layer and electrode free carrier concentrations of $2 \times 10^{18} cm^{-3}$. Again, the J–V curves deviate more significantly from one another as the barrier doping level becomes larger. Figs.2.10 and 2.17 also indicate that very different current density values may be obtained simply by changing the type of barrier dopants. For example, if the $Al_{0.4}Ga_{0.6}As$ layer is doped at $5 \times 10^{17} cm^{-3}$, the current density, J_n, in the n–type barrier structure is about one order of magnitude greater than the current density, J_p, in the analogous p–type barrier structure. If the barrier is doped at $1 \times 10^{18} cm^{-3}$, J_n is approximately 2.5 orders of magnitude greater than J_p.

When the barrier is sufficiently thick or heavily doped, its conduction band

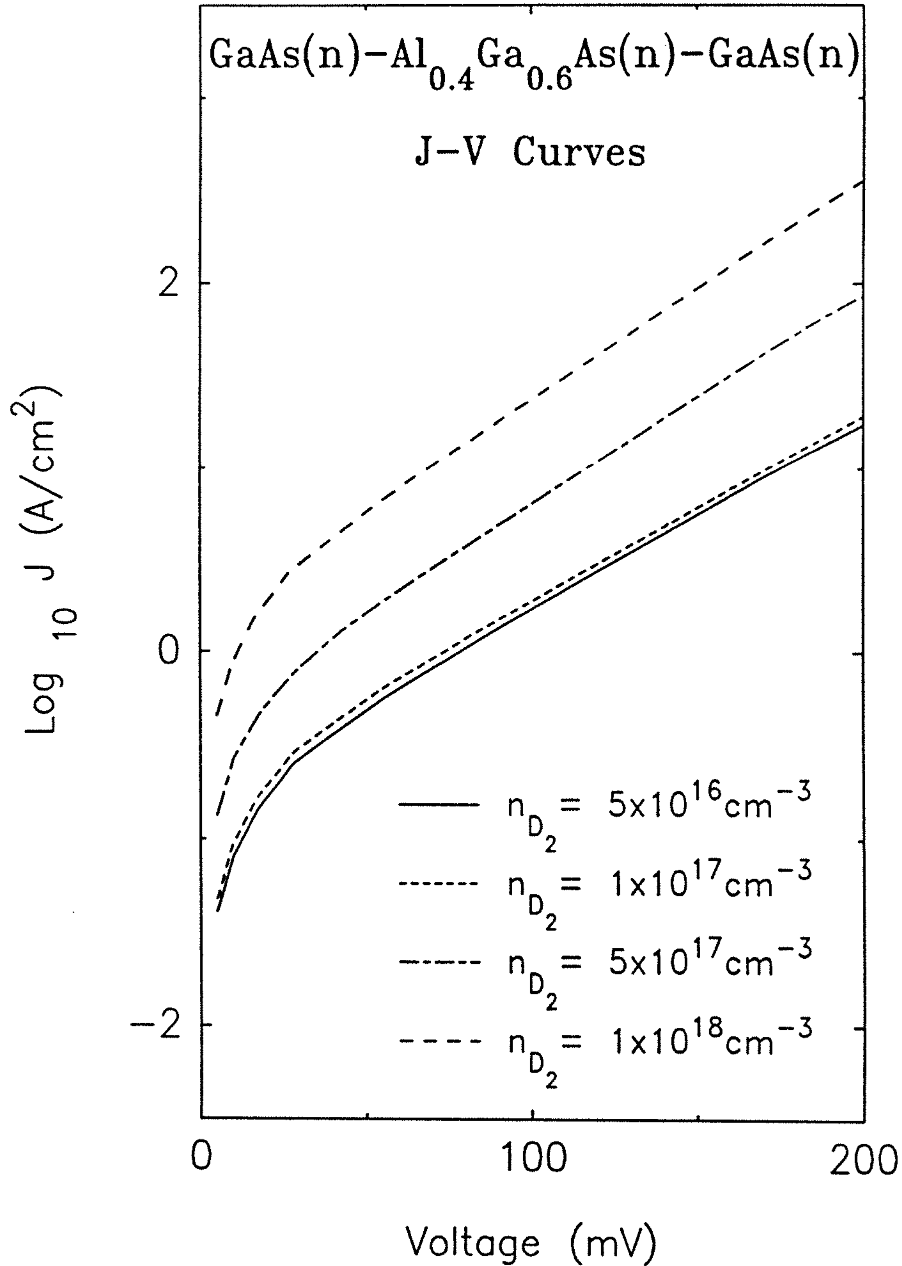

Figure 2.17: Theoretical J–V characteristics for elastic tunneling through n^+–n–n^+ GaAs–$Al_{0.4}Ga_{0.6}As$–GaAs heterostructures having 120 Å thick barrier layers and electrode free carrier densities of $2 \times 10^{18} cm^{-3}$. The four J–V curves correspond to densities of ionized donors in the $Al_{0.4}Ga_{0.6}As$ barrier ranging between 5×10^{16} and $1 \times 10^{18} cm^{-3}$.

may no longer be fully depleted of electrons. For instance, in GaAs–$Al_{0.4}Ga_{0.6}As$–GaAs heterostructures having a 200 Å thick barrier layer, this occurs for $n_{D_2} \geq 1.6\times10^{18}cm^{-3}$ if $n_{D_1}(\equiv n_{D_3}) = 1\times10^{18}cm^{-3}$. Similarly, if $n_{D_1} = 1\times10^{18}cm^{-3}$ and $n_{D_2} = 5\times10^{17}cm^{-3}$, this happens when the barrier becomes thicker than 406 Å. If a or n_{D_2} are further increased, more electrons occupy conduction band states in $Al_{0.4}Ga_{0.6}As$ and, eventually, a region with bulk–like properties appears in the barrier layer. Throughout this region, the bands remain flat and the electric field vanishes. As long as this flat band layer does not exist, the energy band profiles may be found using the same approach as before, generalized, however, to include the possibility of having a non–fully depleted barrier conduction band. Eqs.(2.22)–(2.24) and (2.26)–(2.28) still hold in the electrodes. In regions of the barrier where the conduction band remains totally depleted, the band edges are still parabolic. However, if electrons occupy barrier conduction band states over a distance $d_2 \leq x \leq c_2$, where $0 < d_2 < c_2 < a$, the energy band profile in that region may be found by integrating

$$[y'_2(x)]^2 = 2\left(\frac{e^2 n_{D_2}\delta_2}{\epsilon_0\epsilon_{r_2}}\right)\left\{\frac{2}{5}\left[\frac{y_2(x)}{\delta_2}\right]^{5/2} - \left[\frac{y_2(x)}{\delta_2}\right]\right\} + [y'_2(d_2)]^2 \qquad (2.37)$$

numerically.

The electroneutrality condition (2.29) also needs to be modified as

$$A_1\int_{c_1}^{d_1}[y_1(x)]^{3/2}\,dx + A_2\int_{d_2}^{c_2}[y_2(x)]^{3/2}\,dx + A_3\int_{d_3}^{c_3}[y_3(x)]^{3/2}\,dx$$
$$+c_1 n_{D_1} - a n_{D_2} - (c_3 - a)n_{D_3} = 0. \qquad (2.38)$$

When a flat band region exists in the barrier, the energy band profiles may be calculated using the same approach, except that in the bulk–like layer, $\rho_2(x) = 0$ and $y_2(x) = \delta_2$. In this instance, the structure may also be viewed as two independent n^+–n^+ heterojunctions back to back. A single n^+–n^+ heterojunction in which an interface at $x = x_0$ separates two semiconductors (I) and (II), is

schematically illustrated in Fig.2.18. Using the same simplifying assumptions as before and the notations of Fig.2.18, the energy band profiles may be obtained from the following equations.

$x \leq c_1$: Neutral bulk semiconductor in region (I)

$$y_1(x) \equiv E_{f_1} - E_{c_1}(x) = \delta_1 \equiv \frac{\hbar^2}{2m_1^*}(3\pi^2 n_{D_1})^{2/3}. \tag{2.39}$$

$c_1 < x \leq x_0$: Accumulation layer in region (I)

$$[y'_1(x)]^2 = 2\left(\frac{e^2 n_{D_1}\delta_1}{\epsilon_0 \epsilon_{r_1}}\right)\left\{\frac{2}{5}\left[\frac{y_1(x)}{\delta_1}\right]^{5/2} - \left[\frac{y_1(x)}{\delta_1}\right] + \frac{3}{5}\right\}. \tag{2.40}$$

$x_0 \leq x < d_2$: Totally depleted space–charge layer in region (II)

$$E_{c_2}(x) = \left(\frac{e^2 n_{D_2}}{\epsilon_0 \epsilon_{r_2}}\right)\frac{(x-x_0)^2}{2} + E'_{c_2}(x_0)\,(x-x_0) + E_{c_2}(x_0), \tag{2.41}$$

with

$$E_{c_2}(x_0) = E_{f_1} - y_1(x_0) + \Delta E_c,$$
$$E'_{c_2}(x_0) = -\left(\frac{\epsilon_{r_1}}{\epsilon_{r_2}}\right) y'_1(x_0).$$

$d_2 \leq x < c_2$: Partially depleted space–charge layer in region (II)

$$[y'_2(x)]^2 = 2\left(\frac{e^2 n_{D_2}\delta_2}{\epsilon_0 \epsilon_{r_2}}\right)\left\{\frac{2}{5}\left[\frac{y_2(x)}{\delta_2}\right]^{5/2} - \left[\frac{y_2(x)}{\delta_2}\right] + \frac{3}{5}\right\}, \tag{2.42}$$

with

$$E_{c_2}(x) = E_{f_1} - eV - y_2(x).$$

$x \geq c_2$: Neutral bulk semiconductor in region (II)

$$y_2(x) \equiv E_{f_2} - E_{c_2}(x) = \delta_2 \equiv \frac{\hbar^2}{2m_2^*}(3\pi^2 n_{D_2})^{2/3}. \tag{2.43}$$

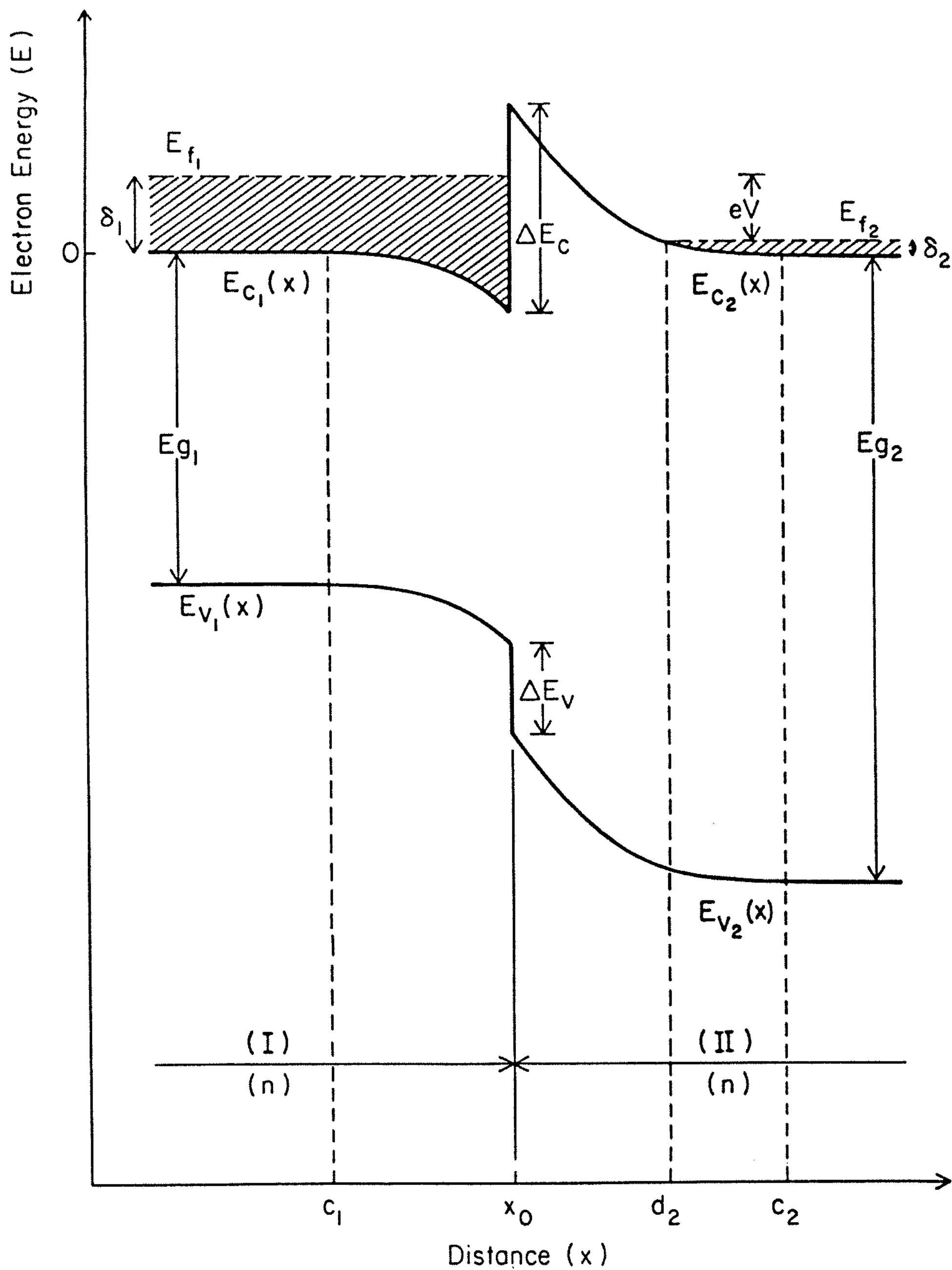

Figure 2.18: Schematic energy band diagram for a single n^+–n^+ heterojunction in which the left semiconductor is biased negatively with respect to the right one. ΔE_c (ΔE_v) denotes the conduction (valence) band discontinuity at the interface.

In this case, the width $(d_2 - x_0)$ of the totally depleted space–charge layer in region (II) takes a simple form. From $E_{c_2}(d_2) = \delta_1 - eV$, and the continuity of the slope of $E_{c_2}(x)$ at $x = d_2$, we get:

$$(d_2 - x_0) = \left(\frac{\epsilon_0 \epsilon_{r_2}}{e^2 n_{D_2}}\right)\left\{\left(\frac{\epsilon_{r_1}}{\epsilon_{r_2}}\right) y'_1(x_0) - \sqrt{\frac{6}{5}\left(\frac{e^2 n_{D_2} \delta_2}{\epsilon_0 \epsilon_{r_2}}\right)}\right\}. \tag{2.44}$$

It follows that $y_1(x_0)$ satisfies the following equation:

$$\left[\frac{y_1(x_0)}{\delta_1}\right]^{5/2} + \frac{5}{2}\left\{\left(\frac{n_{D_2}\epsilon_{r_2}}{n_{D_1}\epsilon_{r_2}}\right) - 1\right\}\left[\frac{y_1(x_0)}{\delta_1}\right] - \frac{3}{2}\left(\frac{n_{D_2}\epsilon_{r_2}\delta_2}{n_{D_1}\epsilon_{r_2}\delta_1}\right)\left\{1 + \frac{5}{3}\left(\frac{\Delta E_c + eV}{\delta_2}\right)\right\} + \frac{3}{2} = 0. \tag{2.45}$$

Once $y_1(x_0)$ is found, Eqs.(2.40)–(2.42) may be used to obtain the energy band profile of the single heterojunction under any applied bias.

Two such heterojunctions may be put together back to back to form n^+–n–n^+ structures. The original single barrier problem thus becomes that of two thinner barriers in series separated by a bulk layer of the central semiconductor. Since the electroneutrality condition is independently satisfied in both heterojunctions, an additional equation is required to find the voltage drop distribution across each one of them. If V_a denotes the total bias applied to the structure, the voltages V_l and V_r occurring across the two heterojunctions having their interfaces at $x = 0$ and $x = a$, satisfy:

$$V_a = V_l + V_r. \tag{2.46}$$

Furthermore, if w_l and w_r denote the widths of the corresponding fully depleted space–charge regions, it is assumed that

$$\frac{V_l}{V_r} = \frac{w_l}{w_r}. \tag{2.47}$$

An example of these calculations is illustrated in Fig.2.19 in the case of GaAs–AlAs–GaAs heterostructures. Using a valence band discontinuity at GaAs/AlAs interfaces of 0.55 eV,[23] the Γ– and X–point conduction band offsets are found to be 1.04 eV and 0.19 eV, respectively. Therefore, if the AlAs layer is sufficiently thick and the n–type doping densities are large enough, the AlAs Γ–point

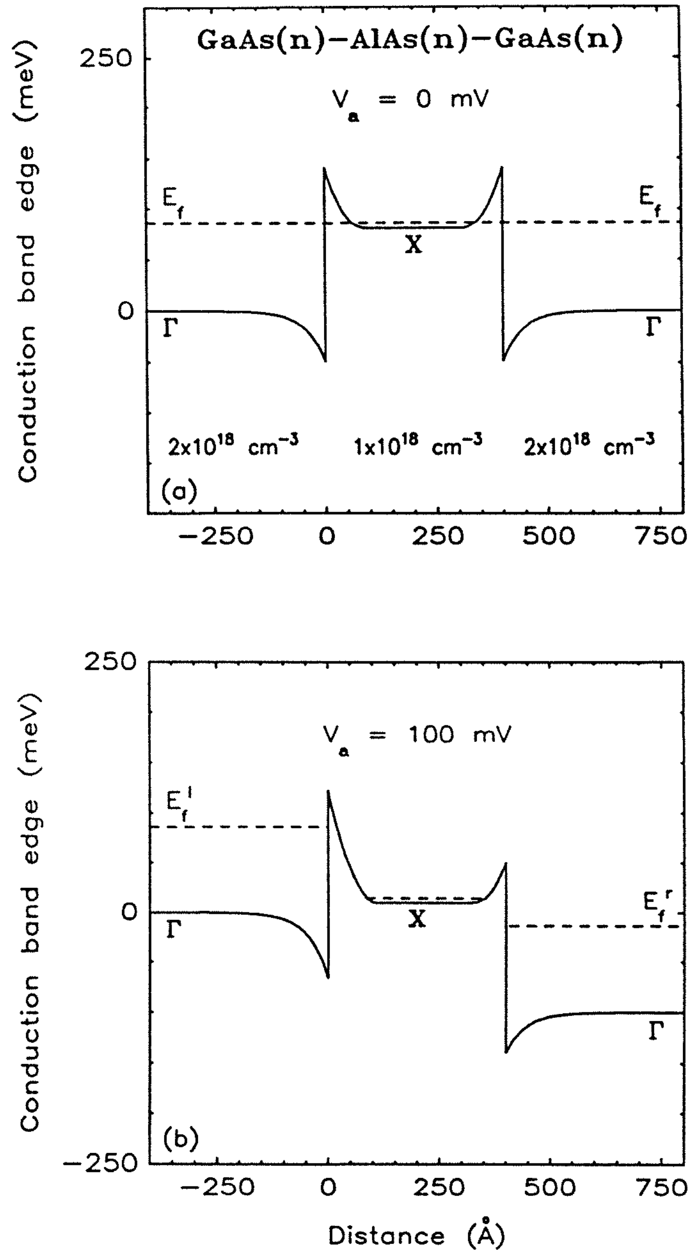

Figure 2.19: Calculated conduction band edges for a symmetric n^+–n–n^+ GaAs–AlAs–GaAs heterostructure featuring a bulk region in the central AlAs layer. The GaAs electrodes are doped at $2 \times 10^{18} cm^{-3}$. The AlAs layer is 400 Å thick and doped at $1 \times 10^{18} cm^{-3}$. The symmetry points of interest are the Γ–point in the cladding layers and the X–point in the AlAs. The conduction band offset at the heterojunction interfaces is taken to be 190 meV. (a) corresponds to the unbiased structure, and (b) to an applied voltage of 100 mV.

conduction band may still be fully depleted while electrons may occupy X–point states in the AlAs conduction band. When this occurs, calculating the shapes of the conduction band edges at the Γ–point in the GaAs electrodes and at the X–point in AlAs becomes essential in determining what the dominant current transport mechanisms are. Fig.2.19 depicts energy band profiles for a structure having a 400 Å thick AlAs layer and free electron densities of $2 \times 10^{18} cm^{-3}$ in the electrodes and $1 \times 10^{18} cm^{-3}$ in AlAs. Fig.2.19(a) corresponds to zero bias and Fig.2.19(b) to a total applied voltage of 100 mV. The electron effective mass, m_2^*, in the AlAs layer is taken to be the density–of–states mass: $m_2^* = 0.78\, m_0$.[22] Fig.2.19(a) reveals that the potential energy barrier for GaAs Γ–point electrons near the Fermi level is not a 400 Å thick AlAs barrier but two reduced AlAs X–point barriers which are only 56 meV high and 62 Å thick.

For given doping densities, these reduced barriers remain identical regardless of AlAs layer thicknesses provided a bulk–like region exists in AlAs. For given AlAs layer thickness and electrode doping concentrations, decreasing the doping density, n_{D_2}, in region (II) makes the two fully depleted AlAs barriers higher and broader, and the electrode accumulation layers smaller. The central AlAs bulk–like region thus becomes progressively thinner, until it eventually vanishes for low enough values of n_{D_2}. If the AlAs layer thickness and doping level are kept the same and the electrode doping density is increased, the Fermi level rises, the electrode accumulation layers decrease and the two fully depleted AlAs reduced barriers become lower and thinner.

These results suggest that energy band profiles are important in determining the nature of the dominant current transport mechanisms occurring in n^+–n–n^+ heterostructures. In particular, when the barrier layer is thick enough and/or sufficiently doped, electrons in the cladding layers do not tunnel through a single barrier but through two reduced barriers separated by a bulk layer of the central

semiconductor. This should yield large experimental current densities, $J_{exp}(V_a)$, even when the physical thickness a of region (II) is large enough that tunneling through the whole barrier would be negligible. For given doping concentrations, $J_{exp}(V_a)$ should be independent of a as long as a flat band region exists in the central layer. However, $J_{exp}(V_a)$ should be an increasing function of electrode and barrier doping densities. Experimental evidence of these effects has been reported in Se–doped GaAs–AlAs–GaAs heterostructures grown by MOCVD.[25] A number of samples were studied with AlAs layer thicknesses ranging between 85 and 730 Å, electrode free carrier concentrations between 3×10^{18} and $5 \times 10^{18} cm^{-3}$, and barrier doping densities between 5×10^{17} and $1 \times 10^{18} cm^{-3}$. High current densities were observed at 4.2 K, even through thick AlAs layers ($a > 300$Å). Furthermore, as expected from the above discussion, the experimental current densities of all the samples having energy band profiles in the form of two reduced AlAs X–point barriers separated by a bulk–like region depended strongly upon the electrode and barrier doping concentrations but only weakly upon the AlAs layer thickness, a.

2.6 Other Structures

Other cases of interest are structures in which the electrodes are degenerately doped p–type and current transport occurs via the tunneling of holes.[10] The energy band diagrams of single barrier heterostructures having p^+–cladding layers are best described in terms of the valence band edges. However, the band profiles may be obtained using the same approach as in the case of n^+–electrodes. The effective mass of interest is now the density–of–states effective mass for holes in the valence band, m_h^*, given by Eq.(2.12). In GaAs, $m_h^* = 0.48\, m_0$.[22] Fig. 2.20 depicts the valence band edges of three symmetric GaAs–$Al_{0.3}Ga_{0.7}$As–GaAs het-

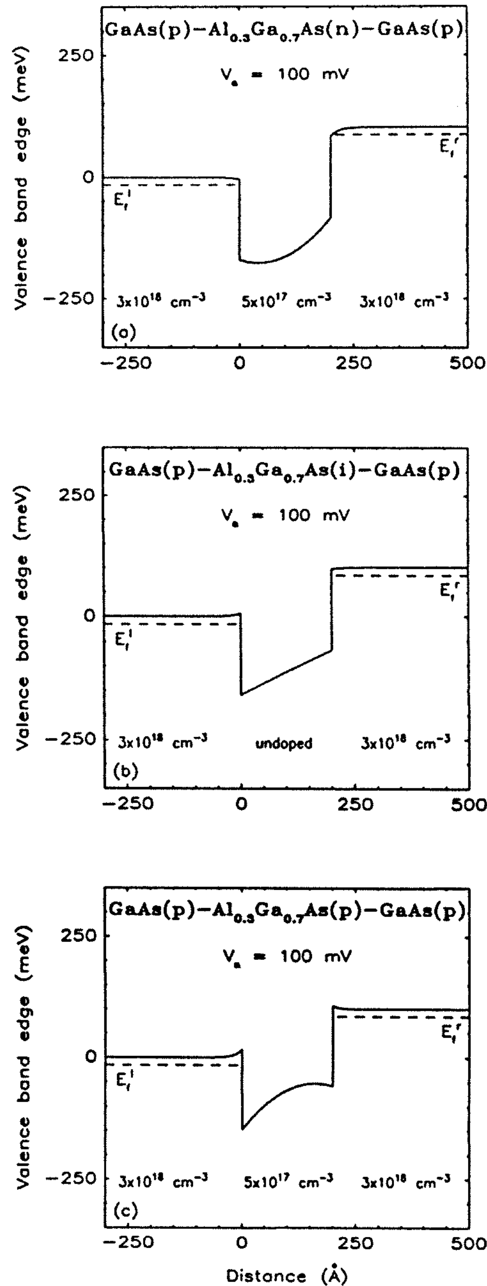

Figure 2.20: Calculated valence band edges for GaAs–$Al_{0.3}Ga_{0.7}As$–GaAs heterostructures in which the electrodes are degenerately doped *p*–type. The structures have a 200 Å thick barrier layer and electrode free carrier densities of $3 \times 10^{18} cm^{-3}$. In (a), the barrier is doped *n*–type at $5 \times 10^{17} cm^{-3}$. In (b), the $Al_{0.3}Ga_{0.7}As$ region is undoped. In (c), it is doped *p*–type at $5 \times 10^{17} cm^{-3}$. All three structures are under an applied bias of 100 mV. The valence band offset at the heterojunction interfaces is taken to be 165 meV.

erostructures. Each one of them has a 200 Å thick barrier layer and a free carrier doping density of $3 \times 10^{18} cm^{-3}$ in the cladding layers. The Fermi level then lies 16 meV below the valence band edge in the GaAs neutral regions. The valence band discontinuity is taken to be 165 meV.[23] In Fig.2.20(a), the barrier is doped n–type at $5 \times 10^{17} cm^{-3}$. This causes the bands to bend down at zero bias and the electrode space–charge layers to be partially depleted of holes. In Fig.2.20(b), the $Al_{0.3}Ga_{0.7}As$ layer is undoped and the bands are flat in the unbiased structure. In Fig.2.20(c), the barrier is doped p–type at $5 \times 10^{17} cm^{-3}$. As a result, the bands bend up at zero bias and holes accumulate in the cladding layers near the heterojunction interfaces. In Fig.2.20, a positive bias of 100 mV is applied to the left electrode with respect to the right cladding layer.

Novel negative differential resistance devices based on tunneling through single quantum barrier heterostructures have recently been proposed and analyzed theoretically.[2,3] When the cladding layers are doped n–type, negative differential resistances are anticipated if electrons tunnel through the band gap of the central semiconductor at energies which are much closer to the valence band edge energy than they are to the conduction band edge energy. This occurs because in the vicinity of the valence band edge, the imaginary part of the electron wave vector becomes small, resulting in a large tunneling probability. As the bias applied to the heterostructure is increased, the tunneling electrons move to higher energies with respect to the band edges in the barrier. As a result, the imaginary parts of their wave vectors become larger, their tunneling probabilities are reduced, and the current decreases. In these structures, the amount of voltage dropping across the barrier layer is an essential quantity since the change in barrier shape is responsible for the decrease in tunneling probabilities. However, band bending calculations indicate that voltage drops in the cladding layers reduce the fraction of applied bias dropped in the barrier. This effect would tend to make the nega-

tive slopes in the J–V curves more gradual. Another effect which competes with the mechanism by which negative differential resistances may be obtained is the creation of an accumulation layer near the first heterojunction interface, which causes the number of electrons available for tunneling to increase with applied voltage. Energy band diagrams should thus be useful in choosing the parameters of the structures and in predicting their device performance. In order to increase the amount of voltage dropping in the barrier, the central layer should be made undoped and sufficiently thick. The voltage drops in the cladding layers may be reduced by increasing the doping density. However, the electrode Fermi levels should remain small compared to the barrier height if electrons are to tunnel near the barrier valence band edge. To conciliate these two competing effects, an optimum value must be found for the electrode doping concentration.

To be specific, let us consider the case of $Hg_{1-x}Cd_xTe$–CdTe–$Hg_{1-x}Cd_xTe$ double heterojunctions.[3] Band offsets at $Hg_{1-x}Cd_xTe$/CdTe interfaces are still a matter of debate. Since different experimental measurements have yielded conflicting results,[26] we will simply assume the validity of the common anion rule and take the valence band discontinuity to be zero. Fig.2.21 shows the energy band diagrams of two symmetric $Hg_{0.7}Cd_{0.3}Te$–CdTe–$Hg_{0.7}Cd_{0.3}Te$ heterostructures under an applied bias of 150 mV. At 4.2 K, the $Hg_{0.7}Cd_{0.3}Te$ electrodes (CdTe barrier layer) have an electron effective mass of $0.025\, m_0$ ($0.19\, m_0$), an energy gap of 0.25 eV (1.60 eV), and a relative dielectric constant of 16.7 (11.0).[27] In both structures, the undoped CdTe barrier layer is 200 Å thick. In Fig.2.21(a), the electrode free carrier density is taken to be $1 \times 10^{17} cm^{-3}$, corresponding to a Fermi energy of 31 meV. In Fig.2.21(b), the cladding layers are doped at $1 \times 10^{18} cm^{-3}$, and the Fermi energy is 146 meV. As a result, 53% of the applied voltage drop across the barrier in Fig.2.21(a), whereas $V_2 = 0.65\, V_a$ in Fig.2.21(b). It would thus be desirable to use large doping densities in the

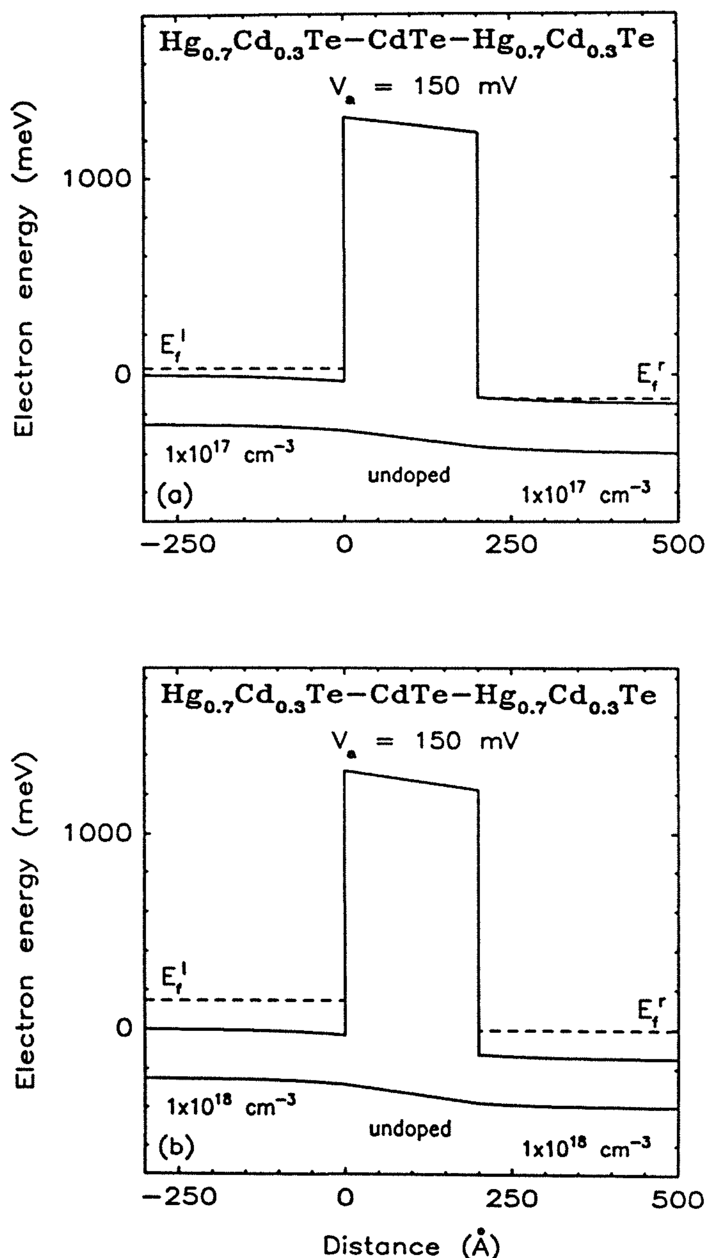

Figure 2.21: Calculated conduction and valence band edges for symmetric n^+–i–n^+ $Hg_{0.7}Cd_{0.3}Te$–CdTe–$Hg_{0.7}Cd_{0.3}Te$ heterostructures having a 200 Å thick barrier layer. The electrode doping densities are 1×10^{17} and $1 \times 10^{18} cm^{-3}$ in (a) and (b), respectively. The valence band offset at the heterojunction interfaces is assumed to be zero. The energy gaps in the $Hg_{0.7}Cd_{0.3}Te$ electrodes and the CdTe barrier are taken to be 0.25 and 1.60 eV, respectively, resulting in a conduction band offset of 1.35 eV.

cladding layers, provided that the electrode Fermi levels remain small compared to the mid–gap energy in the barrier. In that respect, it may be of interest to use materials such as InAs and $In_{1-x}Ga_xAs$, which can be grown with higher doping levels than those currently attainable in $Hg_{1-x}Cd_xTe$/CdTe heterostructures.[28] Furthermore, the properties of $Hg_{1-x}Cd_xTe$ vary drastically with Cd composition when x is small. For example, if $x = 0.2$, the band gap at 4.2 K is only 70 meV and the electron effective mass is $0.0065\, m_0$.[27] This band gap reduction would allow electrons to tunnel closer to the barrier valence band edge than when x is larger. However, electrons occupying valence band states in the left electrode would begin to tunnel to the right electrode when the total applied voltage is slightly greater than the band gap in the cladding layers. At this point, positive differential resistances will reappear. It is therefore necessary to maintain a band gap in the cladding layers which is larger than the desired operating voltage for the device. Furthermore, it is a general property of energy band diagrams that when the effective mass is decreased in the cladding layers, the electrode Fermi energies become larger, the cladding layer space–charge regions broaden and the amount of voltage dropping across the barrier is reduced. For example, in a $Hg_{0.8}Cd_{0.2}Te$–CdTe–$Hg_{0.8}Cd_{0.2}Te$ heterostructure having an electrode free carrier density of $1 \times 10^{17} cm^{-3}$, the Fermi level in the bulk cladding layers would be as large as 121 meV, as opposed to 31 meV when $x = 0.3$. In addition, in the case of a 200 Å thick undoped barrier layer, the voltage drop across the barrier would only be $0.36\, V_a$ when $V_a = 150$ mV, as opposed to $0.53\, V_a$ when $x = 0.3$. This illustrates the necessity of optimizing the Cd composition in the cladding layer alloys in addition to the doping levels.

2.7 Summary

The objective of this study was to calculate the energy band diagrams of single barrier heterostructures and to discuss their implications on the electronic properties of a few tunnel structures of current interest. Energy band profiles were calculated by solving Poisson's equation self–consistently after making four simplifying assumptions: (*i*) the interfaces are abrupt; (*ii*) the temperature is taken to be 0 K; (*iii*) two–dimensional energy subbands in accumulation layers are ignored; and (*iv*) band tailing effects in degenerate semiconductors are neglected. Relaxing these assumptions would basically result in more complex numerical integrations, but would not qualitatively alter the main results of this study. These results may be summarized as follows. (*i*) Energy band diagrams make it possible to describe heterostructures in a more realistic way than the usual models which assume that the band edges remain flat in unbiased structures and that the entire applied voltage drops linearly across the barrier layer in biased structures. They could thus be useful in tailoring quantum barriers to particular heights and shapes. (*ii*) When the heterostructures are biased, they give the voltage drop distribution in the cladding layers as well as in the barrier. It was shown that this distribution may differ significantly from that obtained when band bending is ignored, and that energy band diagram calculations are important whether the barrier is doped or not. (*iii*) Energy band profiles revealed that band bending plays a more important role for larger applied voltages, thicker barrier layers, smaller electrode doping densities, and larger barrier doping concentrations. (*iv*) They were also found to be useful in determining what the dominant low temperature current transport mechanisms occurring in single barrier tunnel structures are. In some cases, they revealed that these mechanisms may be quite different from those expected when band bending is neglected. This occurs, for example, in n^+–n–n^+ heterostructures having thick and/or heavily

doped barrier layers. The dominant current transport mechanism then becomes tunneling through two reduced barriers separated by a non–depleted layer of the central semiconductor. (*v*) Energy band diagrams are important in calculating tunneling *J–V* characteristics, which are extremely sensitive to the actual shape of the barrier through which the charge carriers tunnel. They may thus provide information about certain structure parameters which are difficult to determine accurately, such as band offsets and ultra–thin layer doping densities. (*vi*) They can also be used to study the novel electronic properties of single barrier tunnel structures from which negative differential resistances are anticipated. Although this was illustrated in the case of $Hg_{1-x}Cd_xTe$–CdTe–$Hg_{1-x}Cd_xTe$ double heterojunctions, other materials could be similarly analyzed. An example is the InAs/$In_{1-x}Ga_xAs$ system. Such heterostructures have interesting potential device applications, but band bending calculations indicated that a number of effects compete with the mechanism by which negative differential resistances may be obtained. Energy band diagrams could thus be useful for making the proper compromises in choosing the parameters of these stuctures and for optimizing their device performance.

References

1. R. J. Hauenstein, L. J. Schowalter, B. D. Hunt, O. J. Marsh, and T. C. McGill, in *Proc. of the Mat. Res. Soc.*, Palo Alto, 1986 (to be published).

2. J. Heremans, D. L. Partin, and P. D. Dresselhaus, Appl. Phys. Lett **48**, 644 (1986).

3. D. H. Chow, and T. C. McGill, Appl. Phys. Lett. **48**, 1485 (1986).

4. R. Tsu, and L. Esaki, Appl. Phys. Lett. **22**, 562 (1973).

5. L. L. Chang, L. Esaki, and R. Tsu, Appl. Phys. Lett. **24**, 593 (1974).

6. T. C. L. G. Sollner, W. D. Goodhue, P. E. Tannenwald, C. D. Parker, and D. D. Peck, Appl. Phys. Lett. **43**, 588 (1983).

7. A. R. Bonnefoi, R. T. Collins, T. C. McGill, R. D. Burnham, and F. A. Ponce, Appl. Phys. Lett. **46**, 285 (1985).

8. T. J. Shewchuk, P. C. Chapin, P. D. Coleman, W. Kopp, R. Fischer, and H. Morkoç, Appl. Phys. Lett. **46**, 508 (1985).

9. M. A. Reed, "Excited State Resonant Tunneling in GaAs–$Al_xGa_{1-x}As$ Double Barrier Heterostructures," to be published in *Superlattices and Microstructures*, (Academic Press).

10. E. E. Mendez, W. I. Wang, B. Ricco, and L. Esaki, Appl. Phys. Lett. **47**, 415 (1985).

11. P. D. Coleman, S. Goedeke, T. J. Shewchuk, P. C. Chapin, J. M. Gering, and H. Morkoç, Appl. Phys. Lett. **48**, 422 (1986).

12. F. Capasso, and R. A. Kiehl, J. Appl. Phys. **58**, 1366 (1985).

13. A. R. Bonnefoi, D. H. Chow, and T. C. McGill, Appl. Phys. Lett. **47**, 888 (1985).

14. A. R. Bonnefoi, T. C. McGill, and R. D. Burnham, IEEE Elect. Dev. Lett. **EDL–6**, 636 (1985).

15. I. Hase, H. Kawai, K. Kaneko, N. Watanabe, Electon. Lett. **20**, 491 (1984).

16. D. Delagebeaudeuf, P. Delescluse, P. Etienne, J. Massies, M. Laviron, J. Chaplart, and N. T. Linh, Electron. Lett. **18**, 85 (1982).

17. P. Guéret, and U. Kaufmann, Electron. Lett. **21**, 344 (1985).

18. R. T. Collins, J. Lambe, T. C. McGill, and R. D. Burnham, Appl. Phys. Lett. **44**, 532 (1984).

19. A. R. Bonnefoi, D. H. Chow, T. C. McGill, R. D. Burnham, and F. A. Ponce, J. Vac. Sci. Technol. B **4**, 988 (1986).

20. R. D. Burnham, private communication.

21. E. O. Kane, *Physics of III–V Compounds, Vol. 1, Ch. 3,* (Academic Press, New York, 1966) pp.75–100.

22. H. C. Casey, and M. B. Panish, *Heterostructure Lasers. Part A,* (Academic Press, New York, 1978), p.192.

23. J. Batey, and S. L. Wright, J. Appl. Phys. **59**, 200 (1986).

24. P. Dawson, G. Duggan, H. I. Ralph, and K. Woodbridge, Superlattices and Microstructures **1**, 231 (1985).

25. A. R. Bonnefoi, D. H. Chow, T. C. McGill, and R. D. Burnham, Bulletin of the American Physical Society **31**, 395 (1986).

26. S. P. Kowalczyk, J. T. Cheung, E. A. Kraut, and R. W. Grant, Phys. Rev. Lett. **56**, 1605 (1986).

27. R. Dornhaus, G. Nimtz, and B. Schlicht, *Narrow–Gap Semiconductors* (Springer–Verlag, Berlin, 1983), p.163.

28. D. H. Chow, and T. C. McGill, to be published.

Chapter 3

Elastic and Inelastic Tunneling Processes in GaAs–AlAs–GaAs Heterostructures Grown by Metalorganic Chemical Vapor Deposition

3.1 Introduction

Single quantum barrier heterostructures are frequently fabricated from GaAs and $Al_xGa_{1-x}As$ using techniques such as molecular beam epitaxy (MBE) and metalorganic chemical vapor deposition (MOCVD) to achieve small characteristic dimensions.[1-4] In these structures, an important current transport mechanism is electron tunneling. The associated tunneling effects yield novel electronic properties, some of which remain to be fully understood. Most of the theoretical and experimental studies use $Al_xGa_{1-x}As$ quantum barriers in which the

Al composition, x, is small enough that the alloy is still direct. Furthermore, experimental investigations are usually performed on MBE grown wafers. Only a few studies have been reported on single quantum barrier heterostructures grown by MOCVD,[3,4] and/or in which the barriers consisted of indirect band gap $Al_xGa_{1-x}As$[3], or pure AlAs[4].

In Chapter 2, a simple theoretical model was developed to calculate the energy band diagrams and the current–voltage (I–V) characteristics of single barrier tunnel structures. In this chapter, these concepts are related to an experimental study of elastic and inelastic tunneling processes in GaAs–AlAs–GaAs double heterojunctions grown by MOCVD in the [100]–direction.

Section 3.2 briefly presents the sample growth and preparation procedures, as well as the measurement techniques. Section 3.3 deals with structures in which the AlAs barrier layers are doped p–type. It is first shown, in section 3.3.1, that the dominant current transport mechanisms at low temperatures are tunneling through the AlAs band gap at both the Γ– and X–points. This is achieved by calculating the low temperature I–V characteristics due to elastic tunneling through the AlAs band gap at the Γ–point, using the actual shapes of the quantum barriers obtained from band bending calculations. Upon comparing the calculated and experimental I–V curves, it is found that tunneling through the AlAs Γ–point barriers fails to explain the experimental data. This indicates that other transport mechanisms must contribute to the total current. Tunneling through the AlAs band gap at the X–point is then discussed. Good theoretical fits of the experimental I–V characteristics can be obtained by considering tunneling through both the AlAs Γ– and X–point barriers. Section 3.3.2 introduces a new element to the calculation of the theoretical I–V curves: the presence of trap levels in the AlAs band gap, due to defects or impurities. A simple model is developed to calculate the impurity–assisted tunneling current. It is shown

that this current, which becomes more important as the quantum barriers are made thicker, can actually become the dominant current transport mechanism through thick enough barriers. In section 3.3.3, the p–type barrier samples are classified into two categories depending upon the nature of the inelastic processes which may be identified in the derivatives, $(dI/dV)(V)$ and $(d^2I/dV^2)(V)$, of the I–V characteristics. A few structures also feature anomalous zero–bias conductances. These so–called "zero–bias anomalies" are discussed in section 3.3.4. Section 3.4 deals with GaAs–AlAs–GaAs double heterojunctions in which the AlAs barrier layers are doped n–type. First, samples having thick AlAs layers (140–730 Å) are presented in section 3.4.1. The current densities obtained at low temperatures from these heterostructures are very large and do not display the exponential dependence upon barrier thickness usually expected from tunneling through a potential energy barrier. However, these observations may be explained by calculating the energy band diagrams of the structures, which reveal that the AlAs conduction band at the X–point is not totally depleted of electrons. As a result, the dominant low temperature current transport mechanism is tunneling through two reduced AlAs X–point barriers, in a two–step process, and not tunneling through a single potential energy barrier. These results are consistent with the inelastic tunneling processes observed experimentally. Section 3.4.2 deals with heterostructures in which the n–type AlAs barrier layers are thin enough that they remain totally depleted of free carriers. Consequently, tunneling occurs through the AlAs band gap in a one–step process. Another important property of these structures is that they show experimental evidence of interactions between interface plasmons and longitudinal optical (LO) phonons in GaAs and AlAs. Finally, the results of this study are summarized in section 3.5.

3.2 Experimental Procedures

Each of the GaAs–AlAs–GaAs single barrier tunnel structures used in this study was grown by an MOCVD technique[5,6] on a [100]–oriented GaAs substrate doped n–type with Si at 2–3 $\times 10^{18} cm^{-3}$. A first epitaxial layer of GaAs, degenerately doped n–type with Se, was grown 2–3 μm thick. This layer was followed by a thin AlAs quantum barrier, doped either p–type with Mg,[7,8] or n–type with Se. Finally, a top GaAs cladding layer was grown, degenerately doped with Se. Samples were fabricated with GaAs doping densities ranging between 1×10^{18} and $5.5 \times 10^{18} cm^{-3}$, and AlAs layer thicknesses between 48 and 730 Å. The most important structure parameters are summarized in Table 3.1. The second column gives the intended AlAs barrier thicknesses. The third column lists the actual thicknesses obtained from transmission electron microscopy (TEM) measurements, accurate to within one monolayer (one monolayer is taken to be 2.83 Å). In the p–type barrier samples, both values are usually close, except in the structures having the thicker barrier layers. However, in most of the n–type samples, the AlAs layers are much thicker than anticipated from the growth parameters. The electrode doping densities were obtained from Polaron doping profiles. The barrier doping levels were estimated from the flow rates used during growth. They could thus be in error due to background doping and dopant memory effects, and to the difficulty of accurately calibrating ultra–thin layer doping concentrations.

Devices were made by defining mesas on the epitaxial face of each sample using conventional photolithography and a GaAs etch (4:1:1, H_2SO_4:H_2O_2:H_2O). The mesas were circular and 50–700 μm in diameter. Ohmic contacts were made on the surface of the mesas and on the substrate by evaporating Au–Ge, or Au–Ge, Ni, Au, and annealing at 380–410°C for 20–30 s.

Table 3.1: Sample information for single barrier tunnel structures.

Sample	Barrier Thickness		Doping Densities (cm^{-3})	
	Grown	TEM	Electrodes	Barrier
H115	150 Å	235 Å (83 monolayers)	Se–5.0 × 10^{18}	Mg–1 × 10^{18}
H125	50 Å	48 Å (17 monolayers)	Se–4.0 × 10^{18}	Mg–3 × 10^{18}
H135	100 Å	189.5 Å (67 monolayers)	Se–4.0 × 10^{18}	Mg–1 × 10^{18}
H151	150 Å	181 Å (64 monolayers)	Se–1.2 × 10^{18}	Mg–1 × 10^{18}
H160	50 Å	54 Å (19 monolayers)	Se–3.0 × 10^{18}	Mg–5 × 10^{17}
H381	35 Å	—	Se–3.0 × 10^{18}	Mg–1 × 10^{18}
H894	50 Å	79 Å (28 monolayers)	Se–1.2 × 10^{18}	Mg–5 × 10^{17}
T007	50 Å	54 Å (19 monolayers)	Se–3.0 × 10^{18}	Mg–1 × 10^{18}
H930	100 Å	87.5 Å (31 monolayers)	Se–2.0 × 10^{18}	Mg–1 × 10^{18}
H931	75 Å	76.5 Å (27 monolayers)	Se–2.3 × 10^{18}	Mg–1 × 10^{18}
H003	50–100 Å	693 Å (245 monolayers)	Se–5.5 × 10^{18}	Se–5 × 10^{17}
H056	50–100 Å	141.5 Å (50 monolayers)	Se–5.0 × 10^{18}	Se–5 × 10^{17}
H083	75–150 Å	339.5 Å (120 monolayers)	Se–5.0 × 10^{18}	Se–5 × 10^{17}
H098	100–200 Å	589 Å (208 monolayers)	Se–5.5 × 10^{18}	Se–5 × 10^{17}
H099	150–300 Å	730 Å (258 monolayers)	Se–5.5 × 10^{18}	Se–5 × 10^{17}
Y760	50 Å	85 Å (30 monolayers)	Se–3.0 × 10^{18}	Se–1 × 10^{18}

Measurements of current–voltage, I–V, characteristics, as well as first, $(dI/dV)(V)$, and second, $(d^2I/dV^2)(V)$, derivatives of the I–V curves, were performed at temperatures ranging from 300 to 4.2 K. The I–V curves were measured with an HP 4145 semiconductor parameter analyzer. The first and second derivative spectra were obtained using modulation techniques at 5 and 50 kHz, respectively.[9] Typical modulation voltages ranged between a fraction of millivolt and 5 mV peak–to–peak. Derivative curves are particularly useful in identifying inelastic tunneling processes. This is because tunneling electrons can create fundamental excitations when the applied bias is increased above the excitation energy ($\hbar\omega_0$). Therefore, there exists a threshold voltage $V_0 = \hbar\omega_0/e$, which corresponds to a change in the slope of the I–V characteristics. Since the structures are symmetric, the same changes should occur in forward and reverse bias. As a result, steps which are symmetric with respect to bias appear in the first derivative spectra at voltages $\pm V_0$. The second derivative curves show peaks at the same voltages, but antisymmetric with respect to bias.

3.3 Samples with p–Type AlAs Barrier Layers

3.3.1 Tunneling Through AlAs Γ– and X–Point Barriers

In this section, the dominant current transport mechanisms in GaAs–AlAs–GaAs single barrier tunnel structures having p–type AlAs barrier layers are investigated. A number of studies have reported that low temperature current transport through $Al_xGa_{1-x}As$ quantum barriers is dominated by elastic tunneling through the $Al_xGa_{1-x}As$ direct band gap at the Γ–point.[1–3] In these studies, theoretical I–V curves were calculated assuming trapezoidal shapes for the quantum barriers under applied bias, and compared to experimental data on logarithmic scales. Nevertheless, discrepancies were observed,[1] which indicated

that other current transport mechanisms can compete with elastic Γ–point tunneling. Theoretical studies have also reported that Γ–point electrons in the GaAs electrodes should tunnel through $Al_xGa_{1-x}As$ Γ–point barriers even in indirect alloys.[10,11] However, it is shown here that the experimental data obtained from structures with pure AlAs barriers cannot be explained by Γ–point tunneling alone. It is proposed that there is also a small, but non–negligible, probability that incident electrons tunnel through the AlAs band gap at the X–point.

Current densities are calculated using the following approach. First, the actual shapes of the conduction band edges in the electrodes and the barrier are determined from band bending calculations. As shown in Chapter 2, energy band diagrams are of critical importance, particularly in samples having heavily doped barrier layers. The transmission coefficient for the tunneling electrons is then calculated using the WKB approximation. The attenuation constant in the barrier is determined from a two–band model, **k.p** theory formula[12] for electrons tunneling through the AlAs Γ–point barrier, and a simple one–band model formula for electrons tunneling through the AlAs band gap at the X–point. Finally, the current density, J, is found as a function of applied voltage, V, using the approach of Tsu and Esaki.[13]

Although this study was performed on several samples and at temperatures ranging from 300 to 4.2 K, we only illustrate here the most important results by discussing data obtained at low temperatures from one structure (sample H125). A more detailed discussion, including results for other heterostructures, is presented in section 3.3.3.

In the sample of interest, the GaAs electrodes are doped n–type with Se at 4 $\times 10^{18} cm^{-3}$. The doping density in the p–type AlAs barrier layer is estimated to be on the order of $3 \times 10^{18} cm^{-3}$. The barrier is 48 Å thick. Fig.3.1 shows the calculated conduction band edges at the Γ– and X–points as functions of distance

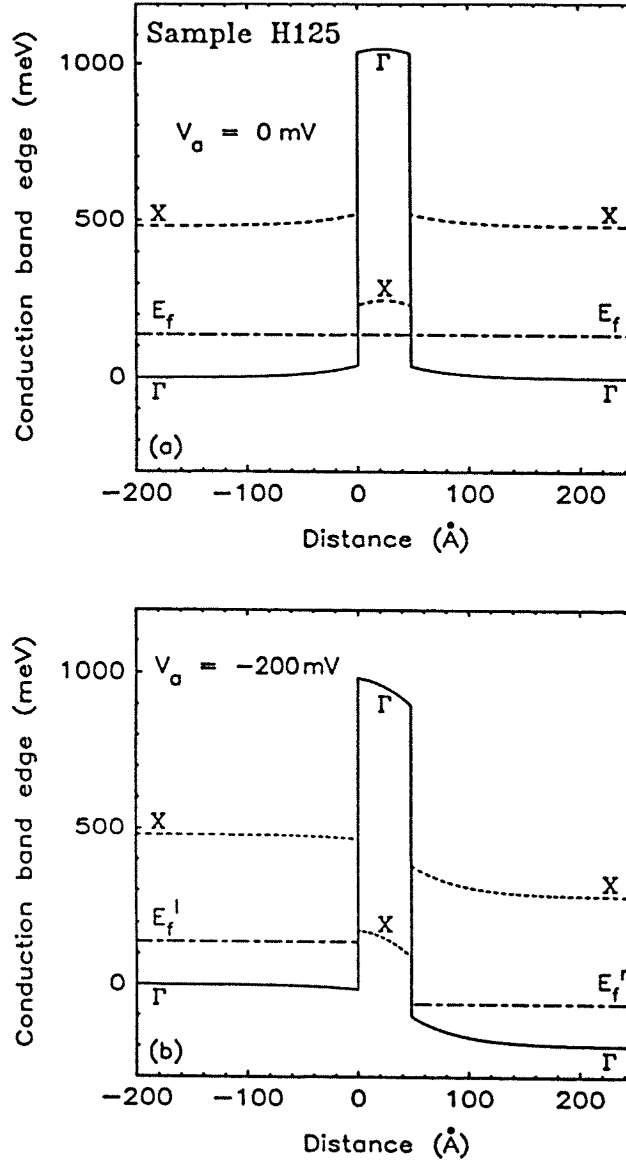

Figure 3.1: Calculated conduction band edges at the Γ–point (solid lines) and at the X–point (dashed lines), as functions of distance in the direction perpendicular to the planes of the layers, for sample H125. The GaAs electrodes are doped n–type at $4 \times 10^{18} cm^{-3}$. The AlAs barrier is 48 Å thick and doped p–type at $3 \times 10^{18} cm^{-3}$. The conduction band discontinuities at the X– and Γ–points are taken to be 0.19 and 1.04 eV, respectively. (a) depicts the unbiased structure. (b) corresponds to a negative voltage, $V_a = -200$ mV, applied to the left GaAs electrode with respect to the right cladding layer. The solid–dashed lines correspond to the Fermi level, E_f, in the electrodes.

in the direction perpendicular to the heterojunction interfaces. Fig.3.1(a) depicts the unbiased structure, ($V_a = 0$). Fig.3.1(b) corresponds to a negative voltage, $V_a = -200$ mV, applied to the left electrode with respect to the right cladding layer. In energy band diagram calculations, the values of the band offsets are key parameters in determining the shapes of the barriers through which the electrons tunnel. These values are still a matter of debate. In a recent experimental study, Batey *et al.* obtained a valence band discontinuity in GaAs/AlAs heterostructures of 0.55 eV.[14] Using this result, values close to 0.19 and 1.04 eV can be calculated for the conduction band offsets at the X– and Γ–points, respectively. It should be noted that when such values are used, the X–point conduction band edges lie at higher energies in GaAs than in AlAs. This is illustrated in Fig.3.1, with the solid lines corresponding to the Γ–point conduction band edges and the dashed lines to the X–point conduction band edges. Fig.3.1(a) reveals that the quantum barrier is totally depleted of carriers and that the effect of band bending is to increase the average height of the barrier through which the electrons tunnel. Fig.3.1(b) indicates that a bias applied across the structure alters the shapes of the conduction band edges in the cladding layers as well as in the barrier. This is another essential factor in calculating tunneling currents. Fig.3.2 shows the experimental characteristic, $J_{exp}(V)$, at 4.2 K in the voltage range 0–200 mV and, on the same linear scale, the calculated current density, $J_{el}^{\Gamma}(V)$, for elastic Γ–point tunneling. Since the structure is symmetric, the J–V curves are symmetric with respect to the origin, and only the forward bias direction is shown. The two curves are in good agreement at very low biases (≤ 20 mV), but start to deviate significantly in magnitude and shape at higher voltages. While J_{el}^{Γ} varies almost linearly with voltage, J_{exp} displays a nearly exponential voltage dependence. It should be mentioned that leakage has been eliminated as a possible source of current by verifying that the experimental J–V characteristics were

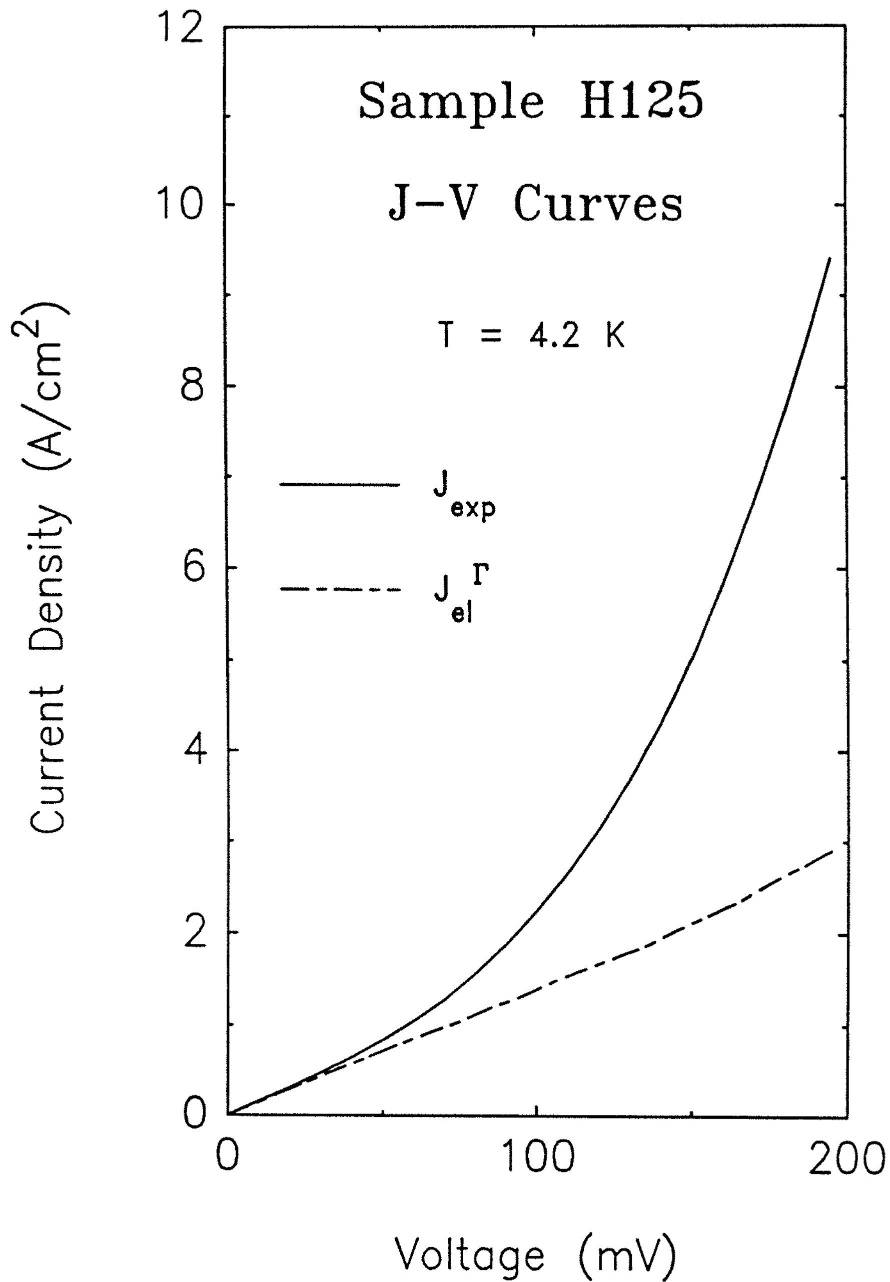

Figure 3.2: Experimental and theoretical J–V characteristics at 4.2 K for the single barrier structure shown in Fig.3.1 (H125). The solid line corresponds to the experimental current density, J_{exp}. The dashed line is the calculated current density, J_{el}^{Γ}, for elastic Γ–point tunneling.

reproducible and independent of device area. Similar discrepancies between experimental and theoretical data are obtained from all the samples. These results indicate that elastic tunneling through the AlAs band gap at the Γ–point does not account for all of the experimental current, and that other transport mechanisms are present. These observations are further supported by derivative spectra which reveal threshold voltages for impurity–assisted and/or inelastic tunneling processes. This is illustrated in the second derivative curve, $(d^2I/dV^2)(V)$, depicted in Fig.3.3. The spectrum displays prominent and broad features, peaked at approximately ± 20 and ± 80 mV. These have been labeled (a) and (b) in forward bias. It also reveals narrower peaks at ± 37 and ± 50 mV. These have been attributed previously to electron–longitudinal optical (LO) phonon coupling in the GaAs electrodes, and to the excitation of LO phonons in the AlAs barrier, respectively.[4]

The behavior of the elastic Γ–point tunneling current can easily be understood in terms of the complex band structure of AlAs: in the band gap, the imaginary part of the complex wave vector at the Γ–point varies very slowly with energy, except near the conduction and valence band edges. This is due to the small Γ–point effective mass. Therefore, because of the large conduction band offset ($\approx$1 eV), the Γ–point tunneling current remains slowly varying with voltage up to about 0.8 V. In order to tentatively explain the discrepancies observed between the experimental J–V curves and the calculated Γ–point elastic tunneling currents, a number of transport mechanisms can be suggested. The simplest is the emission of phonons or the excitation of collective modes by electrons tunneling through the AlAs Γ–point barrier. Although some of these inelastic processes may be resolved in derivative spectra, they yield currents which are typically at least two or three orders of magnitude smaller than elastic currents, and therefore too small to account for the observed discrepancies. Another possible current

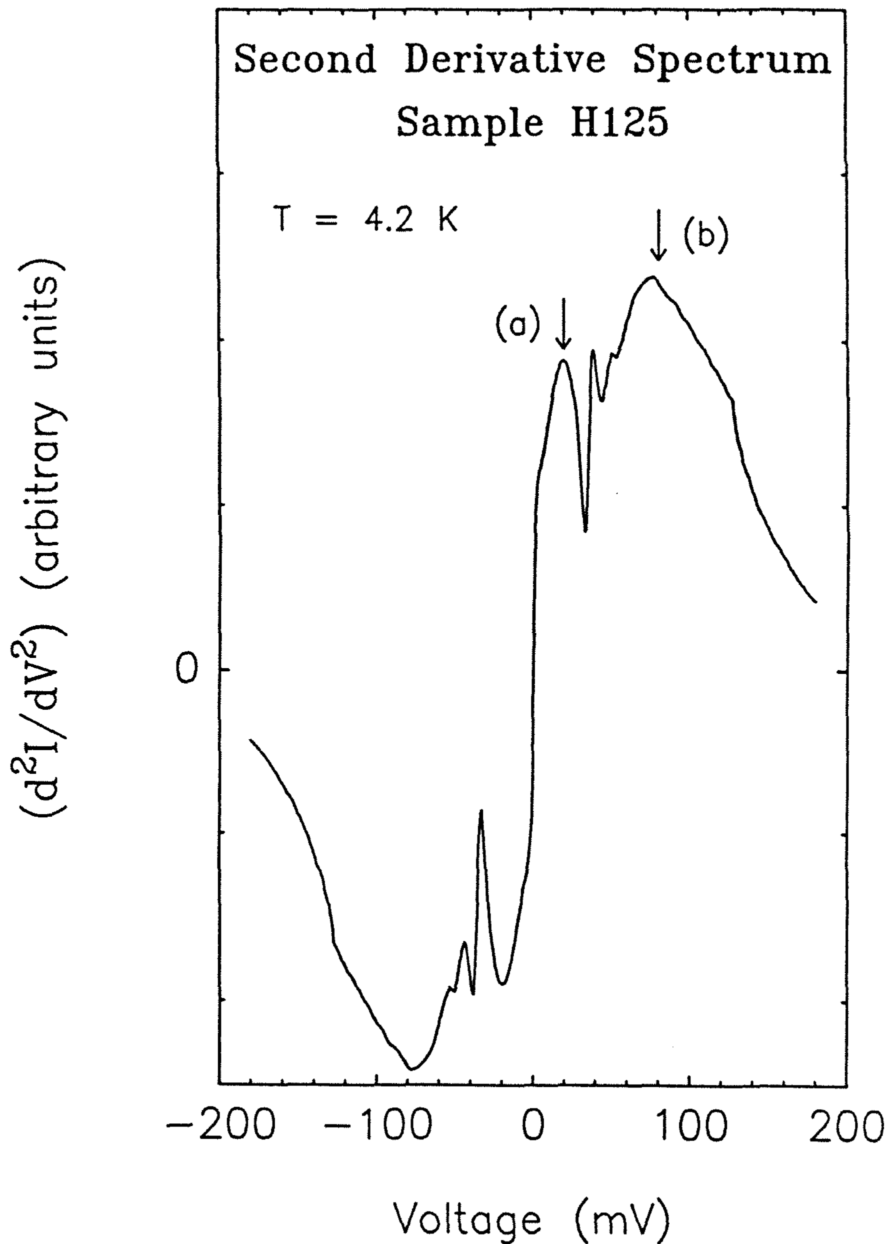

Figure 3.3: Experimental $(d^2I/dV^2)(V)$ spectrum at 4.2 K for H125. The most prominent peaks, labeled (a) and (b) in forward bias, may correspond to inelastic processes by which GaAs Γ–point electrons scatter into AlAs X–point states. The narrow peaks at ± 37 and ± 50 mV have been attributed previously to electron–longitudinal optical (LO) phonon coupling in the GaAs electrodes, and to the excitation of LO phonons in the AlAs barrier, respectively.[4]

transport mechanism is tunneling via energy states localized in the AlAs band gap or at the GaAs/AlAs interfaces. A simple model for impurity–assisted tunneling is developed in section 3.3.2. Assuming that no impurity bands or clusters are formed, this mechanism produces negligible current densities in the case of the 48 Å barrier structure under discussion. Another possibility is to take into account tunneling through the AlAs band gap at symmetry points other than the Γ–point. In the case of epitaxial growth in the [100]–direction, an important contribution could come from the AlAs X–point valleys. For electrons tunneling from left to right, new channels open when the Fermi level in the left electrode aligns with the X–point conduction band edge in the right electrode. However, such processes can only occur at voltages $\geq$ 350 meV in sample H125. This is again in disagreement with the experimental data. Other mechanisms can allow electrons occupying Γ–point states in both GaAs electrodes to tunnel through the AlAs X–point barrier. Two such processes are discussed below.

First, Γ–point electrons near the GaAs–AlAs interface may scatter inelastically into virtual states beneath the four AlAs X–valleys lying along the k_y– and k_z–directions, parallel to the planes of the layers. They may then tunnel through the AlAs band gap at the X–point, and scatter again, near the AlAs–GaAs interface, into the Γ–valley in the right electrode. Since electrons travel along the x–axis, perpendicular to the planes of the layers, the effective mass to consider in the barrier is the small transverse effective mass $m_t^* = 0.19\, m_e$, where m_e is the free electron mass. Such inelastic processes, which require two scattering events, can occur through a number of mechanisms, such as the excitation of phonons for example. Calculations of scattering matrix elements and current densities are necessary to determine which of these processes may explain the experimental data. The matrix elements can be complicated functions of the scattering mechanism, applied voltage, structure characteristics, electron energy, and tem-

perature. In this study, it is simply assumed that there is a small probability that incident electrons tunnel through the AlAs band gap at the X–point and that the scattering matrix element for a given process is constant. The calculated current density for any such mechanism thus contains an empirical factor, B_{in}. Threshold voltages for these inelastic processes are chosen to coincide with some of the most prominent peaks observed in experimental second derivative spectra. The total theoretical current density, $J_{th}(V)$, is then calculated by summing the contributions from Γ–point elastic tunneling and X–point inelastic tunneling. Fig.3.4 is a plot of J_{th} as a function of applied voltage for sample H125. Only two inelastic processes are used to calculate the X–point tunneling current. These two processes are assigned threshold voltages of 20 and 80 mV, and empirical B_{in}'s of 0.6×10^{-4} and 1.3×10^{-4}, respectively. The threshold voltages correspond to the two most prominent second derivative peaks labeled (a) and (b) in Fig.3.3. Since two scattering events are required to allow electrons to tunnel through the AlAs X–point barrier, peaks should be observed in the $(d^2I/dV^2)(V)$ spectra at voltages corresponding to the sum of the two scattering energies. Peak (a) would thus be consistent with the inelastic excitation of two X–point transverse acoustic (TA) phonons. On the other hand, the broad peak (b) may result from a number of scattering mechanisms which are not individually resolved in the spectrum shown in Fig.3.3. Such inelastic processes could be the excitation of X–point longitudinal acoustic (LA), transverse optical (TO), and longitudinal optical (LO) phonons, for example. It should be noted that the experimental and theoretical J–V curves displayed in Figs.3.2 and 3.4 are in good agreement.

Another possible way for electrons to tunnel through the AlAs band gap at the X–point arises from the coupling of AlAs X–point states with GaAs Γ–point states due to the breaking of translational symmetry in the direction perpendicular to the heterojunction interfaces. This makes it possible for Γ–point electrons

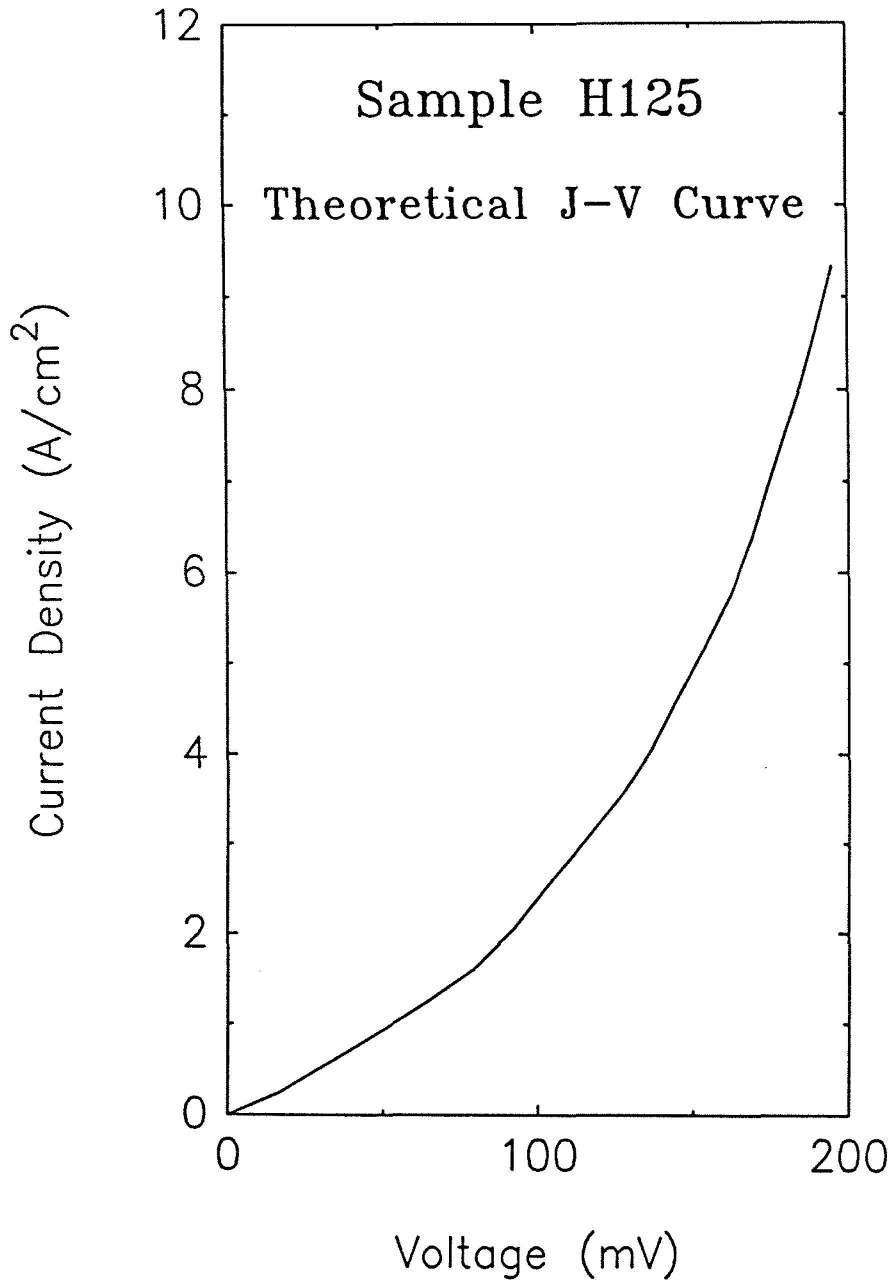

Figure 3.4: Total theoretical current density for sample H125, J_{th}, obtained by summing the contributions of Γ–point elastic tunneling and two X–point inelastic tunneling processes. For the inelastic processes, threshold voltages of 20 and 80 mV are taken, in agreement with the prominent experimental second derivative peaks (a) and (b) shown in Fig.3.3. The corresponding empirical B_{in}'s are 0.6×10^{-4} and 1.3×10^{-4}, respectively.

in one GaAs electrode to tunnel elastically through the AlAs X–point barrier, into Γ–point states in the other GaAs electrode. In this process, the virtual X–point states to consider are those below the two X–valleys lying along the k_x–direction, perpendicular to the planes of the layers. Since electrons travel along the x–axis, the effective mass of importance in the barrier is the large longitudinal effective mass $m_l^* = 1.1\,m_e$. Preliminary calculations indicate that the coupling of states having different symmetries in GaAs and AlAs may be significant in the heterostructures studied and could yield current densities large enough to account for the discrepancies observed between experimental and Γ–point elastic tunneling currents.

Two separate mechanisms by which Γ–point electrons in the GaAs electrodes may tunnel through the AlAs X–point barrier have been proposed. In fact, both processes may occur simultaneously, and the empirical factors used to calculate the theoretical current densities can be modified accordingly. More detailed calculations of scattering matrix elements and the mixing of states of different symmetry should be performed to obtain a quantitative picture of electron transport in these structures. Nevertheless, the results presented here indicate that (*i*) elastic tunneling through the AlAs Γ–point barrier is inconsistent with the experimental current densities; (*ii*) elastic and inelastic tunneling through the AlAs band gap at the X–point could account for the observed discrepancies; and (*iii*) theoretical current densities in good agreement with the experimental data can be obtained provided both Γ– and X–point tunneling contributions are taken into account.

3.3.2 Impurity–Assisted Tunneling

In this section, a new element is added to the current density calculations, namely the effect of impurity states localized in the AlAs band gap. Impurity

atoms and crystal defects can create localized energy levels (traps) in the AlAs barrier.[15,16] If these "impurity states" lie in the AlAs band gap, they can affect tunneling currents through the structure. In this study, traps are viewed as intermediate states through which two–step tunneling processes may occur: an electron first tunnels from one GaAs electrode to an intermediate state, and then from the intermediate state to the other electrode.[17] This approach is similar to that used by Parker and Mead in their treatment of traps in Schottky barriers.[18]

A simple expression for the two–step tunneling current can be derived by assuming that there are N localized trap states per unit volume of AlAs, with each trap energy level, E_i, being at a fixed energy, E_o, below the AlAs conduction band edge, E_c. For an arbitrary voltage applied to the structure, the AlAs conduction band edge and thus the trap energy level vary with position, x:

$$E_i(x) = E_c(x) - E_o. \tag{3.1}$$

In Fig.3.5, this concept is illustrated by plotting the Γ–point conduction band edge and a trap energy level for a single p–type barrier heterostructure under applied bias. This figure is the result of a band bending calculation, in which the electrode and barrier doping densities are taken to be 3×10^{18} and $1 \times 10^{18} cm^{-3}$, respectively. The barrier thickness is 100 Å and the applied voltage is -150 mV. The impurity level is taken to be 870 meV below the AlAs Γ–point conduction band edge.

The elastic tunneling current density, J_1, between a trap state at position x_o and the left GaAs electrode is of the form:

$$J_1 \quad \propto \quad T_1(E_i(x_o), x_o)\{f_l(E_i(x_o)) - F(E_i(x_o))\}, \tag{3.2}$$

where T_1 is the WKB transmission probability for an electron with energy $E_i(x_o)$ tunneling from the left electrode to x_o; f_l is the occupation probability of the left

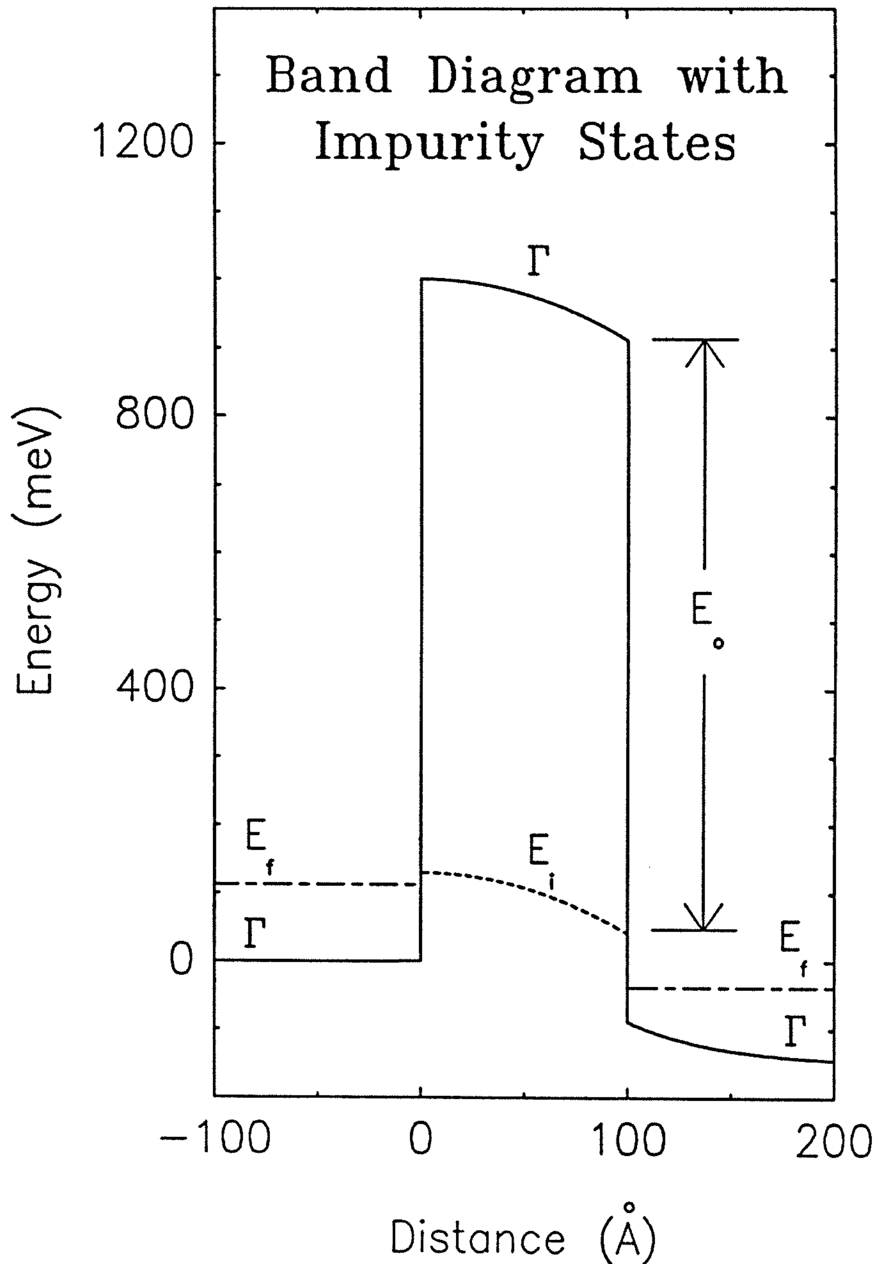

Figure 3.5: Calculated Γ–point conduction band edge (solid line), for a GaAs–AlAs–GaAs single barrier heterostructure having an impurity level in the AlAs layer. The impurity state (dashed line) lies 870 meV below the Γ–point conduction band edge in the barrier. The GaAs electrodes are doped n–type at $3 \times 10^{18} cm^{-3}$. The AlAs barrier layer is 100 Å thick, and doped p–type at $1 \times 10^{18} cm^{-3}$. A voltage of −150 mV is applied to the structure.

electrode state with energy $E_i(x_o)$; and F is the occupation probability of the trap state.

Similarly, the elastic tunneling current density, J_2, between the trap state at position x_o and the right electrode is given by:

$$J_2 \quad \propto \quad T_2(E_i(x_o), x_o)\{F(E_i(x_o)) \; - \; f_r(E_i(x_o))\}, \tag{3.3}$$

where T_2 is the transmission probability for an electron with energy $E_i(x_o)$ tunneling from x_o to the right electrode; and f_r is the occupation probability of the right electrode state with energy $E_i(x_o)$.

Under steady–state conditions, the trap level occupation probability, F, will adjust itself to make the two current densities J_1 and J_2 equal. It follows that the impurity–assisted tunneling current, J_{imp}, takes the form:

$$J_{imp} = J_1 = J_2 \quad \propto \quad \frac{T_1 T_2}{T_1 + T_2}\{f_l(E_i(x_o))\}. \tag{3.4}$$

A comparison of Eq.(3.4) with the usual expression for the one–step elastic tunneling current,[13] J_{el}, reveals that:

$$J_{imp} \quad = \quad C \; J_{el} \; \frac{1}{T_t(E_i)} \; \frac{T_1 T_2}{T_1 + T_2}, \tag{3.5}$$

where $T_t(E_i)$ is the transmission coeffecient for electrons with energy E_i tunneling from the left electrode to the right electrode; and C is a constant which is proportional to the number of trap levels per unit volume, N, and to the effective cross–sectional area of the traps, σ.

Fig.3.6 shows a calculated plot of J_{imp} as a function of AlAs barrier thickness. The calculations are performed using a p–type barrier doping of 1×10^{18} cm^{-3}, and an n–type electrode doping of 3×10^{18} cm^{-3}. The applied voltage is 100 mV and the impurity energy level is taken to be 950 meV below the AlAs Γ–point conduction band edge. N is chosen to be 1×10^{17} cm^{-3}, and σ is assigned a value of 10 times the cross–sectional area of the AlAs primitive cell. Changes in

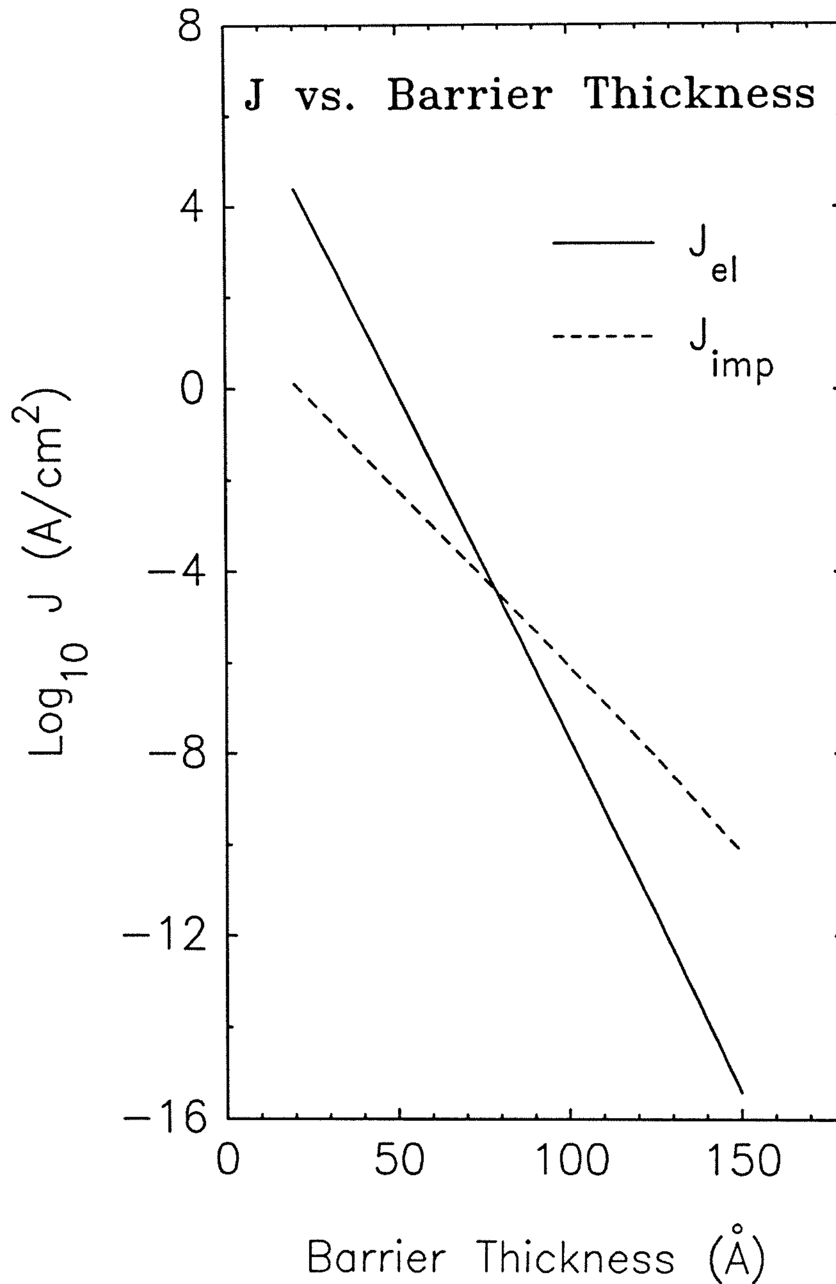

Figure 3.6: Calculated current densities vs. barrier thickness for one–step elastic tunneling (solid line) and impurity–assisted tunneling (dashed line). The doping densities in the GaAs electrodes and the AlAs barrier are 3×10^{18} and $1 \times 10^{18} cm^{-3}$, respectively. The applied voltage is 100 mV. The trap level is taken to lie 950 meV below the AlAs Γ–point conduction band edge.

N and σ alter only the multiplicative constant, C, in Eq.(3.5), and therefore, do not change the qualitative behavior of J_{imp}. J_{el} is also calculated and plotted in Fig.3.6 for comparison with J_{imp}. This reveals that the contribution to the total current density of one–step elastic tunneling is larger than that of impurity–assisted tunneling in heterostructures with thin barriers (this would be the case in sample H125). The opposite is true in structures with thicker barriers. For the parameters used in Fig.3.6, the impurity–assisted tunneling current becomes larger than the one–step elastic current when the AlAs layer is thicker than about 80 Å.

3.3.3 Inelastic Tunneling Processes

Experimental results obtained from sample H125 were used in section 3.3.1 to show that low temperature current transport in heterostructures having thin p–type AlAs barrier layers is dominated by tunneling through the AlAs band gap at both the Γ– and X–points. This section presents experimental data obtained from the other p–type barrier structures listed in Table 3.1. These samples are classified into two categories depending upon the nature of the inelastic processes which are identified in their derivative spectra. This provides information about the relative importance of the different current transport mechanisms occurring in these heterostructures.

The first category of samples includes H125, H160, H381 and H931. All four structures display similar peaks in their low temperature second derivative curves. These peaks are consistent with the excitation by the tunneling electrons of both Γ– and X–point phonons. These samples may be classified further into those which do not feature anomalous zero–bias conductances (H125), and those which do (H160, H381, H931).

The other category of samples includes H894, T007 and H930. For these

heterostructures, the most prominent second derivative peaks are consistent with the creation of AlAs X–point phonons alone. Furthermore, these are different from the X–point phonons identified in the structures of the first type.

Samples H115, H135 and H151 have not been classified in either category. Because they have thick tunnel barriers, these structures are characterized by very small current densities. As a result, their derivative curves are dominated by noise and do not reveal any prominent features which may be unambiguously interpreted.

a) Structures of the First Type (H125, H160, H381, H931)

Fig.3.7 displays $(d^2I/dV^2)(V)$ spectra at four different temperatures in the voltage range $[-100\,,100]$ mV for sample H125. All the curves have been averaged for 20 mn using modulation amplitudes smaller than 1 mV peak–to–peak. Their resolution is significantly better than that of the spectrum depicted in Fig.3.3, the purpose of which was simply to illustrate the most prominent second derivative peaks obtained at low temperatures. In Fig.3.7, sharp peaks are observed at 4.2 K at ± 37 and ± 50 mV. The former correspond to the energy of Γ–point LO phonons in GaAs.[19,20] They have previously been attributed to a density–of–state effect due to the coupling of GaAs LO phonons with the tunneling electrons.[4] The peaks at ± 50 mV correspond to the energy of AlAs Γ– or X–point LO phonons.[20–24] They arise from the inelastic excitation of AlAs LO phonons by electrons tunneling through the AlAs band gap at the Γ–point or at the X–point. Other prominent peaks are obtained at lower applied voltages. They are centered about ± 22 mV. Shoulders superposed to these broad peaks are visible at ± 11 and ± 29 mV. These are consistent with the creation of AlAs X–point transverse acoustic (TA), and longitudinal acoustic (LA) phonons, respectively.[21–23] The peaks at ± 22 mV may thus be attributed to the inelastic excitation of two AlAs

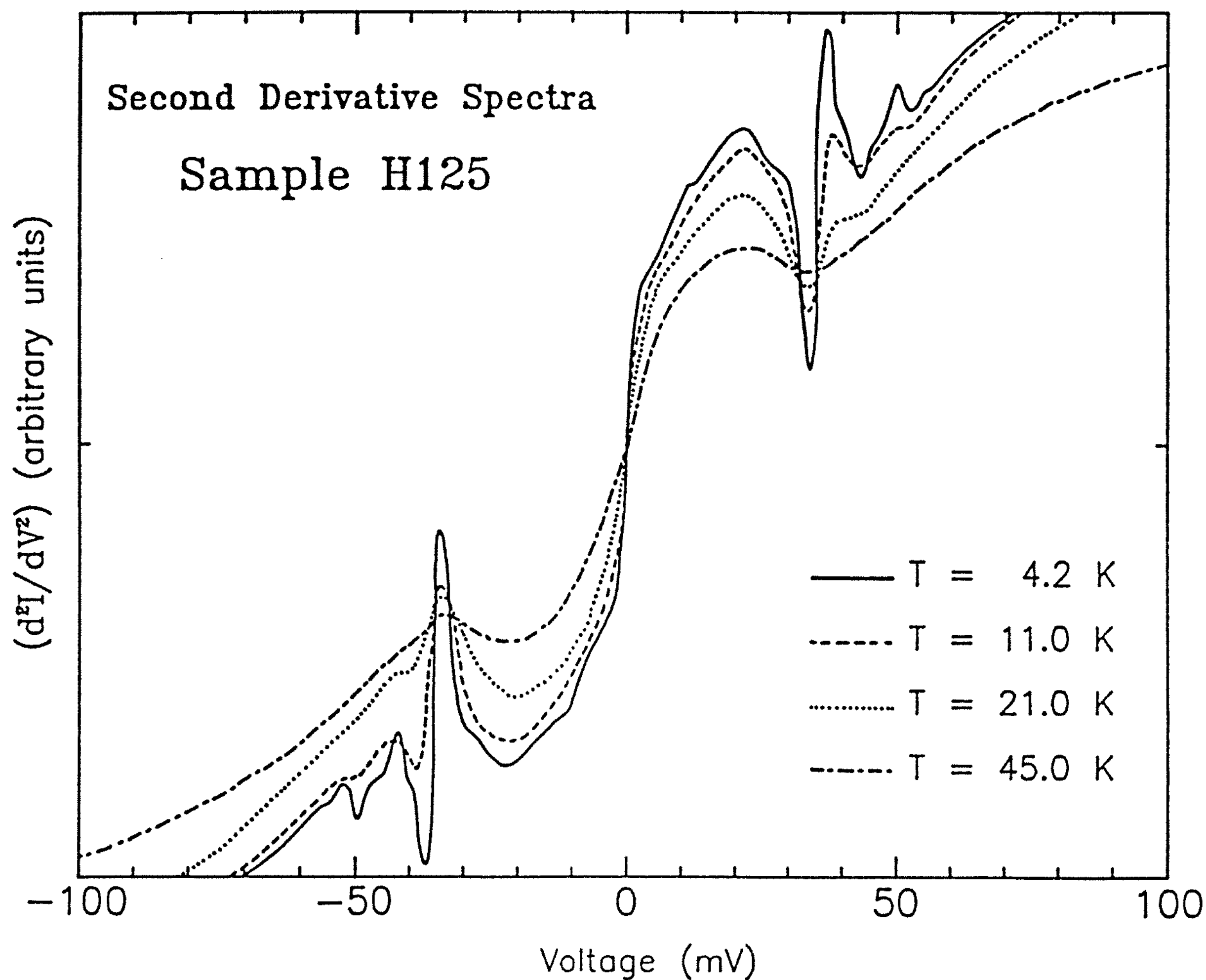

Figure 3.7: Experimental second derivative spectra at four different temperatures for sample H125. At 4.2 K, the most prominent features are centered about ± 22 mV. Sharp peaks are obtained at ± 37 and ± 50 mV. Shoulders are also visible at ± 11, ± 29, ± 40, ± 45 and ± 55 mV.

X–point TA phonons. Other reproducible shoulders are visible at ± 40, ± 45 and ± 55 mV. The features at ± 45 mV could correspond to AlAs transverse optical (TO) phonons at the Γ–point or at the X–point.[20,21] The shoulders at ± 40 and ± 55 mV could be due to two–phonon processes in the AlAs barrier layer or near the GaAs/AlAs interfaces, (TA+LA) and (TA+TO), respectively. As shown in Fig.3.3, other broad peaks exist, centered about ± 80 mV. These may result from a number of multiple inelastic scattering mechanisms, such as the excitation of two X–point LA phonons, two TO phonons, two LO phonons, and/or combinations of these.

The four second derivative spectra depicted in Fig.3.7 correspond to temperatures ranging between 4.2 and 45 K. As the temperature is increased, all the peaks broaden and decrease in amplitude. The shoulders visible at 4.2 K vanish first. Then, the peaks obtained at ± 50 mV disappear at about 13 K. The sharp structure at ± 37 mV is no longer visible at 45 K. The broad peaks near zero–bias vanish last, at approximately 90 K. This temperature dependence is consistent with attributing the second derivative peaks to the creation of phonons by the tunneling electrons.

Fig.3.8 shows $(d^2I/dV^2)(V)$ curves at 4.2 K in the voltage range $[-100, 100]$ mV for samples H160 and H931. These two curves are very similar, indicating that the dominant current transport mechanisms are the same in both heterostructures. In sample H160, the AlAs layer is 54 Å thick and the doping density in the GaAs electrodes is $3 \times 10^{18} cm^{-3}$. In H931, the barrier layer is 76.5 Å thick, and the GaAs electrodes are doped at $2.3 \times 10^{18} cm^{-3}$. As for sample H125, prominent second derivative peaks are obtained at ± 22, ± 37 and ± 50 mV. Shoulders are also visible at ± 29, ± 44 and ± 55 mV. However, the slopes of the $(d^2I/dV^2)(V)$ curves near zero–bias are positive in the case of H125, but negative for H160 and H931. This reveals that the last two samples feature

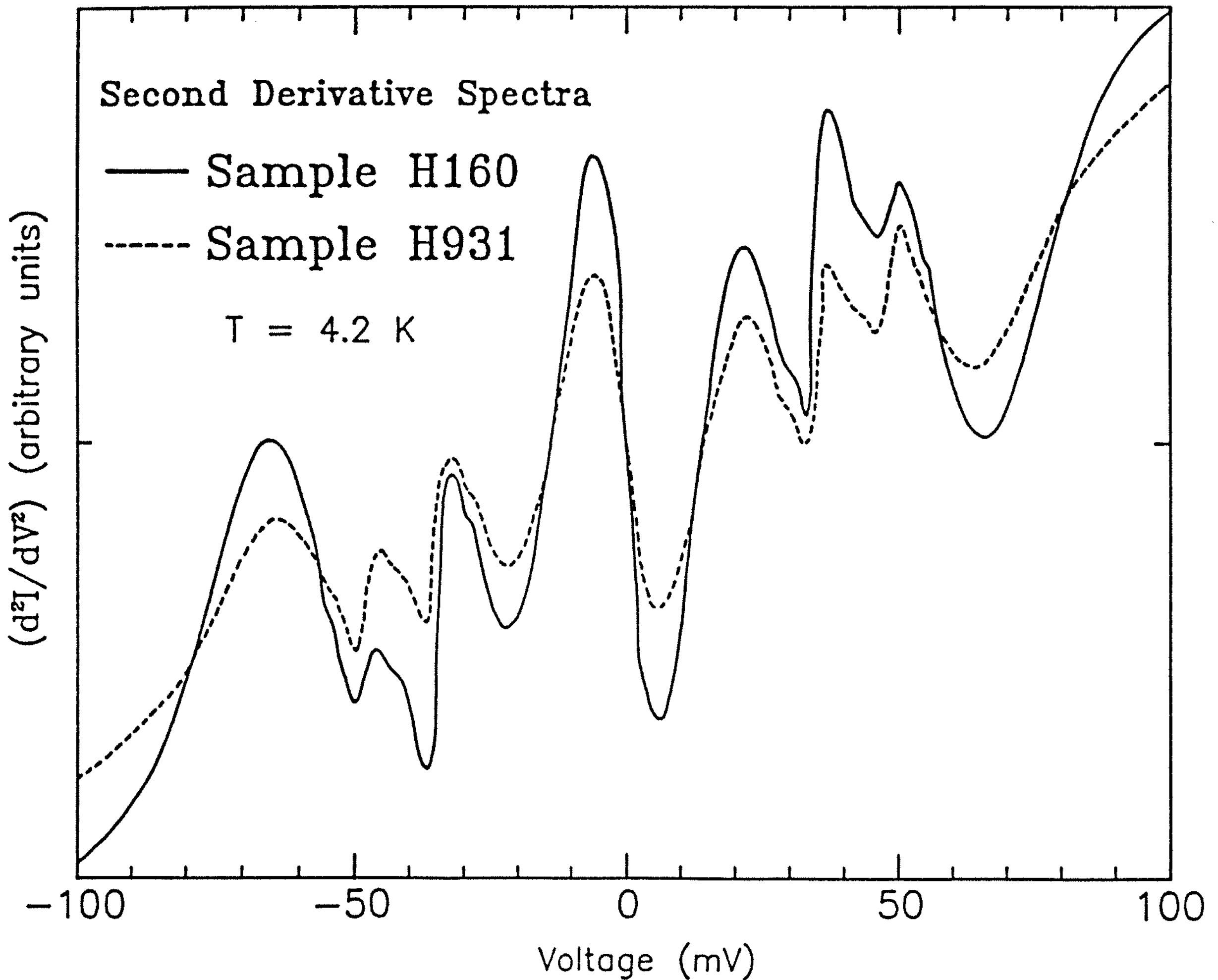

Figure 3.8: Experimental second derivative spectra at 4.2 K for the p–type barrier samples H160 and H931. In H160 (H931), the AlAs barrier layer is 54 (76.5) Å thick, and the GaAs electrodes are doped n–type at 3×10^{18} (2.3×10^{18}) cm^{-3}. The most prominent peaks are obtained at ± 22, ± 37 and ± 50 mV. Shoulders are visible at ± 29, ± 44 and ± 55 mV. The dips near zero–bias correspond to an anomalous zero–bias conductance maximum.

anomalous zero–bias conductance maxima at low temperatures. In addition, this phenomenon is manifested by second derivative dips which remain temperature independent as long at T$\leq$ 70 K, and progressively decay in amplitude at higher temperatures. However, a different type of anomalous zero–bias conductance is obtained from sample H381. These effects are discussed in section 3.3.4.

The four samples presented in this section (H125, H160, H381, H931) all have similar derivative spectra except in the low voltage regions ($|V_a| < 15$ mV) of the curves. The identification of the second derivative peaks provides useful information about the low temperature current transport mechanisms occurring in these heterostructures. First, the creation by the tunneling electrons of single Γ–point phonons could be identified. Because the corresponding peaks are prominent, it may be concluded that inelastic tunneling and thus elastic tunneling through the AlAs band gap at the Γ–point are important. Most of the other peaks are consistent with the excitation of X–point phonons in the AlAs layer or near the GaAs/AlAs interfaces. This indicates that tunneling through the AlAs X–point barrier is another essential current transport mechanism in these structures. In section 3.3.1, two processes were proposed by which electrons may tunnel through the AlAs band gap at the X–point. In the first mechanism, which is inherently inelastic, electrons scatter near both heterojunction interfaces. This is consistent with the two–phonon processes observed in the derivative spectra. The second mechanism is based upon the coupling of AlAs X–point states with GaAs Γ–point states due to the breaking of translational symmetry in the direction perpendicular to the planes of the layers. As a result, Γ–point electrons in one GaAs electrode may tunnel elastically through the AlAs X–point barrier, into Γ–point states in the other GaAs electrode. During this process, electrons can also excite single AlAs X–point phonon modes. This inelastic contribution to the total current is manifested in Figs.3.7 and 3.8 by the shoulders observed

at ± 11, ± 29, and ± 45 mV.

In summary, these results suggest that the important low temperature current transport mechanisms in samples H125, H160, H381 and H931 are the following: (*i*) elastic Γ–point tunneling; (*ii*) inelastic Γ–point tunneling with the creation of LO phonons; (*iii*) inelastic X–point tunneling via the four AlAs X–valleys lying along the k_y– and k_z–directions, parallel to the planes of the layers; this process requires two scattering events, one near each heterojunction interface; (*iv*) elastic X–point tunneling via the two AlAs X–valleys lying along the k_x–direction, perpendicular to the planes of the layers; this is due to the mixing of AlAs X–point states and GaAs Γ–point states; and (*v*) single phonon emission while electrons are tunneling through the AlAs X–point barrier via the mechanism mentioned in (*iv*).

b) Structures of the Second Type (H894, T007, H930)

Samples H894, T007 and H930 have similar derivative curves. However, these spectra differ significantly from those obtained from the structures of the first type. Fig.3.9 illustrates $(d^2I/dV^2)(V)$ curves at 4.2 K in the voltage range $[-100\,,100]$ mV for all three heterostructures. The most prominent peaks are observed at ± 11, ± 29 and ± 44 mV. They are consistent with the excitation of AlAs X–point TA, LA and TO phonons, respectively. Other peaks are obtained at ± 55 mV. These may be attributed to the creation of two AlAs X–point phonons, one TA and one TO. Shoulders are also visible at ± 22, ± 40, ± 73 and ± 88 mV. These may arise from the emission of two AlAs X–point phonons: (2 TA), (TA+LA), (LA+TO), and (2 TO), respectively. These results indicate that all the second derivative peaks observed in Fig.3.9 are consistent with the excitation of X–point phonons in the AlAs barrier layer or near the GaAs/AlAs interfaces. As opposed to the samples of the first type, the three heterostructures

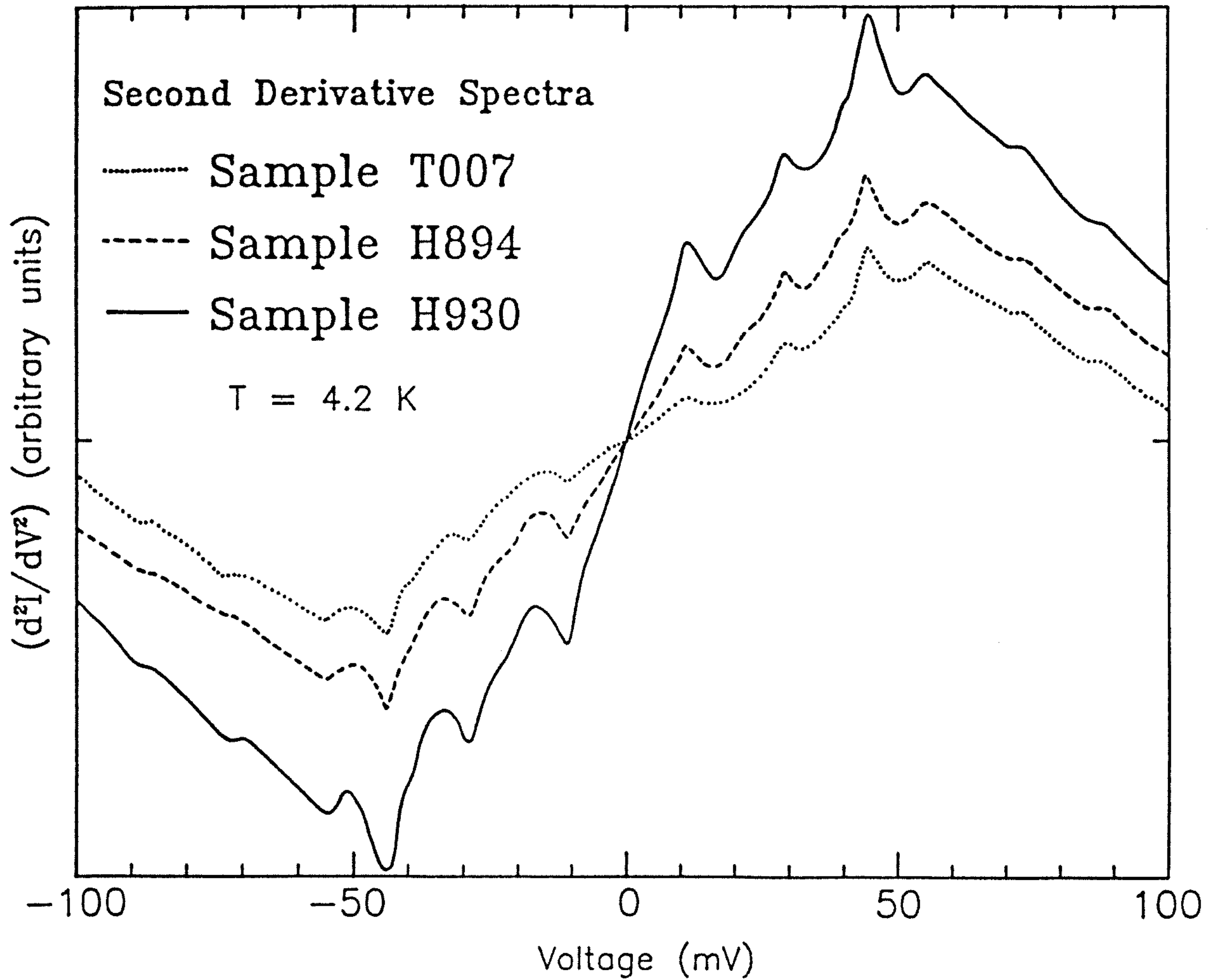

Figure 3.9: Experimental second derivative spectra at 4.2 K for the p–type barrier samples H894, T007 and H930. The most prominent peaks, obtained at ± 11, ± 29 and ± 44 mV, may be attributed to the excitation of AlAs X–point TA, LA and TO phonons, respectively. The shoulders at ± 22, ± 40, ± 55, ± 73 and ± 88 mV are consistent with the emission of two AlAs X–point phonons.

discussed here do not show evidence of the creation of Γ–point phonons. It may thus be concluded that tunneling through the AlAs X–point barrier in H894, T007 and H930 is more important than tunneling through the AlAs band gap at the Γ–point. As in the structures of the first category, one– and two–phonon processes have been identified. This reveals that both mechanisms for tunneling through the AlAs X–point barrier also take place in H894, T007 and H930. However, the relative importance of these two mechanisms is reversed in both types of samples. On the one hand, the most prominent peaks observed at ± 11, ± 29 and ± 44 mV in Fig.3.9 correspond to shoulders in Figs.3.7 and 3.8. On the other hand, while shoulders are obtained at ± 22 mV from H894, T007 and H930, prominent peaks are visible at the same voltages in the second derivative spectra of the structures of the first type. This indicates that the strength of the interactions between tunneling electrons and barrier phonons is different in both categories of samples. Furthermore, whereas the shoulders observed in Fig.3.9 correspond to two–phonon scattering events, the most prominent peaks are produced by one–phonon processes. This is in contrast with the results obtained from H125, H160, H381 and H931. This suggests that the first mechanism for tunneling through the AlAs band gap at the X–point, which requires two scattering events, is more important in the samples of the first type than in the other heterostructures. The opposite is true for the other tunneling mechanism, in which AlAs X–point states couple to GaAs Γ–point states through the breaking of translational symmetry in the direction perpendicular to the heterojunction interfaces. These results reveal that the dominant current transport mechanisms taking place in single barrier heterostructures may vary depending upon the samples studied. However, no correlation has been found with any particular structure parameter. For example, Table 3.1 indicates that H160 and T007 have the same barrier thicknesses and electrode doping concentrations. Nevertheless,

their dissimilar derivative spectra suggest that electronic transport is different in both samples. The nature of the dominant current transport mechanisms should thus be related to the presence of impurities, defects and scattering centers, and to the quality of the heterojunction interfaces. This is consistent with the TEM pictures of the structures, which reveal that the interfaces are sharp and defect-free in H894, T007 and H930, but not quite as good in the other heterostructures. As a result, scattering near the heterojunction interfaces should be easier in the samples of the first category than in those of the second type. This may explain why the first mechanism for tunneling through the AlAs X-point barrier, which requires the scattering of electrons near both GaAs/AlAs interfaces, is more important in samples H125, H160, H381 and H931 than in H894, T007 and H930.

In summary, low temperature current transport in H894, T007 and H930 should occur primarily through (*i*) elastic Γ-point tunneling; (*ii*) inelastic X-point tunneling via the four AlAs X-valleys lying along the k_y- and k_z-directions, parallel to the planes of the layers; and (*iii*) elastic and inelastic X-point tunneling via the two AlAs X-valleys lying along the k_x-direction, perpendicular to the heterojunction interfaces. It is also found that electronic transport may vary from sample to sample, depending upon the quality of the materials and the heterojunction interfaces.

3.3.4 Zero-Bias Anomalies

Tunneling experiments have been used extensively to study the properties of tunnel diodes, Schottky barriers and metal-insulator-metal (M-I-M) structures. Anomalous conductances near zero-bias, usually referred to as zero-bias anomalies, have been reported in all of these structures.[25-30] These anomalies may correspond to conductance dips, peaks, or combinations of these shapes.[25,26,28]

The detailed structure is a strong function of the choice of the materials, the presence of impurities, the nature of the dopants and the doping levels. It may also depend on the temperature of the measurements,[25,28] vary with magnetic field strength,[25] and be light sensitive.[30]

Numerous interpretations have been proposed to explain the origin of zero–bias anomalies. These have been attributed to polaron effects, phonon–assisted tunneling, logarithmic singularities in the density of states of bulk semiconductors, resonant tunneling via impurity states located in tunnel barriers, and electron bottleneck effects arising from the blocking of tunneling states due to non–zero electron relaxation times.[27,30,31] However, no definitive explanation has been found yet.

This section reports the observation of zero–bias anomalies in three p–type barrier samples, H160, H931 and H381. As illustrated in Fig.3.8, the second derivative spectra of the first two heterostructures display pronounced dips near zero–bias, centered about ± 6 mV. These dips correspond to a decrease in conductivity at low applied voltages, and thus to a conductance maximum at zero–bias. This appears more clearly in the first derivative spectra, $(dI/dV)(V)$, shown in Fig.3.10 for both samples. These curves, which are proportional to the conductivity of the heterostructures, reveal large zero–bias conductance peaks. The temperature dependence of the zero–bias anomalies provides information about their possible origin. Fig.3.11 shows $(d^2I/dV^2)(V)$ spectra at three different temperatures for sample H160. The same behavior is obtained from H931. As the temperature, T, is increased from 4.2 K, the peaks which have been attributed to the creation of phonons by the tunneling electrons all broaden and decrease in amplitude. However, the dips near zero–bias remain practically temperature independent as long as $T \leq 70$ K. They are gradually reduced at higher temperatures. The temperature of 70 K at which the zero–bias anomaly starts

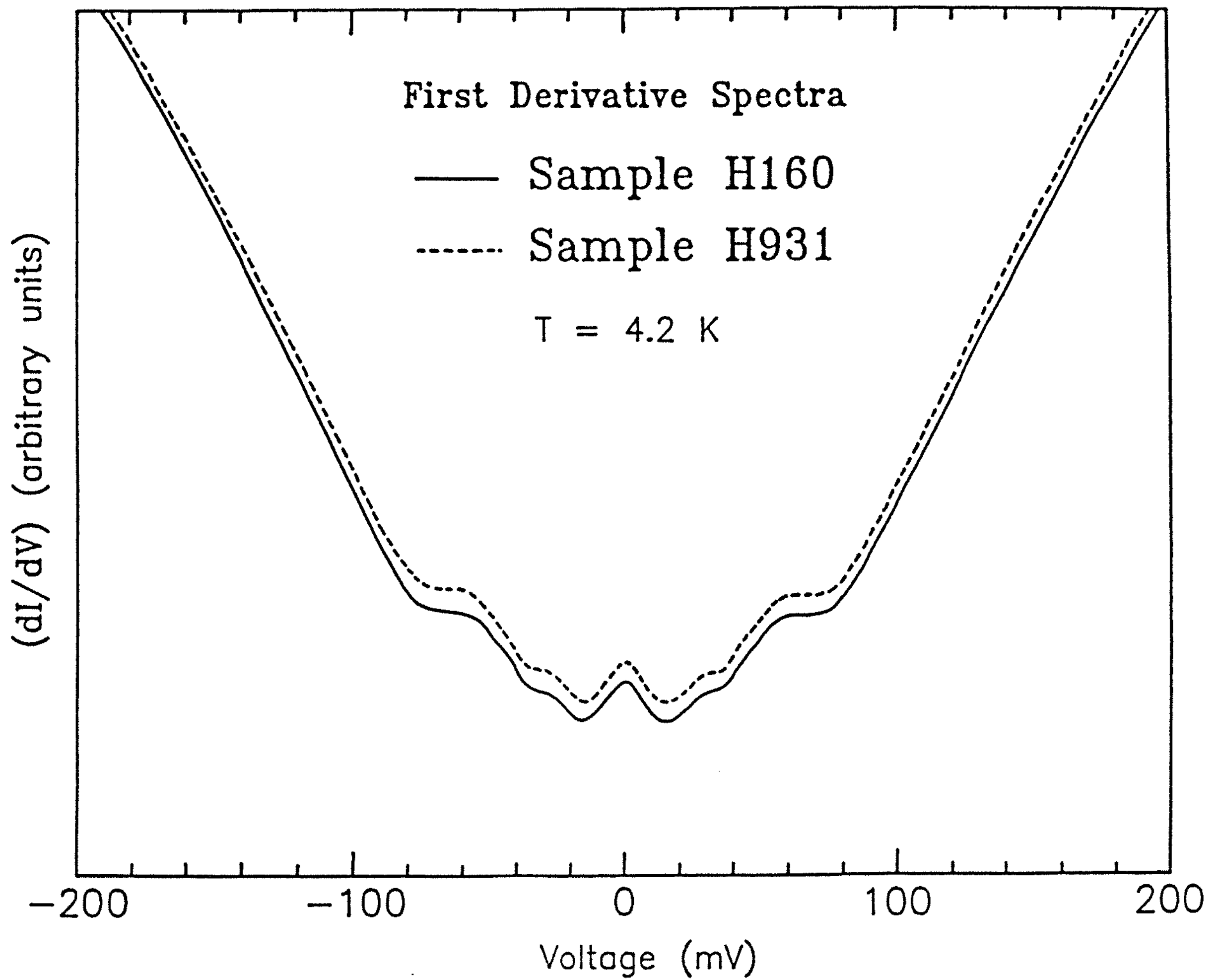

Figure 3.10: Experimental first derivative spectra, $(dI/dV)(V)$, at 4.2 K for samples H160 and H931, showing the anomalous zero–bias conductance maxima characteristic of these heterostructures.

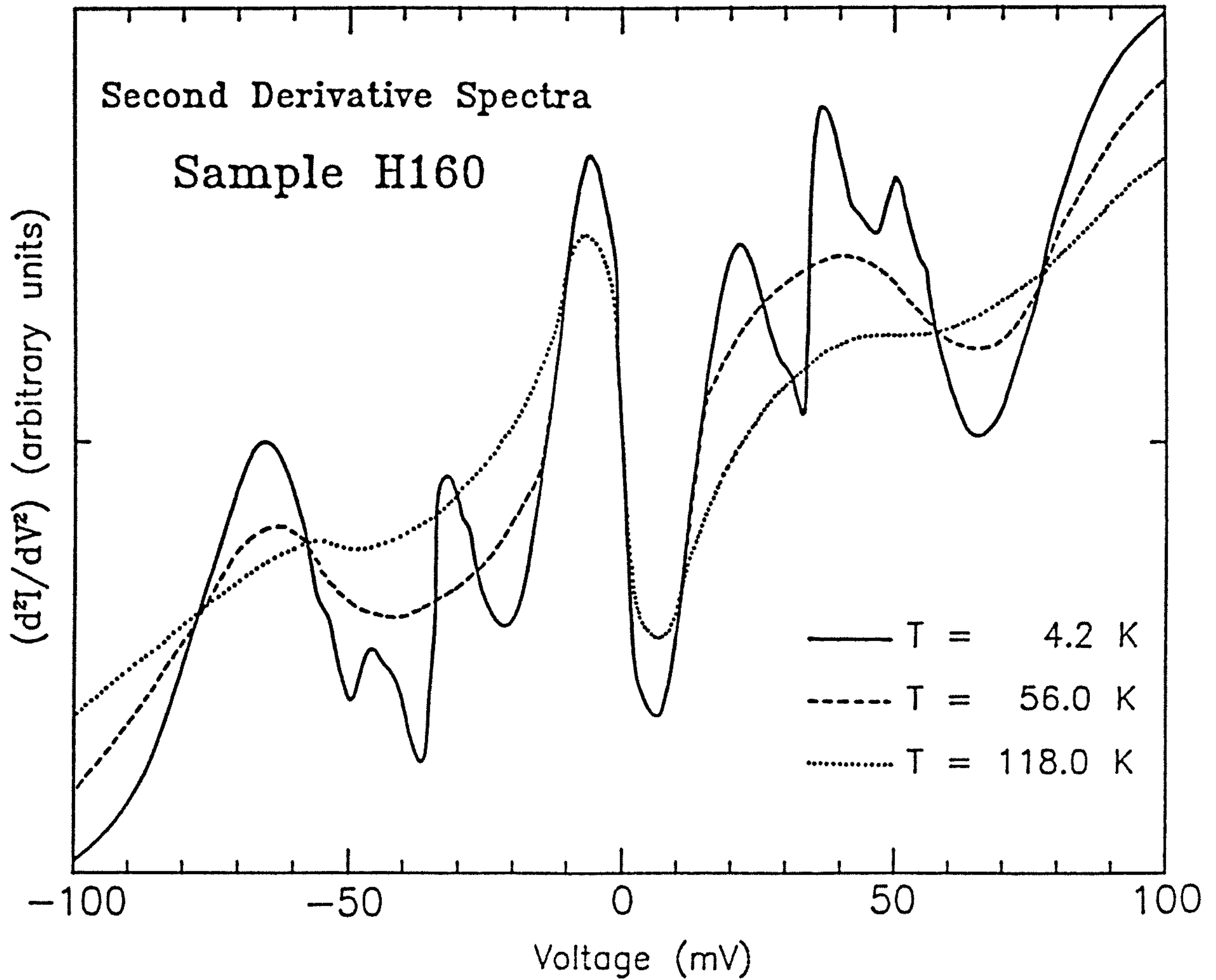

Figure 3.11: Experimental second derivative spectra at three different temperatures for sample H160. They reveal that the zero–bias anomaly remains practically temperature independent as long as $T \leq 70$ K, but is gradually reduced at higher temperatures.

decaying corresponds to a thermal energy of 6 meV. This suggests that a continuum of interface states or of trap levels located in the barrier and/or near the heterojunction interfaces must exist. The highest state of this continuum should lie at 4.2 K about 6 meV above the Fermi level in the unbiased structure. These states are schematically illustrated in the energy band diagram depicted in Fig.3.12 for sample H160. Band bending calculations indicate that when a negative voltage $V_a = -14$ mV is applied to the left GaAs electrode with respect to the right cladding layer, the highest level of the continuum of states at the first heterojunction interface ($x = 0$) coincides in energy with the Fermi level, E_f^l, in the left cladding layer. Consequently, if these states act as electron traps, electrons cannot tunnel through the barrier from left to right at 4.2 K as long as $-14 \leq V_a \leq 0$ mV. This is in good agreement with the decrease in conductivity near zero–bias observed in Figs.3.10 and 3.11. When $V_a < -14$ mV, electrons in the left GaAs electrode have energies greater than the highest trap state at $x = 0$. These electrons can tunnel through the AlAs barrier, causing the conductivity to increase. Because the structure is symmetric, the same occurs in the other bias direction, for electrons tunneling from right to left. The temperature dependence of the zero–bias conductance peak may be explained qualitatively by assuming that increasing the temperature from 0 to T mainly results in raising the Fermi level by (kT). When T > 70 K, (kT) > 6 meV, and some electrons have enough energy to tunnel through the barrier. As a result, the decrease in conductivity near zero–bias is reduced, and the corresponding second derivative dips become broader and smaller in amplitude.

Zero–bias anomalies are also obtained from sample H381. Fig.3.13 shows $(d^2I/dV^2)(V)$ spectra at four different temperatures for this heterostructure, in the voltage range $[-50, 50]$ mV. Except in the low bias regions of the curves, ($|V_a| < 15$ mV), these spectra are similar to those of H160 and H931. How-

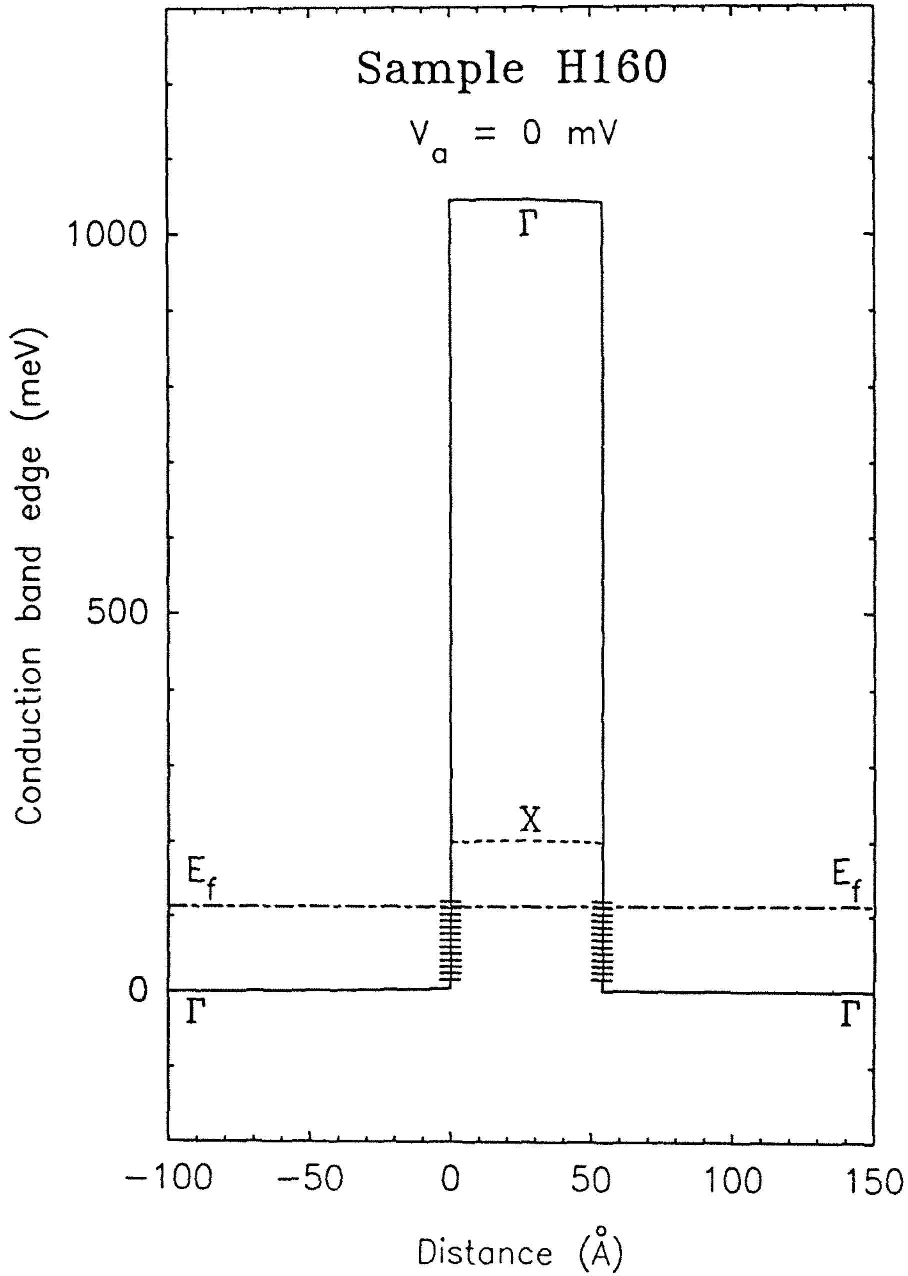

Figure 3.12: Calculated energy band diagram for sample H160, showing schematically a continuum of interface states at each heterojunction interface. The highest level in each continuum is assumed to lie at low temperatures about 6 meV above the Fermi level in the unbiased structure.

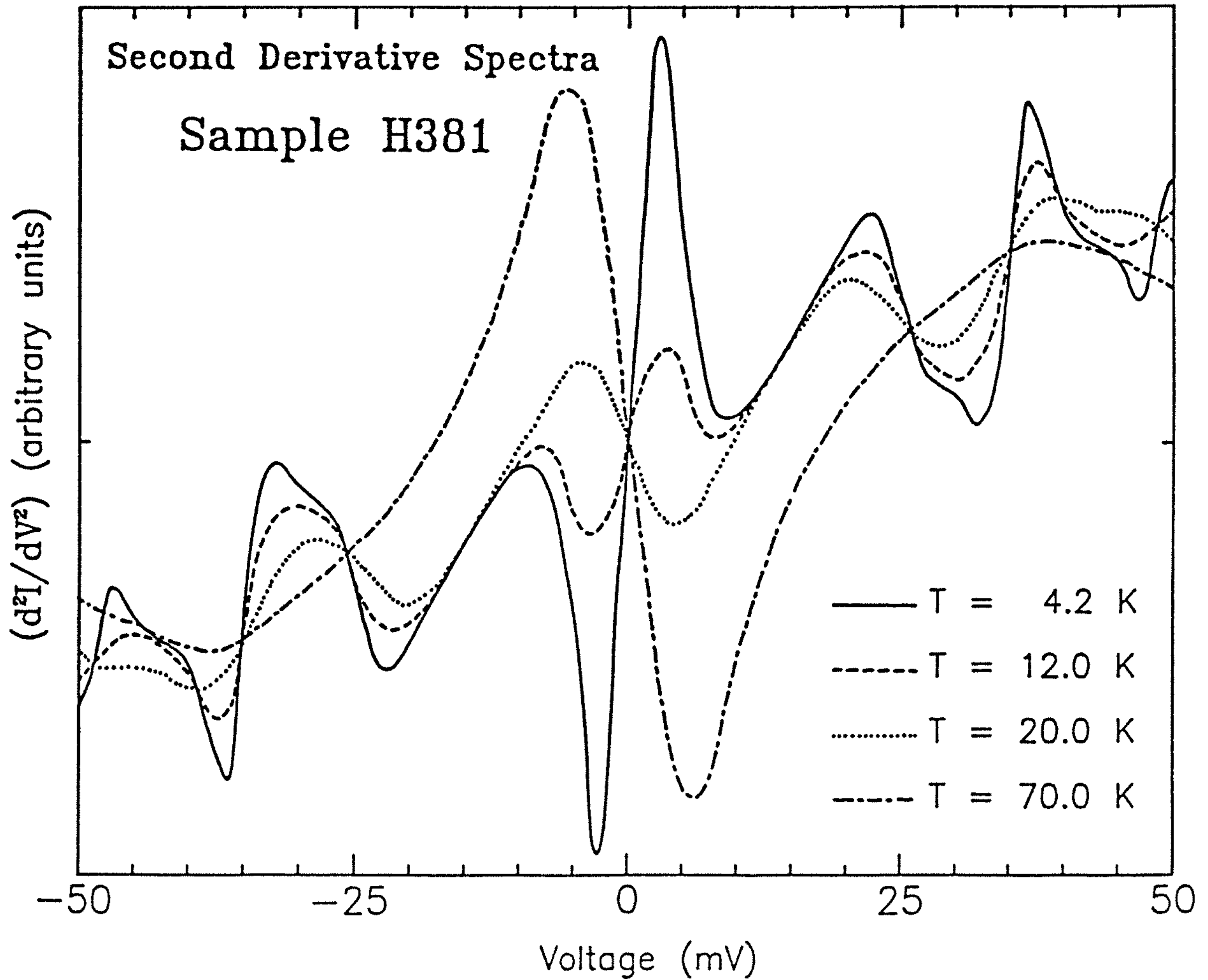

Figure 3.13: Experimental second derivative spectra at four different temperatures for sample H381, illustrating the temperature dependence of the zero–bias anomaly.

ever, in Fig.3.13, prominent peaks are observed near zero–bias at 4.2 K. This is indicative of a zero–bias conductance minimum, as opposed to the zero–bias conductance maxima obtained from H160 and H931. Furthermore, sample H381 features a zero–bias anomaly which is extremely temperature sensitive. As illustrated in Fig.3.13, the sharp peaks visible at 4.2 K near zero–bias decay very rapidly with increasing temperature. They vanish at 14 K. As the temperature is further increased, they are replaced by dips, which become more pronounced and reach their maximum amplitude at 50 K. The dips then remain practically identical as long as T $\leq$ 70 K. However, they broaden and decrease in amplitude at higher temperatures. These results reveal that the zero–bias anomaly has a more complex temperature dependence in sample H381 than in H160 and H931. In particular, the zero–bias conductance minimum obtained at 4.2 K from H381 becomes a conductance maximum at 14 K. As in H160 and H931, this zero–bias anomaly may be tentatively attributed to a set of interface states or to trap levels located in the AlAs barrier and/or at the heterojunction interfaces. If E^t_{min} (E^t_{max}) denotes the energy of the lowest (highest) trap state, the Fermi level, E_f(T), in the unbiased structure should be such that $E_f < E^t_{min} < E^t_{max}$ at 4.2 K. As the temperature is increased, $(E^t_{min} - E_f)$ is reduced and less electrons may tunnel through the barrier at low applied voltages. This causes the peaks observed near zero–bias in Fig.3.13 to decay. Dips which increase with temperature are obtained when $E^t_{min} \leq E_f \leq E^t_{max}$. However, when T is high enough that $E_f > E^t_{max}$, more electrons may tunnel through the barrier, and the dips are reduced.

In conclusion, two types of anomalous zero–bias conductances have been described in this section. In samples H160 and H931, the zero–bias anomaly is a conductance peak. In sample H381, it is a conductance minimum for T $\leq$ 14 K, and a conductance maximum at higher temperatures. No definitive explanation

for the origin of these effects has been found. However, they may be tentatively attributed to interface states or to trap levels located in the AlAs barrier and/or at the heterojunction interfaces. Because they are only observed in three of the samples, these zero–bias anomalies should be closely related to the quality of the materials and, more particularly, of the interfaces.

3.4 Samples with n–Type AlAs Barrier Layers

3.4.1 Current Transport Through Thick n–Type AlAs Layers

This section deals with MOCVD grown GaAs–AlAs–GaAs double heterojunctions in which the AlAs barrier layers are doped n–type with Se. The parameters of the samples are listed in Table 3.1. All the heterostructures are characterized by high doping densities in the AlAs layers as well as in the GaAs electrodes. Furthermore, with the exception of Y760, all the samples have thick AlAs layers (140–730 Å). As in the of p–type barrier structures, the experimental J–V curves display increasing resistance with decreasing temperature. This indicates that tunneling is an important current transport mechanism at low temperatures in the n–type barrier structures as well. However, the high current densities observed are inconsistent with tunneling through the thick AlAs layers characteristic of these heterostructures. This is illustrated in the experimental J–V curve at 4.2 K shown in Fig.3.14 for sample H003. This curve may be compared to the J–V characteristic displayed in Fig.3.2 for the p–type barrier structure H125. As indicated in Table 3.1, the AlAs layer in H003 is 693 Å thick, almost 15 times thicker than in H125. Nevertheless, low temperature current densities are about 40 times greater in H003 than in H125. In addition, the n–type barrier samples do not display the proper relationship between current density and barrier thick-

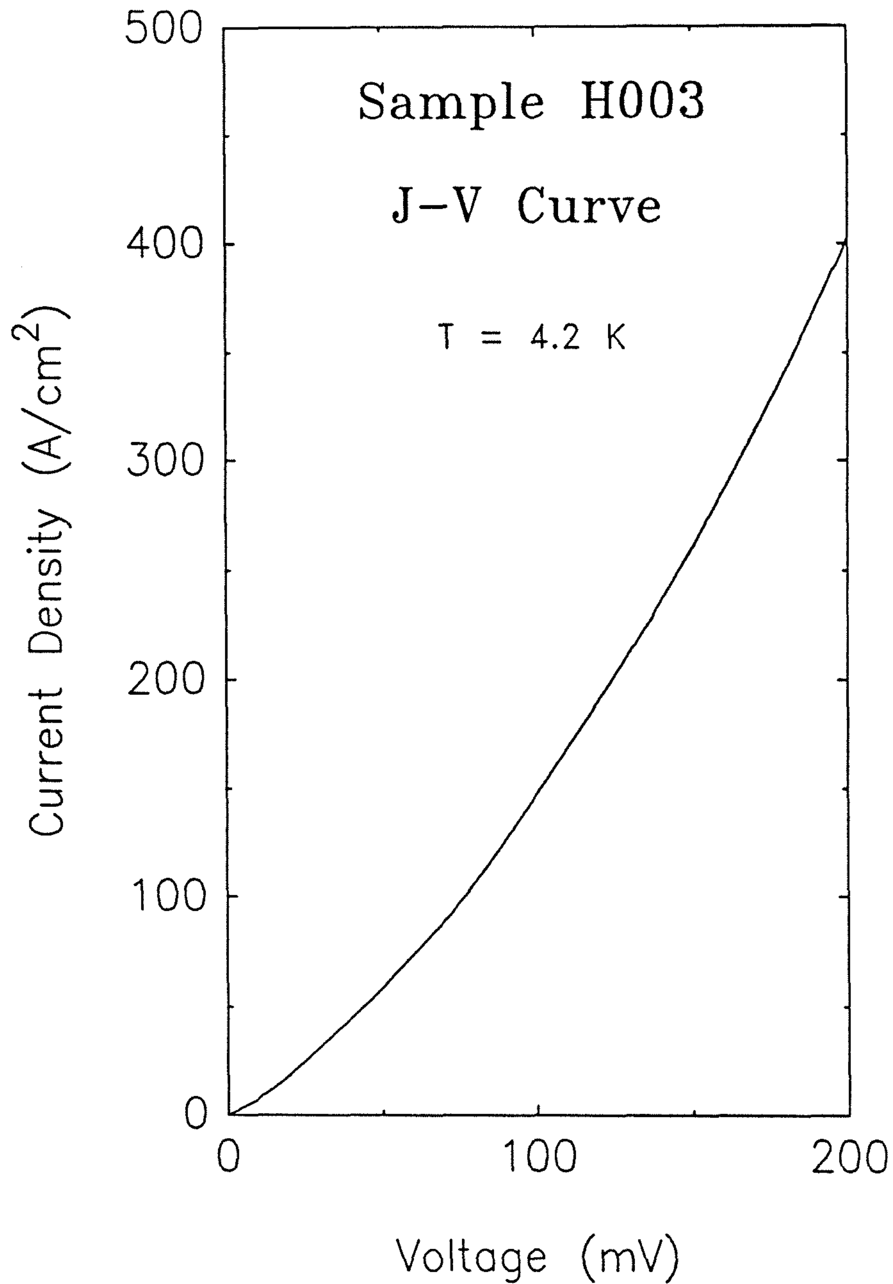

Figure 3.14: Experimental J–V curve at 4.2 K for the n–type barrier sample H003. The AlAs barrier layer is 693 Å thick. It is doped with Se at about $5\times10^{17}cm^{-3}$. The doping density in the n–type GaAs electrodes is $5.5\times10^{18}cm^{-3}$.

ness expected for tunnel structures. In particular, almost identical J–V curves are obtained from H003, H098 and H099. Table 3.1 reveals that these samples have similar doping densities, but AlAs layer thicknesses ranging between 589 and 730 Å. This suggests that when the n–type AlAs layers are thick enough, the experimental J–V characteristics of heterostructures having the same doping concentrations are independent of AlAs layer thicknesses. Furthermore, smaller current densities are obtained from H056 and H083. This is apparently inconsistent with the structure parameters listed in Table 3.1: although both samples have slightly lower electrode doping densities than H003, H098 and H099, they have much thinner AlAs layers (141.5 and 339.5 Å, respectively). Finally, sample Y760 has a thin AlAs quantum barrier and a doping density of $3 \times 10^{18} cm^{-3}$ in the GaAs cladding layers. However, its current density is only twice as large as in H003, H098 and H099. This confirms that the thickness of the barrier through which the electrons actually tunnel must not be increasing with the physical width of the AlAs layer.

These apparently inconsistent results may be explained by calculating the energy band diagrams of the structures using the approach developed in Chapter 2. These calculations reveal that if the AlAs layer is sufficiently thick and the n–type doping densities are large enough, the AlAs conduction band may be fully depleted of electrons at the Γ–point but not at the X–point. When this occurs, calculating the shapes of the conduction band edges at the Γ–point in the GaAs electrodes and at the X–point in the AlAs layer becomes essential in determining the nature of the dominant current transport mechanisms. Energy band profiles indicate that in this instance, electrons occupying Γ–point states in the GaAs cladding layers do not tunnel through a single potential energy barrier, but through two reduced AlAs X–point barriers separated by a central AlAs bulk–like region. Fig.3.15 shows two such energy band diagrams for sample

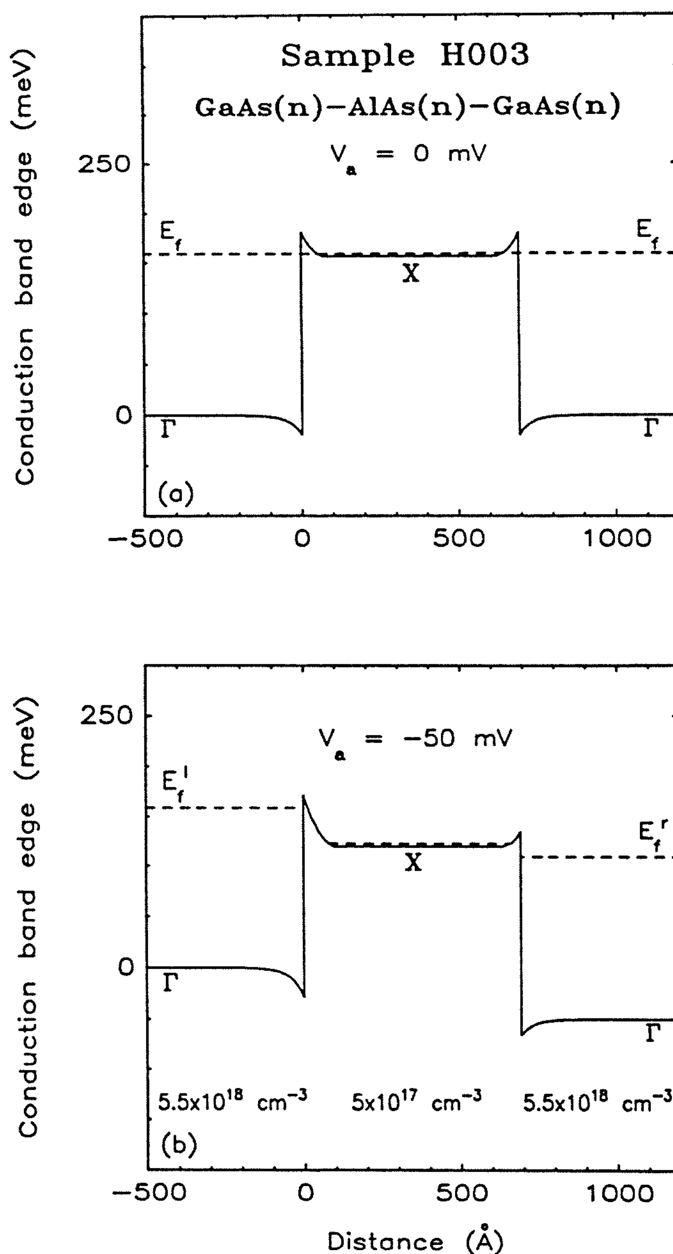

Figure 3.15: Calculated conduction band edges at the Γ–point in the GaAs electrodes, and at the X–point in the AlAs layer, for sample H003. (a) depicts the unbiased structure. (b) corresponds to a total applied voltage $V_a = -50$ mV. These energy band diagrams show that tunneling occurs through two reduced AlAs X–point barriers separated by a bulk region of AlAs.

H003. Fig.3.15(a) depicts the unbiased structure. Fig.3.15(b) corresponds to a total applied voltage of −50 mV. Fig.3.15(a) reveals that GaAs Γ–point electrons near the Fermi level do not tunnel through a 693 Å thick AlAs barrier layer but through two reduced AlAs X–point barriers which are only 22 meV high and 49 Å thick.

For given doping densities, these reduced barriers remain identical regardless of AlAs layer thicknesses provided a bulk–like region exists in AlAs. For given AlAs layer thicknesses and GaAs doping concentrations, reducing the AlAs doping density causes the accumulation layers in the electrodes to decrease, and the two reduced barriers to become higher and broader. As a result, the central AlAs bulk–like region becomes progressively thinner until it eventually vanishes. If the doping level and the thickness of the AlAs layer are kept the same, increasing the electrode doping density causes the Fermi level to rise, the electrode accumulation layers to decrease, and the two reduced barriers to become lower and thinner.

It results from the above discussion that large experimental current densities, $J_{exp}(V)$, can be expected, even when the physical thickness, a, of the AlAs layer is large enough that tunneling through the whole barrier is negligible. Furthermore, for given doping concentrations, $J_{exp}(V)$ should be independent of a as long as a bulk–like region exists in AlAs. In addition, $J_{exp}(V)$ should be an increasing function of electrode and barrier doping densities. These results explain why samples H003, H098 and H099 have almost identical J–V characteristics despite their different AlAs layer thicknesses. They also explain why H056 and H083 have smaller current densities than H003, H098 and H099: although both heterostructures are characterized by thinner AlAs layers, they have lower electrode doping concentrations, and thus thicker and higher reduced AlAs X–point barriers. In the case of sample H083 for example, the two reduced tunnel barriers

are 30 meV high and 64 Å thick under no applied bias. Energy band diagram calculations also indicate that the AlAs layer in sample Y760 is thin enough that it remains totally depleted of carriers at both the Γ– and X–points. As a result, the dominant current transport mechanisms at low temperatures are expected to be different in Y760 than in the other n^+–n–n^+ heterostructures. As in the p–type barrier samples, electronic transport in Y760 should be dominated by tunneling through the AlAs band gap at both the Γ– and X–points, in a one–step process, and not through two reduced X–point barriers separated by a bulk layer of AlAs.

Another important property of heterostructures having thick n–type AlAs layers is that changes in slope are visible in the low temperature J–V curves and reproducible features are observed in the derivative spectra. This is indicative of inelastic tunneling processes. Fig.3.16 illustrates a second derivative curve at 4.2 K for sample H003. The two sharp peaks near zero–bias correspond to a pronounced zero–bias anomaly. Six additional peaks are obtained in each bias direction. The most prominent ones occur at ± 50 and ± 73 mV. Smaller peaks are observed at ± 125 and ± 145 mV. Shoulders are also visible at ± 25 and ± 80 mV. Samples H098 and H099 yield the same $(d^2I/dV^2)(V)$ spectra as H003. H056 and H083 have similar second derivative curves, but the peak positions are shifted by 5–10 mV. Very different spectra are obtained from sample Y760. They are discussed in section 3.4.2. These observations suggest that the features obtained in the derivative curves may be due to fundamental processes related to the dominant current transport mechanisms taking place in the heterostructures. A definitive explanation for the origin of these features has not been found, but some possible interpretations may be proposed. The peaks observed in Fig.3.16 may arise from the excitation of vibrational modes of impurities located in the AlAs layer or at the GaAs/AlAs interfaces. They can also be attributed to the

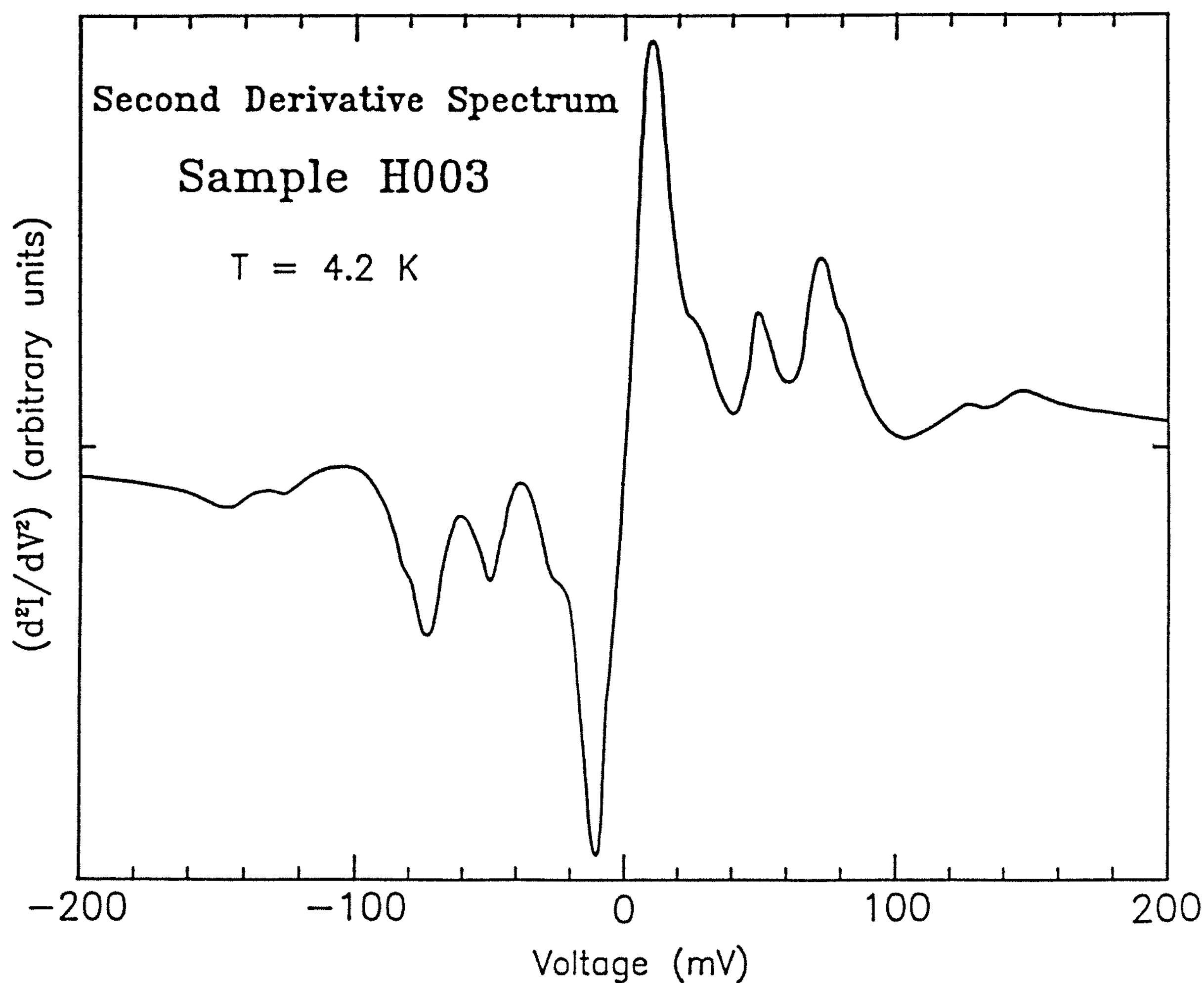

Figure 3.16: Experimental second derivative curve at 4.2 K for sample H003. The same spectra are obtained from H098 and H099. H056 and H083 yield similar $(d^2I/dV^2)(V)$ curves, but the peak positions are shifted by 5–10 mV.

emission of phonons by the tunneling electrons. In the samples under discussion, electrons occupying Γ–point states in one GaAs electrode tunnel through the first reduced AlAs X–point barrier, into the conduction band of the central AlAs bulk–like region. Electrons then tunnel through the second AlAs X–point barrier, into Γ–point states in the other GaAs electrode. As in *p*–type barrier structures, this may occur by two mechanisms. First, electrons may scatter inelastically into the X–valleys lying along the directions parallel to the planes of the layers. This mechanism thus requires two scattering events, one near each heterojunction interface. Secondly, the coupling of AlAs X–point states to GaAs Γ–point states due to the breaking of translational symmetry in the direction perpendicular to the planes of the layers makes it possible for electrons to tunnel elastically through the AlAs X–point barriers. During this process, electrons may also excite X–point phonons in AlAs. The major difference with *p*–type barrier structures is that current transport now occurs in a two–step process. As a result of the voltage drops across the two reduced AlAs barriers, an inelastic scattering event corresponding to the excitation energy ($\hbar\omega_0$) will not be manifested at the applied bias $V_0 = \hbar\omega_0/e$, but at a total applied voltage $V_0' > V_0$. Energy band diagrams indicate that when the heterostructures are symmetrically doped, the voltage drop across the first AlAs barrier through which the electrons tunnel is always larger than that across the other AlAs barrier. This is illustrated in Fig.3.15(b) in the case of sample H003. Consequently, a given inelastic process should be observed at a smaller applied voltage if it occurs in the first AlAs barrier or near the GaAs–AlAs interface than if it takes place in the second AlAs barrier or near the AlAs–GaAs interface. In particular, a single scattering event should be manifested at a total applied bias $V_0^{(1)} < 2V_0$ in the first case, but at $V_0^{(2)} > 2V_0$ in the second case. Depending upon where it occurs, any inelastic scattering process may thus produce two second derivative peaks. Furthermore, the peak

positions are functions of the total applied bias and the voltage drop distribution across the barriers. As a result, they depend upon the growth parameters of the heterostructures. This explains why the peak positions obtained from samples H056 and H083 differ slightly from those observed in the $(d^2I/dV^2)(V)$ curves of H003, H098 and H099.

Energy band diagrams may be used to tentatively identify the origin of the second derivative peaks observed in Fig.3.16. They reveal that the prominent features obtained at ± 50 mV are consistent with the excitation of a longitudinal acoustic phonon at the X–point ($V_0^{LA} = 29$ mV) in the first AlAs barrier or near the GaAs–AlAs interface. If these peaks correspond to two–phonon modes, the phonon created in the other AlAs barrier or near the second heterojunction interface would be a transverse acoustic phonon ($V_0^{TA} = 11$ mV). The peaks visible at ± 73 mV could arise from the emission of a transverse optical phonon at the X–point ($V_0^{TO} = 44$ mV) in the first AlAs barrier, or the creation of an LA phonon in the second AlAs barrier. Because these peaks are broader and more pronounced than those obtained at ± 50 mV, both mechanisms may actually occur simultaneously. If they correspond to two–phonon processes, the peaks are consistent with the excitation of a TO phonon in the first barrier and either a TA or an LA phonon in the second barrier, or with the creation of an LA phonon in the second barrier and either a TA or an LA phonon in the first barrier. The structure visible at ± 25 mV could arise from the emission of a TA phonon in the second barrier. In a two–phonon process, another TA phonon would also be created in the first barrier. The mechanism in which a single TA phonon would be emitted in the first AlAs barrier should be manifested at about ± 17 mV. However, no structure is observed at these voltages in experimental second derivative spectra. This is because the sharp peaks corresponding to the zero–bias anomalies would dominate the small structure produced by the TA

phonon emission. The shoulders observed at ± 80 mV agree with the excitation of a longitudinal optical phonon at the X–point ($V_0^{LO} = 50$ mV) in the first AlAs barrier. In a two–phonon process, the phonon created in the second AlAs barrier could be a TA or an LA phonon. The excitation of an LO phonon in the second AlAs barrier is consistent with the peaks obtained at ± 145 mV. The peaks at ± 125 mV could arise from the emission of a TO phonon in the second barrier. If these peaks are due to two–phonon processes, the other phonon could be any AlAs X–point phonon (TA, LA, TO, LO). These results are summarized in Table 3.2.

It may thus be concluded that all the peaks observed in the $(d^2I/dV^2)(V)$ curves are consistent with the excitation of X–point phonons in the AlAs layer or near the heterojunction interfaces. Since the peaks could correspond to either one– or two–phonon processes, it is not possible to determine unambiguously by which mechanism electrons tunnel through the AlAs X–point barriers. Furthermore, it is found that each scattering event may produce two second derivative peaks. This is because the peak positions depend upon where the scattering events take place and the voltage drop distribution across the two barriers through which the electrons tunnel.

3.4.2 Current Transport Through Thin n–Type AlAs Layers

a) Experimental Results

Samples in which the n–type AlAs layer is sufficiently thick and the doping densities are large enough, are characterized by a central AlAs bulk–like region. However, if the AlAs barrier layer is thin enough, it remains totally depleted of carriers. This is the case of sample Y760. It results that the electronic properties

Table 3.2: Tentative identification of second derivative peaks obtained from n–type barrier samples having thick AlAs layers (Fig.3.16).

Peak Positions (mV)	Peak Description	Phonon Modes	
		First Reduced Barrier, or near First Interface	Second Reduced Barrier, or near Second Interface
±25	Shoulders	—	TA
		TA	TA
±50	Sharp Peaks	LA	—
		LA	TA
±73	Sharp Peaks	—	LA
		TA, LA	LA
		TO	—
		TO	TA, LA
±80	Shoulders	LO	—
		LO	TA, LA
±125	Small Peaks	—	TO
		TA, LA, TO, LO	TO
±145	Small Peaks	—	LO
		TA, LA, TO, LO	LO

of this heterostructure are quite different from those of the n–type barrier samples discussed in section 3.4.1.

As indicated in Table 3.1, the AlAs layer in Y760 is 85 Å thick. The GaAs electrodes are doped n–type with Se at $3 \times 10^{18} cm^{-3}$. The AlAs doping density is estimated to be on the order of $1 \times 10^{18} cm^{-3}$. Fig.3.17 shows two energy band diagrams for the sample. Fig.3.17(a) depicts the unbiased structure. Fig.3.17(b) corresponds to a negative voltage, $V_a = -100$ mV, applied to the left GaAs cladding layer with respect to the right electrode. Both the direct Γ–point and the indirect X–point conduction band edges are shown in the barrier. Fig.3.17(a) reveals that because of the n–type doping in the AlAs layer, the band edges bend down at zero–bias and electrons accumulate in the GaAs electrodes near the heterojunction interfaces. Fig.3.17(b) shows further that applying a negative bias to the heterostructure reduces the accumulation layer in the right electrode but causes more electrons to accumulate in the left cladding layer.

Because the AlAs quantum barrier is fully depleted of electrons, tunneling occurs in sample Y760 in a one–step process, through the AlAs band gap at the X–point and/or at the Γ–point. This fundamental difference in electronic transport between Y760 and the n–type barrier samples presented in section 3.4.1 is manifested in the derivative spectra of the structures. A $(d^2I/dV^2)(V)$ curve at 4.2 K is illustrated in Fig.3.18 for Y760. It displays three peaks in each bias direction, at ± 32, ± 43, and ± 62 mV. This spectrum is significantly different from that depicted in Fig.3.16 for sample H003. In particular, it has fewer and smaller peaks. This indicates that inelastic processes in Y760 are not as important as in the other n–type barrier structures. The peaks at ± 32 and ± 43 mV could be attributed to the excitation by the tunneling electrons of transverse optical phonons at the Γ–point in the GaAs electrodes, and at the Γ– or X–point in the AlAs barrier, respectively. However, they correspond to slightly lower

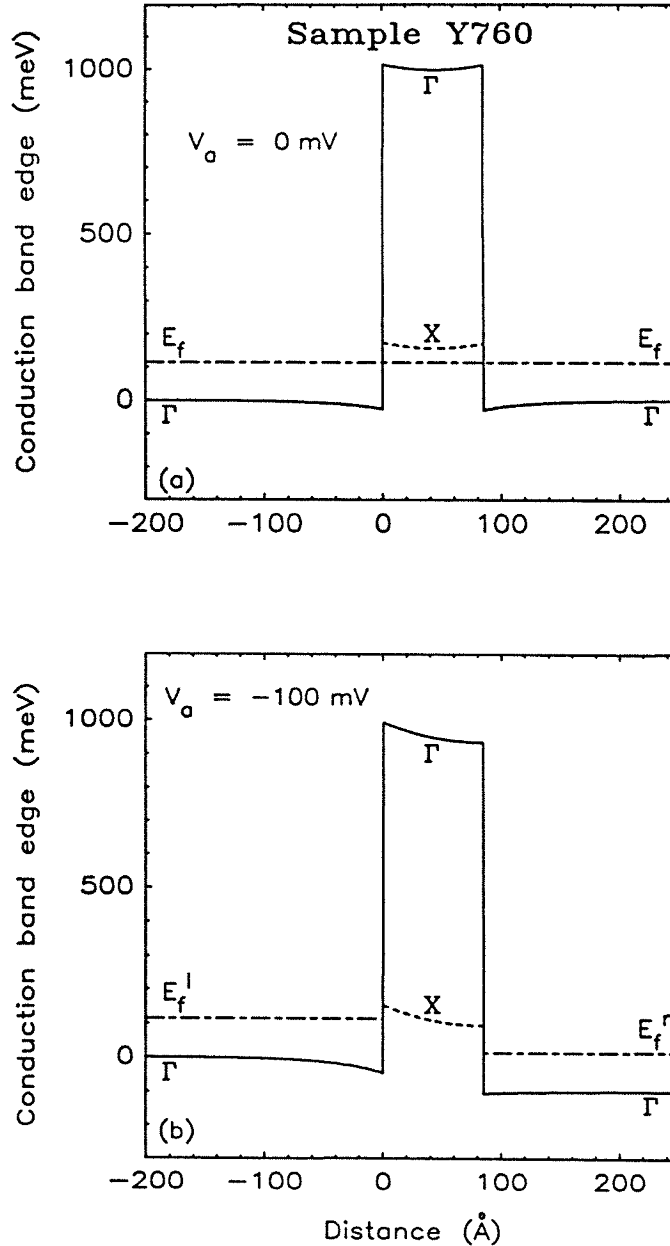

Figure 3.17: Calculated conduction band edges at the Γ–point (solid lines) and at the X–point (dashed lines), for sample Y760. The doping density in the n^+–GaAs electrodes is $3 \times 10^{18} cm^{-3}$. The AlAs barrier, which is doped n–type with Se at about $1 \times 10^{18} cm^{-3}$, is only 85 Å thick. As a result, the quantum barrier remains totally depleted of electrons, and tunneling occurs in a one–step process, through the AlAs band gap at the X–point and/or at the Γ–point.

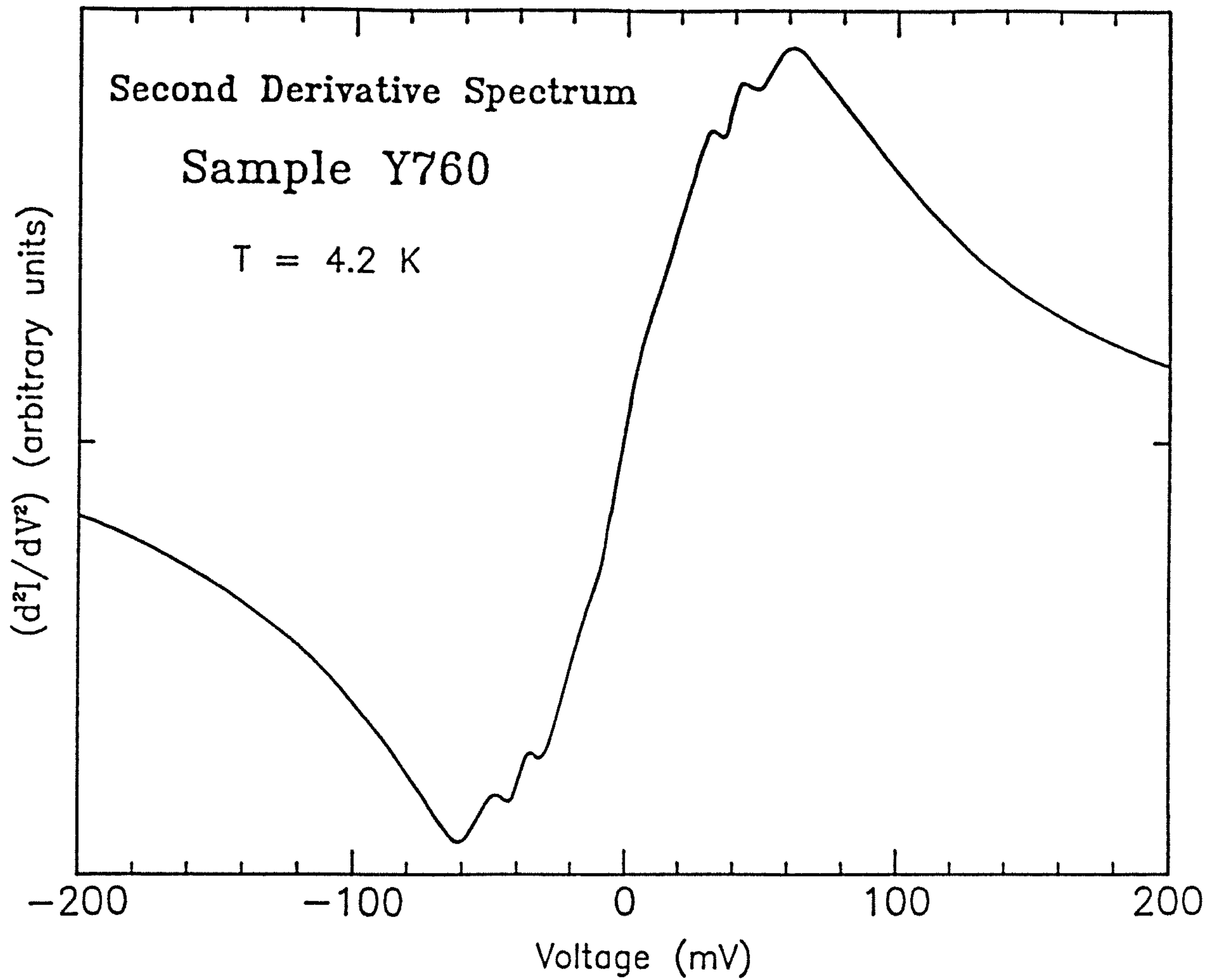

Figure 3.18: Experimental second derivative spectrum at 4.2 K for sample Y760. Three peaks are observed in each bias direction, at ± 32, ± 43, and ± 62 mV. They correspond to the excitation by the tunneling electrons of mixed interface plasmon–LO phonon modes.

energies than those reported for GaAs and AlAs TO phonons: $(\omega_{TO}^{\Gamma})_{GaAs} = 33$ meV, $(\omega_{TO}^{X})_{AlAs} = 44$ meV, and $(\omega_{TO}^{\Gamma})_{AlAs} = 45$ meV.[19-22] Furthermore, the only GaAs lattice vibrations which have been identified in other samples are Γ–point LO phonons in *p*–type barrier structures. Finally, the peaks at ±62 mV are inconsistent with any of the inelastic processes previously identified. In fact, it is shown in this section that the three peaks obtained in each bias direction in Fig.3.18 can simultaneously and consistently be interpreted by considering the interactions between phonons and interface plasmons. This is a unique property of heterostructures having *n*–type barrier layers, since it is only in these cases that enough electrons accumulate at low biases in the GaAs electrodes, near the heterojunction interfaces. As a result, electron gases exist at the GaAs/AlAs interfaces, and interface plasmons may be excited by the tunneling electrons. Because these plasmons can interact with GaAs and AlAs phonons, the nature of the collective modes present in the structures may be strongly modified. Furthermore, since GaAs and AlAs are polar semiconductors, the plasmon–phonon coupling is expected to be strongest with longitudinal optical modes.[32]

In section **b)**, the normal modes resulting from the coupling of interface plasmons with GaAs and AlAs LO phonons are calculated for a single GaAs–AlAs interface. In section **c)**, we consider two semi–infinite GaAs electrodes separated by a slab of AlAs. Finally, the results of these calculations are used in section **d)** to interpret the experimental data shown in Fig.3.18 for sample Y760.

b) Plasmon–LO Phonon Interactions for a Single GaAs–AlAs Interface

A well–known property of an electron gas is its ability to undergo collective motions (plasma oscillations). Interfaces separating materials with different electronic properties may induce new modes of plasma oscillations. In principle, these modes can be excited by incident electrons in tunneling experiments and thus

can be detected experimentally. Furthermore, interface plasmons may couple to lattice vibrations. In degenerate (III–V) semiconductors having doping densities on the order of $1 \times 10^{18} cm^{-3}$, interface plasmons and LO phonons have comparable frequencies and can interact very strongly. This plasmon–phonon coupling may then lead to important changes in the nature of the collective modes. In contrast, metals have higher electron densities and plasmon frequencies, causing the effect of this coupling to be negligible.

Interface plasmons have been identified in a number of tunneling experiments performed on metal–insulator–metal[33] and metal–semiconductor[34–36] tunnel junctions. For these structures, interface plasmons have also been described theoretically.[37,38] In addition, the interactions between plasmons and phonons in polar semiconductors have been studied in the case of semiconductor–dielectric interfaces,[39] and also for semiconductors having free surfaces.[40,41] However, no experimental or theoretical work has been reported on plasmon–phonon coupling in tunnel structures in which the electrodes and the barrier layers consisted of semiconductors.

The investigation of plasma oscillations is based upon Maxwell's equations. For the purpose of the calculations presented here, electrostatic considerations are sufficient for an adequate description of the phenomena. We thus wish to find solutions to the following equations:

$$\nabla \cdot \mathbf{D} = 0, \tag{3.6}$$

$$\nabla \cdot \mathbf{H} = 0, \tag{3.7}$$

$$\nabla \times \mathbf{E} = -\frac{1}{c}\frac{\partial \mathbf{H}}{\partial t}, \tag{3.8}$$

$$\nabla \times \mathbf{H} = \frac{1}{c}\frac{\partial \mathbf{D}}{\partial t}. \tag{3.9}$$

In these equations, the magnetic permeability μ is taken to be equal to unity.

If $\epsilon(\omega)$ denotes the frequency dependent dielectric function, **D** and **E** are related by

$$\mathbf{D} = \epsilon(\omega)\,\mathbf{E}. \tag{3.10}$$

We seek solutions corresponding to the propagation of waves along a direction z parallel to the interfaces separating the different media. The x–axis is assumed to be perpendicular to these interfaces. Any component of the fields can thus be written as

$$F(x,z,t) = Re\;\; F(x)\,e^{i(\omega t - qz)}, \tag{3.11}$$

where q denotes the magnitude of the two–dimensional wave vector parallel to the interfaces.

If we restrict ourselves to "electric waves" (TM) and neglect the "magnetic waves" (TE), which are purely transverse, $H_x = H_z = E_y \equiv 0$ in any material. As a result, the field amplitudes inside each medium may be found by using

$$E_z(x) = (-\frac{i}{q})\,\frac{dE_x}{dx}, \tag{3.12}$$

$$H_y(x) = \left(\frac{\omega\,\epsilon(\omega)}{cq}\right) E_x, \tag{3.13}$$

and integrating

$$\frac{d^2 E_x}{dx^2} - Q^2\,E_x = 0, \tag{3.14}$$

where

$$Q = \sqrt{q^2 - \frac{\omega^2}{c^2}\,\epsilon(\omega)}, \quad Re\,Q > 0. \tag{3.15}$$

The general solution of Eq.(3.14) is a linear combination of the two independent solutions $e^{Q\,x}$ and $e^{-Q\,x}$.

In this section, we consider a single interface at $x = 0$, separating two semi–infinite semiconductors, (I) and (II). This configuration is illustrated in Fig.3.19(a). The solution for E_x which remains finite at infinity is

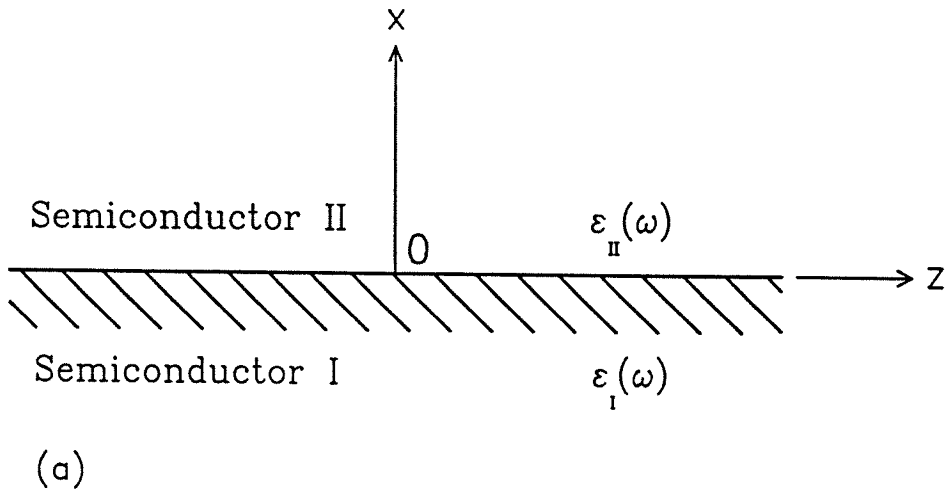

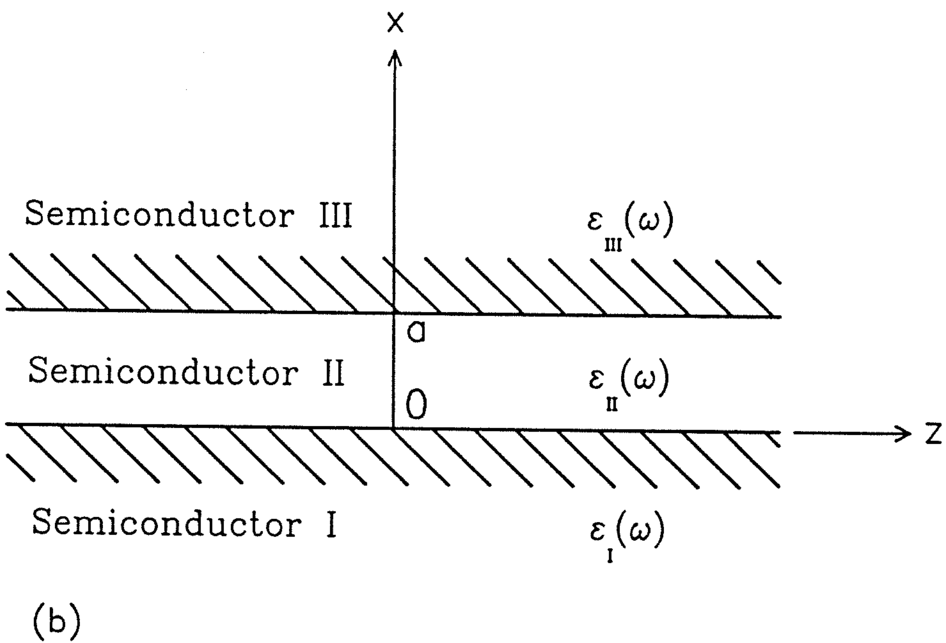

Figure 3.19: (a) Single interface at $x = 0$, separating two semiconductors I and II. Semiconductor I (II), corresponding to $x < 0$ ($x > 0$), has a frequency dependent dielectric function $\epsilon_I(\omega)$ ($\epsilon_{II}(\omega)$). (b) Two interfaces, at $x = 0$ and $x = a$, separating semiconductors I and II, and II and III, respectively.

$$E_x = \begin{cases} A_I\, e^{Q_I x}, & x < 0; \\ A_{II}\, e^{-Q_{II} x}, & x > 0. \end{cases} \tag{3.16}$$

Eqs.(3.12) and (3.13) can be used to calculate the corresponding E_z and H_y. Finally, the continuity of the fields across the interface yields the following dispersion relation:

$$\frac{Q_I\, \epsilon_{II}(\omega)}{Q_{II}\, \epsilon_I(\omega)} = -1. \tag{3.17}$$

For (qc) large compared to ω, but still sufficiently small so that the local dielectric function $\epsilon(\omega)$ can be used, the frequencies of the coupled modes are determined by the locations of the zeros of the total dielectric function:

$$\epsilon_I(\omega) + \epsilon_{II}(\omega) = 0. \tag{3.18}$$

For a degenerate n–type semiconductor, the dielectric function including the plasma frequency is given by[32]

$$\epsilon(\omega) = \epsilon(\infty) + \frac{\epsilon(0) - \epsilon(\infty)}{\left(1 - \frac{\omega^2}{\omega_{TO}^2}\right)} - \frac{4\pi n e^2}{m^* \omega^2}, \tag{3.19}$$

where $\epsilon(0)$ is the static dielectric constant, $\epsilon(\infty)$ is the high–frequency limit of the dielectric function, n is the free electron density, m^* is the electron effective mass, and ω_{TO} is the TO phonon frequency in the absence of coupling.

In cubic crystals having two atoms per unit cell, such as GaAs and AlAs, ω_{TO} is related to the LO phonon frequency, ω_{LO}, by the Lyddane–Sachs–Teller relation:

$$\frac{\omega_{LO}^2}{\omega_{TO}^2} = \frac{\epsilon(0)}{\epsilon(\infty)}. \tag{3.20}$$

To be specific, let us consider a single GaAs–AlAs interface. If the GaAs layer is degenerately doped n–type, its dielectric function is given by Eq.(3.19), with $n_{GaAs} \neq 0$. If the AlAs conduction band is totally depleted of carriers, $n_{AlAs} = 0$, and the dielectric response of AlAs reduces to the first two terms in Eq.(3.19).

In this instance, the frequencies of the coupled modes are the roots of

$$\epsilon_{GaAs}(\infty)+\epsilon_{AlAs}(\infty)+\frac{\epsilon_{GaAs}(0)-\epsilon_{GaAs}(\infty)}{\left(1-\frac{\omega^2}{(\omega_{TO})^2_{GaAs}}\right)}+\frac{\epsilon_{AlAs}(0)-\epsilon_{AlAs}(\infty)}{\left(1-\frac{\omega^2}{(\omega_{TO})^2_{AlAs}}\right)}-\frac{4\pi n_{GaAs}e^2}{m^*_{GaAs}\omega^2}=0. \tag{3.21}$$

This is a cubic equation in ω^2. For each value of n_{GaAs}, three normal modes are found for the coupled system interface plasmon–GaAs LO phonon–AlAs LO phonon. In Fig.3.20, the three branches of the dispersion relation are plotted versus the free electron density in GaAs, for values of n_{GaAs} ranging between 1×10^{17} and $1 \times 10^{19} cm^{-3}$. In GaAs (AlAs), $\epsilon(0)$ and $\epsilon(\infty)$ are 13.2 (10.1) and 10.9 (8.2), respectively. $(\omega_{TO})_{GaAs}$ is taken to be the frequency of the GaAs Γ–point TO phonon: $\omega_{TO}^{\Gamma} = 33$ meV.[19,20] In AlAs, the Γ– and X–point TO phonons both have the same energy within 1 meV: $\omega_{TO}^{\Gamma} = 45$ meV and $\omega_{TO}^{X} = 44$ meV.[21,22] The curves depicted in Fig.3.20 could thus correspond to an AlAs LO phonon at either the Γ– or the X–point.

The three branches are labeled (A), (B), and (C) in Fig.3.20. Because the plasma frequency is a strong function of n_{GaAs}, the normal modes also depend upon the GaAs doping concentration. When n_{GaAs} is small ($n_{GaAs} < 2\times10^{17}cm^{-3}$), or very large ($n_{GaAs} > 8\times10^{18}cm^{-3}$), the frequency of the interface plasmon differs significantly from those of the LO phonons, and the interaction is weak. The normal modes are then essentially those of the uncoupled system. As indicated in Fig.3.20, we get an interface plasmon (A), a GaAs LO phonon (B), and an AlAs LO phonon (C), for small values of n_{GaAs}. For large values of n_{GaAs}, the three modes have the energies of a GaAs TO phonon (A), an AlAs TO phonon (B), and an interface plasmon (C). In the limit of high GaAs electron concentrations, the LO phonon modes vibrate at the corresponding TO phonon frequencies because the charge carriers have shielded out the polarization of the lattice vibrations.[42] For intermediate values of n_{GaAs}, the plasma frequency becomes comparable to the LO phonon frequencies and the coupling is strong. As a

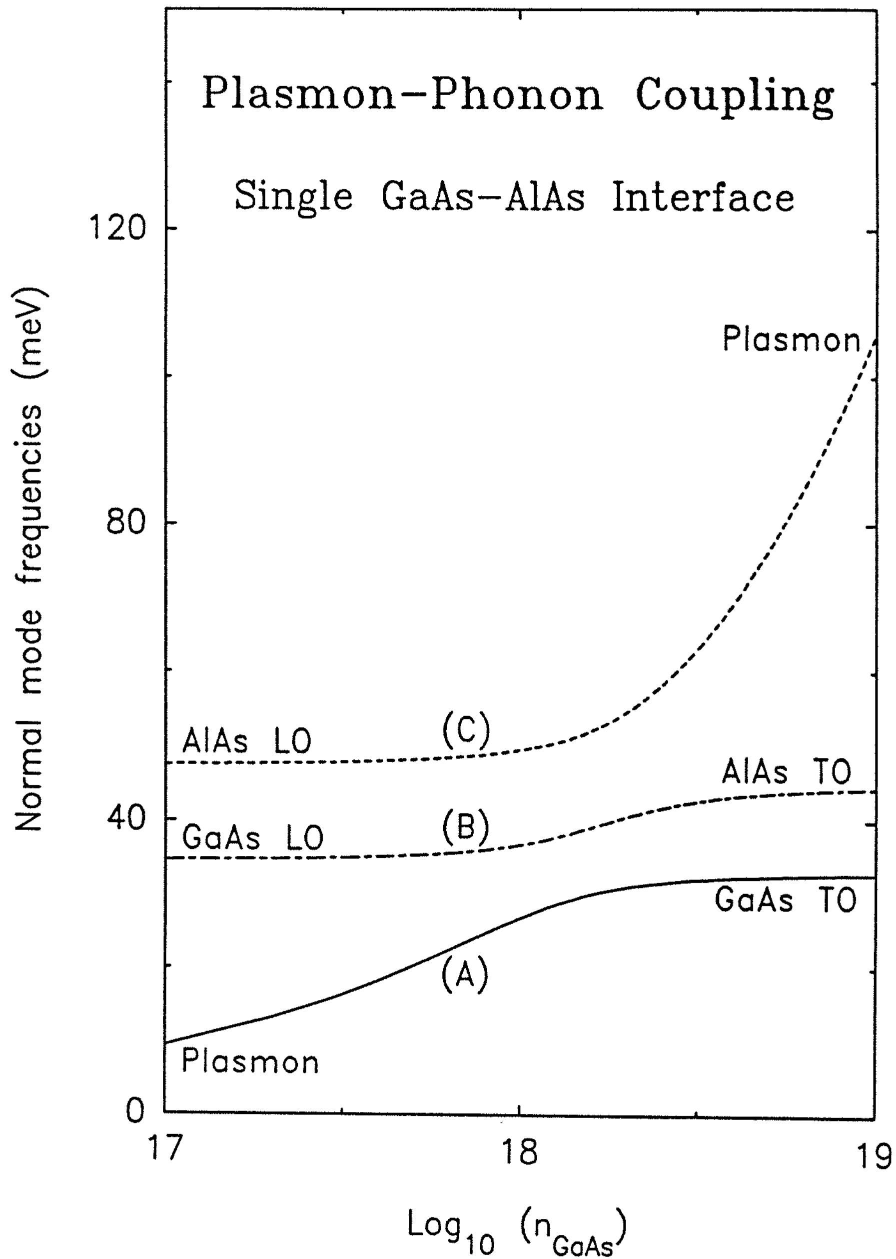

Figure 3.20: Calculated dispersion relation for the coupled system interface plasmon–GaAs LO phonon–AlAs LO phonon, in the case of a single GaAs–AlAs interface. n_{GaAs} is the free electron density in the GaAs layer. The AlAs conduction band is assumed to be totally depleted of carriers ($n_{AlAs} = 0$).

result, the modes repel one another to avoid intersecting, and the normal modes of the system are no longer the individual phonons and the interface plasmon, but mixed plasmon–phonon modes. Fig.3.20 reveals that the interaction is strongest for values of n_{GaAs} ranging between 8×10^{17} and $3 \times 10^{18} cm^{-3}$.

c) Plasmon–LO Phonon Interactions for two GaAs/AlAs Interfaces

Calculations of interface plasmon–LO phonon coupling have also been performed in the case of two semi–infinite materials separated by a thin layer of another semiconductor. This configuration is illustrated in Fig.3.19(b). It is that of a single barrier tunnel structure. The two interfaces are located at $x = 0$ and $x = a$, between semiconductors (I) and (II), and semiconductors (II) and (III), respectively.

The dispersion relation describing the interaction between the plasmons at both interfaces and the LO phonons in all three materials may be obtained using the same approach as in the case of a single interface. This dispersion relation is given by

$$R_I \, R_{III} + (R_I + R_{III}) \, coth(a \, Q_{II}) + 1 = 0, \tag{3.22}$$

where

$$R_I = \frac{Q_I \, \epsilon_{II}(\omega)}{Q_{II} \, \epsilon_I(\omega)}, \tag{3.23}$$

and

$$R_{III} = \frac{Q_{III} \, \epsilon_{II}(\omega)}{Q_{II} \, \epsilon_{III}(\omega)}. \tag{3.24}$$

If regions (I) and (III) are identical, Eq.(3.22) takes the form

$$\Big(\frac{Q_I \, \epsilon_{II}(\omega)}{Q_{II} \, \epsilon_I(\omega)}\Big)^2 + 2 \, \Big(\frac{Q_I \, \epsilon_{II}(\omega)}{Q_{II} \, \epsilon_I(\omega)}\Big) \, coth(a \, Q_{II}) + 1 = 0. \tag{3.25}$$

When $(a \, Q_{II}) \gg 1$, both interfaces become independent and Eq.(3.25) reduces to the dispersion relation obtained for a single interface (Eq.(3.17)).

To be specific, let us consider a GaAs–AlAs–GaAs double heterojunction in which the GaAs cladding layers are degenerately doped n–type but the conduction band in the AlAs barrier layer is fully depleted of electrons. In Figs.3.21(a) and (b), the four branches of the dispersion relation are plotted versus (qa) for GaAs doping densities of 3×10^{18} and $5 \times 10^{18} cm^{-3}$, respectively. When (qa) becomes sufficiently large, the two interfaces are decoupled, and the four branches tend asymptotically toward the three modes plotted in Fig.3.20 for a single GaAs–AlAs interface. For example, these asymptotic values are 32.5, 44 and 77 meV in Fig.3.21(b). They correspond precisely to the energies of the three modes obtained in Fig.3.20 for $n_{GaAs} = 5 \times 10^{18} cm^{-3}$. Figs.3.21(a) and (b) also indicate that as the energies of the interface plasmons and LO phonons become more comparable, the plasmon–phonon interactions remain strong over a wider range of values of (qa). For example, if $n_{GaAs} = 5 \times 10^{18} cm^{-3}$, the coupling is important for $(qa) < 0.35$. When $n_{GaAs} = 3 \times 10^{18} cm^{-3}$, the plasmons and interface plasmons interact strongly for $(qa) < 0.7$.

d) Interpretation of Experimental Results

The energies of the normal modes anticipated from the interactions between LO phonons and interface plasmons in sample Y760 may be found by using the theoretical approach presented in section **c)**. For a GaAs doping density of $3 \times 10^{18} cm^{-3}$, the four branches of the dispersion relation are plotted in Fig.3.21(a). However, for electrons near the Fermi energy, tunneling through the AlAs barrier layer, (qa) is sufficiently large that the two interfaces are independent. Consequently, only the three asymptotic modes need to be considered. Their energies may thus be found directly from Fig.3.20. For $n_{GaAs} = 3 \times 10^{18} cm^{-3}$, $\omega_A = 32$ meV, $\omega_B = 43$ meV and $\omega_C = 62.5$ meV. These values are in good agreement with the threshold voltages of the inelastic scatter-

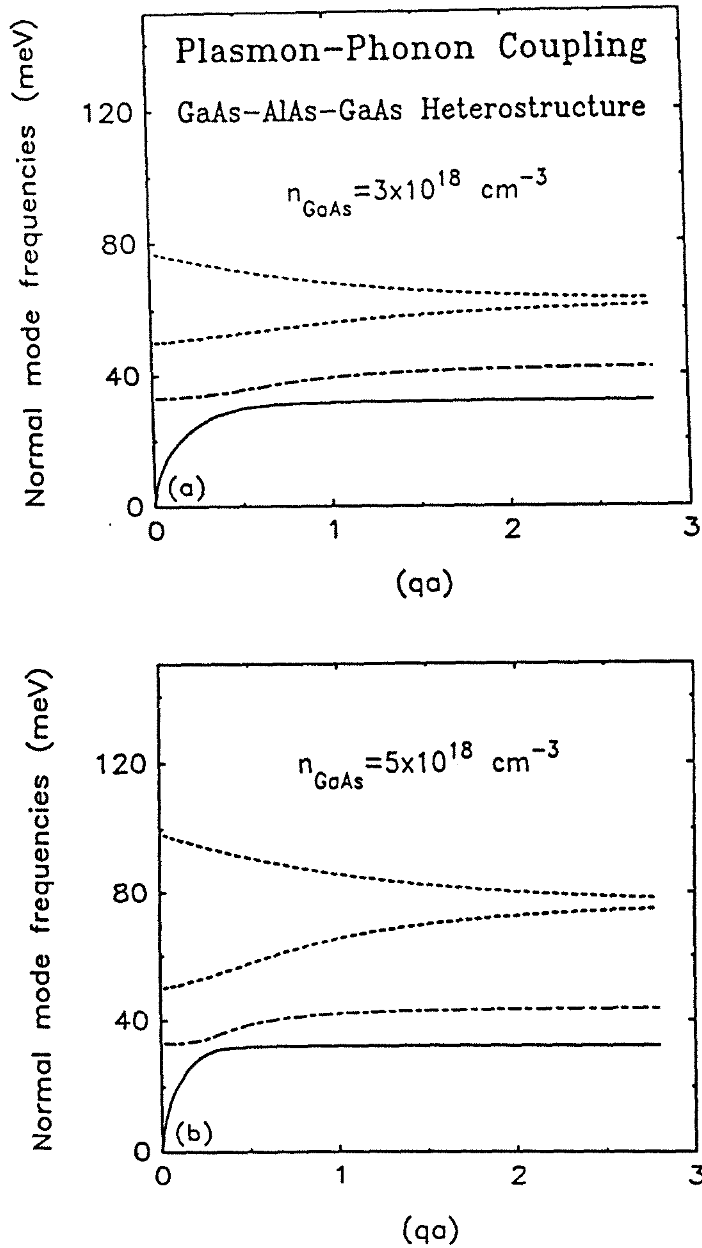

Figure 3.21: Calculated dispersion relation for the coupled system interface plasmon–GaAs LO phonon–AlAs LO phonon, in the case of two semi-infinite GaAs layers separated by a thin slab of AlAs. q is the two–dimensional wave vector parallel to the interfaces, and a is the thickness of the AlAs layer. The GaAs electrodes are degenerately doped n–type at $n_{GaAs} = 3 \times 10^{18} cm^{-3}$ in (a), and $n_{GaAs} = 5 \times 10^{18} cm^{-3}$ in (b). The AlAs barrier layer is assumed to be totally depleted of electrons ($n_{AlAs} = 0$).

ing processes observed in the low temperature second derivative spectra of the sample, at ± 32, ± 43 and ± 62 mV. Therefore, it may be be concluded that the peaks obtained in Fig.3.18 arise from the coupling of plasmons located at the GaAs/AlAs interfaces with LO phonons in the GaAs electrodes and the AlAs barrier layer. As indicated in Fig.3.20, plasmon–phonon interactions are strong in this heterostructure because $n_{GaAs} = 3 \times 10^{18} cm^{-3}$ and the frequencies of the interface plasmon and LO phonons are comparable. It should be mentioned that whereas these phonons are clearly Γ–point LO phonons in GaAs, they may be either Γ– or X–point phonons in AlAs. Consequently, it is not possible to determine without ambiguity whether it is the direct or indirect AlAs band gap which governs electron tunneling in sample Y760.

Similar interface plasmon–LO phonon interactions may also exist in the n–type barrier samples presented in section 3.4.1. However, such interactions have not been mentioned in the discussion of the second derivative peaks obtained from these structures. There are two main reasons for this. Firstly, negligible plasmon–LO phonon interactions are expected from these samples because the doping densities in the GaAs cladding layers are greater than $5 \times 10^{18} cm^{-3}$. Secondly, electronic transport occurs through different processes than in heterostructures having thin AlAs barrier layers. The excitation of mixed plasmon–phonon modes by the tunneling electrons could thus be dominated by other current transport mechanisms. A complete understanding of these phenomena would thus require the investigation of a wide variety of samples having different barrier thicknesses, barrier doping densities and electrode doping concentrations.

3.5 Summary

The objective of this study was to investigate elastic and inelastic tunneling

processes in GaAs–AlAs–GaAs double heterojunctions grown by MOCVD in the [100]–direction. The GaAs electrodes in the heterostructures studied were degenerately doped n–type with Se. The AlAs quantum barriers were doped either p–type with Mg or n–type with Se. The electronic properties of the samples were investigated by performing measurements of current–voltage, I-V, characteristics, as well as first, $(dI/dV)(V)$, and second, $(d^2I/dV^2)(V)$, derivatives of the I-V curves, at temperatures ranging from 300 to 4.2 K.

Experimental and theoretical results made it possible to identify the dominant current transport mechanisms taking place at low temperatures in structures with thin p–type AlAs barrier layers. (*i*) First, electrons may tunnel elastically through the AlAs Γ–point barrier. (*ii*) They may also tunnel inelastically and/or elastically through the AlAs band gap at the X–point. Inelastic X–point tunneling, which may occur via virtual states beneath the four X–point valleys lying parallel to the planes of the layers, requires electron scattering near both heterojunction interfaces. Elastic X–point tunneling, which is due to the coupling of AlAs X–point states with GaAs Γ–point states, can take place via virtual states below the two AlAs X–point valleys lying in the direction perpendicular to the planes of the layers. (*iii*) Finally, electrons tunneling through the AlAs band gap at the Γ–point and/or at the X–point can create fundamental excitations, such as phonons.

A theoretical model, which treats trap levels in the AlAs barrier as intermediate states for two–step tunneling processes, was developed and discussed in the case of p–type barrier structures. Calculations indicated that this impurity–assisted tunneling mechanism can become important when the AlAs barrier is thick enough.

The p–type barrier samples were classified into two categories depending on the nature of the inelastic tunneling processes which could be identified in their

derivative spectra. In particular, it was found that the first mechanism by which electrons may tunnel through the AlAs band gap at the X–point, and which requires two scattering events, was more important in the stuctures of the first type than in those of the second type. The opposite was true for the other tunneling mechanism, in which AlAs X–point states couple to GaAs Γ–point states through the breaking of translational symmetry in the direction perpendicular to the heterojunction interfaces. These results revealed that the dominant current transport mechanisms taking place in single barrier heterostructures may vary from sample to sample. Such effects should be related primarily to the quality of the materials and the heterojunction interfaces.

A number of *p*–type barrier samples also showed anomalous zero–bias conductances. These so–called zero–bias anomalies may be attributed to interface states or to trap levels located in the AlAs barrier and/or near the heterojunction interfaces.

Structures in which the AlAs layers were doped *n*–type were characterized by high current densities at low temperatures, even when the AlAs layers were very thick (140–730 Å). Furthermore, these samples did not display the proper relationship between current density and barrier thickness expected from tunnel structures. Energy band diagram calculations revealed that when the AlAs layer is thick enough and/or sufficiently doped, the AlAs conduction band at the X–point is not fully depleted of electrons. In this instance, the dominant low temperature current transport mechanism is tunneling through two reduced AlAs X–point barriers separated by a bulk layer of AlAs. These results were consistent with the peaks observed in the second derivative spectra of the samples. These peaks could be attributed to the creation by the tunneling electrons of single AlAs X–point phonons in the barriers, or to the excitation of two AlAs X–point phonons, one near each GaAs/AlAs heterojunction interface.

In samples having sufficiently thin n–type AlAs layers, the AlAs conduction band remains totally depleted of carriers. Tunneling thus occurs in a one–step process, through the AlAs band gap at the X–point and/or at the Γ–point. In these structures, plasmons located at the GaAs/AlAs interfaces may interact with LO phonons in GaAs and AlAs. This occurs when the GaAs doping density is such that the plasma frequency becomes comparable to the LO phonon frequencies. When this coupling is strong, the normal modes of the system are no longer the individual phonons and the interface plasmons, but mixed plasmon–phonon modes. These modes, which can be excited by the tunneling electrons, have been observed experimentally. Peak positions in $(d^2I/dV^2)(V)$ spectra were found to be in good agreement with the calculated energies of the modes arising from the coupling of interface plasmons with GaAs Γ–point LO phonons and AlAs Γ– or X–point LO phonons.

References

1. D. Delagebeaudeuf, P. Delescluse, P. Etienne, J. Massies, M. Laviron, J. Chaplart, and N. T. Linh, Electron. Lett. **18**, 85 (1982).

2. P. Guéret, and U. Kaufmann, Electron. Lett. **21**, 344 (1985).

3. I. Hase, H. Kawai, K. Kaneko, N. Watanabe, Electon. Lett. **20**, 491 (1984).

4. R. T. Collins, J. Lambe, T. C. McGill, and R.D. Burnham, Appl. Phys. Lett. **44**, 532 (1984).

5. H. M. Manasevit, Appl. Phys. Lett. **12**, 156 (1968).

6. R. D. Dupuis, and P. D. Dapkus, Appl. Phys. Lett. **31**, 466 (1977).

7. C. R. Lewis, W. T. Dietze, and M. J. Ludowise, Electron. Lett. **18**, 569 (1982).

8. R. D. Burnham, W. Streifer, D. R. Scifres, C. Lindstrom, T. L. Paoli, and N. Holonyak, Electron. Lett. **18**, 1095 (1982).

9. R. T. Collins, *Ph.D. thesis*, California Institute of Technology (1985).

10. G. C. Osbourn, J. Vac. Sci. Technol. **17**, 1104 (1980).

11. C. Mailhiot, and T. C. McGill, J. Vac. Sci. Technol. B **1**, 637 (1983).

12. E. O. Kane, *Physics of III–V Compounds, Vol. 1, Ch. 3* (Academic Press, New York, 1966) pp.75–100.

13. R. Tsu, and L. Esaki, Appl. Phys. Lett. **22**, 562 (1973).

14. J. Batey, and S. L. Wright, J. Appl. Phys. **59**, 200 (1986).

15. T. K. Woodward, T. E. Schlesinger, T. C. McGill, and R.D. Burnham, Appl. Phys. Lett. **47**, 631 (1985).

16. H. P. Hjalmarson, Superlattices and Microstructures **1**, 379 (1985).

17. The calculation of the impurity–assisted tunneling current was developed by D. H. Chow.

18. G. H. Parker, and C. A. Mead, Appl. Phys. Lett. **14**, 21 (1969).

19. S. S. Mitra, Phys. Rev. **132**, 986 (1963).

20. M. Ilegems, and G. L. Pearson, Phys. Rev. B **1**, 1576 (1970).

21. W. Hörig, H. Neumann, P. Fischer, and G. Kühn, Phys. Stat. Sol. **42**, 193 (1970).

22. B. Monemar, Phys. Rev. B **8**, 5711 (1973).

23. M. R. Lorenz, R. Chicotta, G. D. Pettit, and P. J. Dean, Sol. St. Comm. **8**, 693 (1970).

24. A. Onton, in *Proc. I.C.P.S. Conf.*, Cambridge Mass., (1970), pp.107.

25. R. A. Logan, and J. M. Rowell, Phys. Rev. Lett. **13**, 404 (1964).

26. J. Shewchun, and R. M. Williams, Phys. Rev. Lett. **15**, 160 (1965).

27. G. D. Mahan, and C. B. Duke, Phys. Rev. **149**, 705 (1966).

28. J. M. Rowell, and L. Y. L. Shen, Phys. Rev. Lett. **17**, 15 (1966).

29. C. B. Duke, S. D. Silverstein, and A. J. Bennett, Phys. Rev. Lett. **19**, 315 (1967).

30. A. M. Andrews, H. W. Korb, N. Holonyak, Jr., C. B. Duke, and G. G. Kleiman, Phys. Rev. B **5**, 4191 (1972).

31. J. D. Adler, H. J. Kreuzer, and J. Straus, Phys. Rev. B **11**, 2812 (1975).

32. B. B. Varga, Phys. Rev. **137**, A1896 (1965).

33. J. Lambe, and S. L. McCarty, Phys. Rev. Lett. **37**, 9234 (1976).

34. D. C. Tsui, Phys. Rev. Lett. **22**, 293 (1969).

35. C. B. Duke, M. J. Rice, and F. Steinrisser, Phys. Rev. **181**, 733 (1969).

36. M. Mikkor, and W. C. Vassell, Phys. Rev. B **2**, 1875 (1970).

37. E. N. Economou, Phys. Rev. **182**, 39 (1969).

38. K. L. Ngai, and E. N. Economou, Phys. Rev. B **4**, 2132 (1971).

39. K. W. Chiu, and J. J. Quinn, Phys. Lett. **35A**, 469 (1971).

40. V. V. Bryxin, D. N. Mirlin, and I. I. Reshina, Sol. St. Comm. **11**, 695 (1972).

41. R. F. Wallis, and J. J. Brion, Sol. St. Comm. **9**, 2099 (1971).

42. A. Mooradian, and G. B. Wright, Phys. Rev. Lett. **16**, 999 (1966).

Chapter 4

Resonant Tunneling in $GaAs/Al_xGa_{1-x}As$ Double Barrier Heterostructures

4.1 Introduction

Negative differential resistance devices based on resonant tunneling through double barrier heterostructures are the object of considerable theoretical and experimental work.[1-10] In most studies, the main current transport mechanism is electron tunneling through two ultra–thin $Al_xGa_{1-x}As$ tunnel barriers separated by a GaAs quantum well. The most important electronic properties of these structures are the presence of negative differential resistances in their current–voltage (I–V) characteristics, and their high–speed capabilities. As a result, they have potential applications in millimeter–wave oscillators,[10] mixers and high density logic circuits. Furthermore, new classes of three–terminal devices using resonant tunneling through quantum well and quantum barrier heterostructures are being proposed.[11-14] These devices could be used as fast switches, frequency

multipliers, multistate memories and high–speed analog–to–digital converters.[11]

In a typical two–terminal double barrier heterostructure, electrons tunnel between two degenerately doped electrodes through two quantum barriers separated by a quantum well. In the direction perpendicular to the heterojunction interfaces, the quantum well is characterized by a spectrum of discrete quasi–stationary energy levels. Tunneling electrons moving perpendicular to the barriers with an energy equal to these resonant states have a large transmission probability. Since the structures are three–dimensional and charge carriers in the well are free to move parallel to the planes of the layers, the quasi–stationary levels are in fact the minima of two–dimensional energy subbands. In considering elastic tunneling perpendicular to the barriers, two conditions must be satisfied: (*i*) conservation of energy, and (*ii*) conservation of the transverse component of the electron wave vector. This second condition is essential in obtaining negative differential resistances. Let E_1 be the lowest resonant state in the quantum well. As long as E_1 is higher in energy than the Fermi level in the incident cladding layer, E_f^i, no electrons are allowed to tunnel through the subband associated with E_1. Tunneling through the entire structure is possible but exponentially small. If the applied bias is increased, E_1 is lowered with respect to E_f^i. When both levels coincide in energy, resonant tunneling via E_1 is initiated. As the applied voltage becomes larger, the current increases rapidly, until E_1 lines up with the conduction band edge in the incident electrode. Then, resonant tunneling via E_1 is no longer possible: although there are states available for tunneling in the two–dimensional subband associated with E_1, the transverse component of the electron wave vector cannot be conserved. This causes the tunneling current to decrease, i.e., produces negative differential resistance. Higher energy subbands will yield the same phenomena.

The I–V curves anticipated from resonant tunneling double barrier het-

erostructures were first calculated by R. Tsu and L. Esaki in the square potential approximation.[1] Vassell *et al.* improved this model by assuming trapezoidal shapes of the tunnel barriers under applied biases.[3] Both formalisms predict negative differential resistances characterized by very large peak–to–valley current ratios (I_p/I_v) at low temperatures. For example, in structures having two 20 Å thick $Al_xGa_{1-x}As$ barrier layers separated by a 50 Å wide GaAs quantum well, I_p/I_v is found to be on the order of 150 for the first resonance when the barrier height is taken to be 0.5 eV.[1] This is in conflict with experimental results since one of the best values of I_p/I_v realized to date has been 10 at 77 K.[15] However, the discrepancies observed between calculated and experimental I–V curves may be reduced by making the barriers lower and thinner, and also by growing the structures with sharper interfaces and fewer impurities in the quantum barriers and well.[15] Furthermore, processes such as phonon–induced inelastic tunneling have been shown to set an upper limit to the peak–to–valley current ratios anticipated from resonant tunneling alone.[16] As the barrier layers become thicker and higher, experimental I–V characteristics deviate more significantly from theoretical predictions based on direct band gap resonant tunneling. This indicates that competing current transport mechanisms become more important. When the $Al_xGa_{1-x}As$ tunnel barriers are made of indirect band gap alloys ($x > 0.40$–0.45), the resonant energy levels in the GaAs well correspond to states confined by the $Al_xGa_{1-x}As$ X–point potential energy barriers as well as the $Al_xGa_{1-x}As$ Γ–point barriers. These additional energy levels are expected to increase the current densities and reduce the peak–to–valley current ratios of the negative differential resistances.

This chapter discusses the main results of a study of resonant tunneling through GaAs/$Al_xGa_{1-x}As$ double barrier heterostructures. Emphasis is placed on identifying the quasi–stationary energy levels in the GaAs quantum well

which produce negative differential resistances in experimental I–V characteristics. This is achieved by calculating the energy band diagrams of the structures. Energy band profiles are important in determining the actual shapes of the potential energy barriers through which the electrons tunnel. Furthermore, they give the voltage drop distributions, not only in the quantum barriers and well, but also in the cladding layers. These distributions may differ significantly from those based on the usual assumption that the entire applied voltage drops linearly across the barriers and well. As a result, energy band diagrams are essential in finding the positions of the resonant states in the quantum well and in identifying the origin of the negative differential resistances observed experimentally. This is particularly important in structures having indirect band gap $Al_xGa_{1-x}As$ barrier layers because some of the peaks in current are found to be inconsistent with resonances in the GaAs well confined by the $Al_xGa_{1-x}As$ Γ–point potential energy barriers. However, the experimental I–V data can usually be accounted for by considering tunneling via resonant states in the well bound by the $Al_xGa_{1-x}As$ X–point potential energy barriers in addition to resonant tunneling via quasi–stationary Γ–states. This is in conflict with the commonly made assumption that the only symmetry point to consider in the barriers should be the Γ–point, even when $Al_xGa_{1-x}As$ is indirect.

Samples featuring negative differential resistances in their I–V characteristics are listed in Tables 4.1 and 4.2, along with their most important parameters. Except for one MBE grown structure, 489, all of the samples were fabricated by MOCVD. The tunnel barrier and quantum well thicknesses indicated in Table 4.1 for sample 489 were estimated from the growth parameters. However, the layer thicknesses given for the other heterostructures were obtained from TEM measurements, accurate to within one monolayer (one monolayer is taken to be 2.83 Å). In Table 4.1, Barrier No.1 refers to the $Al_xGa_{1-x}As$ layer closer to the

Table 4.1: Sample information for double barrier tunnel structures.

Sample	Growth Technique	Barrier Composition	Quantum Barrier and Well Thicknesses (TEM measurements) Barrier No.2	GaAs Well	Barrier No.1
489	MBE	$Al_{0.35}Ga_{0.65}As$	79 Å (28 monolayers)	48 Å (17 monolayers)	79 Å (28 monolayers)
H283	MOCVD	AlAs	68 Å (24 monolayers)	90.5 Å (32 monolayers)	56.5 Å (20 monolayers)
H392	MOCVD	AlAs	37 Å (13 monolayers)	51 Å (18 monolayers)	71 Å (25 monolayers)
H408	MOCVD	AlAs	42 Å (15 monolayers)	62 Å (22 monolayers)	51 Å (18 monolayers)
H418	MOCVD	AlAs	37 Å (13 monolayers)	28.5 Å (10 monolayers)	48 Å (17 monolayers)
H475	MOCVD	AlAs	71 Å (25 monolayers)	76.5 Å (27 monolayers)	79 Å (28 monolayers)
H919	MOCVD	AlAs	39.5 Å (14 monolayers)	34 Å (12 monolayers)	42.5 Å (15 monolayers)
H927	MOCVD	AlAs	85 Å (30 monolayers)	45 Å (16 monolayers)	71 Å (25 monolayers)
H943	MOCVD	$Al_{0.35}Ga_{0.65}As$	59.5–62 Å (21–22 monolayers)	31–36.5 Å (11–13 monolayers)	59.5–62 Å (21–22 monolayers)
H945	MOCVD	$Al_{0.35}Ga_{0.65}As$	51–59.5 Å (18–21 monolayers)	25.5–28.5 Å (9–10 monolayers)	51–53.5 Å (18–19 monolayers)
S009	MOCVD	$Al_{0.35}Ga_{0.65}As$	59.5 Å (21 monolayers)	51 Å (18 monolayers)	59.5 Å (21 monolayers)
S008	MOCVD	$Al_{0.35}Ga_{0.65}As$	110.5 Å (39 monolayers)	65 Å (23 monolayers)	110.5 Å (39 monolayers)
S031	MOCVD	$Al_{0.75}Ga_{0.25}As$	124.5 Å (44 monolayers)	68 Å (24 monolayers)	116 Å (41 monolayers)
S032	MOCVD	$Al_{0.75}Ga_{0.25}As$	102 Å (36 monolayers)	45 Å (16 monolayers)	104.5 Å (37 monolayers)

Table 4.2: Doping densities (cm^{-3}).

Sample	Top Electrode	Back Electrode	Barrier Layers	GaAs Well
489	Si–1×10^{18}	Si–1×10^{18}	undoped	undoped
H283	Se–4.5×10^{18}	Se–4.0×10^{18}	Mg–2×10^{17}	undoped
H392	Se–2.0×10^{18}	Se–1.7×10^{18}	Mg–6×10^{17}	undoped
H408	Se–1.75×10^{18}	Se–1.75×10^{18}	Mg–6×10^{17}	undoped
H418	Se–1.5×10^{18}	Se–1.5×10^{18}	Mg–6×10^{17}	undoped
H475	Se–4.7×10^{17}	Se–5.0×10^{17}	Mg–2×10^{17}	undoped
H919	Se–1.5×10^{18}	Se–1.2×10^{18}	Mg–6×10^{17}	undoped
H927	Se–1.5×10^{18}	Se–1.3×10^{18}	Mg–6×10^{17}	undoped
H943	Se–1.1×10^{18}	Se–1.0×10^{18}	Mg–2×10^{17}	undoped
H945	Se–1.3×10^{18}	Se–1.3×10^{18}	Mg–2×10^{17}	undoped
S009	Se–1.2×10^{18}	Se–1.2×10^{18}	Mg–2×10^{17}	undoped
S008	Se–3.1×10^{18}	Se–2.5×10^{18}	undoped	undoped
S031	Se–3.0×10^{18}	Se–1.5×10^{18}	undoped	undoped
S032	Se–1.5×10^{18}	Se–1.2×10^{18}	undoped	undoped

substrate, while Barrier No.2 corresponds to the barrier adjacent to the top electrode. It should be noted that the GaAs quantum well is nominally undoped in all the samples. However, the barriers are doped p–type with Mg in a number of MOCVD grown structures. This is because better sample quality and experimental results were originally obtained when the barrier layers were doped p–type than when they were doped n–type or nominally undoped.

The structures listed in Tables 4.1 and 4.2 may be classified into two categories. The first type includes samples fabricated to study the fundamental electronic properties of resonant tunneling heterostructures as two–terminal devices. These samples may be divided further into those having $Al_xGa_{1-x}As$ barrier layers (489, H943, H945, S009), and those with pure AlAs tunnel barriers (H283, H392, H408, H418, H475, H919, H927). Although it did not always result to be so in practice, these structures were intended to be grown symmetrically. All of them were fabricated on [100]–oriented n^+–GaAs substrates. A first epitaxial layer of degenerate n^+–GaAs was grown 2–3 μm thick. It was followed by two thin layers of $Al_xGa_{1-x}As$ or pure AlAs, separated by a layer of GaAs forming the quantum well. Finally, a GaAs top layer was grown, degenerately doped n–type. The electrode doping densities given in Table 4.2 were obtained from Polaron doping profiles. The doping concentrations in the quantum barriers and well were estimated from the flow rates (MOCVD) or beam fluxes (MBE) used during growth. They could thus be in error due to background doping and dopant memory effects, and to the difficulty of accurately calibrating ultra–thin layer doping levels. Furthermore, it has been reported that the level of electrical activity of Mg as a p–type dopant is very low in GaAs but increases rapidly with Al composition in $Al_xGa_{1-x}As$.[17] As a result, a given Mg flow rate is expected to produce larger p–type barrier doping concentrations when pure AlAs is grown than when a small Al content is used. To be consistent, it was assumed,

whenever possible, that the p–type barrier doping densities were the same in all heterostructures grown with a given Al composition in the barrier layers. As indicated in Table 4.2, a value of $2 \times 10^{17} cm^{-3}$ was taken in samples having Mg–doped $Al_{0.35}Ga_{0.65}As$ barriers (H943, H945, S009). In structures with pure AlAs layers, the barrier doping concentration was assumed to be $6 \times 10^{17} cm^{-3}$, except in H283 and H475. For both samples, this value was found to be inconsistent with experimental results, and the AlAs barrier doping level was taken to be $2 \times 10^{17} cm^{-3}$ only. The second category of samples includes heterostructures fabricated to study our first three–terminal resonant tunneling devices (S008, S031, S032). These structures are characterized by a low doped GaAs buffer layer grown between the degenerately doped GaAs electrode adjacent to the substrate and the first $Al_xGa_{1-x}As$ barrier layer (Barrier No.1). For these samples, the Al composition and doping density in the quantum barriers, as well as the average doping level in the back cladding layer listed in Tables 4.1 and 4.2 are estimated values. These values were taken to be consistent with the peak positions of the negative differential resistances observed in the experimental I–V characteristics of the heterostructures.

Section 4.2 presents the theoretical approach by which the energy band diagrams of resonant tunneling double barrier heterostructures are calculated and used to identify the resonances in the quantum well producing the experimental negative differential resistances. In section 4.3, the validity of the model is illustrated in the case of samples having direct band gap $Al_xGa_{1-x}As$ barrier layers. In these structures, tunneling occurs unambiguously via resonant states in the GaAs quantum well bound by the $Al_xGa_{1-x}As$ Γ–point potential energy barriers. In section 4.4, the same approach is applied to GaAs/AlAs double barrier heterostructures. Experimental evidence is shown of resonant tunneling via quasi–stationary levels in the well confined by the AlAs X–point potential energy

barriers as well as the AlAs Γ–point barriers. Section 4.5 discusses the relative contributions to the total current of tunneling via resonant Γ– and X–states in the well. These contributions are found to vary from sample to sample. In certain structures, they also depend upon the sign of the applied bias. Such results suggest that these contributions should be related primarily to the quality of the materials and the heterojunction interfaces. The samples of the second kind (S008, S031, S032) are presented in section 4.6. For these heterostructures, the peak positions of the negative differential resistances corresponding to a given quasi–stationary level in the well are observed at very different applied voltages in forward bias than in reverse bias. This may be used to estimate the degree of asymmetry in the cladding layer doping densities. Finally, the results of this study are summarized in section 4.7.

4.2 Theoretical Model

The theoretical approach used to calculate the energy band diagrams of resonant tunneling heterostructures is similar to that developed in Chapter 2 for single barrier tunnel structures. Energy band profiles are obtained by solving Poisson's equation in the direction perpendicular to the planes of the layers. A major approximation is made in that neither the two–dimensional energy subbands in accumulation layers nor the quasi–stationary states in the quantum well are solved for self–consistently along with the energy band edges. This arises from the complexity of calculating the proper charge distributions on subband levels and the difficulty of evaluating the amount of charge localized in the well.

Once the band edges and the voltage drops have been determined in each layer, the resonant states in the quantum well are found in the quasi–classical approximation.[18] In this approach, the transfer–matrix technique for a general

potential energy function $E_p(x)$ is used to calculate the transmission coefficient for resonant tunneling through the double barrier heterostructures. The energies of the quasi–stationary states in the quantum well are then determined implicitly from the condition for resonance:

$$\int_a^b k(x)\,dx = arctan\left(\frac{m_w^*}{m_l^*}\frac{\rho_l(a)}{k(a)}\right) + arctan\left(\frac{m_w^*}{m_r^*}\frac{\rho_r(b)}{k(b)}\right) + (n-1)\,\pi\,, \quad n = 1, 2, ... \tag{4.1}$$

where $k(x) \equiv \sqrt{\frac{2m_w^*}{\hbar^2}[E - E_p(x)]}$ denotes the electron wave vector in the well; $\rho_i(x) \equiv \sqrt{\frac{2m_i^*}{\hbar^2}[E_p(x) - E]}$ is the attenuation constant in barrier i; a and b correspond to the classical turning points in the quantum well at the energy E of the tunneling electron; and the subscripts l and r indicate the left and right barriers, respectively.

When the barrier layers are made of direct band gap alloys, the resonances in the GaAs well are determined by the $Al_xGa_{1-x}As$ Γ–point potential energy barriers. However, for large Al compositions ($x > 0.40$–0.45), $Al_xGa_{1-x}As$ becomes indirect, and three sets of resonant states may be calculated in the quantum well. First, these states may be quasi–stationary levels confined by the $Al_xGa_{1-x}As$ Γ–point potential energy barriers. They may be called "quasi–bound Γ–states." Other quasi–stationary states of interest are those which are confined by the $Al_xGa_{1-x}As$ X–point potential energy barriers and correspond to the large longitudinal X–point electron mass in $Al_xGa_{1-x}As$. These levels should be considered because the breaking of translational symmetry in the direction perpendicular to the heterojunction interfaces allows $Al_xGa_{1-x}As$ X–point states to couple to GaAs Γ–point states.[19] The other resonances to consider in the GaAs quantum well are those which are bound by the $Al_xGa_{1-x}As$ X–point potential energy barriers and correspond to the small transverse X–point effective mass in $Al_xGa_{1-x}As$. These levels should be considered if electrons are allowed to scatter into virtual states beneath the four $Al_xGa_{1-x}As$ X–valleys lying along the k_y–

and k_z–directions, parallel to the planes of the interfaces.[19]

Once the energy band diagrams and the quasi–stationary levels in the GaAs well have been calculated using the simple model described above, it becomes possible to identify the resonances giving rise to the negative differential resistances observed in experimental *I–V* characteristics. This is particularly useful in studying the nature of the dominant current transport mechanisms taking place in double barrier heterostructures.

4.3 Resonant Tunneling in Structures with Direct Band Gap $Al_xGa_{1-x}As$ Barrier Layers

The validity of the theoretical approach presented in section 4.2 may be illustrated in the case of structures having direct band gap $Al_xGa_{1-x}As$ barrier layers. In this instance, the peaks in current obtained in the low voltage regions of the *I–V* curves may be attributed without ambiguity to resonant tunneling via quasi–bound Γ–states in the GaAs quantum well.[9]

Sample S009 is a double barrier heterostructure having $Al_{0.35}Ga_{0.65}As$ quantum barriers. These barriers are 59.5 Å thick (21 monolayers), and their *p*–type doping concentration is estimated to be $2 \times 10^{17} cm^{-3}$. The GaAs electrodes are degenerately doped *n*–type with Se at $1.2 \times 10^{18} cm^{-3}$. The nominally undoped GaAs quantum well is 51 Å wide (18 monolayers). Fig.4.1 depicts an experimental *I–V* characteristic at 4.2 K for a circular device, 50 μm in diameter. One negative differential resistance appears in each bias direction. The peak currents correspond to applied voltages of ± 255 mV. The valley currents occur at about ± 300 mV. The inflections observed in the regions with negative slopes arise from the difficulty of performing stable curve tracer measurements of negative differential resistances. For the structures discussed in this study, reverse bias ($V_a < 0$)

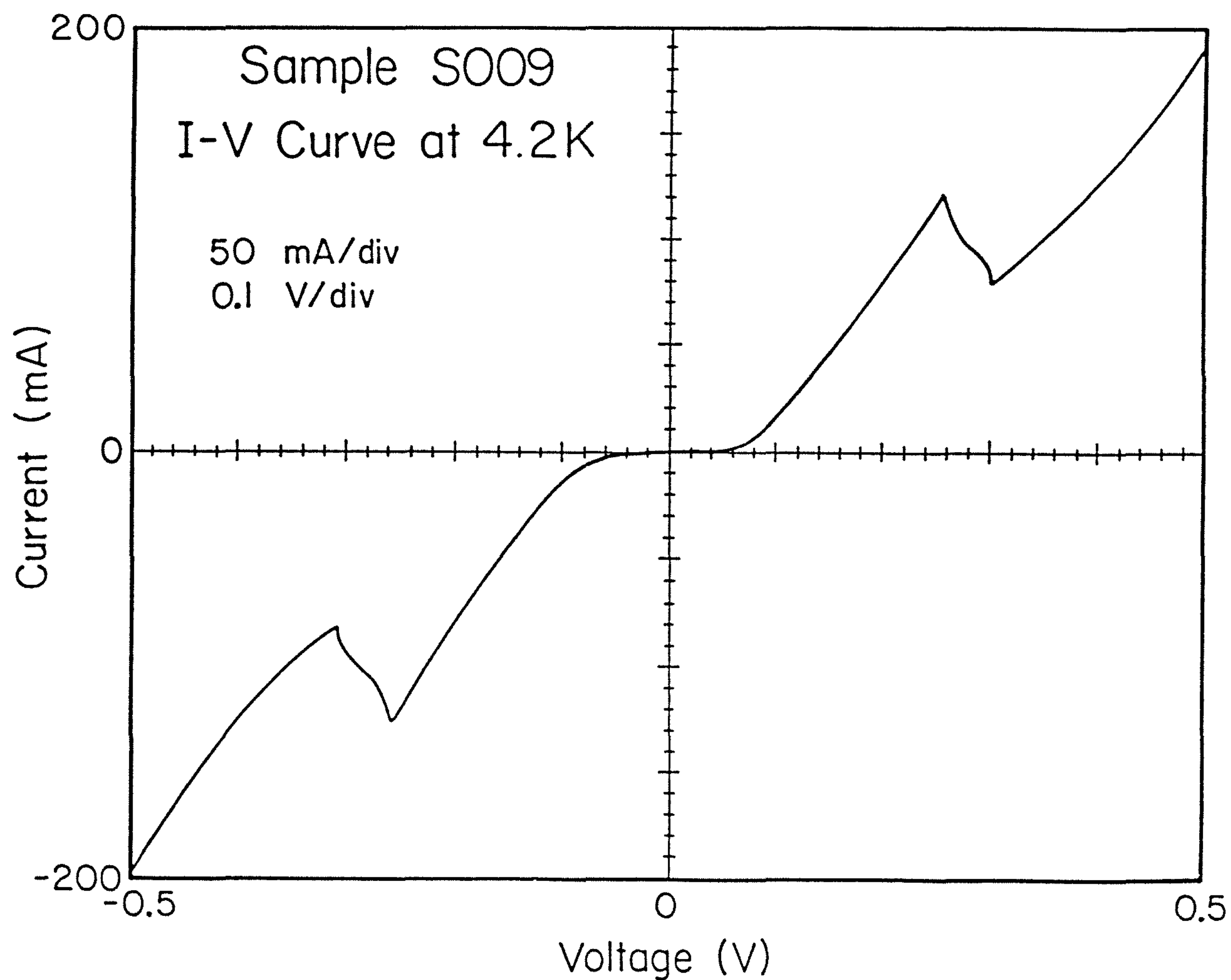

Figure 4.1: Experimental *I–V* characteristic at 4.2 K for a circular device, 50 μm in diameter, fabricated on a GaAs/$Al_{0.35}Ga_{0.65}As$ double barrier heterostructure (sample S009). The GaAs electrodes are degenerately doped n–type with Se at $1.2 \times 10^{18} cm^{-3}$. The 59.5 Å thick barrier layers are doped p–type with Mg at $2 \times 10^{17} cm^{-3}$. The nominally undoped GaAs quantum well is 51 Å wide.

corresponds to a negative voltage applied to the top GaAs electrode with respect to the substrate. Figs.4.2(a) and (b) show calculated conduction band edges for the same heterostructure under applied biases of -60 and -255 mV, respectively. In GaAs ($Al_{0.35}Ga_{0.65}As$), the low temperature band gap is assumed to be 1.52 eV (1.96 eV), the effective mass is taken to be $0.067\,m_0$ ($0.096\,m_0$), and the relative dielectric constant is 13.18 (12.05).[20] A valence band discontinuity of $(0.55 \times x)$ eV is assumed at GaAs/$Al_xGa_{1-x}As$ interfaces,[21] resulting here in a conduction band offset of 245 meV. Using these values, two resonant states are found in the GaAs quantum well in the unbiased structure. Their energies, measured from the conduction band edge at the middle of the well, are $E_1^\Gamma = 73$ meV for the ground state, and $E_2^\Gamma = 242$ meV for the first excited state. These values are listed in Table 4.3. At low applied voltages, ($|V_a| < 60$ mV), E_1^Γ remains above the Fermi energy E_f^i in the incident electrode and the current is very small. As shown in Fig.4.2(a), E_1^Γ lines up with E_f^i when $|V_a| = 60$ mV. At this point, resonant tunneling via E_1^Γ is initiated. This corresponds to the turn–ons in current observed in Fig.4.1. As $|V_a|$ becomes larger, more electrons may tunnel resonantly via the subband associated with E_1^Γ, and the current increases rapidly. Fig.4.2(b) indicates that $E_c^i(x = 0)$, the conduction band edge in the incident GaAs electrode at the first heterojunction interface, coincides in energy with E_1^Γ when $|V_a| = 255$ mV. At higher applied voltages, $E_c^i(x = 0) > E_1^\Gamma$, and it becomes impossible for an electron tunneling through the ground state subband to simultaneously conserve energy and the transverse component of its wave vector. It follows that the tunneling transmission coefficient is reduced and the current decreases. The results predicted by the energy band diagrams are thus in excellent agreement with the experimental data shown in Fig.4.1. They are summarized in Table 4.4. In fact, this agreement is surprisingly good considering the simplifying assumptions used in calculating the energy band profiles and the

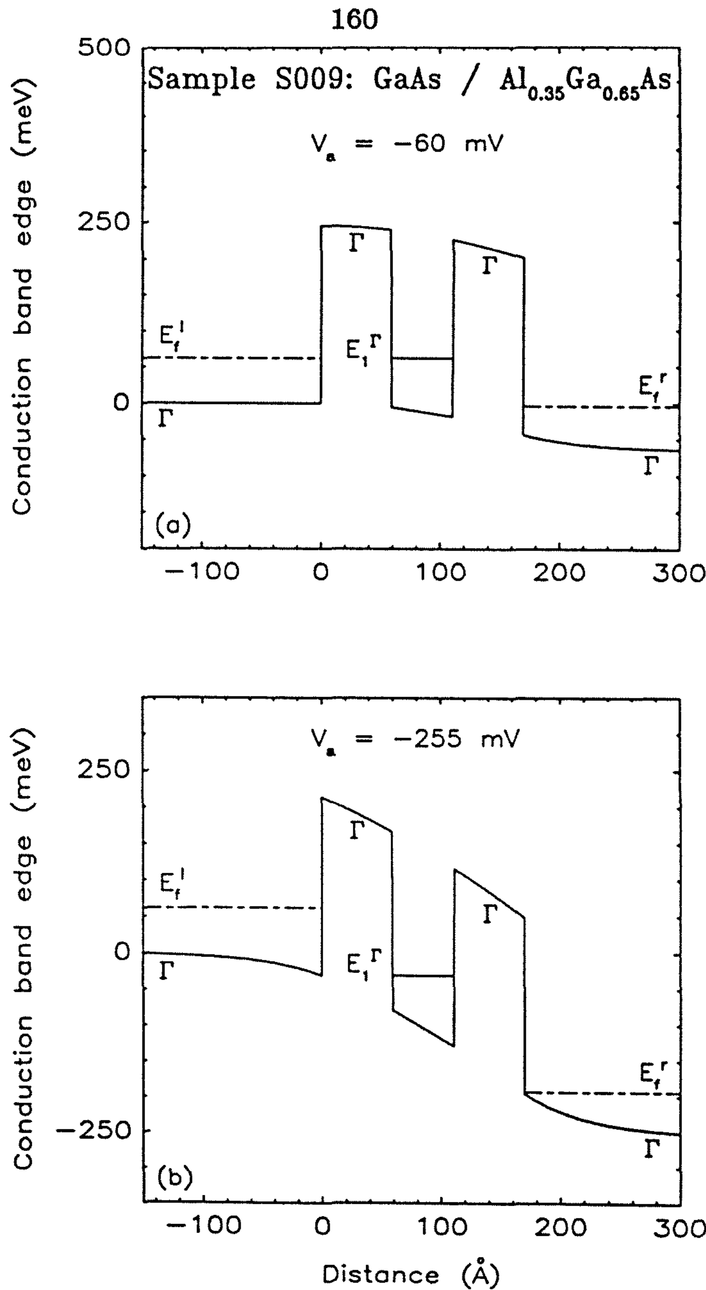

Figure 4.2: Calculated Γ–point conduction band edges, as functions of distance in the direction perpendicular to heterojunction interfaces, for the same heterostructure as in Fig.4.1 (sample S009). (a) and (b) correspond to applied biases of −60 and −255 mV, respectively. The Fermi level in the left (right) GaAs electrode is E_f^l (E_f^r). The conduction band discontinuity at the heterojunction interfaces is taken to be 245 meV. E_1^Γ denotes the first resonant state in the quantum well confined by the $Al_{0.35}Ga_{0.65}As$ Γ–point potential energy barriers.

uncertainties within which the band offsets and the barrier doping densities are known.

The energy band diagrams depicted in Fig.4.2 reveal that the shapes of the band edges may deviate significantly from those obtained when band bending is neglected. In particular, an accumulation layer adjacent to the first heterojunction interface is formed in the incident electrode when the structure is sufficiently biased. It follows that the number of available incident carriers increases with $|V_a|$. Furthermore, if $E_c^b(x = 0)$ denotes the barrier conduction band edge at $x = 0$, $\Delta E_{eff} \equiv E_c^b(x = 0) - E_f^i$, the effective conduction band offset for electrons tunneling near the Fermi energy E_f^i, is a decaying function of $|V_a|$. When band bending is ignored, the bands remain flat in the cladding layers, ΔE_{eff} is constant, and the number of available incident electrons is independent of V_a. The resonant states in the well, the tunneling transmission coefficients and the theoretical I–V curves calculated using these two approaches are thus expected to be different. For example, if band bending is neglected and the entire applied voltage is assumed to drop linearly across the barriers and well in the heterostructure illustrated in Figs.4.1 and 4.2, resonant tunneling via E_1^Γ should be initiated at about ± 25 mV instead of ± 60 mV. Similarly, the peaks in current should occur at approximately ± 150 mV, and not at ± 255 mV. This demonstrates that band bending effects and cladding layer voltage drops are important in interpreting the experimental results.

The energy band profiles shown in Fig.4.2 indicate further that negative differential resistances are obtained when $E_c^i(x = 0)$, the conduction band edge in the incident electrode at the first heterojunction interface, coincides in energy with the quasi–stationary states in the quantum well. In fact, two–dimensional energy subbands exist in accumulation layers, and the peaks in current should occur when the resonances in the well line up with the lowest two–dimensional

subband. However, the GaAs electrodes in the heterostructures studied are usually heavily doped. Consequently, the accumulation layers are not very large and the role of subband levels is reduced. Furthermore, as long as the resonances are not too high in energy, the negative differential resistances are obtained at reasonably low applied biases, and the accumulation layer in the incident electrode remains small. As a result, the error introduced by neglecting the two–dimensional subbands which exist near the first heterojunction interface should not be significant. This is the case in Fig.4.2(b). However, for high energy states in the well, this error is expected to become larger. The fact that the peaks in current occur when the quasi–stationary levels in the GaAs well coincide in energy with $E_c^i(x = 0)$ may also be due to band tailing effects in the degenerately doped electrodes. These effects are difficult to evaluate quantitatively. Nevertheless, because electronic states exist in the cladding layers right below the conduction band edges, the peaks in current may actually occur when these states line up with the resonances in the quantum well. Band tailing effects may also be related to the widths of the negative differential resistances observed in the I–V characteristics.

Other heterostructures having direct band gap $Al_xGa_{1-x}As$ barrier layers have been studied using the same approach. They are briefly discussed below. Sample 489 was fabricated by MBE with nominally undoped quantum barriers and well. The GaAs electrodes are degenerately doped n–type with Si at $1\times10^{18}cm^{-3}$. The GaAs quantum well and $Al_{0.35}Ga_{0.65}As$ barrier layers were grown to be approximately 50 and 80 Å thick, respectively. However, no TEM measurements were performed on this sample, and energy band diagram calculations actually predict that the GaAs quantum well should be narrower than 50 Å. Fig.4.3 depicts an experimental I–V curve at 4.2 K for a circular device, 50 μm in diameter. One negative differential resistance is obtained in each bias direction. Since the I–V

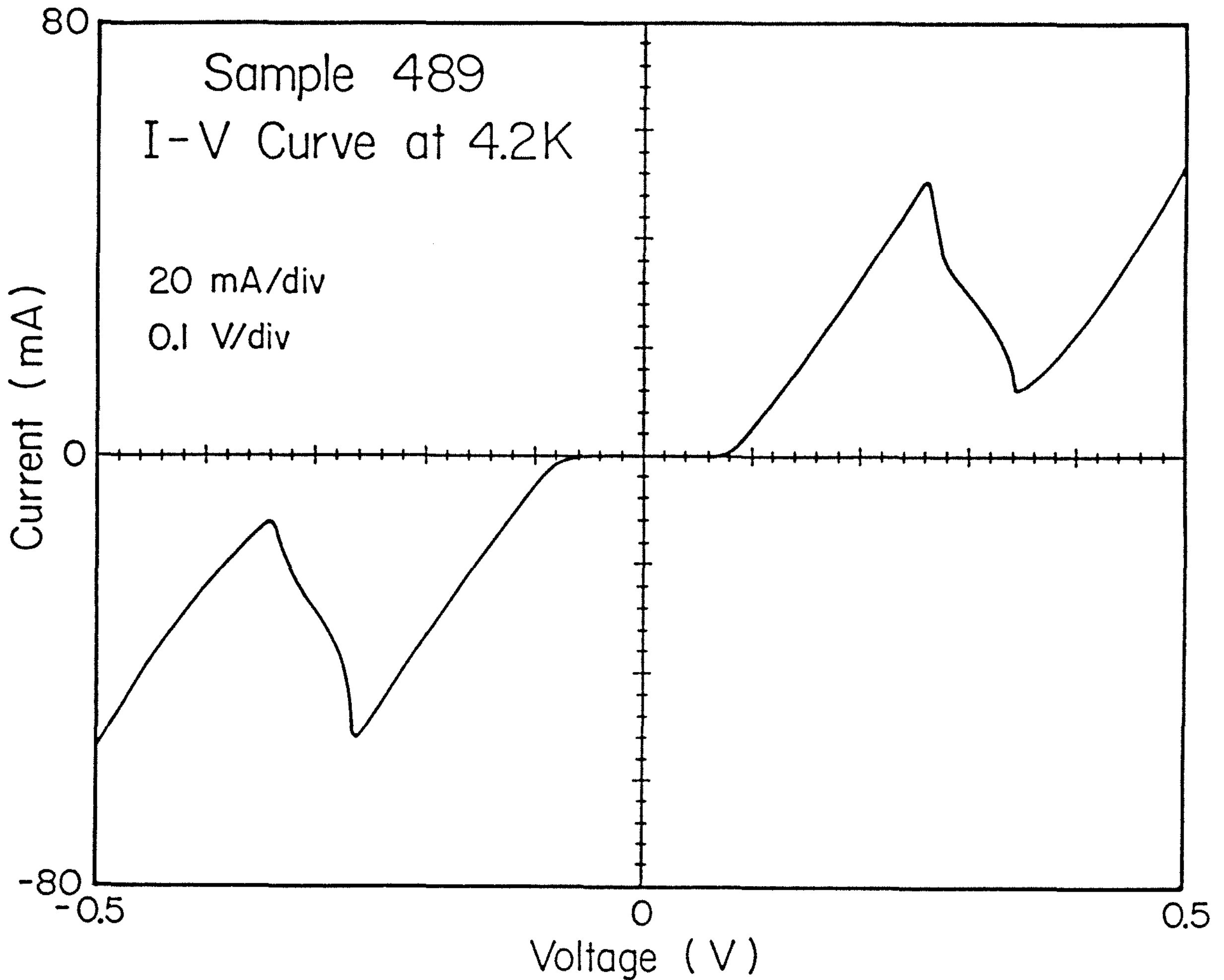

Figure 4.3: Experimental *I–V* characteristic at 4.2 K for a circular device, 50 μm in diameter, fabricated on sample 489. 489 is an MBE grown $GaAs/Al_{0.35}Ga_{0.65}As$ double barrier heterostructure. The GaAs electrodes are degenerately doped n–type with Si at $1 \times 10^{18} cm^{-3}$. The GaAs quantum well and the 79 Å thick barrier layers are nominally undoped.

characteristic is symmetric with respect to the origin, the structure itself must be symmetric. The I–V curve reveals that resonant tunneling is initiated at about ± 75 mV and turns off at ± 260 mV. If the GaAs well is assumed to be 48 Å wide (17 monolayers), one quasi–bound Γ–state is found in the unbiased structure, 77 meV above the bottom of the well. However, energy band diagram calculations indicate that in order to obtain turn–on voltages of ± 75 mV and turns–off voltages of ± 260 mV in the I–V characteristics, the corresponding resonant level should lie about 90 meV above the bottom of the well in the unbiased structure. If the well is taken to be 42.5 Å wide (15 monolayers), $E_1^\Gamma = 89$ meV, and the energy band profile illustrated in Fig.4.4(a) reveals that E_1^Γ lines up with E_f^l precisely when $V_a = -75$ mV. Similarly, Fig.4.4(b) shows that E_1^Γ coincides in energy with $E_c^l(x = 0)$ when $V_a = -260$ mV. These results, which are summarized in Tables 4.3 and 4.4, thus indicate that the GaAs quantum well must be narrower than expected from the growth parameters. They also suggest that the well thicknesses of resonant tunneling double barrier heterostructures may be determined from the experimental I–V data and the energy band diagrams of the structures.

Sample H943 is an MOCVD grown heterostructure in which the GaAs electrodes are degenerately doped n–type with Se at about $1 \times 10^{18} cm^{-3}$. The p–type doping concentration in the $Al_{0.35}Ga_{0.65}As$ barrier layers is taken to be $2 \times 10^{17} cm^{-3}$. The barriers are 59.5–62 Å thick (21–22 monolayers). The nominally undoped GaAs quantum well is 31–36.5 Å wide (11–13 monolayers). These fluctuations in layer thicknesses cause the experimental I–V characteristics to be non uniform. In fact, a number of I–V curves display sequences of negative differential resistances in each bias direction. This indicates that the corresponding devices include areas of the sample characterized by different barrier and well

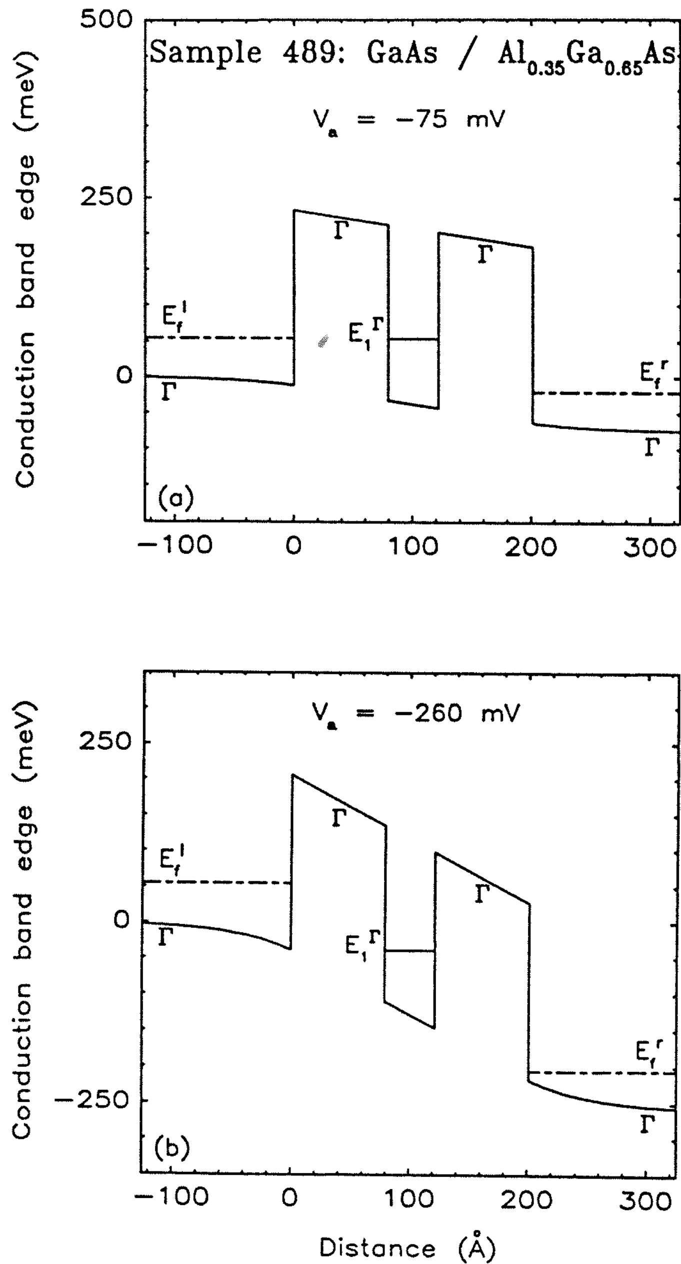

Figure 4.4: Calculated Γ–point conduction band edges for sample 489. (a) and (b) correspond to applied biases of −75 and −260 mV, respectively. E_1^Γ denotes the resonant state in the quantum well confined by the $Al_{0.35}Ga_{0.65}As$ Γ–point potential energy barriers.

thicknesses. However, a number of small devices feature uniform and symmetric I–V curves. This is the case in Fig.4.5. As indicated in Table 4.3, if the GaAs well is taken to be 34 Å wide (12 monolayers), only one quasi–bound Γ–state is found, 110 meV above the bottom of the well in the unbiased structure. The energy band profiles depicted in Fig.4.6 show that E_1^Γ then lines up with E_f^i and $E_c^i(x = 0)$ when $V_a = \pm 150$ and $V_a = \pm 420$ mV, respectively. These values agree with the turn–on and turn–off voltages of resonant tunneling observed in Fig.4.5.

Sample H945 is similar to H943. Its parameters are listed in Tables 4.1 and 4.2. In this structure, the barrier thicknesses range between 51 and 59.5 Å (18–21 monolayers), and the width of the GaAs quantum well varies between 25.5 and 28.5 Å (9–10 monolayers). As in H943, these fluctuations result in non–uniform experimental I–V characteristics. However, Fig.4.7 depicts a symmetric I–V curve at 4.2 K for a circular device, 50 μm in diameter. The energy band diagrams displayed in Fig.4.8 correspond to a 25.5 Å wide GaAs well. They indicate that resonant tunneling via E_1^Γ is initiated when $V_a = \pm 170$ mV, and that peaks in current are expected in the I–V characteristics at ± 550 mV. These results agree with the experimental data shown in Fig.4.7. They are summarized in Table 4.4.

It may be concluded from the above discussions that good agreement may be found between the experimental I–V curves and the quasi–bound Γ–states in the well provided that the energy band profiles of the heterostructures are used. This confirms the importance of taking into account the voltage drops in all the layers and the actual shapes of the band edges. Energy band diagrams should thus be essential in interpreting the experimental results obtained from samples having indirect band gap $Al_xGa_{1-x}As$ barrier layers, and in which the tunnel-

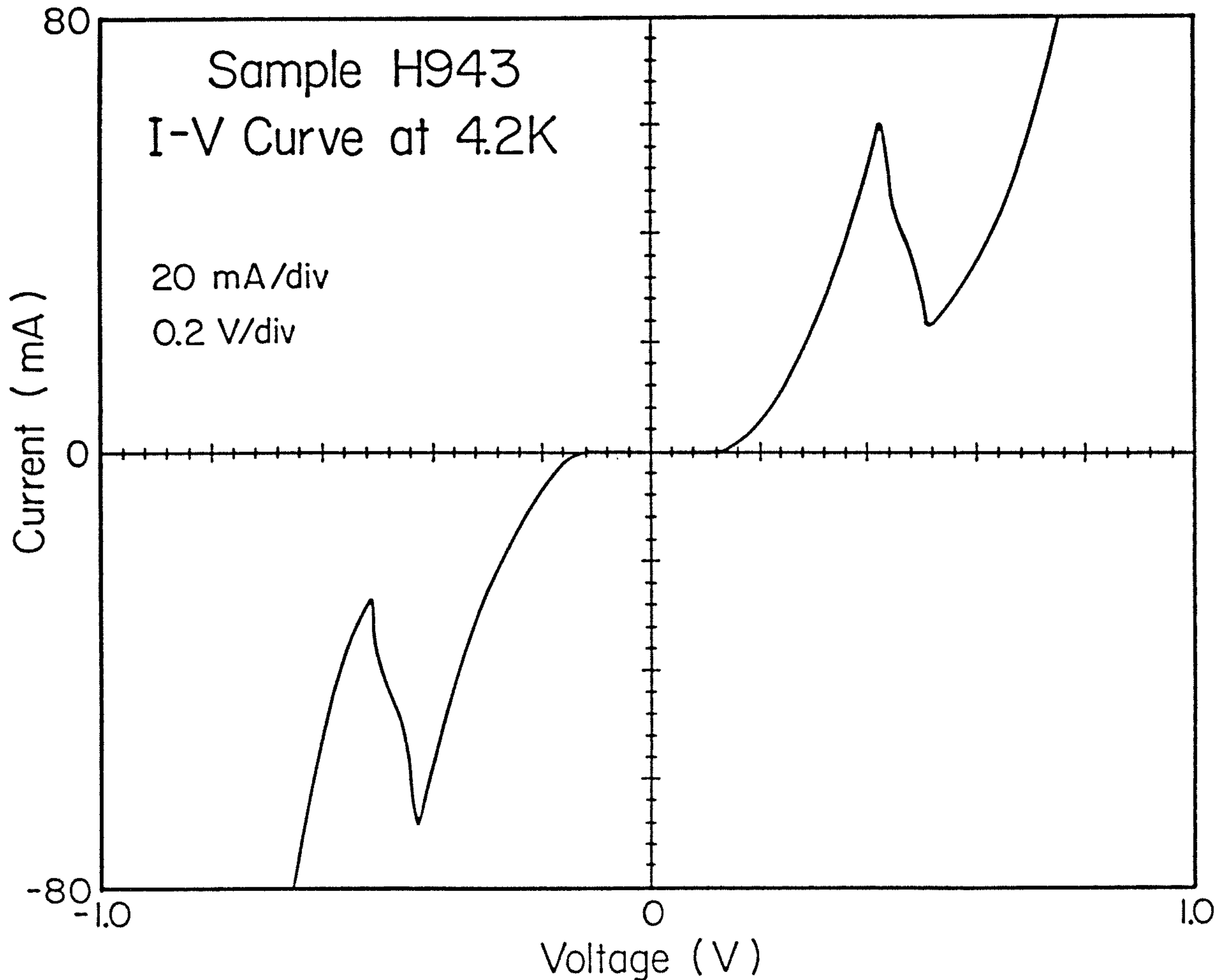

Figure 4.5: Experimental *I–V* characteristic at 4.2 K for a circular device, 50 μm in diameter, fabricated on sample H943. H943 is an MOCVD grown GaAs/$Al_{0.35}Ga_{0.65}As$ double barrier heterostructure. The GaAs electrodes are degenerately doped n–type with Se at $1 \times 10^{18} cm^{-3}$. The barrier layers are 59.5–62 Å thick. They are doped p–type with Mg at $2 \times 10^{17} cm^{-3}$. The nominally undoped GaAs quantum well is 31–36.5 Å wide.

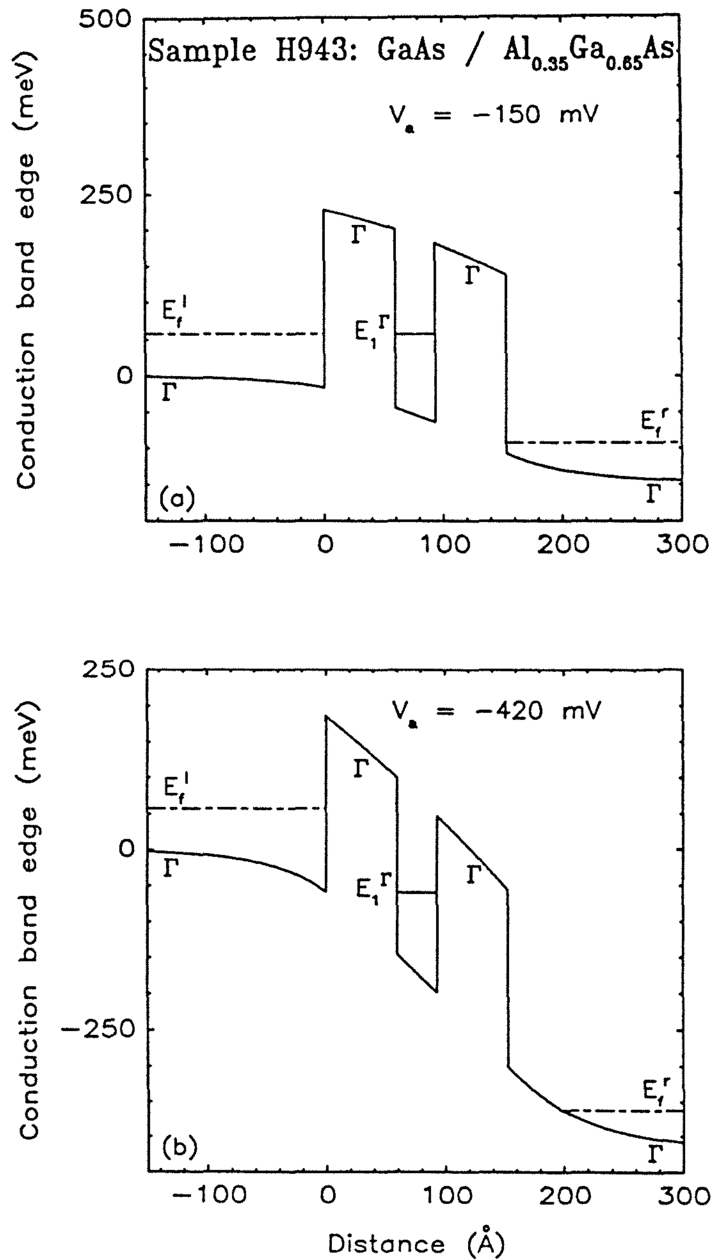

Figure 4.6: Calculated Γ–point conduction band edges for sample H943. (a) and (b) correspond to applied biases of −150 and −420 mV, respectively. E_1^{Γ} denotes the resonant state in the quantum well confined by the $Al_{0.35}Ga_{0.65}As$ Γ–point potential energy barriers.

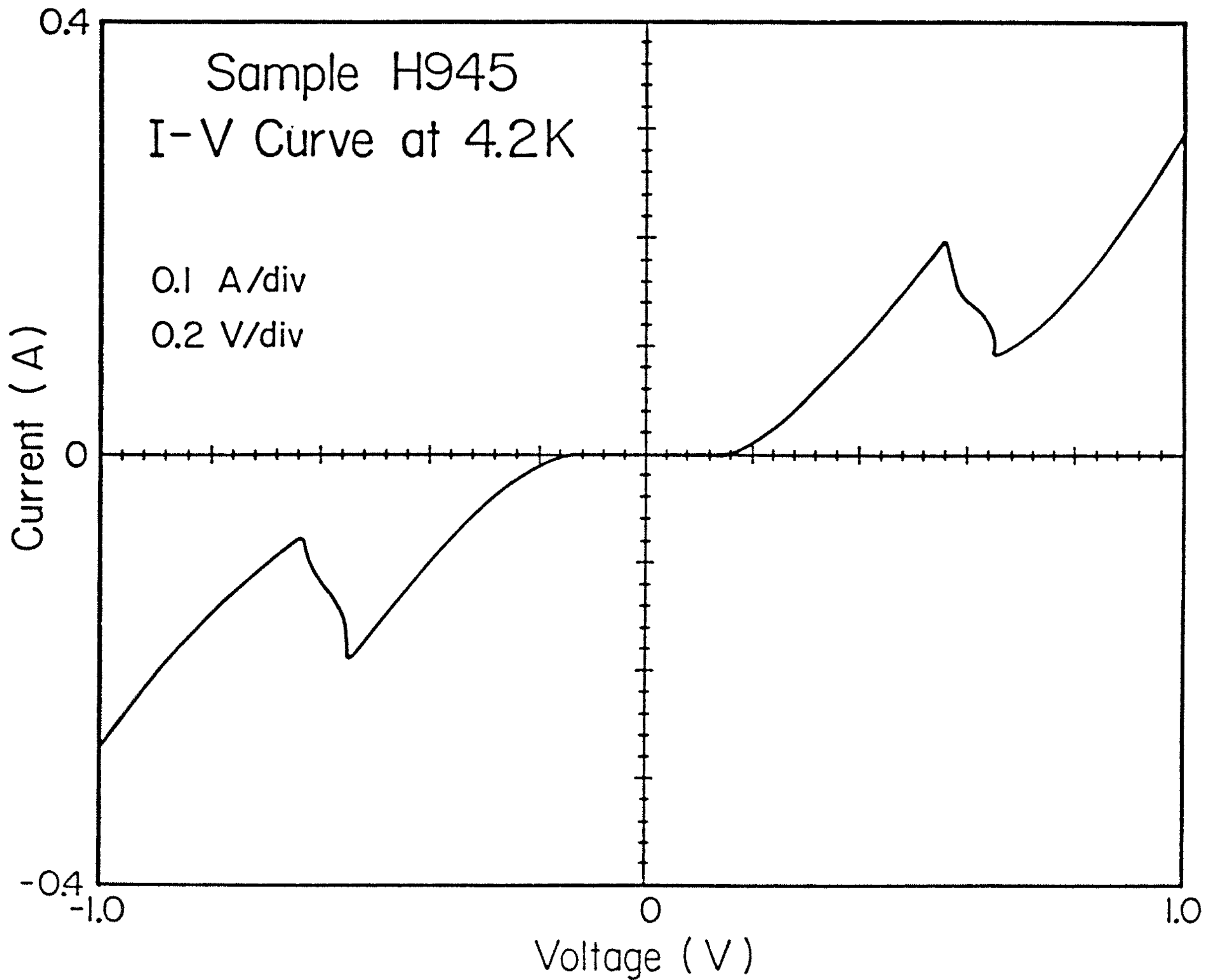

Figure 4.7: Experimental *I–V* characteristic at 4.2 K for a circular device, 50 μm in diameter, fabricated on sample H945. H945 is an MOCVD grown GaAs/$Al_{0.35}Ga_{0.65}As$ double barrier heterostructure. The GaAs electrodes are degenerately doped *n*–type with Se at $1.3 \times 10^{18} cm^{-3}$. The barrier layers are 51–59.5 Å thick. They are doped *p*–type with Mg at $2 \times 10^{17} cm^{-3}$. The nominally undoped GaAs quantum well is 25.5–28.5 Å wide.

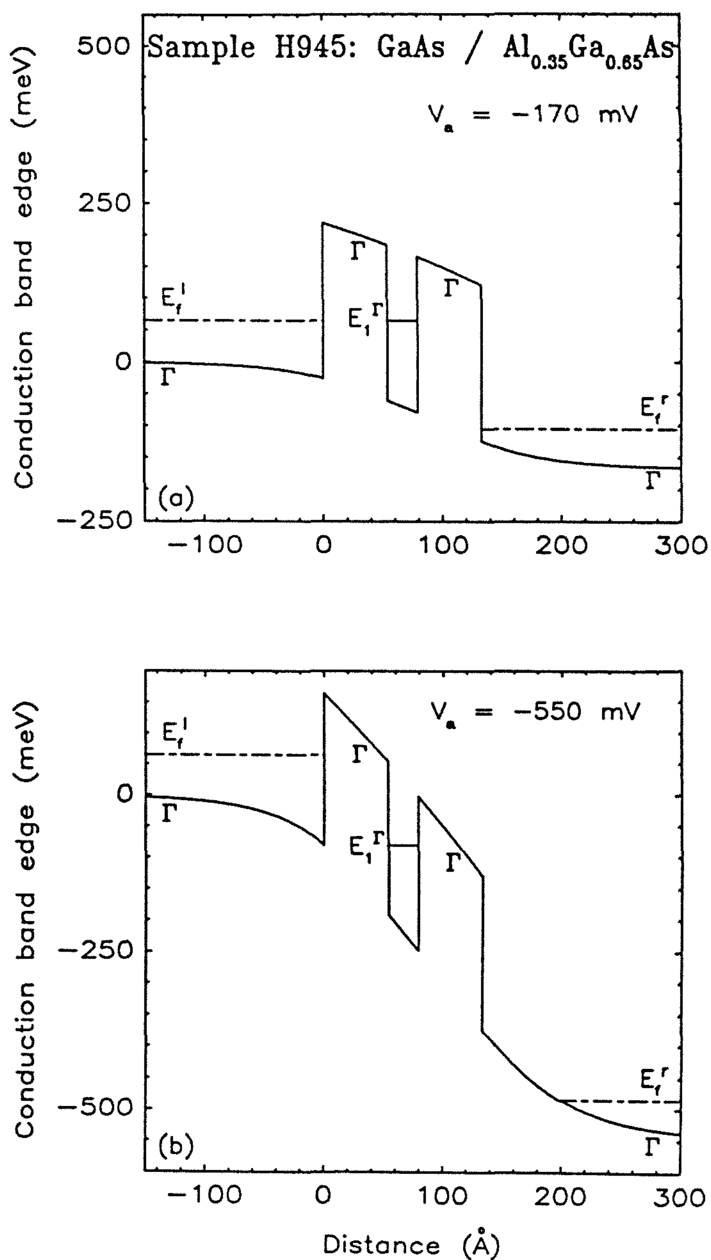

Figure 4.8: Calculated Γ–point conduction band edges for sample H945. (a) and (b) correspond to applied biases of −170 and −550 mV, respectively. E_1^Γ denotes the resonant state in the quantum well confined by the $Al_{0.35}Ga_{0.65}As$ Γ–point potential energy barriers.

ing mechanisms are more complex than in structures with direct $Al_xGa_{1-x}As$ quantum barriers.

4.4 Resonant Tunneling in Structures with Indirect Band Gap $Al_xGa_{1-x}As$ Barrier Layers

This section shows experimental evidence of resonant tunneling via quasi–stationary X–point states in GaAs/AlAs double barrier heterostructures grown epitaxially in the [100]–direction. As before, the quantum well resonant energy levels giving rise to the negative differential resistances observed in the experimental I–V characteristics are identified by calculating the energy band profiles of the structures. These resonant energy levels correspond to states confined in the GaAs well not only by the AlAs Γ–point potential energy barriers but also by the AlAs X–point barriers. The quasi–bound X–states are associated with the large longitudinal effective mass in AlAs corresponding to the direction perpendicular to the heterojunction interfaces.

In sample H927, the doping densities in the GaAs electrodes are slightly asymmetric: $1.5 \times 10^{18} cm^{-3}$ in the top cladding layer and $1.3 \times 10^{18} cm^{-3}$ in the electrode adjacent to the substrate. The nominally undoped GaAs well is 45 Å wide (16 monolayers). The p–type doping concentration in the AlAs layers is estimated to be $6 \times 10^{17} cm^{-3}$. The AlAs barrier closer to the substrate is 71 Å thick (25 monolayers). The other barrier is 85 Å thick (30 monolayers). This asymmetry in barrier thicknesses should cause a given resonance in the well to be manifested at a larger applied voltage in forward bias than in reverse bias ($|V_a^F| > |V_a^R|$). Fig.4.9 shows an experimental I–V characteristic at 4.2 K for a circular device, 50 μm in diameter. Two weak negative differential resistances exist in each bias direction. In forward bias, the peak currents occur at $V_1^F = 240$

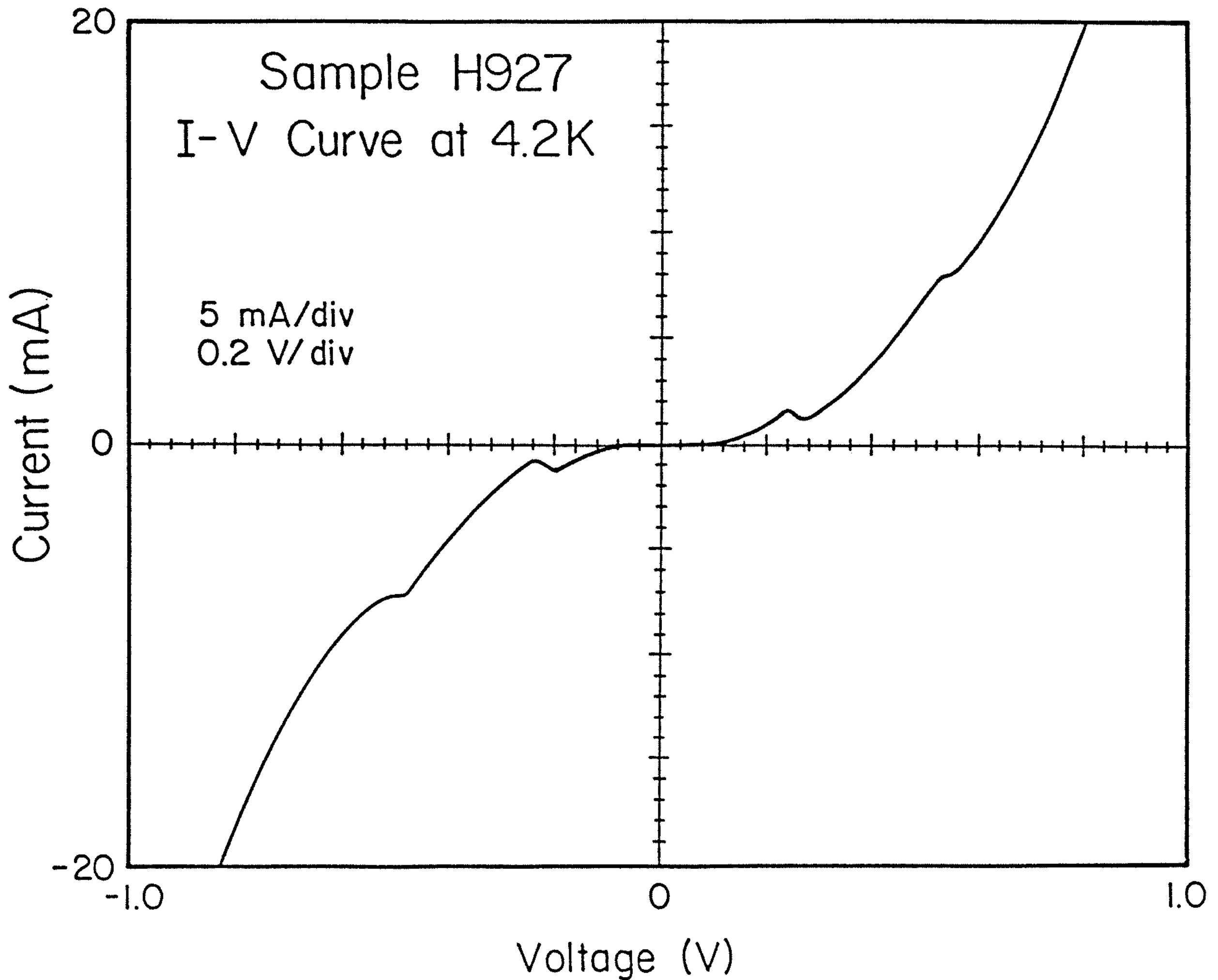

Figure 4.9: Experimental I–V characteristic at 4.2 K for a circular device, 50 μm in diameter, fabricated on sample H927. H927 is a GaAs/AlAs double barrier heterostructure in which the nominally undoped GaAs quantum well is 45 Å wide. The doping densities in the n–type GaAs electrodes are $1.5 \times 10^{18} cm^{-3}$ in the top cladding layer and $1.3 \times 10^{18} cm^{-3}$ in the electrode adjacent to the substrate. The barrier layers are doped p–type with Mg at $6 \times 10^{17} cm^{-3}$. The AlAs barrier closer to the substrate is 71 Å thick. The other barrier is 85 Å thick.

mV and $V_2^F = 530$ mV. In reverse bias, they take place at $V_1^R = -200$ mV and $V_2^R = -480$ mV. The I–V curve also reveals that resonant tunneling is initiated at approximately ± 100 mV. To calculate the resonant states in the well confined by the AlAs Γ–point potential energy barriers, the effective mass in AlAs is taken to be $m_\Gamma^* = 0.15\, m_0$,[20] and the conduction band offsets at the heterojunction interfaces are assumed to be 1.04 eV.[21] Using these values, two quasi–bound Γ–states are found in the unbiased structure, at energies $E_1^\Gamma = 125$ meV and $E_2^\Gamma = 517$ meV above the conduction band edge at the middle of the well. To obtain the states confined by the AlAs X–point potential energy barriers, the conduction band offsets are taken to be 0.19 eV.[21] When the large longitudinal X–point electron mass $m_{X_l}^* = 1.1\, m_0$ is used in the barriers, one quasi–stationary state, $E_1^X = 30$ meV, is found in the GaAs well. The level associated with the small transverse electron mass $m_{X_t}^* = 0.19\, m_0$ has an energy $\epsilon_1^X = 59$ meV from the bottom of the well. Two energy band profiles for the structure are illustrated in Fig.4.10. They correspond to reverse biases of -200 and -480 mV, respectively. Both Γ– and X–point conduction band edges are shown in the AlAs barriers. These energy band diagrams may be used to illustrate three fundamental properties of sample H927: (*i*) resonant tunneling via quasi–bound Γ–states alone is inconsistent with the experimental I–V data; (*ii*) energy band profiles are essential to properly account for the voltage drops in all the layers, and to identify without ambiguity the resonances in the well producing the negative differential resistances observed experimentally; and (*iii*) the sample I–V characteristics may be explained by resonant tunneling via E_1^X in addition to E_1^Γ.

If quasi–bound Γ–states alone are considered, the resonances of importance are E_1^Γ and E_2^Γ. These lie 125 and 517 meV above the conduction band edge at the middle of the well in the unbiased structure. If band bending is neglected and the

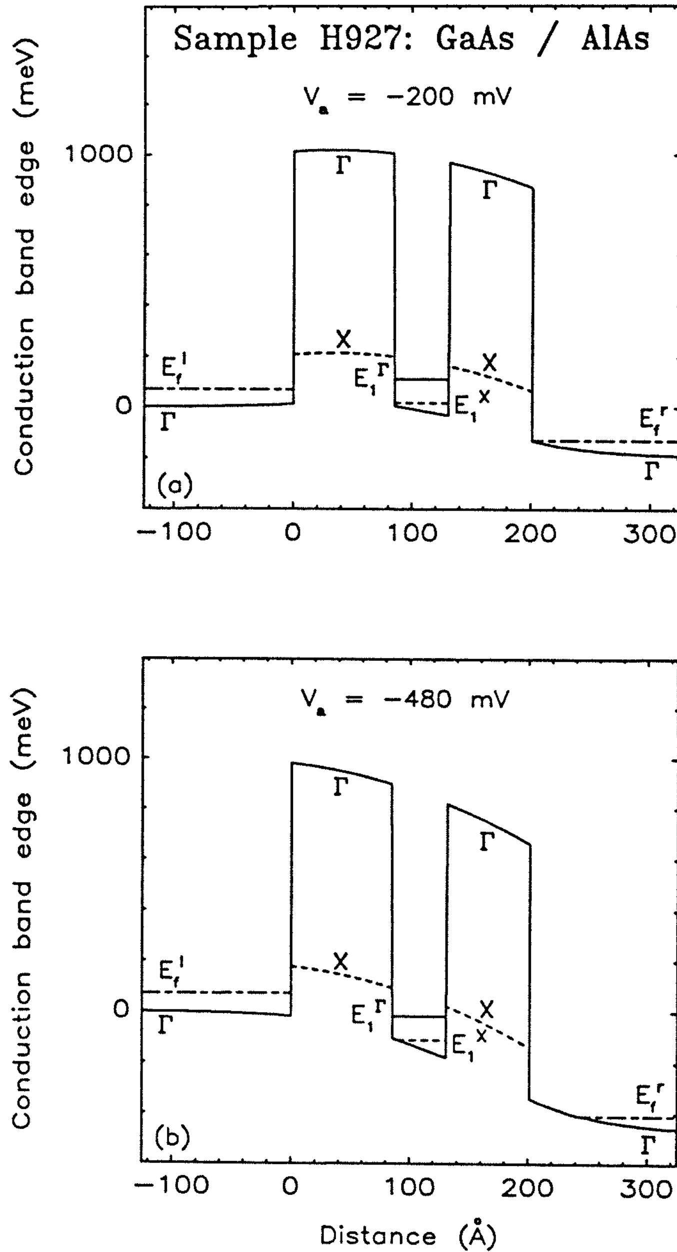

Figure 4.10: Calculated Γ–point (solid lines) and X–point (dashed lines) conduction band edges, for sample H927. The conduction band discontinuities at the heterojunction interfaces are 1.04 eV at the Γ–point and 0.19 eV at the X–point. In the GaAs quantum well, E_1^Γ (solid line) denotes the first quasi–bound Γ–state, and E_1^X (dashed line) is the resonant X–state corresponding to the large longitudinal AlAs X–point electron mass in the direction perpendicular to the interfaces.

entire applied voltage is assumed to drop linearly across the quantum barriers and well, the peaks in current corresponding to E_1^Γ should occur in the I–V curves at about ± 250 mV. This could be consistent with the negative differential resistances observed at -200 and 240 mV in Fig.4.9. However, E_2^Γ should appear in the I–V characteristics at voltages $|V_a| > 1$ V. This is in disagreement with the experimental results. If band bending is taken into account, the cladding layers sustain part of the applied bias. This reduces the amount of voltage dropping across the barriers and well. As a result, the disagreement with the experimental data becomes even larger than when band bending is neglected. It may thus be concluded that resonant tunneling via quasi–bound Γ–states alone is inconsistent with the sample I–V characteristics. However, the energy band diagram illustrated in Fig.4.10(b) indicates that in reverse bias, E_1^Γ lines up with $E_c^l(x = 0)$ when $V_a = -480$ mV. Similarly, energy band profile calculations reveal that the peak in current due to E_1^Γ should occur in forward bias at $V_a = 530$ mV. These values correspond precisely to the negative differential resistances observed in Fig.4.9 at V_2^R and V_2^F, respectively. The peaks in current at $V_1^R = -200$ mV and $V_1^F = 240$ mV should then necessarily correspond to a quasi–stationary X–state. Fig.4.10(a) reveals that E_1^X coincides in energy with $E_c^l(x = 0)$ when $V_a = -200$ mV. Similarly, the peak in current associated with E_1^X is anticipated in forward bias at $V_a = 240$ mV. Energy band diagrams also indicate that resonant tunneling via E_1^X should be initiated at -90 and 110 mV in reverse and forward bias, respectively. These results are in good agreement with the experimental data. It may thus be concluded that the negative differential resistances obtained in the I–V characteristics of sample H927 correspond to E_1^X, the quasi–stationary X–state associated with the large longitudinal X–point effective mass in the AlAs barriers, and E_1^Γ, the lower quasi–bound Γ–state. This is summarized in Table 4.5. Fig.4.9 reveals further that the two peaks in current

observed in each bias direction are comparable in size. This indicates that both resonances are equally important in current transport through sample H927. In fact, it is shown in section 4.5 that the relative contributions to the total current of resonant tunneling via quasi–stationary Γ– and X–states depend upon the structures studied.

These concepts are further illustrated on another double barrier heterostructure with pure AlAs barrier layers. In sample H408, the GaAs electrodes are doped n–type at $1.75 \times 10^{18} cm^{-3}$. The nominally undoped GaAs quantum well is 62 Å wide (22 monolayers). As in H927, the AlAs layers are doped p–type at $6 \times 10^{17} cm^{-3}$. The barrier closer to the substrate is 51 Å thick (18 monolayers), whereas the one adjacent to the top electrode is only 42 Å thick (15 monolayers). As a result of this asymmetry, a given resonant state in the well is manifested at a larger applied voltage in reverse bias than in forward bias ($|V_a^R| > |V_a^F|$). Fig.4.11 shows an experimental I–V characteristic at 4.2 K for a circular device, 20 μm in diameter. The I–V curve reveals that the first peaks in current occur at $V_1^F = 135$ mV in forward bias and $V_1^R = -140$ mV in reverse bias. Other resonances appear at 650 and -750 mV. The temperature dependence of the device I–V curves may be used to interpret the shapes of the broad negative differential resistances observed at $|V_a| < 280$ mV. At room temperature, inflections are visible at about ± 140 mV. As the temperature, T, is decreased, the low voltage regions of the I–V curves ($|V_a| < 140$ mV) remain almost identical, while the background current decays rapidly for larger values of $|V_a|$. As a result, the negative differential resistances become more pronounced. When T $\approx$ 200 K, two new small peaks appear at about ± 240 mV, next to the existing peaks at ± 140 mV. As T is further reduced, all the peaks become more prominent. This temperature dependence is illustrated in the insert of Fig.4.11. It should be mentioned that the I–V characteristics of other devices prepared on the same

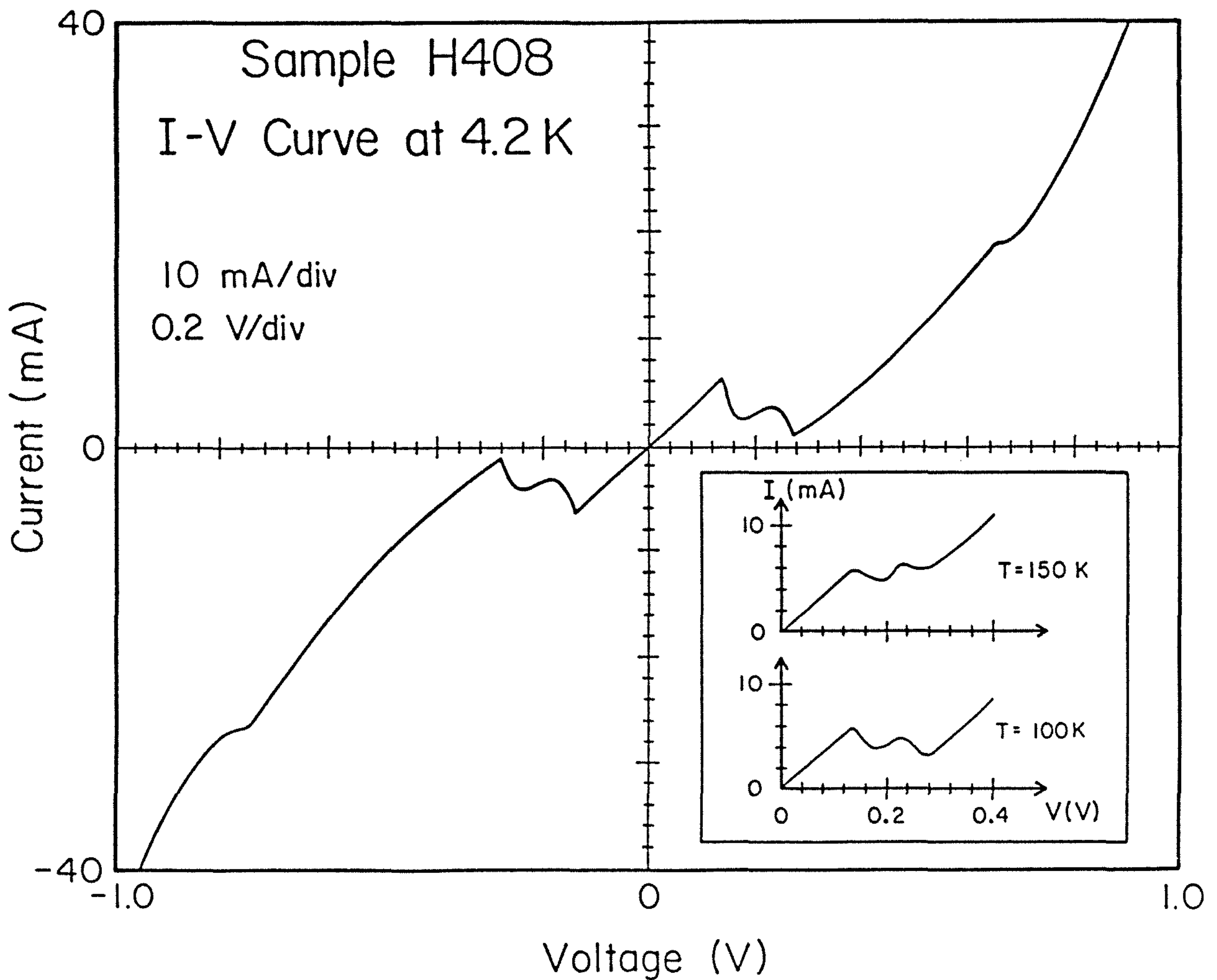

Figure 4.11: Experimental *I–V* characteristic at 4.2 K for a circular device, 20 μm in diameter, fabricated on sample H408. Sample H408 is a GaAs/AlAs double barrier heterostructure in which the nominally undoped GaAs quantum well is 62 Å wide. The GaAs electrodes are doped *n*–type with Se at $1.75 \times 10^{18} cm^{-3}$. The AlAs barrier layers are doped *p*–type with Mg at $6 \times 10^{17} cm^{-3}$. The barrier closer to the substrate is 51 Å thick. The barrier adjacent to the top electrode is 42 Å thick.

sample do not reveal two such distinct current peaks in each bias direction at $|V_a| < 280$ mV, but only one broad negative differential resistance region. These adjacent peaks may thus be due to two resonant states in the quantum well which are close enough in energy that they are not always resolved in the I–V curves.

The energy band diagrams of the heterostructure and the quasi–stationary levels in the GaAs well may be calculated as for sample H927. Three quasi–bound Γ–states are found, at energies $E_1^\Gamma = 78$ meV, $E_2^\Gamma = 325$ meV and $E_3^\Gamma = 730$ meV, in the unbiased structure. The two resonant X–states corresponding to the large longitudinal AlAs X–point mass lie at energies $E_1^X = 22$ meV and $E_2^X = 165$ meV above the bottom of the well. The quasi–stationary X–states associated with the small transverse AlAs X–point mass have energies $\epsilon_1^X = 42$ meV and $\epsilon_2^X = 176$ meV from the conduction band edge at the middle of the well. These values are summarized in Table 4.3. It could be argued that if band bending effects are neglected, the experimental results are consistent with resonant tunneling via the quasi–bound Γ–states E_1^Γ and E_2^Γ alone. However, since the AlAs barriers are doped p–type to a significant level, the band edges actually bend up at zero bias. As a result, the bottom of the well and the resonant states are raised by about 50 meV with respect to the band edges in the electrode bulk regions. Furthermore, it has been shown that the cladding layers sustain significant fractions of the applied voltage. When these two effects are taken into account, the experimental I–V curves are found to be inconsistent with resonant tunneling via Γ–states alone. Two energy band profiles are illustrated in Fig.4.12 for sample H408. They correspond to reverse biases of -140 and -250 mV, respectively. When $V_a = -140$ mV (-250 mV), E_1^X (E_1^Γ) coincides in energy with $E_c^l(x = 0)$. In forward bias, the same would occur at 135 (240) mV. Comparing these values to the experimental results depicted in Fig.4.11 suggests that the broad negative differential resistance regions observed in the

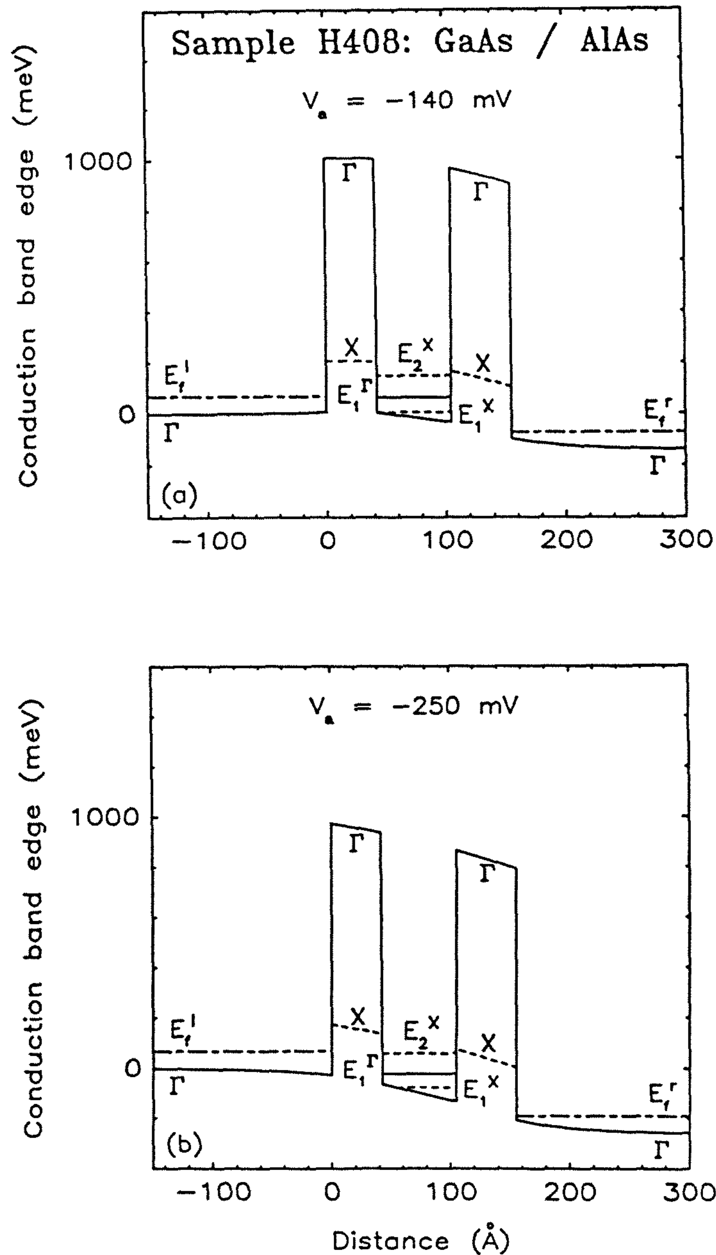

Figure 4.12: Calculated Γ–point (solid lines) and X–point (dashed lines) conduction band edges, for sample H408. (a) and (b) correspond to applied biases of −140 and −250 mV, respectively. In the GaAs quantum well, E_1^Γ (solid line) denotes the first quasi–bound Γ–state, and E_1^X and E_2^X (dashed lines) are the two resonant X–states corresponding to the large longitudinal AlAs X–point effective mass in the direction perpendicular to the interfaces.

I–V characteristics at $|V_a| < 280$ mV arise from tunneling via the two resonant states E_1^X and E_1^Γ. Since the difference in energy between both levels is slightly smaller than the Fermi energy in the bulk electrodes, E_1^X and E_1^Γ are not always resolved. Energy band diagrams indicate further that the small current peaks obtained in Fig.4.11 at -750 and 650 mV are due to resonant tunneling via E_2^X. It may thus be concluded that the I–V characteristics of sample H408 reveal resonant tunneling via the first quasi–bound Γ–state, E_1^Γ, and the two X–states E_1^X and E_2^X, corresponding to the large longitudinal AlAs X–point effective mass. Energy band profiles also make it possible to predict the voltages at which tunneling via each of the quasi–bound states in the well may be initiated. Since E_1^X lies below the Fermi level at zero bias, resonant tunneling via E_1^X starts as soon as a voltage is applied. As a result, the experimental zero–bias resistance is small and the portions of the I–V curves corresponding to $|V_a| < 140$ mV remain almost independent of temperature. Resonant tunneling via E_1^Γ (E_2^X) is initiated when E_1^Γ (E_2^X) coincides in energy with the Fermi level in the incident electrode. For both resonances, this occurs approximately when tunneling via the subband associated with the previous quasi–stationary state in the well turns off. Such effects would thus contribute in reducing the peak–to–valley current ratios of the negative differential resistances.

From the above discussions, it may be anticipated that the dominant low temperature current transport mechanisms in GaAs/$Al_xGa_{1-x}As$ double barrier heterostructures in which the barrier layers are made of indirect band gap alloys should be resonant tunneling via quasi–stationary states in the GaAs quantum well bound by the $Al_xGa_{1-x}As$ Γ– and X–point potential energy barriers.

4.5 Relative Importance of Tunneling via Resonant Γ– and X–states

This section discusses results obtained from three other heterostructures having pure AlAs barrier layers (H283, H418, H475). These samples serve to illustrate that the relative contributions to the total current of the different mechanisms for tunneling through double barrier heterostructures having indirect band gap $Al_xGa_{1-x}As$ quantum barriers may greatly vary with the structure studied. In certain samples, they may also depend upon the sign of the applied bias.

In H283, the doping densities in the GaAs electrodes are slightly asymmetric: $4.5 \times 10^{18} cm^{-3}$ in the top cladding layer and $4.0 \times 10^{18} cm^{-3}$ in the electrode adjacent to the substrate. The nominally undoped GaAs well is 90.5 Å wide (32 monolayers). The AlAs barrier closer to the substrate is 56.5 Å thick (20 monolayers). The other barrier is 68 Å thick (24 monolayers). As a result of the asymmetry in barrier thicknesses, a given resonance in the well should appear in the *I*–*V* characteristics at a larger applied voltage in forward bias than in reverse bias ($|V_a^F| > |V_a^R|$). Fig.4.13 shows an experimental *I*–*V* curve at 4.2 K for a circular device, 80 μm in diameter. This curve is very asymmetric. Two negative differential resistances are obtained in forward bias. The first one, at $V_1^F = 50$ mV, is very weak. The second one, much more pronounced, has a peak in current at $V_2^F = 340$ mV. In reverse bias, only one inflection is visible in the *I*–*V* characteristic, at about −150 mV. However, second derivative spectra, $(d^2I/dV^2)(V)$, reveal a peak at −45 mV in addition to those corresponding to the negative differential resistances and inflections observed in the *I*–*V* curve. This peak should arise from tunneling via the same resonant state as that producing the inflection obtained at $V_1^F = 50$ mV in forward bias. The calculated quasi–stationary levels in the GaAs quantum well are listed in Table 4.3. Four quasi–

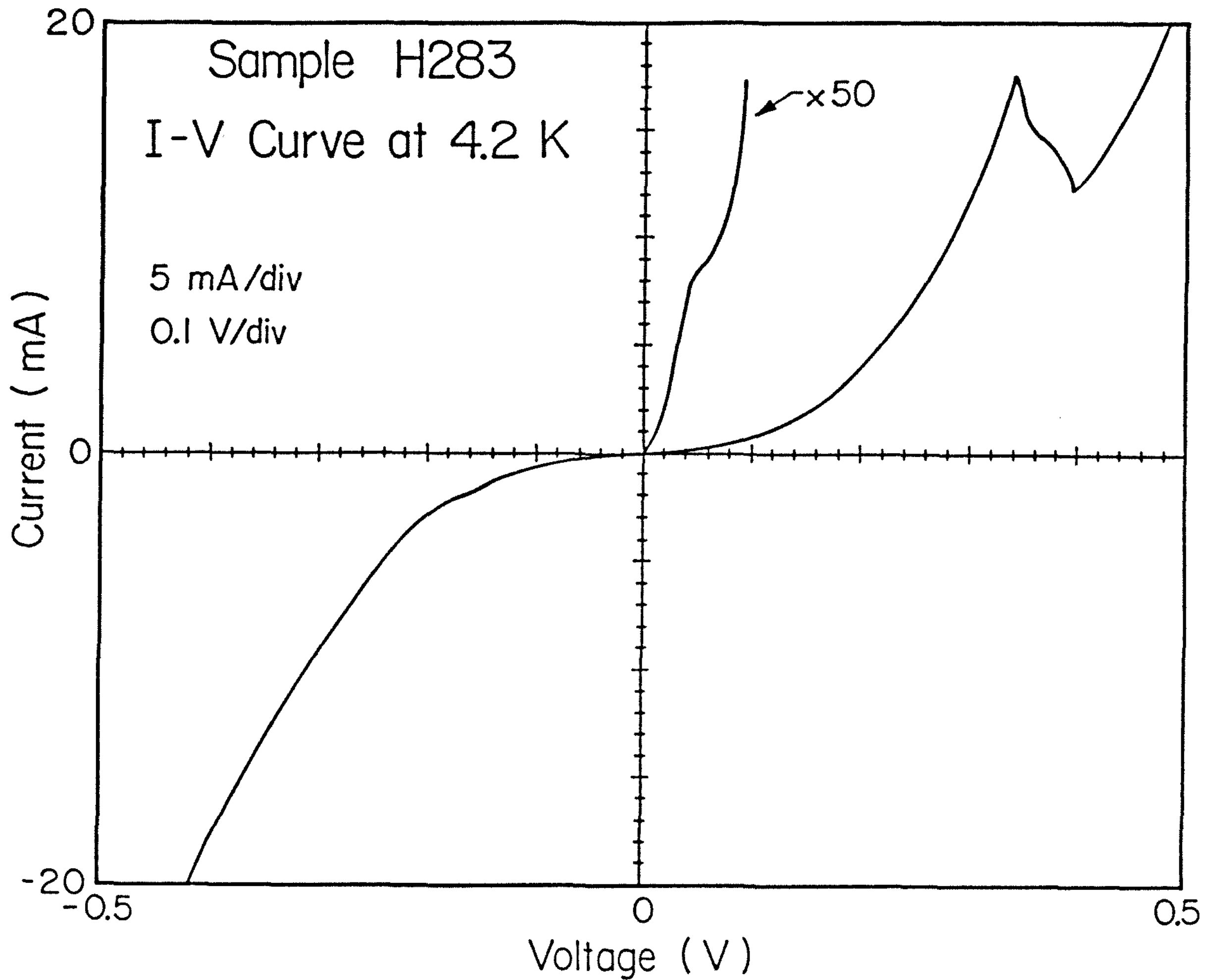

Figure 4.13: Experimental *I–V* characteristic at 4.2 K for a circular device, 80 μm in diameter, fabricated on sample H283. H283 is a GaAs/AlAs double barrier heterostructure in which the nominally undoped GaAs quantum well is 90.5 Å wide. The doping densities in the *n*–type GaAs electrodes are $4.5 \times 10^{18} cm^{-3}$ in the top cladding layer and $4.0 \times 10^{18} cm^{-3}$ in the electrode adjacent to the substrate. The barrier layers are doped *p*–type with Mg at $2 \times 10^{17} cm^{-3}$. The AlAs barrier closer to the substrate is 56.5 Å thick. The other barrier is 68 Å thick.

bound Γ–states are found in the unbiased structure, at energies $E_1^\Gamma = 44$ meV, $E_2^\Gamma = 178$ meV, $E_3^\Gamma = 406$ meV and $E_4^\Gamma = 724$ meV from the conduction band edge at the middle of the well. Two resonant X–states, $E_1^X = 14$ meV and $E_2^X = 92$ meV, correspond to the large longitudinal AlAs X–point effective mass. The resonances observed at −45 and 50 mV are necessarily due to tunneling via a low lying resonant state in the well. Since the AlAs barriers are doped *p*–type and the band edges bend up at zero bias, the only resonant level consistent with these values is E_1^X. However, E_1^X lies close enough to $E_c^i(x=0)$ at zero bias only if the AlAs doping concentration is less than 2–3$\times 10^{17} cm^{-3}$. The energy band profiles of the structure are calculated using the parameters listed in Tables 4.1 and 4.2. They reveal that the peaks in current corresponding to E_1^X, E_1^Γ and E_2^X should occur in reverse bias at −45, −150 and −310 mV, respectively. In forward bias, they should appear at 50, 160 and 330 mV, respectively. These results are illustrated in Fig.4.14 for applied biases of 50 and 330 mV. They are also summarized in Table 4.5. The quasi–stationary levels in the quantum well via which resonant tunneling occurs may be identified by comparing these values to the experimental data shown in Fig.4.13. In forward bias, the inflection at $V_1^F = 50$ mV corresponds to E_1^X and the pronounced peak in current at $V_2^F = 340$ mV should be associated with E_2^X. In reverse bias, resonant tunneling occurs via E_1^X and E_1^Γ, but no evidence is shown of tunneling via E_2^X. Energy band diagram calculations also reveal that E_1^X, E_1^Γ and E_2^X all lie below the Fermi energy at zero bias. This is because the electrode doping densities are large and the GaAs well is wide. As a result, resonant tunneling via all three levels occurs as soon as a voltage is applied to the sample. This explains why some of the resonances are not visible in the *I–V* characteristics, and, in particular, why E_1^X produces weak inflections only. The most important properties of sample H283 may thus be summarized as follows. (*i*) Resonant tunneling via three quasi–stationary levels

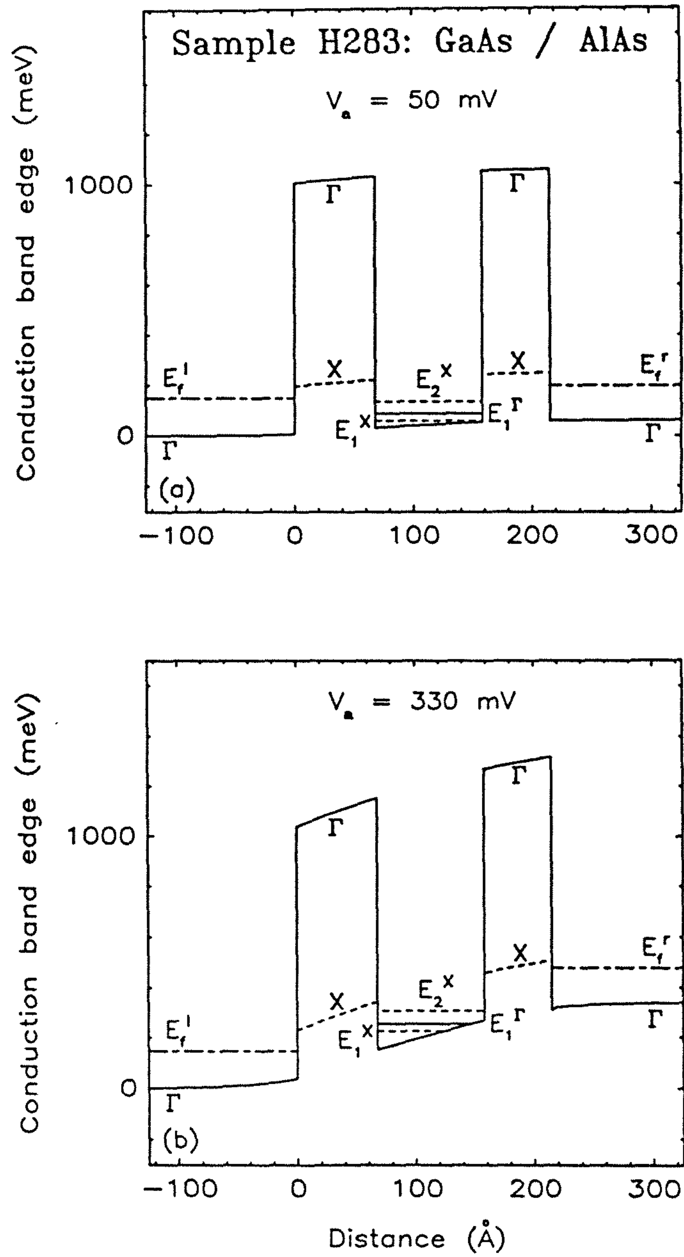

Figure 4.14: Calculated Γ–point (solid lines) and X–point (dashed lines) conduction band edges, for sample H283. (a) and (b) correspond to applied biases of 50 and 330 mV, respectively.

in the well, E_1^X, E_1^Γ and E_2^X, may be observed experimentally. (*ii*) Resonant tunneling via quasi–bound X–states is the dominant low temperature current transport mechanism, at least in forward bias. (*iii*) Resonant tunneling via Γ–states is also present, but is significantly weaker. (*iv*) Because the GaAs well is wide and the electrode doping densities are large, the spacings between the lowest resonant states in the well are less than the Fermi energies in the cladding layers. It results that resonant tunneling occurs as soon as a bias is applied, that E_1^X produces only weak inflections in the experimental I–V characteristics, and that the peak–to–valley current ratios of the negative differential resistances are small. (*v*) The experimental I–V curves are very asymmetric. In particular, the absence of regions with negative slopes in reverse bias reveals the presence of large background currents. Such effects may be related to the quality of the materials and the heterojunction interfaces.

In sample H418, the GaAs electrodes are doped n–type at $1.5 \times 10^{18} cm^{-3}$. The nominally undoped GaAs quantum well is 28.5 Å wide (10 monolayers). The p–type doping density in the AlAs barrier layers is taken to be $6 \times 10^{17} cm^{-3}$. The barrier closer to the substrate is 48 Å thick (17 monolayers). The barrier adjacent to the top electrode is 37 Å thick (13 monolayers). Due to the asymmetric barrier thicknesses, a given resonance in the well is expected in the I–V characteristics at a larger applied voltage in reverse bias than in forward bias ($|V_a^R| > |V_a^F|$). Fig.4.15 shows an experimental I–V characteristic at 4.2 K for a circular device, 20 μm in diameter. The I–V curve reveals one negative differential resistance region in each bias direction. The peaks in current occur at $V_1^R = -1.1$ V in reverse bias and at $V_1^F = 840$ mV in forward bias. Resonant tunneling is initiated at about −400 and 340 mV in reverse and forward bias, respectively. The resonant energy levels in the GaAs well in the unbiased structure are given in

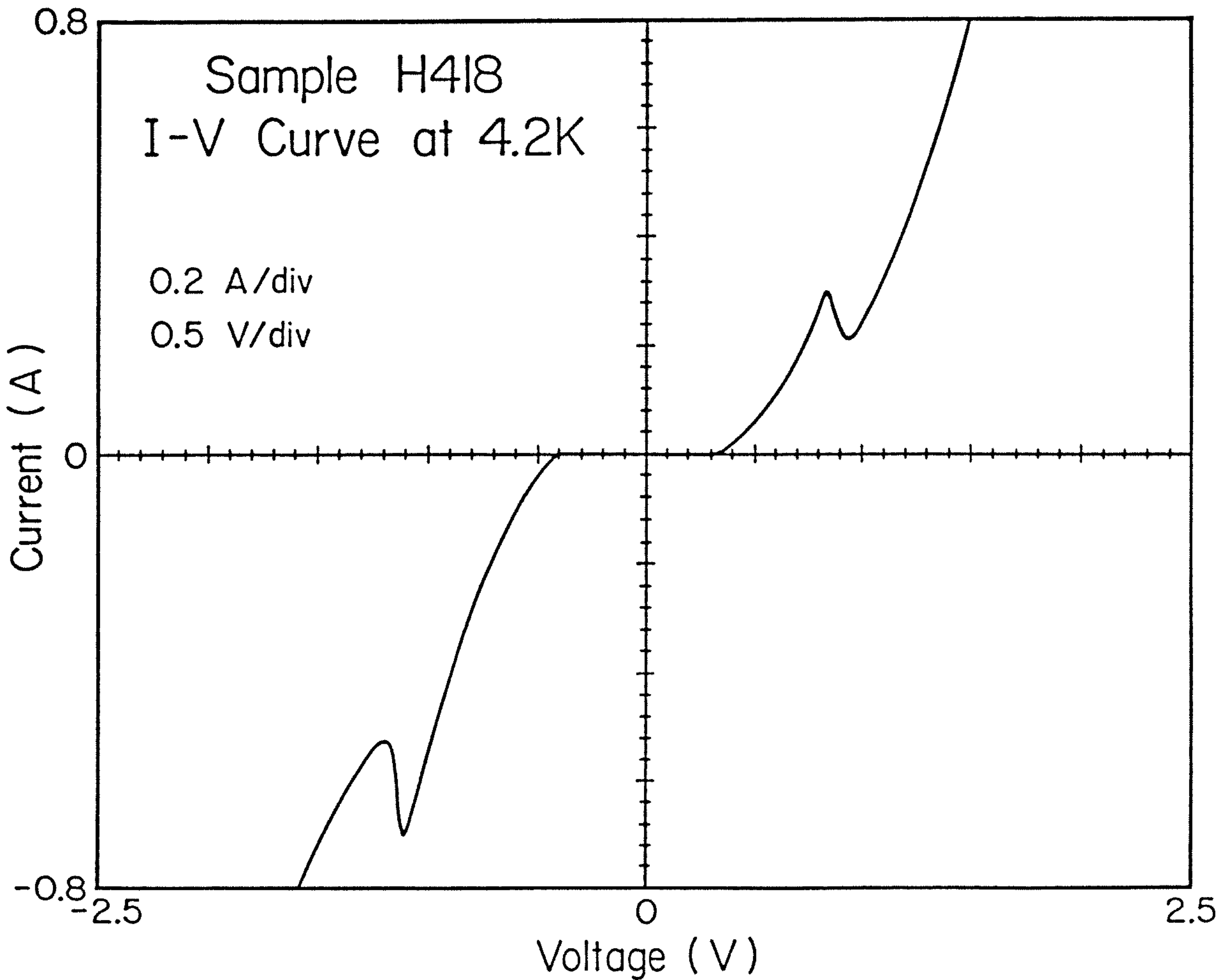

Figure 4.15: Experimental I–V characteristic at 4.2 K for a circular device, 20 μm in diameter, fabricated on sample H418. H418 is a GaAs/AlAs double barrier heterostructure in which the nominally undoped GaAs quantum well is 28.5 Å wide. The GaAs electrodes are doped n–type with Se at $1.5 \times 10^{18} cm^{-3}$. The AlAs barrier layers are doped p–type with Mg at $6 \times 10^{17} cm^{-3}$. The barrier closer to the substrate is 48 Å thick. The barrier adjacent to the top electrode is 37 Å thick.

Table 4.3. In particular, $E_1^X = 47$ meV and $E_1^\Gamma = 225$ meV. Energy band diagram calculations indicate that resonant tunneling via E_1^Γ should be initiated at -420 and 350 mV in reverse and forward bias, respectively. Similarly, the peaks in current corresponding to E_1^Γ are anticipated at -1.1 V and 830 mV. These results are illustrated in Figs.4.16(a) and (b) and summarized in Table 4.5. They are in good agreement with the experimental data depicted in Fig.4.15. It should be emphasized that, as opposed to sample H283, resonant tunneling via E_1^Γ is the dominant low temperature current transport mechanism in sample H418. Furthermore, no sign of tunneling via X–states is visible in the experimental I–V curves. This reveals that the relative contributions to the total current of resonant tunneling via quasi–stationary Γ– and X–states in the GaAs well may greatly vary from sample to sample.

In H475, the doping densities in the GaAs electrodes are $4.7 \times 10^{17} cm^{-3}$ in the top cladding layer and $5.0 \times 10^{17} cm^{-3}$ in the electrode adjacent to the substrate. The nominally undoped GaAs well is 76.5 Å wide (27 monolayers). The AlAs barrier closer to the substrate is 79 Å thick (28 monolayers). The other barrier is 71 Å thick (25 monolayers). This asymmetry in barrier thicknesses causes a given resonant state in the well to appear in the I–V characteristics at a larger applied voltage in reverse bias than in forward bias. However, this effect is partially compensated by the asymmetry in the electrode doping concentrations. Fig.4.17 illustrates an experimental I–V characteristic at 4.2 K for a circular device, 80 μm in diameter. Only one negative differential resistance is observed in reverse bias. The corresponding peak in current occurs at -190 mV. In forward bias, two regions with negative slopes are obtained, at $V_1^F = 90$ mV and $V_2^F = 420$ mV, respectively. The fact that the first peak in current appears in forward bias at an applied voltage as low as 90 mV indicates that the corresponding resonant

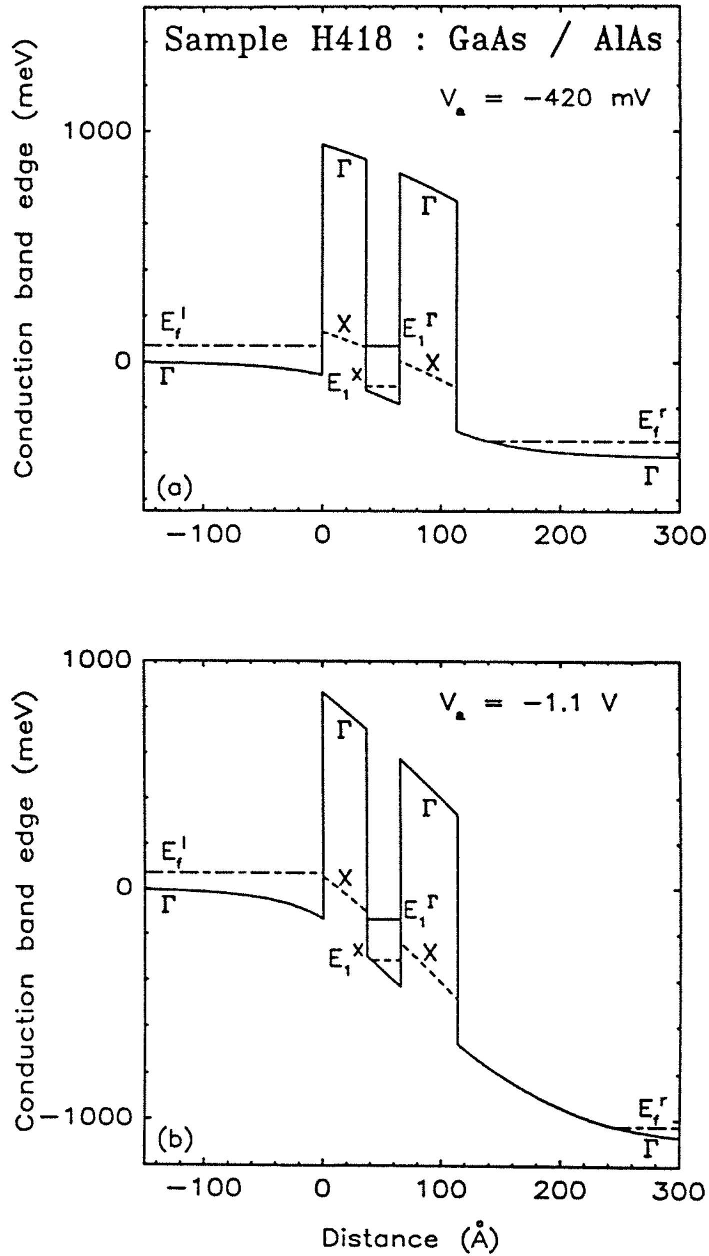

Figure 4.16: Calculated Γ–point (solid lines) and X–point (dashed lines) conduction band edges, for sample H418. (a) and (b) correspond to applied biases of −420 mV and −1.1 V, respectively.

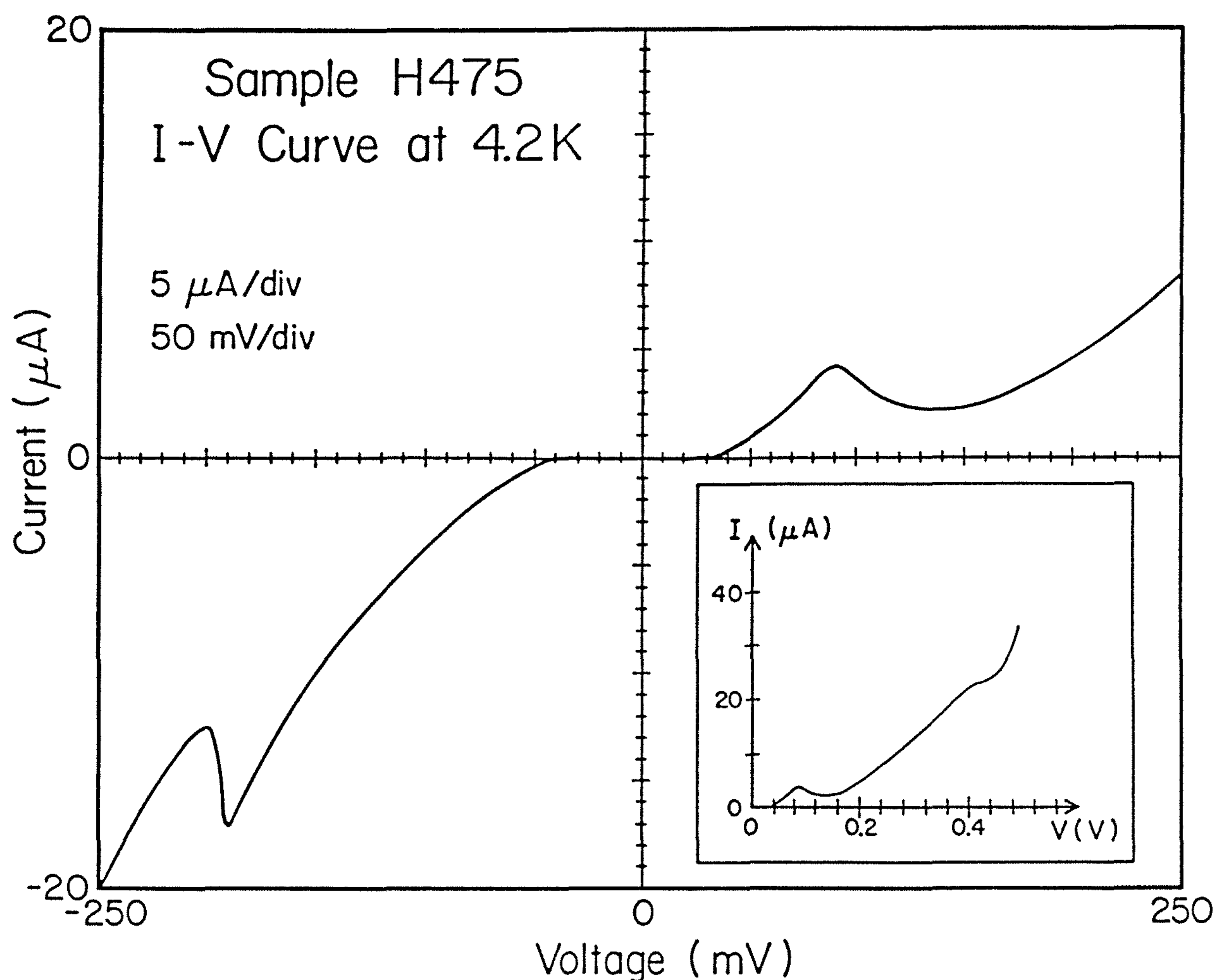

Figure 4.17: Experimental I–V characteristic at 4.2 K for a circular device, 80 μm in diameter, fabricated on sample H475. H475 is a GaAs/AlAs double barrier heterostructure in which the nominally undoped GaAs quantum well is 76.5 Å wide. The doping densities in the n–type GaAs electrodes are $4.7 \times 10^{17} cm^{-3}$ in the top cladding layer and $5.0 \times 10^{17} cm^{-3}$ in the electrode adjacent to the substrate. The barrier layers are doped p–type with Mg at $2 \times 10^{17} cm^{-3}$. The AlAs barrier closer to the substrate is 79 Å thick. The other barrier is 71 Å thick.

state is close to the bottom of the well and that the p–type doping density in the AlAs barriers should be relatively small. To be consistent with H283, the barrier doping concentration is taken to be $2 \times 10^{17} cm^{-3}$. The calculated resonant energy levels in the GaAs quantum well are listed in Table 4.3. In particular, $E_1^X = 17$ meV, $E_1^\Gamma = 57$ meV and $E_2^X = 120$ meV. Energy band diagram calculations using the structure parameters given in Tables 4.1 and 4.2 reveal that resonant tunneling via E_1^X, E_1^Γ and E_2^X should be initiated in reverse (forward) bias at -40 (35), -110 (100) and -240 (200) mV, respectively. Similarly, the corresponding peaks in current should occur at -100, -190 and -450 mV in reverse bias, and at 90, 175 and 420 mV in forward bias. These results are illustrated in Figs.4.18(a) and (b) for applied biases of 90 and -190 mV, respectively. They are also summarized in Table 4.5. They indicate that the two negative differential resistances obtained at V_1^F and V_2^F in Fig.4.17 correspond to tunneling via the resonant X–states E_1^X and E_2^X. In reverse bias, the peak in current observed at -190 mV is consistent with resonant tunneling via E_1^Γ, but no quasi–bound X–state is manifested. These results reveal that the relative importance of tunneling via resonant Γ– and X–states not only differs from sample to sample, but may also depend upon the sign of the applied voltage. Such effects should thus be related primarily to the quality of the materials and the heterojunction interfaces.

Other samples (H392, H919) studied using the same approach have led to similar results and conclusions. Their parameters are listed in Tables 4.1 and 4.2. To be consistent with the other heterostructures, the doping densities in the AlAs barriers are taken to be $6 \times 10^{17} cm^{-3}$. The experimental results and the agreement with energy band diagram calculations are given in Tables 4.3 and 4.5. In sample H392, only one peak in current is observed, in reverse bias. It corresponds to E_1^Γ. In H919, one negative differential resistance is obtained in

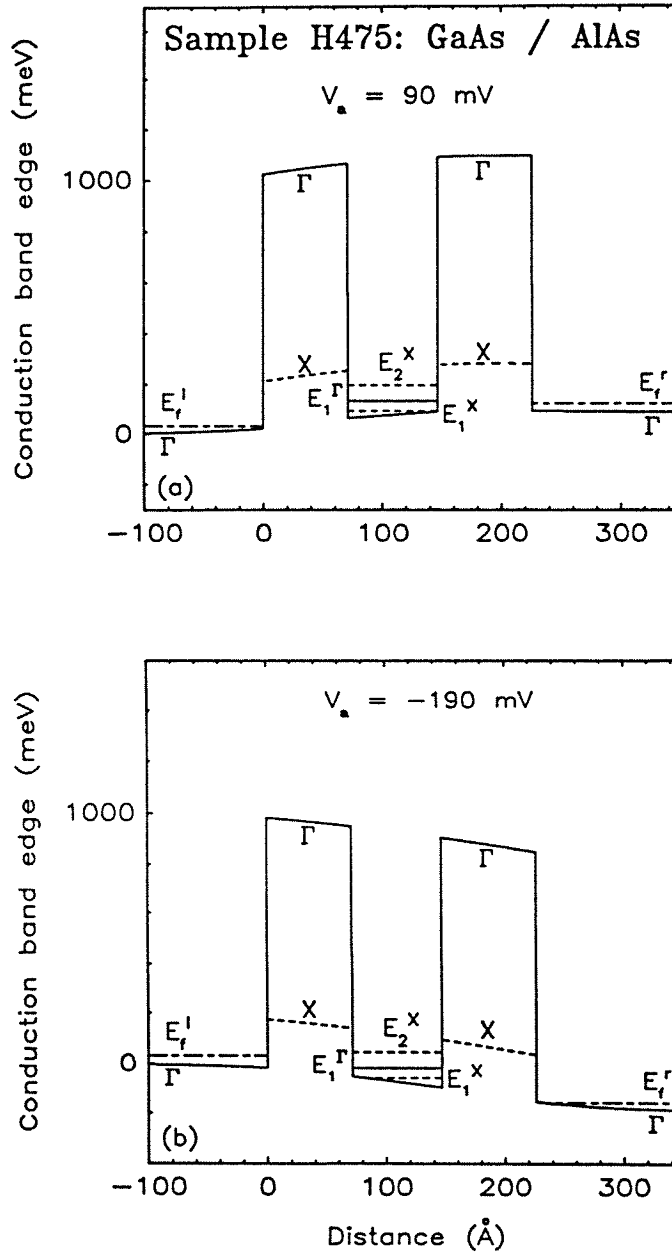

Figure 4.18: Calculated Γ–point (solid lines) and X–point (dashed lines) conduction band edges, for sample H475. (a) and (b) correspond to applied biases of 90 and −190 mV, respectively. In the GaAs quantum well, E_1^Γ (solid line) denotes the first quasi–bound Γ–state, and E_1^X and E_2^X (dashed line) are the two resonant X–states corresponding to the large longitudinal AlAs X–point electron mass in the direction perpendicular to the interfaces.

reverse bias and an inflection is visible in forward bias. As indicated in Table 4.5, these are consistent with resonant tunneling via E_1^Γ.

These observations reveal that current transport is more complex in structures having indirect $Al_xGa_{1-x}As$ barrier layers than in samples in which the quantum barriers are made of direct band gap alloys. Numerous quasi–stationary states are then present in the quantum well, causing resonant tunneling to occur through multiple processes. This produces large background currents and reduced peak–to–valley current ratios. This also explains why certain resonances are not observed in experimental I–V characteristics and that negative differential resistances are totally absent in some samples. For the resonant states to be individually resolved, their energy spacing should be larger than the Fermi levels in the bulk electrodes. This may be achieved by reducing the well width and the electrode doping densities. However, the contributions to the total current of the different tunneling mechanisms seem to be much more sensitive to the presence of defects, impurities and interface states than to the layer thicknesses or doping concentrations themselves.

4.6 Resonant Tunneling in Asymmetrically Doped Structures

This section deals with the three samples of the second kind, S008, S031 and S032. These structures are characterized by a low doped GaAs buffer layer grown before the first $Al_xGa_{1-x}As$ barrier layer (Barrier No.1), on top of the GaAs electrode adjacent to the substrate. In sample S008, this GaAs electrode is doped n–type with Se at $2.8 \times 10^{18} cm^{-3}$. The GaAs buffer layer, approximately 0.2 μm thick, has an n–type doping density of $2.2 \times 10^{17} cm^{-3}$. The top GaAs electrode is degenerately doped n–type at $3.1 \times 10^{18} cm^{-3}$. Both $Al_{0.35}Ga_{0.65}As$

barrier layers are 110.5 Å thick (39 monolayers). The nominally undoped GaAs quantum well is 65 Å wide (23 monolayers). Fig.4.19 depicts an experimental I–V characteristic at 4.2 K for a circular device, 50 μm in diameter. Two negative differential resistances are obtained in each bias direction. The first one is very pronounced, with a peak–to–valley current ratio of 8.5 in reverse bias and 5 in forward bias. The corresponding peaks in current occur at $V_1^R = -140$ mV and $V_1^F = 120$ mV. The other negative differential resistances are inflections visible at $V_2^R = -520$ mV and $V_2^F = 120$ mV. The doping densities in the GaAs cladding layers are asymmetric. As a result, the band edges bend in such a way that resonant tunneling via the subband associated with a given quasi–stationary level in the well occurs at a lower applied voltage in forward bias than in reverse bias. If the doping concentrations in the top and back cladding layers were 3.1×10^{18} and $2.2 \times 10^{17} cm^{-3}$, respectively, the experimental I–V curves would be very asymmetric. This is illustrated in the two energy band diagrams depicted in Fig.4.20. They reveal that resonant tunneling via E_1^Γ would then produce peaks in current at 40 mV in forward bias and -230 mV in reverse bias. Equally large asymmetries in peak positions would be obtained from tunneling via E_2^Γ. These results are inconsistent with the experimental I–V characteristics which are only slightly asymmetric. This suggests that the average doping concentration in the back GaAs cladding layer is significantly greater than $2.2 \times 10^{17} cm^{-3}$, and not very different from the electron density in the top electrode. This occurs because the low doped GaAs buffer layer is much thinner (≈ 0.2 μm) than the adjacent degenerate GaAs electrode (2–3 μm). As indicated in Table 4.2, the average doping level in the back GaAs cladding layer is taken to be $2.5 \times 10^{18} cm^{-3}$. Furthermore, although the barrier layers were intentionally doped p–type, energy band diagrams are consistent with the experimental I–V data only if the barriers are assumed to be practically undoped. Two energy band profiles calculated with

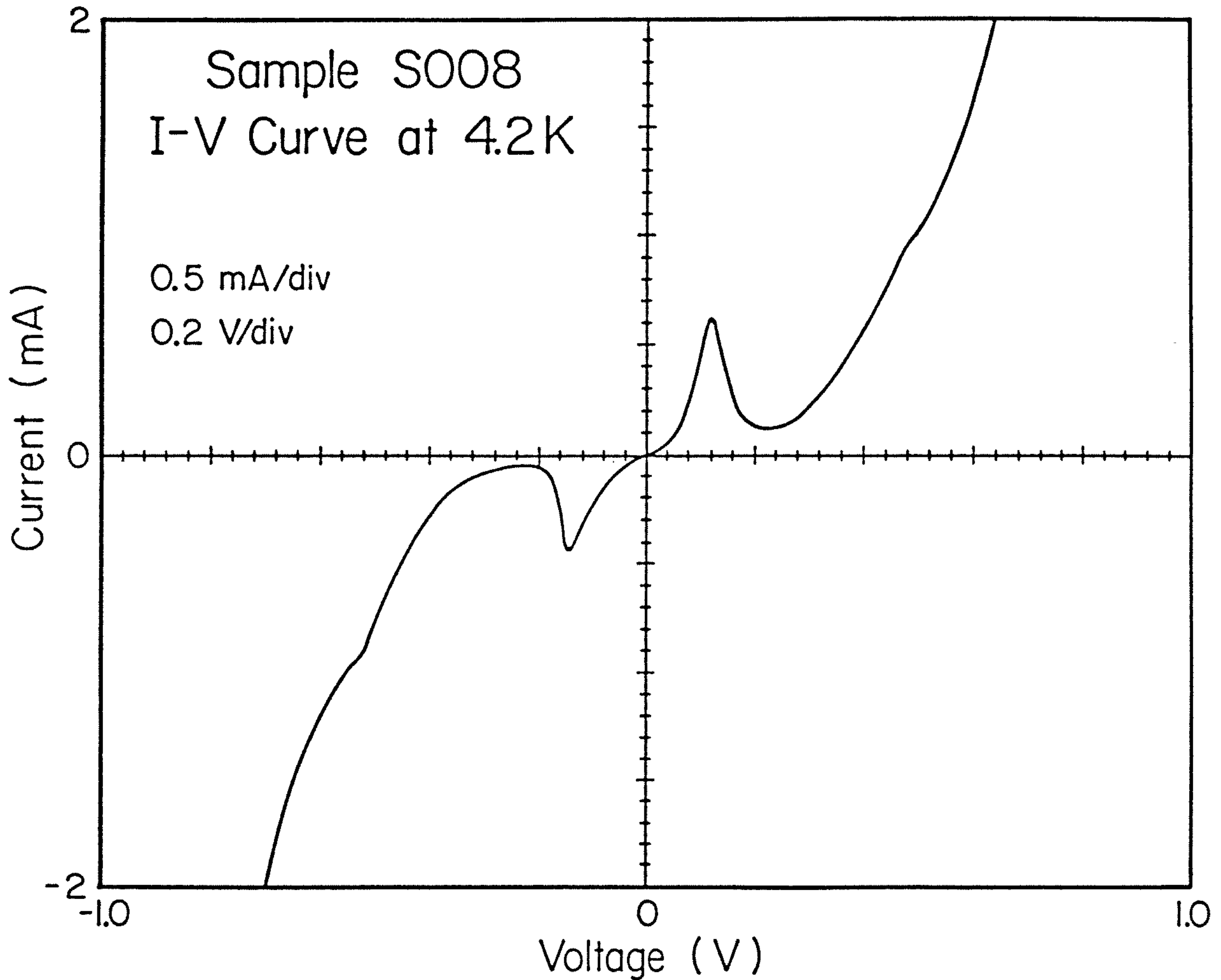

Figure 4.19: Experimental *I–V* characteristic at 4.2 K for a circular device, 50 μm in diameter, fabricated on sample S008. S008 is a GaAs/$Al_{0.35}Ga_{0.65}As$ double barrier heterostructure having a low doped GaAs buffer layer between the first $Al_{0.35}Ga_{0.65}As$ barrier and the GaAs electrode adjacent to the substrate. This GaAs electrode is degenerately doped n–type with Se at $2.8 \times 10^{18} cm^{-3}$. The buffer layer, approximately 0.2 μm thick, has an n–type doping density of $2.2 \times 10^{17} cm^{-3}$. The barriers are 110.5 Å thick. The GaAs quantum well is 65 Å wide. The top GaAs electrode is doped at $3.1 \times 10^{18} cm^{-3}$.

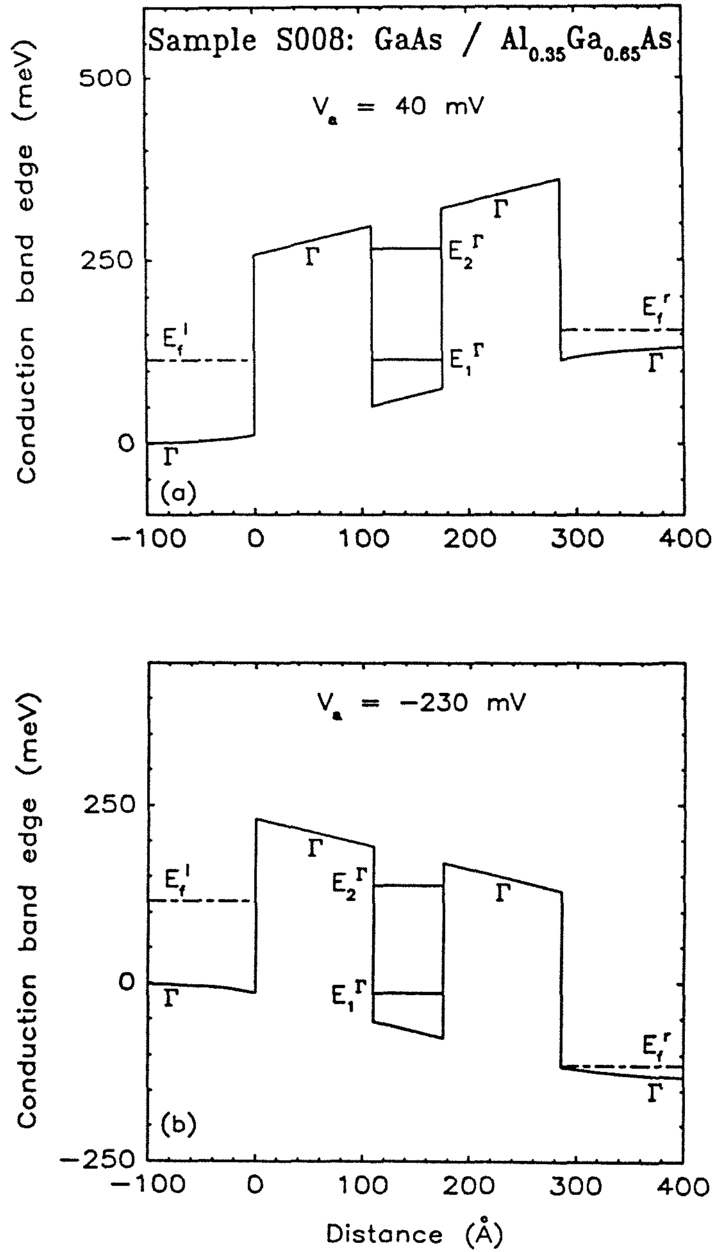

Figure 4.20: Calculated Γ–point conduction band edges for sample S008, assuming that the average doping density in the back GaAs cladding layer is $2.2 \times 10^{17} cm^{-3}$. The barriers and the well are assumed to be undoped. (a) and (b) correspond to applied biases of 40 and −230 mV, respectively. They illustrate the turn–offs of resonant tunneling via E_1^Γ in forward and reverse bias.

these values are depicted in Figs.4.21 (a) and (b). They correspond to applied biases of -140 and -185 mV, respectively. Fig.4.21(a) illustrates the turn–off of resonant tunneling via E_1^Γ (E_1^Γ lines up with $E_c^l(x=0)$). Fig.4.21(b) shows the turn–on of resonant tunneling via E_2^Γ (E_2^Γ coincides in energy with E_f^l). These results, summarized in Table 4.6, are in good agreement with the experimental I–V characteristics. It may thus be concluded that structures grown with a thin and low doped GaAs buffer layer adjacent to a thick and heavily doped GaAs electrode behave as if they had a uniformly doped back GaAs cladding layer. The average doping density in this layer decreases as the GaAs buffer layer is made thicker and/or more lightly doped. This was verified on a number of samples grown with doping levels as low as $2 \times 10^{16} cm^{-3}$ in buffer layers as thick as 2 μm. As expected, the I–V characteristics of these structures were very asymmetric.

Samples S031 and S032 are characterized by larger Al contents in the barrier layers than the other GaAs/$Al_xGa_{1-x}As$ heterostructures. In S031, the electron density in the top GaAs electrode is $3.0 \times 10^{18} cm^{-3}$. The GaAs buffer layer, approximately 0.4 μm thick, is doped n–type at $1.8 \times 10^{17} cm^{-3}$. As a result, the experimental I–V curves are anticipated to be more asymmetric than in sample S008. This is revealed in Fig.4.22. The I–V curve features two negative differential resistances in each bias direction. It also shows that resonant tunneling via the first quasi–stationary level in the well occurs as soon as a voltage is applied. The corresponding peaks in current are obtained at $V_1^R = -90$ mV in reverse bias and $V_1^F = 15$ mV in forward bias. The other negative differential resistances appear at $V_2^R = -190$ mV and $V_2^F = 110$ mV. If the resonant energy levels in the GaAs quantum well are calculated using the structure parameters listed in Tables 4.1 and 4.2, but under the assumption that the barrier layers are made of $Al_{0.35}Ga_{0.65}As$, two Γ–states are found in the unbiased structure, at

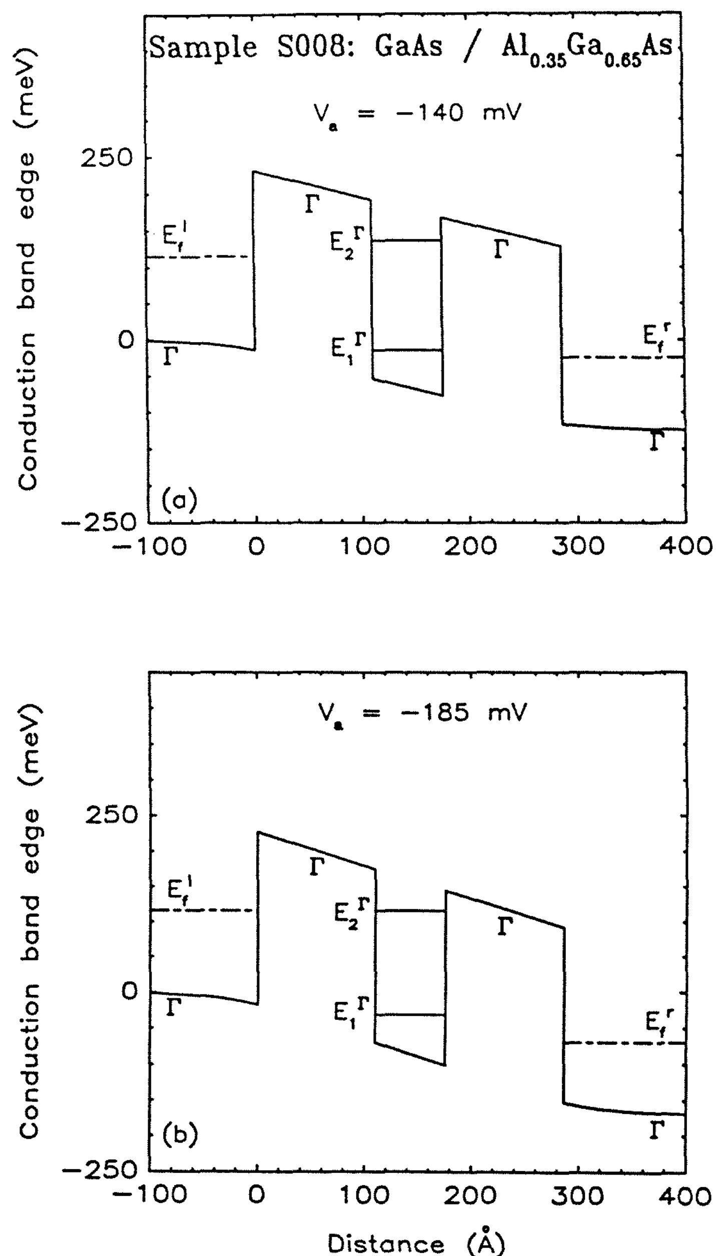

Figure 4.21: Calculated Γ–point conduction band edges for sample S008, assuming that the average doping density in the back GaAs cladding layer is $2.5 \times 10^{18} cm^{-3}$. The barriers and the well are assumed to be undoped. (a) and (b) correspond to applied biases of −140 and −185 mV, respectively. They illustrate the turn–off of resonant tunneling via E_1^Γ and the turn–on of resonant tunneling via E_2^Γ.

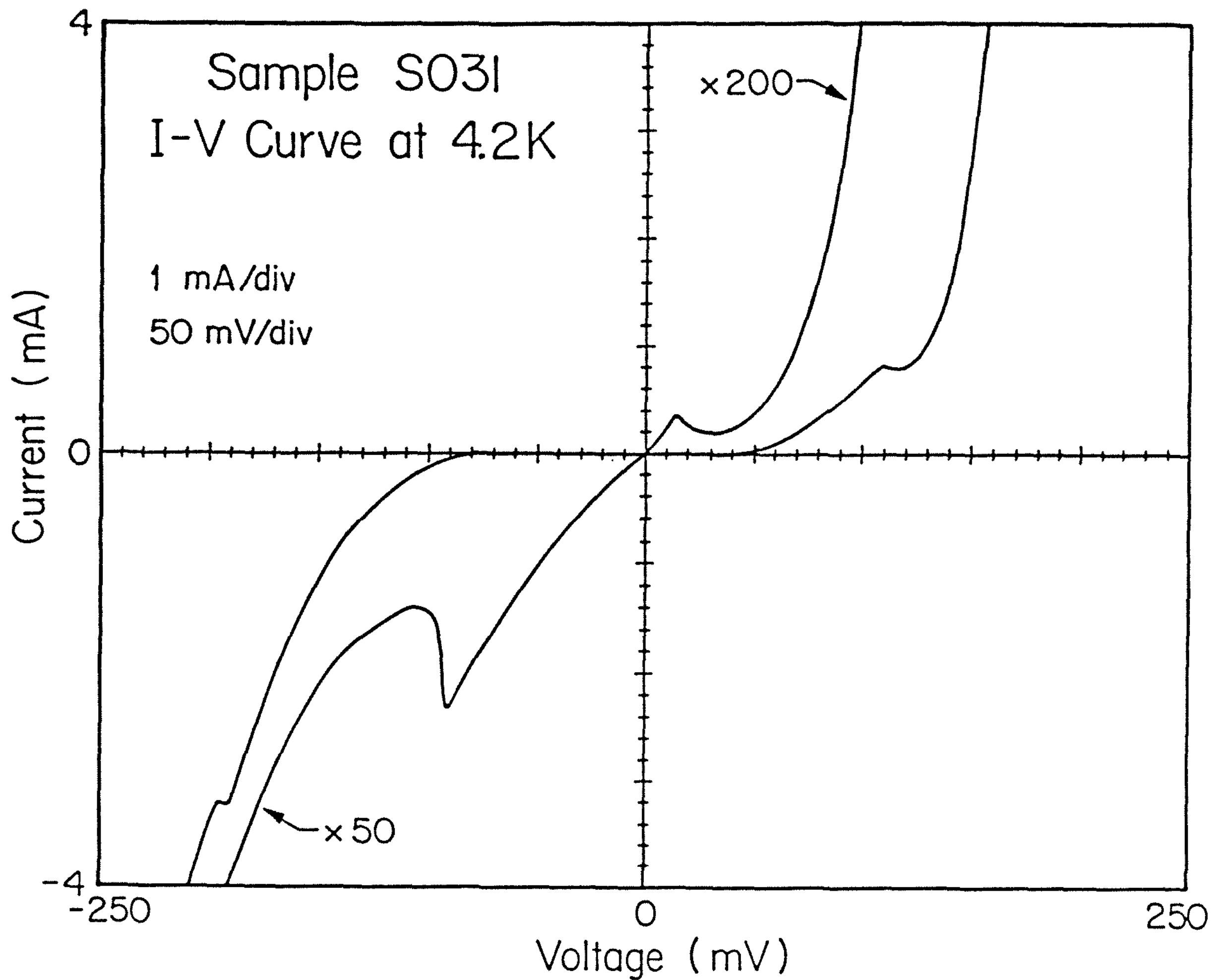

Figure 4.22: Experimental I–V characteristic at 4.2 K for a circular device, 50 μm in diameter, fabricated on sample S031. In sample S031, the 0.4 μm thick GaAs buffer layer is doped n–type at $1.8 \times 10^{17} cm^{-3}$. The doping density in the top GaAs electrode is $3.0 \times 10^{18} cm^{-3}$. The barrier layer closer to the substrate is 116 Å thick. The other barrier is 124.5 Å thick. The GaAs quantum well is 68 Å wide.

energies $E_1^\Gamma = 52$ meV and $E_2^\Gamma = 193$ meV. Both levels are too high in energy to produce the negative differential resistances observed in Fig.4.22. In fact, the experimental I–V data may only be explained by assuming that the barrier layers are made of indirect $Al_xGa_{1-x}As$ alloys. Then, low lying quasi–stationary X–states exist in the quantum well. Furthermore, the higher Γ–point potential energy barriers cause the resonant Γ–states in the well to rise in energy. If the Al content in the barrier layers is as large as 0.75, the resonant states confined by the $Al_{0.75}Ga_{0.25}As$ Γ–point potential energy barriers may be calculated using an effective mass $m_\Gamma^* = 0.13\,m_0$ in the barriers,[20] and a conduction band offset at the heterojunction interfaces of 625 meV.[21] Three quasi–bound Γ–states may then be found in the unbiased structure, at energies $E_1^\Gamma = 63$ meV, $E_2^\Gamma = 256$ meV and $E_3^\Gamma = 562$ meV from the conduction band edge at the middle of the well. To obtain the levels bound by the $Al_{0.75}Ga_{0.25}As$ X–point potential energy barriers, the conduction band discontinuity at the interfaces is taken to be 238 meV. When the large longitudinal $Al_{0.75}Ga_{0.25}As$ X–point electron mass $m_{X_l}^* = 1.15\,m_0$ is used, two quasi–stationary X–states, $E_1^X = 21$ meV and $E_2^X = 151$ meV, are found in the well. These values are listed in Table 4.3. As indicated in Table 4.6, good agreement may then be obtained between the calculated energy band diagrams and the experimental I–V curves. Figs.4.23(a) and (b) show the conduction band edges of the structure under applied biases of 15 and 110 mV. They reveal that these voltages correspond to the turn–offs of resonant tunneling via E_1^X and E_1^Γ, respectively. In reverse bias, peaks in current are anticipated at −90 and −190 mV. These are precisely the voltages at which the negative differential resistances are observed in Fig.4.22. These results suggest that the tunnel barriers are made of indirect $Al_xGa_{1-x}As$ alloys, and that the two peaks in current obtained in the experimental I–V characteristics in each bias direction arise from tunneling via the quasi–stationary levels E_1^X and E_1^Γ in the well.

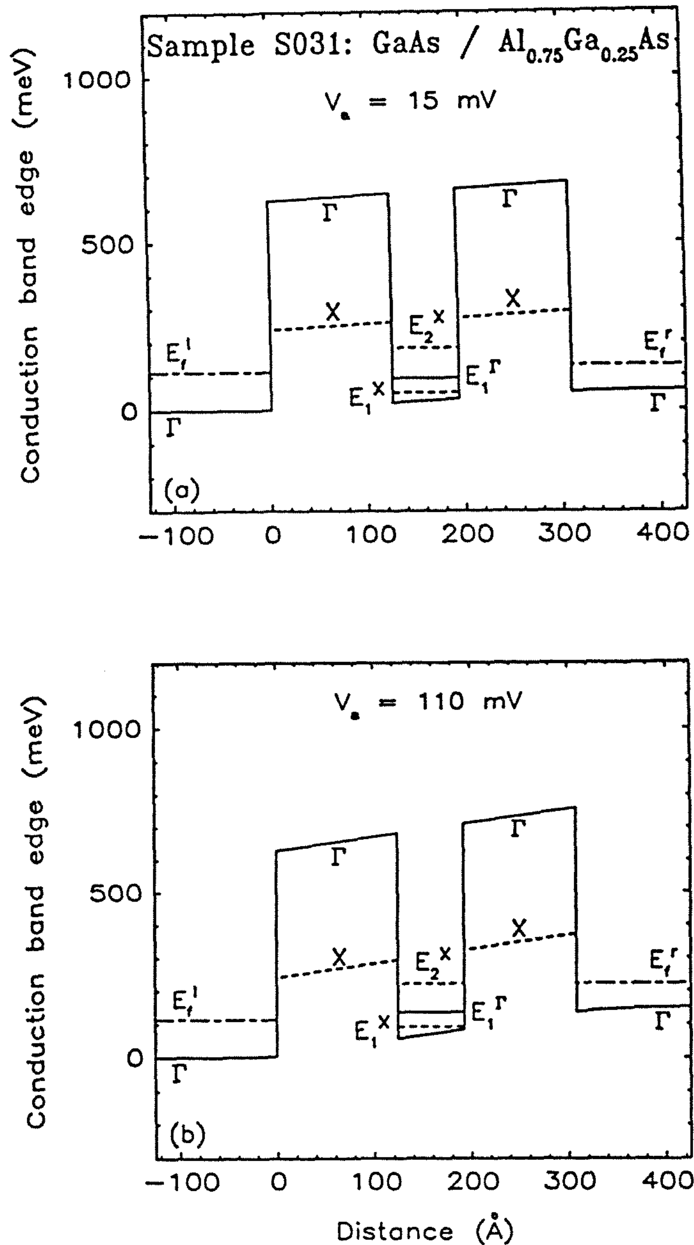

Figure 4.23: Calculated Γ–point conduction band edges for sample S031, assuming that the barrier layers are made of $Al_{0.75}Ga_{0.25}As$ and that the average doping density in the back GaAs cladding layer is $1.5 \times 10^{18} cm^{-3}$. The barriers and the well are assumed to be undoped. (a) and (b) correspond to applied biases of 15 and 110 mV, respectively. They illustrate the turn–offs of resonant tunneling via E_1^X and E_1^Γ.

These concepts may be confirmed by studying sample S032. In this heterostructure, the electron density in the top GaAs electrode is $1.5 \times 10^{18} cm^{-3}$. The GaAs buffer layer, about 0.2 μm thick, is doped n–type at $2 \times 10^{17} cm^{-3}$. The experimental I–V characteristics are thus expected to be more symmetric than in S031. As indicated in Table 4.2, the average doping density in the back GaAs cladding layer is taken to be $1.2 \times 10^{18} cm^{-3}$. Fig.4.24 shows an experimental I–V curve at 4.2 K for a circular device, 50 μm in diameter. As in S031, two negative differential resistances are observed in each bias direction, and resonant tunneling occurs as soon as a voltage is applied to the structure. This indicates that the lowest resonant state is close to the bottom of the well. The first peaks in current occur at $V_1^R = -45$ mV in reverse bias and $V_1^F = 30$ mV in forward bias. The other peaks are obtained at $V_2^R = -340$ mV and $V_2^F = 275$ mV. In this heterostructure, the GaAs well is 45 Å wide. Consequently, only one quasi–bound level, $E_1^\Gamma = 83$ meV, would exist in the well if the barrier layers were made of $Al_{0.35}Ga_{0.65}As$. This is even more inconsistent with the experimental results than in the case of sample S031. However, if the barriers are assumed to be undoped and made of $Al_{0.75}Ga_{0.25}As$, the lowest energy levels in the quantum well are $E_1^X = 32$ meV and $E_1^\Gamma = 112$ meV. The two energy band profiles shown in Figs.4.25(a) and (b) correspond to applied biases of 70 and 270 mV, respectively. They illustrate the turn–on and turn–off of resonant tunneling via E_1^Γ in forward bias. Other results obtained from energy band diagram calculations are given in Table 4.6. They are in reasonably good agreement with the experimental I–V data. As in sample S031, they confirm that the tunnel barriers are made of indirect $Al_xGa_{1-x}As$ alloys, and that the two negative differential resistances observed in the I–V curves in each bias direction are consistent with resonant tunneling via E_1^X and E_1^Γ.

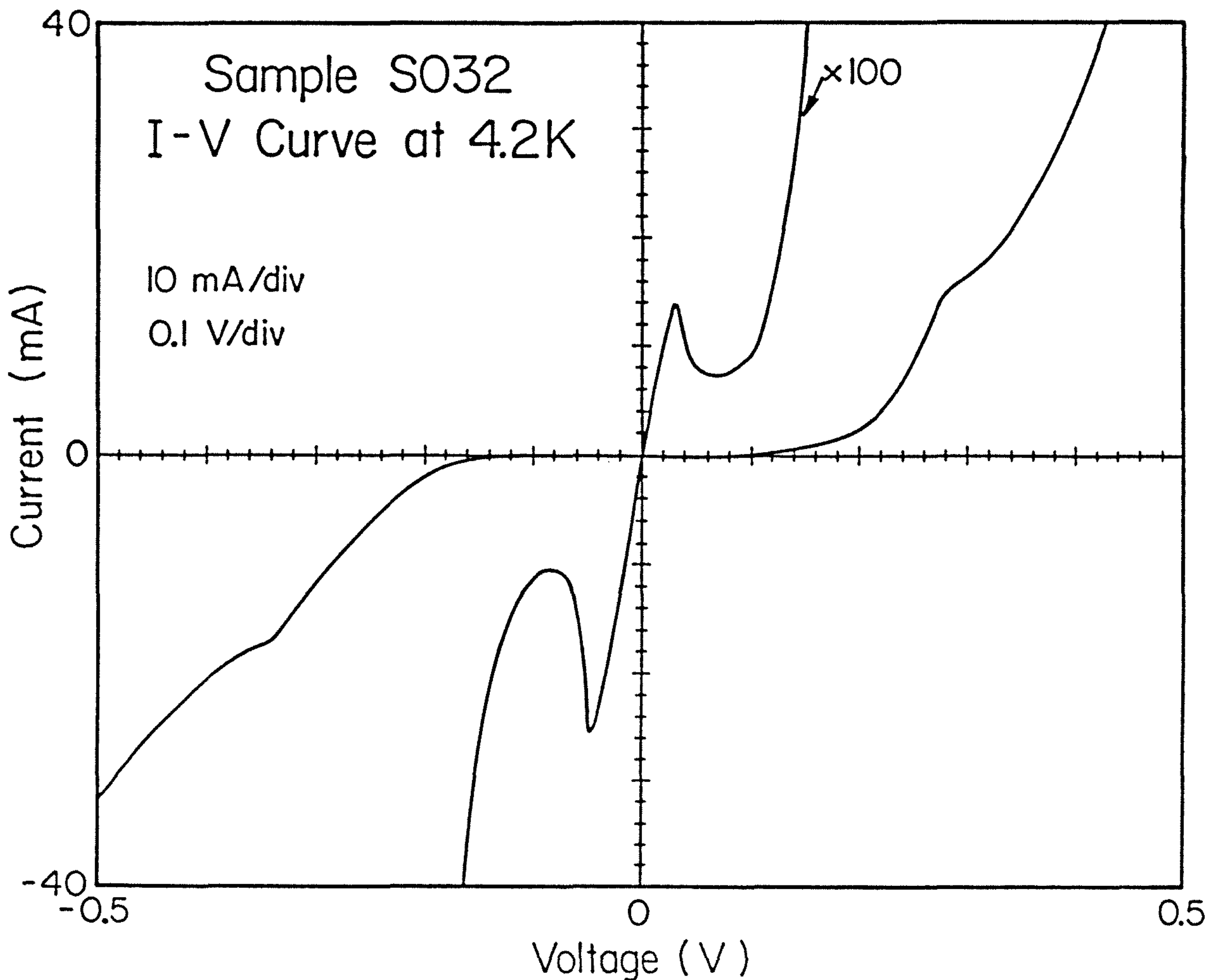

Figure 4.24: Experimental *I–V* characteristic at 4.2 K for a circular device, 50 μm in diameter, fabricated on sample S032. In sample S032, the 0.2 μm thick GaAs buffer layer is doped n–type at $2 \times 10^{17} cm^{-3}$. The doping density in the top GaAs electrode is $1.5 \times 10^{18} cm^{-3}$. The barrier layer closer to the substrate is 104.5 Å thick. The other barrier is 102 Å thick. The GaAs quantum well is 45 Å wide.

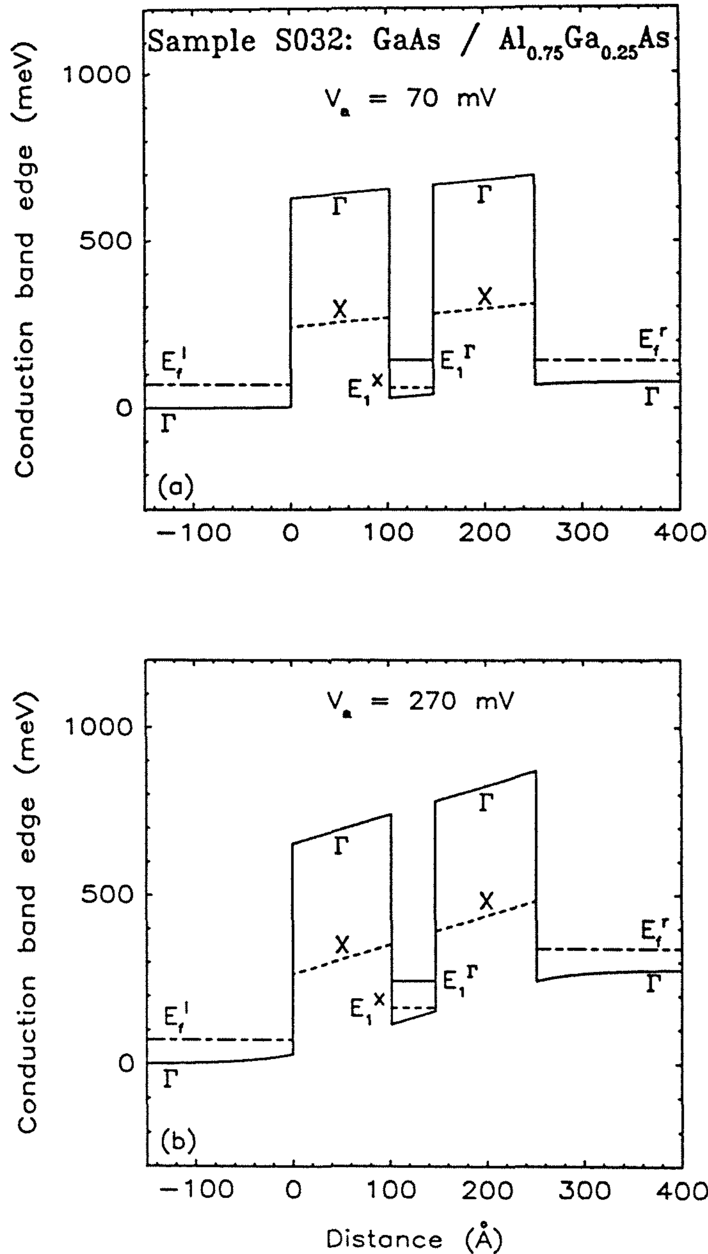

Figure 4.25: Calculated Γ–point conduction band edges for sample S032, assuming that the barrier layers are made of $Al_{0.75}Ga_{0.25}As$ and that the average doping density in the back GaAs cladding layer is $1.2 \times 10^{18} cm^{-3}$. The barriers and the well are assumed to be undoped. (a) and (b) correspond to applied biases of 70 and 270 mV, respectively. They illustrate the turn–on and turn–off of resonant tunneling via E_1^Γ.

4.7 Summary

This chapter presented a study of resonant tunneling in GaAs/$Al_xGa_{1-x}As$ double barrier heterostructures grown epitaxially in the [100]-direction. The objective of this study was to identify the resonant energy levels in the GaAs quantum well which produce the negative differential resistances observed in experimental *I–V* characteristics. This was achieved by comparing the experimental *I–V* data to results anticipated from the calculated energy band diagrams of the structures. This provided useful information, not only about the nature of the dominant tunneling processes occurring in double barrier heterostructures, but also about their relative contributions to the total current. The main results of this study may be summarized as follows. (*i*) Energy band diagrams give the actual shapes of the potential energy barriers through which the charge carriers tunnel. These shapes may differ significantly from those based on the usual assumption that the entire applied voltage drops linearly across the quantum barriers and well. (*ii*) Taking into account band bending effects and the fractions of the applied bias sustained by the cladding layers is critical for obtaining good agreement between the positions of the quasi–stationary levels in the GaAs quantum well and the peaks in current observed in the experimental *I–V* curves. (*iii*) In samples having direct band gap $Al_xGa_{1-x}As$ tunnel barriers, the negative differential resistances arise from resonant tunneling via quasi–stationary states in the well bound by the $Al_xGa_{1-x}As$ Γ–point potential energy barriers. (*iv*) When the barrier layers are made of pure AlAs, tunneling via resonant Γ–states alone is often inconsistent with the *I–V* characteristics of the samples. However, the experimental *I–V* data can usually be explained by tunneling via energy levels confined in the well by the AlAs X–point potential energy barriers in addition to resonant tunneling via states bound by the AlAs Γ–point barriers. Furthermore, the quasi–stationary X–states are found to be associated with

the large longitudinal X–point electron mass in AlAs, and not with the small transverse effective mass. This reveals that tunneling through the indirect AlAs band gap arises primarily from the breaking of translational symmetry in the direction perpendicular to the heterojunction interfaces. This causes electronic states having Γ–symmetry in GaAs and X–symmetry in AlAs to mix. (*v*) The relative contributions to the total current of tunneling via Γ– and X–resonant states in the quantum well are found to vary from sample to sample. In some heterostructures, they also depend upon the sign of the applied bias. Such effects should thus be related to the quality of the materials and the heterojunction interfaces rather than to the layer thicknesses or doping densities. In addition, the multiple current transport mechanisms occurring in GaAs/AlAs resonant tunneling heterostructures are consistent with the small peak–to–valley current ratios usually obtained from these structures. (*vi*) These results suggest that low temperature current transport in double barrier heterostructures having indirect band gap $Al_xGa_{1-x}As$ barrier layers should be dominated by resonant tunneling via quasi–stationary Γ– and X–states. For these structures as well, energy band diagrams should be essential to correlate without ambiguity the experimental negative differential resistances with the resonant states in the GaAs quantum well. Energy band profiles should thus be important in theoretical I–V curve calculations. They may also provide useful information about certain structure parameters which are difficult to determine accurately, such as doping densities and Al compositions in the quantum barriers. (*vii*) Resonant tunneling has also been investigated in double barrier heterostructures in which a low doped GaAs buffer layer is grown between the degenerately doped GaAs electrode adjacent to the substrate and the first $Al_xGa_{1-x}As$ quantum barrier. As long as the buffer layer is thin compared to the GaAs electrode on top of which it is grown, the structure behaves as if it had a uniformly doped back GaAs cladding layer. The

average doping density in this layer decreases as the GaAs buffer layer is made thicker and/or more lightly doped. In these samples, the negative differential resistances corresponding to a given resonant state in the quantum well may be observed in the experimental I–V characteristics at very different applied voltages in reverse bias than in forward bias. This may be used to determine the degree of asymmetry between the doping density in the top GaAs electrode and the average doping level in the back cladding layer.

Table 4.3: Resonant states in the GaAs well, calculated from the conduction band edge at the middle of the well in the unbiased structure.

Sample	Well	X–States :	(transverse $m^*_{X_t}$)	X–States :	(longitudinal $m^*_{X_l}$)		Γ–States	
	Thickness (Å)	ϵ^X_1 (meV)	ϵ^X_2 (meV)	E^X_1 (meV)	E^X_2 (meV)	E^Γ_1 (meV)	E^Γ_2 (meV)	E^Γ_3 (meV)
489	42.5	—	—	—	—	89	—	—
H283	90.5	26	114	14	92	44	178	406
H392	51	52	—	26	—	105	433	948
H408	62	42	176	22	165	78	325	730
H418	28.5	90	—	47	—	225	898	—
H475	76.5	33	142	17	120	57	235	535
H919	34	77	—	40	—	184	755	—
H927	45	59	—	30	—	125	517	—
H943	34	—	—	—	—	110	—	—
H945	25.5	—	—	—	—	139	—	—
S009	51	—	—	—	—	73	242	—
S008	65	—	—	—	—	54	202	—
S031	68	40	177	21	151	63	256	562
S032	45	65	—	32	—	112	448	—

Table 4.4: Resonant states in the GaAs quantum well producing negative differential resistances in the experimental I–V characteristics.

Structures with $Al_{0.35}Ga_{0.65}As$ barrier layers

Sample	Resonance	Energy Band Diagram Calculations: Turn–on Voltage (mV)	Energy Band Diagram Calculations: Turn–off Voltage (mV)	Experimental Results: Turn–on Voltage (mV)	Experimental Results: Turn–off Voltage (mV)	Experimental Results: (I_p/I_v) (4.2 K)	Experimental Results: NDR Width (mV)
489	Reverse Bias:						
	E_1^Γ	−75	−260	−75	−260	4.3	80
	Forward Bias:						
	E_1^Γ	75	260	75	260	4.3	80
H943	Reverse Bias:						
	E_1^Γ	−150	−420	−140	−420	2.5	90
	Forward Bias:						
	E_1^Γ	150	420	140	420	2.6	90
H945	Reverse Bias:						
	E_1^Γ	−170	−550	−160	−550	2.5	80
	Forward Bias:						
	E_1^Γ	170	550	150	550	2.2	90
S009	Reverse Bias:						
	E_1^Γ	−60	−255	−60	−255	1.6	50
	Forward Bias:						
	E_1^Γ	60	255	60	255	1.5	45

Table 4.5: Resonant states in the GaAs quantum well producing negative differential resistances in the experimental I–V characteristics.

Structures with AlAs barrier layers

Sample	Resonance	Energy Band Diagram Calculations: Turn–on Voltage (mV)	Energy Band Diagram Calculations: Turn–off Voltage (mV)	Experimental Results: Turn–on Voltage (mV)	Experimental Results: Turn–off Voltage (mV)	Experimental Results: (I_p/I_v) (4.2 K)	Experimental Results: NDR Width (mV)
H283	Reverse Bias:						
	E_1^X	0	−45	0	−45	in $(d^2I/dv^2)(V)$	—
	E_2^X	0	−310	—	—	—	—
	E_1^Γ	0	−150	0	−150	inflection	—
	Forward Bias:						
	E_1^X	0	50	0	50	inflection	—
	E_2^X	0	330	0	340	1.5	55
	E_1^Γ	0	160	—	—	—	—
H392	Reverse Bias:						
	E_1^Γ	−150	−470	−140	−460	1.4	60
	Forward Bias:						
	E_1^Γ	120	310	—	—	—	—
H408	Reverse Bias:						
	E_1^X	0	−140	0	−140	2.2	40
	E_2^X	−250	−750	≈ −250	−750	inflection	—
	E_1^Γ	−140	−250	≈ −140	−250	4.0	40
	Forward Bias:						
	E_1^X	0	135	0	135	2.6	40
	E_2^X	240	650	≈ 240	650	inflection	—
	E_1^Γ	135	240	≈ 135	240	3.5	40

Sample	Resonance	Energy Band Diagram Calculations:		Experimental Results:			
		Turn–on Voltage (mV)	Turn–off Voltage (mV)	Turn–on Voltage (mV)	Turn–off Voltage (mV)	(I_p/I_v) (4.2 K)	NDR Width (mV)
H418	Reverse Bias:						
	E_1^Γ	−420	−1100	−400	−1100	1.3	70
	Forward Bias:						
	E_1^Γ	350	830	340	840	1.4	70
H475	Reverse Bias:						
	E_1^X	−40	−100	−40	—	—	—
	E_2^X	−240	−450	—	—	—	—
	E_1^Γ	−110	−190	—	−190	1.4	10
	Forward Bias:						
	E_1^X	35	90	35	90	2.1	50
	E_2^X	220	420	≈ 200	420	inflection	—
	E_1^Γ	100	175	—	—	—	—
H919	Reverse Bias:						
	E_1^Γ	−330	−870	≈ −280	−880	1.8	90
	Forward Bias:						
	E_1^Γ	300	740	≈ 250	750	inflection	—
H927	Reverse Bias:						
	E_1^X	−90	−200	−90	−200	1.9	40
	E_1^Γ	−280	−480	≈ −260	−480	inflection	—
	Forward Bias:						
	E_1^X	110	240	100	240	1.6	35
	E_1^Γ	320	530	≈ 300	530	inflection	—

Table 4.6: Resonant states in the GaAs quantum well producing negative differential resistances in the experimental I–V characteristics.

Structures with a GaAs buffer layer between the back GaAs electrode and the first $Al_xGa_{1-x}As$ barrier

Sample	Resonance	Energy Band Diagram Calculations:		Experimental Results:			
		Turn–on Voltage (mV)	Turn–off Voltage (mV)	Turn–on Voltage (mV)	Turn–off Voltage (mV)	(I_p/I_v) (4.2 K)	NDR Width (mV)
S008	Reverse Bias:						
	E_1^Γ	0	−140	0	−140	8.5	100
	E_2^Γ	−185	−520	≈ −185	−520	inflection	—
	Forward Bias:						
	E_1^Γ	0	120	0	120	5.0	100
	E_2^Γ	180	485	≈ 180	480	inflection	—
S031	Reverse Bias:						
	E_1^X	0	−90	0	−90	1.7	15
	E_1^Γ	0	−190	0	−190	inflection	—
	Forward Bias:						
	E_1^X	0	15	0	15	2.0	15
	E_1^Γ	0	110	0	110	inflection	—
S032	Reverse Bias:						
	E_1^X	0	−60	0	−45	2.5	40
	E_1^Γ	−90	−340	≈ −90	−340	inflection	—
	Forward Bias:						
	E_1^X	0	45	0	30	2.0	40
	E_1^Γ	70	270	≈ 70	275	inflection	—

References

1. R. Tsu, and L. Esaki, Appl. Phys. Lett. **22**, 562 (1973).

2. L. L. Chang, L. Esaki, and R. Tsu, Appl. Phys. Lett. **24**, 593 (1974).

3. M. O. Vassell, Johnson Lee, and H. F. Lockwood, J. Appl. Phys. **54**, 5206 (1983).

4. T. C. L. G. Sollner, W. D. Goodhue, P. E. Tannenwald, C. D. Parker, and D. D. Peck, Appl. Phys. Lett. **43**, 588 (1983).

5. A. R. Bonnefoi, R. T. Collins, T. C. McGill, R. D. Burnham, and F. A. Ponce, Appl. Phys. Lett. **46**, 285 (1985).

6. T. J. Shewchuk, P. C. Chapin, P. D. Coleman, W. Kopp, R. Fischer, and H. Morkoç, Appl. Phys. Lett. **46**, 508 (1985).

7. M. A. Reed, "Excited State Resonant Tunneling in GaAs–$Al_xGa_{1-x}As$ Double Barrier Heterostructures," to be published in *Superlattices and Microstructures*, (Academic Press).

8. E. E. Mendez, W. I. Wang, B. Ricco, and L. Esaki, Appl. Phys. Lett. **47**, 415 (1985).

9. E. E. Mendez, E. Calleja, C. E. T. Gonçalves da Silva, L. L. Chang, and W. I. Wang, to be published in Phys. Rev. B.

10. T. C. L. G. Sollner, P. E. Tannenwald, D. D. Peck, and W. D. Goodhue, Appl. Phys. Lett. **45**, 1319 (1984).

11. F. Capasso, and R. A. Kiehl, J. Appl. Phys. **58**, 1366 (1985).

12. A. R. Bonnefoi, D. H. Chow, and T. C. McGill, Appl. Phys. Lett. **47**, 888 (1985).

13. A. R. Bonnefoi, T. C. McGill, and R. D. Burnham, IEEE Electr. Dev. Lett. **EDL–6**, 636 (1985).

14. T. K. Woodward, T. C. McGill, and R. D. Burnham, "Experimental Realization of a Resonant Tunneling Transistor," to be published.

15. M. A. Reed, Private communication.

16. G. Y. Wu, A. R. Bonnefoi, and T. C. McGill, "The Role of Barrier Phonons in the Tunneling *I–V* Characteristics of Double Barrier Heterostructures," to be published.

17. B. A. Joyce, and C. T. Foxon, Inst. Phys. Conf. Ser. **32**, 17 (1977).

18. B. Ricco, and M. Ya. Azbel, Phys. Rev. B **29**, 1970 (1984).

19. A. R. Bonnefoi, D. H. Chow, T. C. McGill, R. D. Burnham, and F. A. Ponce, J. Vac. Sci. Technol. B **4**, 988 (1986).

20. H. C. Casey, and M. B. Panish, *Heterostructure Lasers. Part A*, (Academic Press, New York, 1978), p.192.

21. J. Batey, and S. L. Wright, J. Appl. Phys. **59**, 200 (1986).

Chapter 5

Resonant Tunneling Transistors

5.1 Introduction

Electronic devices based on tunneling are a source of increasing interest. In particular, resonant tunneling in structures made of two GaAs electrodes separated by two thin $Al_xGa_{1-x}As$ barriers and a GaAs quantum well have been extensively studied.[1–6] Two important properties of these double barrier heterostructures are (*i*) the presence of negative differential resistances in their current–voltage (*I*-*V*) characteristics, and (*ii*) expected operating frequencies in the terahertz range.[2] While it is true that these two–terminal tunnel structures have a number of potential applications, three–terminal devices would be preferable in many cases.[7]

In this chapter, we propose and analyze three–terminal devices based on resonant tunneling through quantum well and quantum barrier heterostructures. Although other semiconductors could be used, the devices are presented in the context of $GaAs/Al_xGa_{1-x}As$ heterojunction technology. Since tunneling is the main current transport mechanism, these devices should feature the high–speed capabilities associated with tunnel structures.

Two types of resonant tunneling transistors are proposed. The first kind includes devices in which, in order to achieve large emitter–collector current transfer ratios, the relative positions of the base and collector are interchanged with respect to the conventional emitter–base–collector sequence. These devices may thus be called "Inverted Base–Collector Tunnel Transistors." Two configurations are presented and discussed in section 5.2. In the three–terminal devices of the second kind, the current through a resonant tunneling double barrier heterostructure is modulated by a Schottky barrier gate placed along the path of the electrons. In fact, these devices can be viewed simply as tunnel structures integrated with Schottky barrier field effect transistors (FET's). Three configurations are proposed and analyzed in section 5.3. Finally, the results of this chapter are summarized in section 5.4.

5.2 Inverted Base–Collector Tunnel Transistors

Two novel three–terminal devices based on tunneling in quantum well and quantum barrier heterostructures are proposed and analyzed theoretically. In both devices, the relative positions of the base and collector are interchanged from the conventional emitter–base–collector sequence. This provides a means for obtaining negligible base currents and large current transfer ratios. In both cases, a base voltage controls the emitter–collector tunneling current by shifting the resonances in a quantum well. Calculations indicate that significant variations in the emitter–collector current–voltage characteristics can be obtained for reasonable base–emitter voltages. These two devices are called a "Stark Effect Transistor," and a "Negative Resistance Stark Effect Transistor," respectively.

The idea of making three–terminal devices based on tunneling was pioneered

in 1960 by C. A. Mead.[8] He proposed a metal–insulator–metal–insulator–metal hot–electron transistor. A number of devices based on this concept have been proposed and investigated experimentally.[9–12] All of these structures suffer from very small emitter–collector current transfer ratios due to large base currents.

Recently, Jogai and Wang[13] calculated the tunneling current for a conceptual three–terminal, double–barrier device consisting of alternating layers of GaAs and $Al_xGa_{1-x}As$, forming the emitter, base and collector. They proposed a configuration in which the base contact would be made to the GaAs quantum well and the two barriers would be independently biased. A highly conductive base was required so that a potential could be applied to it, but no base current was allowed to flow. This is a somewhat unphysical and unrealistic assumption. In addition, varying the collector–base voltage did not produce very significant changes in the device current–voltage characteristics.

In this section, we propose and analyze two three–terminal devices which we expect to have reduced base currents and improved device performance. Since tunneling is the main current transport mechanism, these devices should feature the high–speed characteristics associated with tunnel structures. They should also have large emitter–collector current transfer ratios. The key step in achieving this goal is to interchange the relative positions of the base and collector, thus locating the latter in the region where current is most likely to flow. Fig.5.1 shows schematically the first proposed structure, together with its energy band diagram at equilibrium. The emitter is an n–type GaAs layer. Doping concentrations on the order of 5×10^{16}–$5 \times 10^{17} cm^{-3}$ should provide sufficient tunneling currents and, at the same time, allow resonant tunneling effects to be observed at room temperature.[6] The emitter is followed by a thin undoped $Al_{x_1}Ga_{1-x_1}As$ tunneling barrier and a lightly doped n–type quantum well. The collector contact is made to the well. Alloys which give shallow and abrupt ohmic contacts, such as Au/Ge–

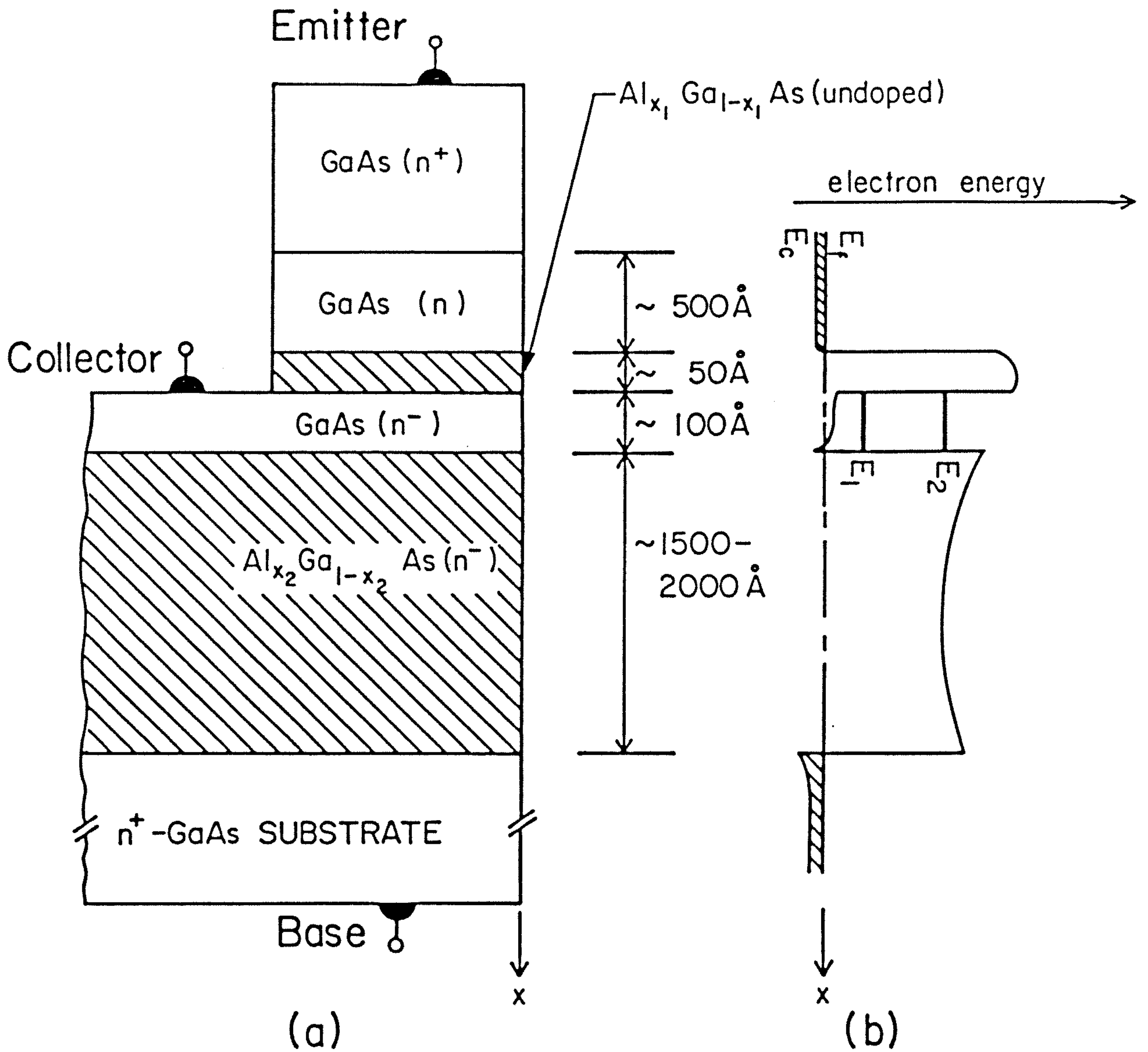

Figure 5.1: Schematic diagrams (not to scale) of: (a) a cross section of the proposed "Stark Effect Transistor" (SET); (b) the conduction band edge at equilibrium as a function of position in the x–direction (perpendicular to the layers).

Ag–Au or Au/Ge–Au–WSi for example, should be used. The next layer is a lightly doped $Al_{x_2}Ga_{1-x_2}As$ barrier, sufficiently thick to prevent electrons from tunneling through it. In addition, an alloy with large Al composition is desirable to minimize thermionic emission over the barrier. Finally, a heavily doped n–type GaAs substrate serves as the base electrode.

The principle of operation of the proposed device is described below. First, let us consider the case in which no base voltage is applied. When the collector is biased positively with respect to the emitter, electrons near the Fermi level in the emitter tunnel through the thin $Al_{x_1}Ga_{1-x_1}As$ barrier into the collector. As long as the emitter Fermi level remains below the first subband in the well, a negligible tunneling current is expected. When the bias voltage is such that the emitter Fermi level reaches the first subband, the current is significantly increased. The current–voltage (I–V) characteristics should thus feature enhancements corresponding to the alignment of the emitter Fermi level with each resonance in the well. If a potential difference, V_{BE}, is now applied between the base and emitter, an electric field perpendicular to the layers is created. The field will modify the positions of the subbands in the well with respect to the emitter Fermi level and thus modulate the tunneling current. The field will penetrate into the quantum well region for the following reasons: (*i*) the barriers and well are lightly doped; (*ii*) the $Al_{x_2}Ga_{1-x_2}As$ barrier is not thick enough to drop all of the base–emitter voltage; (*iii*) the device geometry is such that the collector contact does not completely shield the emitter from the base.

Theoretical I–V characteristics for the device are shown in Fig.5.2.[14] These curves were calculated using Bardeen's many–particle tunneling formalism.[15] In this approach, which starts from Fermi's Golden Rule, the density of final states, ρ_f, appears explicitly in the calculation. In the present case, ρ_f is simply a sum of step functions since each resonance in the well is the bottom of a two–dimensional

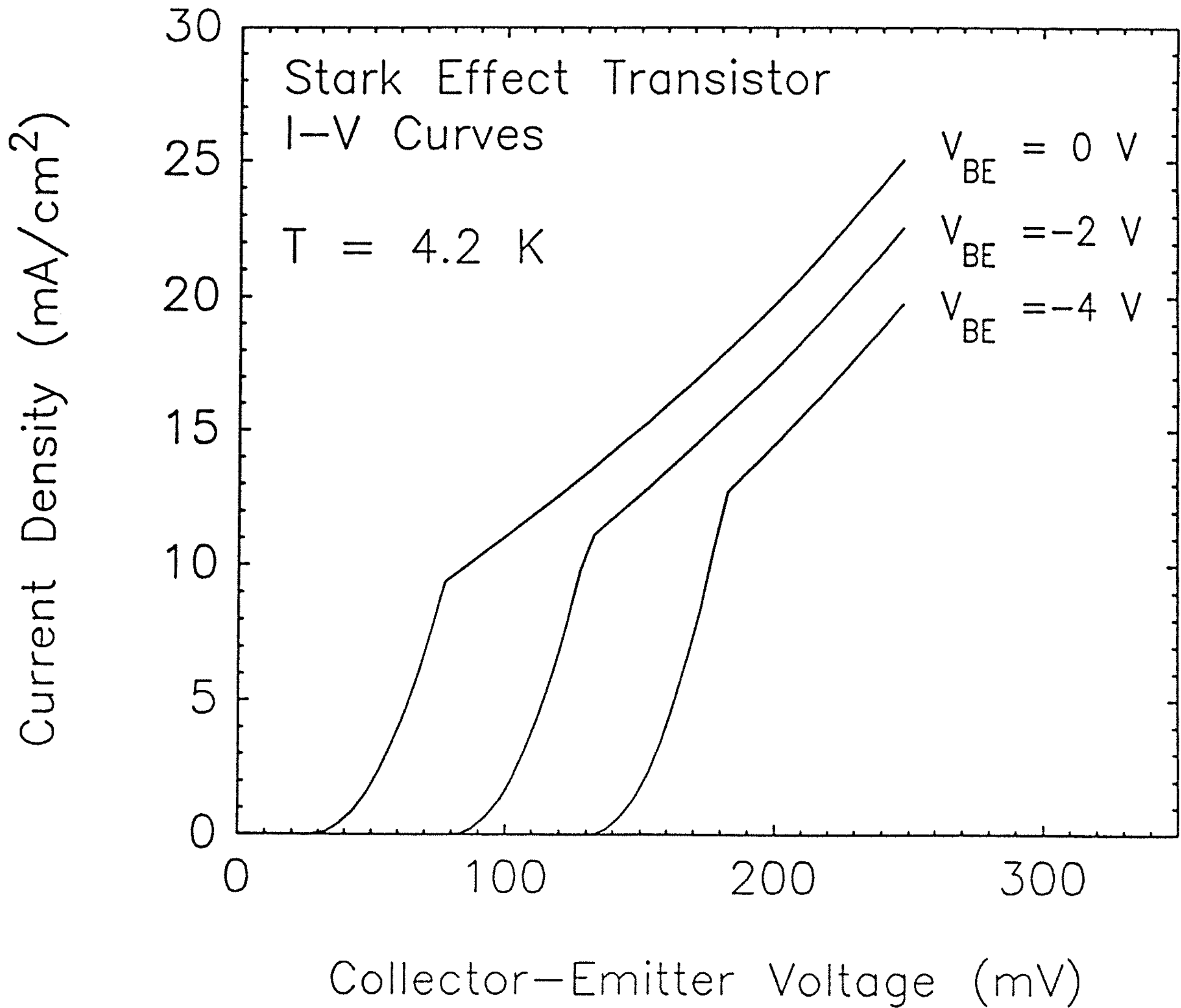

Figure 5.2: Calculated current–voltage characteristics for the "Stark Effect Transistor" (SET). The barriers are pure AlAs, 50 and 1000 Å thick, respectively. The well is a 50 Å thick GaAs layer. The conduction band offset is taken to be 0.96 eV.

energy band. The matrix element was calculated by using WKB wave functions in the barrier region. A two-band model, $\vec{k}.\vec{p}$ theory calculation was used to obtain the complex band structure in the barrier. The calculated curves display the substantial variations of the emitter–collector I–V characteristics which may be obtained by modulating V_{BE}. Base–emitter voltages much higher than those needed to produce significant transistor action can be applied without producing avalanche breakdowns. If V_{BE} is negative, the levels in the well are shifted upwards and a small negative current might flow to the emitter when V_{CE}, the collector–emitter voltage, is small. This is an additional incentive to make the well and the $Al_{x_2}Ga_{1-x_2}As$ barrier lightly doped.

The main advantage of this configuration is a negligible base current and thus a large current transfer ratio. Because the quasi–stationary states in the well are modulated by an electric field to produce transistor I–V characteristics, the proposed device could be called a "Stark Effect Transistor" (SET).

The transistor I–V curves described above can be modified and enhanced by adding a potential step in the GaAs well constituting the collector. The step can be a thin $Al_xGa_{1-x}As$ layer with an Al composition smaller than that of the barriers. Its main effect is to modify the relative positions of the resonant states in the well. The structure can now be designed to obtain a certain energy spectrum or to produce given shifts of some of the subbands. This makes it possible to optimize device performance according to the requirements or applications.

To further illustrate the concept of subband modulation by means of an electric field applied from a controlling electrode, another device configuration is proposed. It is characterized by a resonant tunneling double barrier heterostructure. Such a device structure is shown schematically in Fig.5.3, together with its energy band diagram at equilibrium. This device operates on the same principle as the "Stark Effect Transistor." The values of the fields and the shifts of the lev-

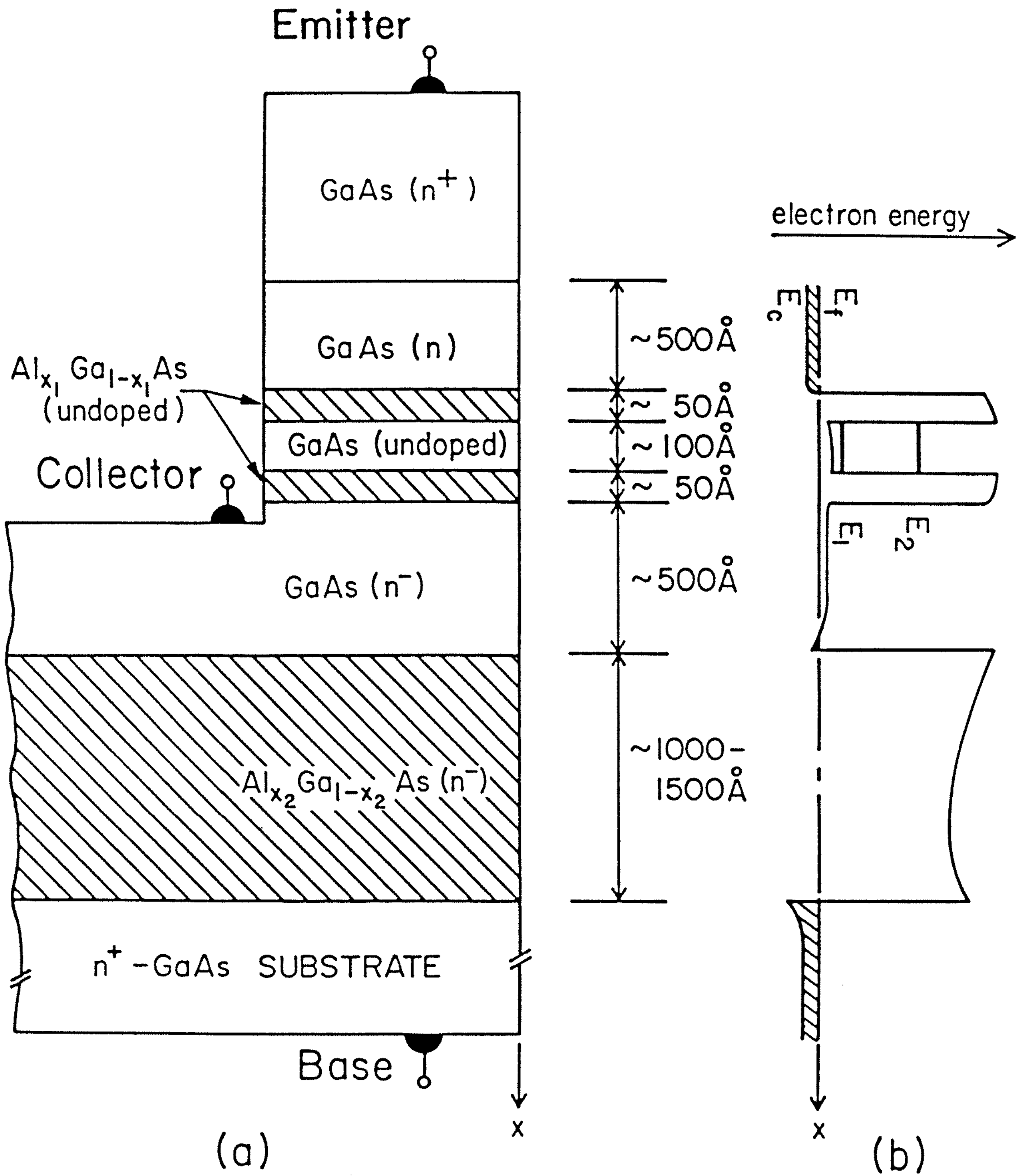

Figure 5.3: Schematic diagrams (not to scale) of: (a) a cross section of the proposed "Negative Resistance Stark Effect Transistor" (NERSET); (b) the conduction band edge at equilibrium as a function of position in the x–direction (perpendicular to the layers).

els resulting from the base–emitter modulating voltage were estimated to be on the same order of magnitude as before. However, in this case, no contact needs to be made to the quantum well. The essential feature of this device configuration is the presence, in the emitter–collector I–V characteristics, of negative differential resistances controlled by the base–emitter voltage.

Theoretical I–V characteristics for the device are shown in Fig.5.4. The approach of Vassell *et al.*[16] was used to calculate the tunneling current through the double barrier heterostructure separating the collector from the emitter. This device, which could be called a "Negative Resistance Stark Effect Transistor" (NERSET), offers several advantages over any double barrier configuration in which the base is located in the quantum well: (*i*) easier fabrication; (*ii*) no base current, and thus larger current transfer ratios; (*iii*) undoped well; (*iv*) no transverse electric fields in the well which destroy the coherence of wave functions across the entire double barrier structure. These last two conditions are essential for optimum resonant tunneling.

5.3 Resonant Tunneling Transistors with Controllable Negative Differential Resistances

The three–terminal devices of the second type are based on resonant tunneling through two quantum barriers separated by a quantum well. Each proposed device consists of a resonant tunneling double barrier heterostructure integrated with a Schottky barrier field effect transistor configuration. The essential feature of these devices is the presence, in their output current–voltage (I_D–V_D) curves, of negative differential resistances controlled by a gate voltage. Because of the high–speed characteristics associated with tunnel structures, these devices could find applications in tunable millimeter–wave oscillators, negative resistance amplifiers

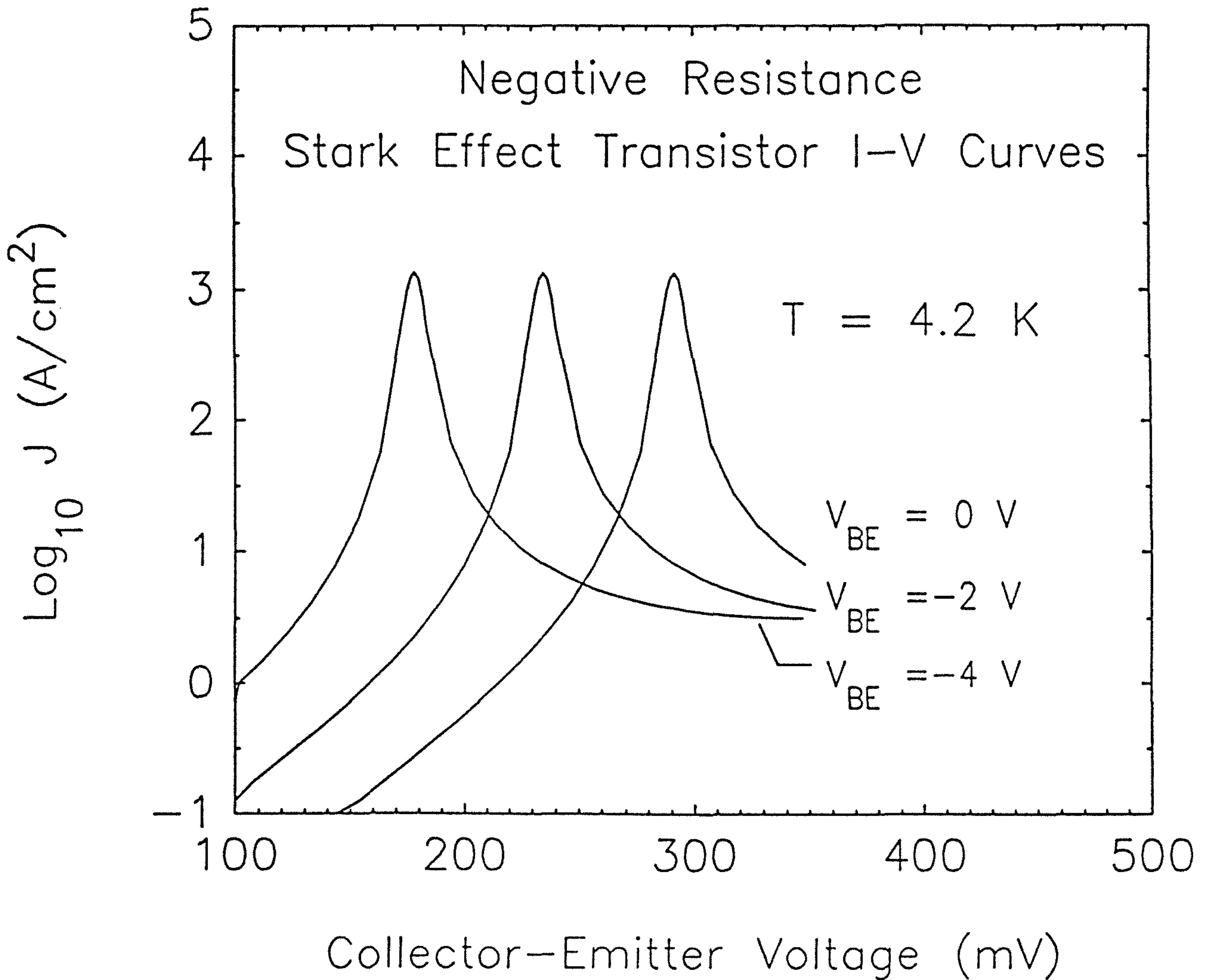

Figure 5.4: Calculated current–voltage characteristics for the "Negative Resistance Stark Effect Transistor" (NERSET). The tunnel barriers are 20 Å thick $Al_{0.6}Ga_{0.4}As$ layers, and the well a 50 Å thick GaAs layer. The conduction band offset is taken to be 0.5 eV.

and high–speed digital circuits.

In this section, we propose and analyze three–terminal devices in which the current through a resonant tunneling double barrier heterostructure is modulated by a Schottky barrier gate placed along the path of the electrons. In fact, these devices can be viewed simply as tunnel structures integrated with Schottky barrier field effect transistors (FET's). For small source–drain bias voltages, an FET operates in its linear mode and acts as a variable resistor controlled by the gate voltage. This property may be used to modulate the amplitude and position of the tunnel structure negative differential resistances. We could observe these effects by simply connecting one of our two–terminal tunnel structures[5] in series with a commercial FET. The I–V characteristics obtained in this simple test are shown in Fig.5.5 as a direct demonstration of this concept. However, by integrating the FET and double barrier heterostructure, dimensions can be reduced and parasitic resistances and noise minimized. These are essential requirements for high frequency performance.

The first proposed device structure is shown schematically in Fig.5.6. It consists of a resonant tunneling heterostructure integrated with a short channel MESFET. After tunneling through the quantum barriers and well, the flow of electrons is controlled by a Schottky barrier gate placed along a thin GaAs channel. The tunnel structure consists of two $Al_xGa_{1-x}As$ barriers, about 20–50 Å thick, separated by an undoped GaAs well, approximately 50 Å thick. For the top GaAs layer, donor concentrations of 5×10^{16}–$5 \times 10^{17} cm^{-3}$ should provide sufficient tunneling currents and, at the same time, allow resonant tunneling effects to be observed at room temperature.[6] Submicron microwave and millimeter–wave FET fabrication techniques can be used to form the gate and the source

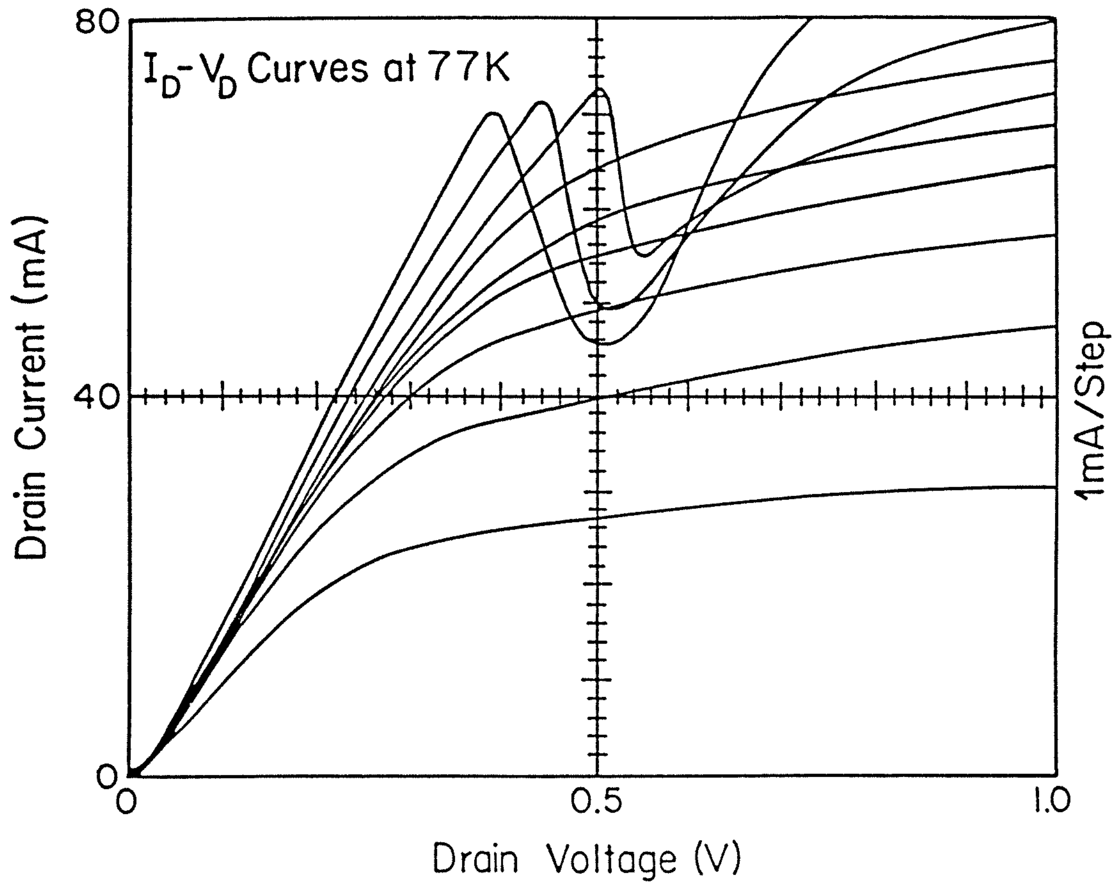

Figure 5.5: Experimental I–V characteristics at 77 K for a two–terminal resonant tunneling structure connected in series with a commercial n–channel enhancement–mode VMOS power FET.

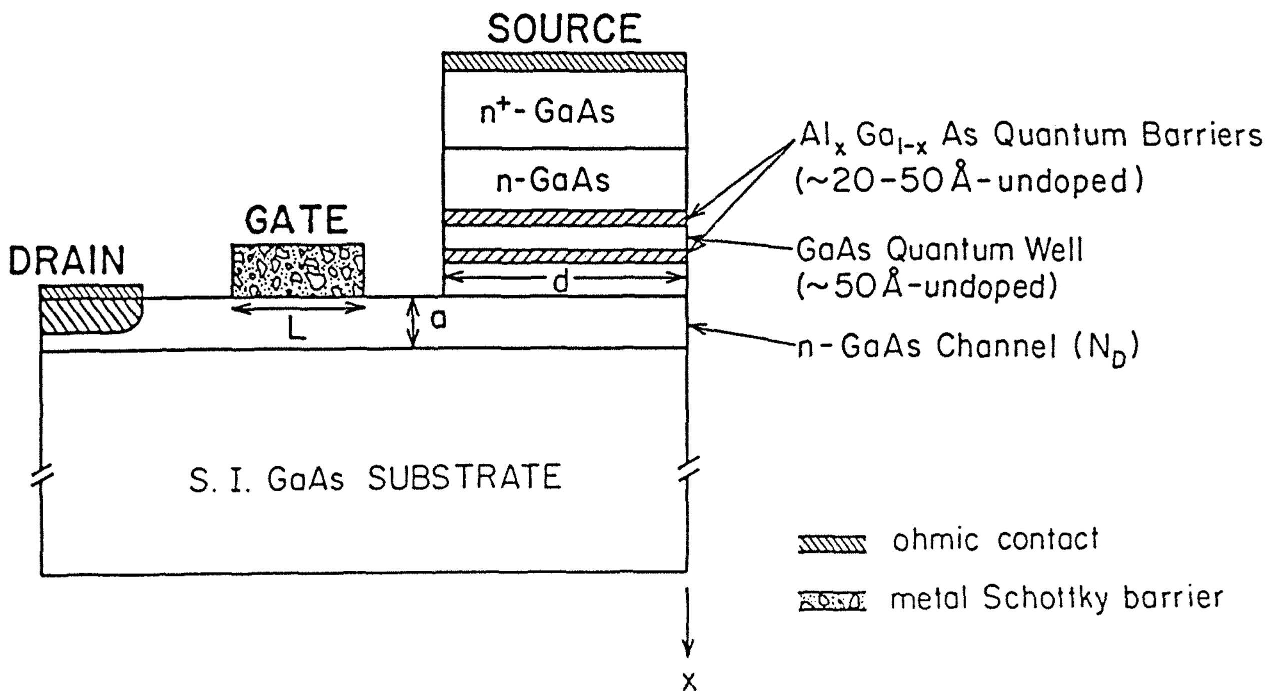

Figure 5.6: Schematic diagram (not to scale) of a cross section of the first proposed transistor structure, the "Resonant Tunneling MESFET." The device can be symmetric with respect to the x–axis to minimize channel resistance.

and drain ohmic contacts.[17–21]

Calculated output current–voltage (I_D–V_D) characteristics for the schematic of the device in Fig.5.6 are shown in Fig.5.7 for the first resonance. Because we are mainly interested in the linear regime of the FET, the two–region model of Pucel *et al.*[22] was used to obtain the velocity–field curve in the channel. For GaAs, this model has been shown to agree perfectly with two–dimensional analysis in the linear region, and to within $\pm 15\%$ in the saturation region.[23] The characteristics of the tunnel structure constituting the source were obtained by measuring the I–V curves of two–terminal resonant tunneling heterostructures. The growth technique, preparation procedure and properties of these two–terminal devices were discussed elsewhere.[3,5] The structure corresponding to Fig.5.7 had pure AlAs barriers, approximately 50 Å thick, and a nominally undoped GaAs quantum well, about 60 Å thick. The curves in Fig.5.7 were calculated using a channel width, a, of 0.20 μm, a gate length, L, of 0.75 μm, and a gate width, perpendicular to the plane of Fig.5.6, of 20 μm. The doping in the channel, N_D, was $1 \times 10^{17} cm^{-3}$. The source length, d, and width, perpendicular to the plane of Fig.5.6, were taken to be 3 and 20 μm, respectively. These curves display the substantial variations of the source–drain I_D–V_D characteristics which may be obtained by modulating the gate voltage. As the latter is decreased, the channel resistance increases, resulting in shifting the positions of the negative differential resistances towards larger drain voltages and eventually reducing their peak–to–valley current ratios. For proper operation, the FET must operate in its linear regime. Furthermore, the channel resistance must be smaller than the absolute value of the tunnel structure negative differential resistances over a reasonably wide range of gate bias voltages. Since typical transit times for tunneling through double barrier heterostructures should be on the order of 1ps or less, the millimeter–wave performance of these devices is limited by the transit

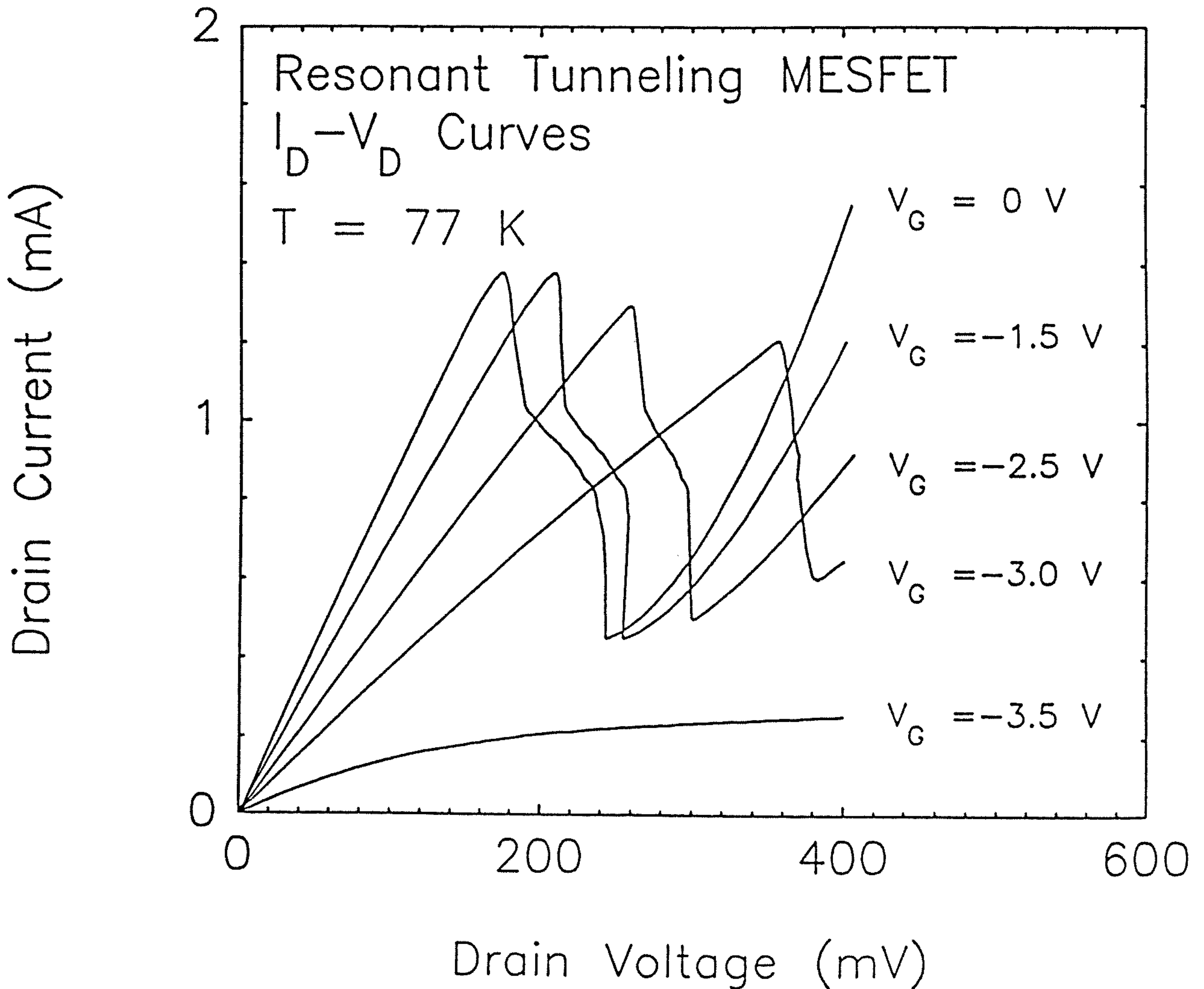

Figure 5.7: Calculated current–voltage (I_D–V_D) characteristics in the voltage range 0–400 mV for the "Resonant Tunneling MESFET" shown schematically in Fig.5.6. The channel width, a, gate length, L, and gate width, perpendicular to the plane of Fig.5.6, are taken to be 0.20 μm, 0.75 μm, and 20 μm, respectively. The doping in the channel, N_D, is $1 \times 10^{17} cm^{-3}$. The source length, d, and width, are taken to be 3 μm and 20 μm, respectively. The device is assumed to be symmetric with respect to the x–axis (Fig.5.6).

time of electrons in the channel. This delay time can be minimized by reducing the gate and channel lengths and by increasing the doping in the channel. Since the minimum gate length in GaAs FET's is about 0.1 μm, the expected maximum frequencies of operation should be on the order of 100 GHz.[23] Because they affect the ultimate performance of the device, the source–gate and gate–drain spacings are key parameters. The best values realized so far are 0.1 μm and 0.2 μm, respectively.[20] It should further be mentioned that charging times, which are important in all tunnel structures, may also influence the speed performance of the proposed devices.

The second proposed device is schematically illustrated in Fig.5.8. It consists of a resonant tunneling heterostructure integrated with a vertical FET.[24] The source contact is made to the top n^+–GaAs layer. It is followed first by the tunnel structure, and then by the GaAs active channel. Motion of the electrons in the channel is controlled by a Schottky barrier gate. The n^+–substrate acts as the drain. It should be noted that the device could also operate in a configuration in which the source and drain electrodes are interchanged. This structure has several advantages over the first proposed device: (*i*) the geometry is such that the path of the electrons remains perpendicular to the tunnel barriers; (*ii*) the fabrication procedure should be easier; (*iii*) the length of the active channel can be further reduced; (*iv*) more accurate control of the drain to source spacing can be achieved. This should result in maximum frequencies of operation substantially greater than those obtainable with the previous device configuration.

The third proposed structure, schematically illustrated in Fig.5.9, is a resonant tunneling heterostructure integrated with a permeable base transistor (PBT).[25,26] After tunneling through the double barrier heterostructure, the flow of electrons is controlled by a thin metal grating which is embedded within GaAs

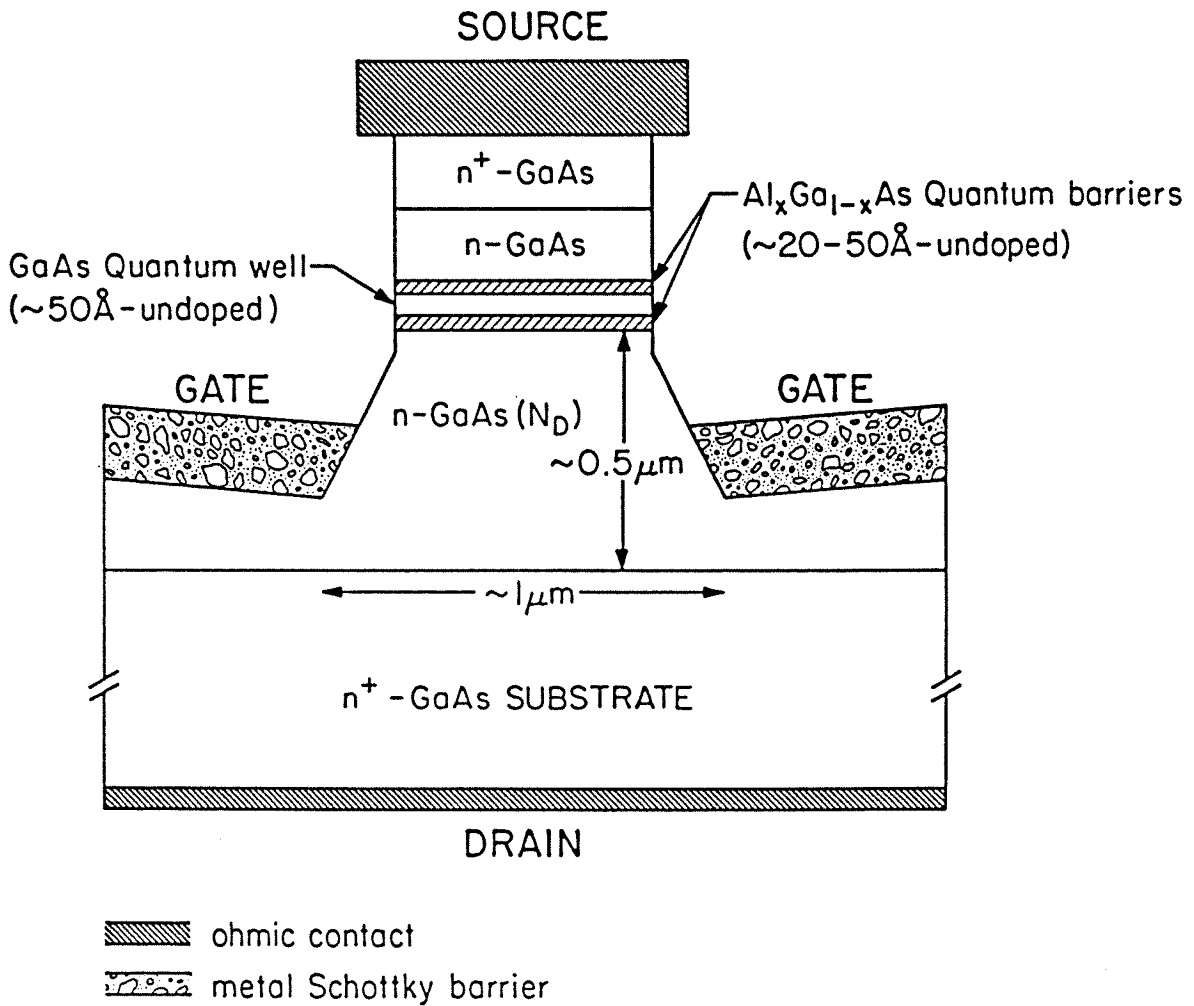

Figure 5.8: Schematic diagram (not to scale) of a cross section of the second proposed transistor structure, the "Resonant Tunneling Vertical FET."

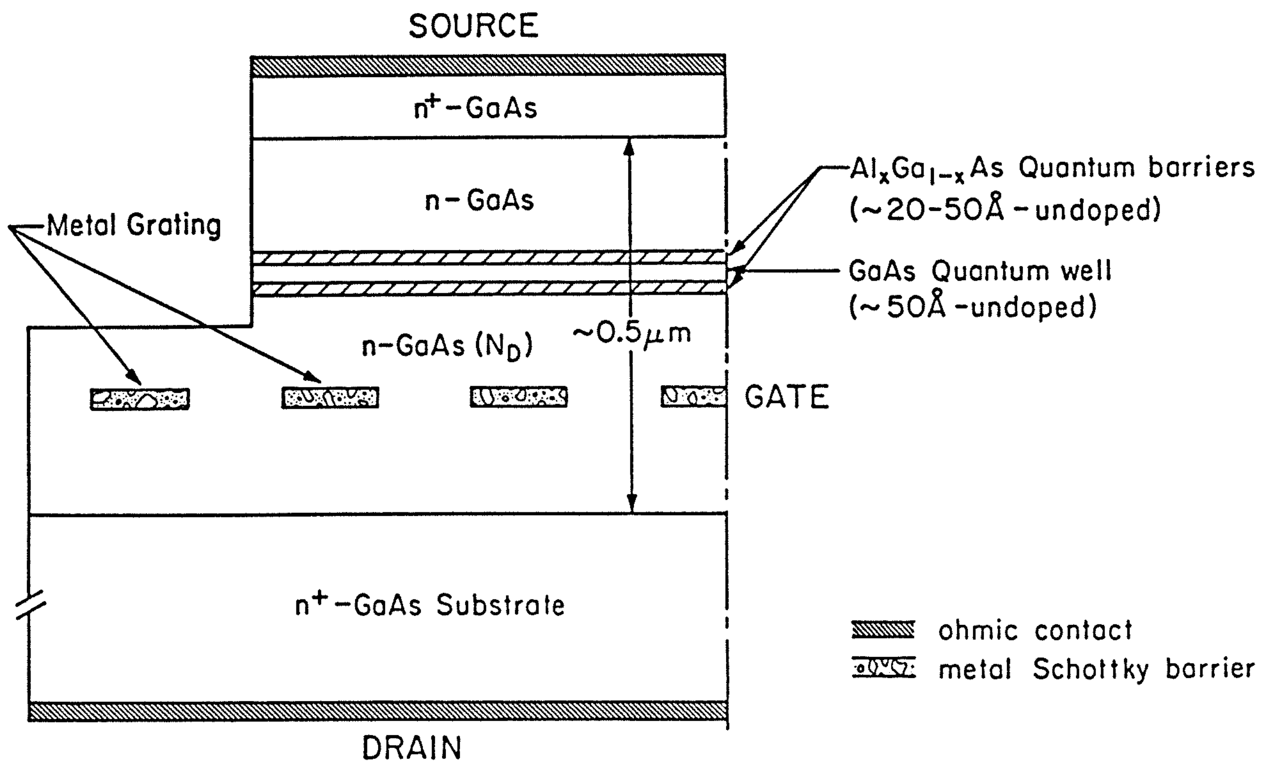

Figure 5.9: Schematic diagram (not to scale) of a cross section of the third proposed transistor structure, the "Resonant Tunneling PBT."

and forms a Schottky barrier gate. As in the previous device, the roles of the source and drain can be interchanged. It has been claimed that permeable base devices could, in principle, be capable of achieving maximum frequencies of oscillation near 1 THz.[25] This makes them promising for modulating tunnel structure negative differential resistances. Although it has been difficult in the past to achieve high quality epitaxial growth over metal films, improved growth techniques, or different approaches such as replacing the metal grating by *p*–type semiconductor grid fingers, appear to be promising.

5.4 Summary

We have proposed and analyzed two types of novel three–terminal devices based on resonant tunneling in quantum well and quantum barrier heterostructures.

The main characteristic of the devices of the first type is that the relative positions of the collector and base electrodes have been interchanged with respect to the conventional emitter–base–collector sequence. This makes it possible to obtain negligible base currents and large current transfer ratios. Electric fields produced by applying a voltage to the base modulate the positions of the subband levels in the quantum well and thus control the emitter–collector tunneling current. Calculations showed that significant variations in the emitter–collector I–V characteristics can be obtained by modulating the base–emitter voltage.

The three–terminal devices of the second type consist of resonant tunneling double barrier heterostructures integrated with microwave field effect transistor configurations. The three proposed devices, shown in Figs.5.6, 5.8, and 5.9, could be called a “Resonant Tunneling MESFET,” a “Resonant Tunneling Vertical FET,” and a “Resonant Tunneling PBT,” respectively. Simulations of

device characteristics showed that substantial modulation of the tunnel structure negative differential resistances can be obtained by applying a gate voltage. Because they could operate in microwave and millimeter–wave regimes, such three–terminal devices should find applications in high–speed digital circuits, tunable millimeter–wave oscillators and negative resistance amplifiers. Although these devices were presented in the context of $GaAs/Al_xGa_{1-x}As$ heterojunction technology, they could be implemented in other materials. It may actually be advantageous to use semiconductors such as $In_{1-x}Ga_xAs$, which have a higher electron mobility than GaAs.

Experimental investigations are being performed by T. K. Woodward to determine the properties of these structures and to explore their possible applications in high frequency analog and digital circuits. The "Resonant Tunneling Vertical FET" has successfully been fabricated using MOCVD grown structures.[27] The experimental data agree with the theoretical results discussed in this chapter.

References

1. R. Tsu, and L. Esaki, Appl. Phys. Lett. **22**, 562 (1973).

2. T. C. L. G. Sollner, W. D. Goodhue, P. E. Tannenwald, C. D. Parker, and D. D. Peck, Appl. Phys. Lett. **43**, 588 (1983).

3. R. T. Collins, A. R. Bonnefoi, J. Lambe, T. C. McGill, and R. D. Burnham, *Proceedings of the 17th International Conference on the Physics of Semiconductors,* San Francisco, 1984, (Springer–Verlag, New York), p.437.

4. T. C. L. G. Sollner, P. E. Tannenwald, D. D. Peck, and W. D. Goodhue, Appl. Phys. Lett. **45**, 1319 (1984).

5. A. R. Bonnefoi, R. T. Collins, T. C. McGill, R. D. Burnham, and F. A. Ponce, Appl. Phys. Lett. **46**, 285 (1985).

6. T. J. Shewchuk, P. C. Chapin, P. D. Coleman, W. Kopp, R. Fischer, and H. Morkoç, Appl. Phys. Lett. **46**, 508 (1985).

7. F. Capasso, and R. A. Kiehl, J. Appl. Phys. **58**, 1366 (1985).

8. C. A. Mead, Proc. IRE **48**, 359 (1960).

9. D. V. Geppert, Proc. IRE **50**, 1527 (1962).

10. M. Heiblum, Solid State Electron. **24**, 343 (1981).

11. M. Heiblum, D. C. Thomas, C. M. Knoedler, and M. I. Nathan, Appl. Phys. Lett. **47**, 1105 (1985).

12. N. Yokoyama, K. Imamura, T. Ohshima, H. Nishi, S. Muto, K. Kondo, and S. Hiyamizu, Jpn. J. Appl. Phys. **23**, L311 (1984).

13. B. Jogai, and K. L. Wang, Appl. Phys. Lett. **46**, 167 (1985).

14. The computer program used to calculate the theoretical *I–V* curves of the "Stark Effect Transistor" was developed by D. H. Chow.

15. J. Bardeen, Phys. Rev. Lett. **6**, 57 (1961).

16. M. O. Vassell, Johnson Lee, and H. F. Lockwood, J. Appl. Phys. **54**, 5206 (1983).

17. B. Kim, H. Q. Tserng, and H. D. Shih, IEEE Elect. Dev. Lett. **EDL–6**, 1 (1985).

18. M. Ogawa, K. Ohata, T. Furutsuka, and N. Kawamura, IEEE Microwave Theory and Tech. **MTT–24**, 300 (1976).

19. Y. Imai, M. Uchida, K. Yamamoto, and M. Hirayama, IEEE Elect. Dev. Lett. **EDL–4**, 99 (1983).

20. S. G. Bandy, Y. G. Chai, R. Chow, C. K. Nishimoto, and G. Zdasiuk, IEEE Elect. Dev. Lett. **EDL–4**, 42 (1983).

21. P. Baudet, M. Binet, and Boccon–Gibod, IEEE Microwave Theory and Tech. **MTT–24**, 372 (1976).

22. R. A. Pucel, H. A. Haus, and H. Statz, *Advances in Electronics and Electron Physics*, L. Martin Ed., Vol.38, 1975, (Academic Press, New York), p.195.

23. S. M. Sze, *Physics of Semiconductors*, (J. Wiley and Sons, New York, 1981, Second Edition), p.340.

24. E. Kohn, U. Mishra, and L. F. Eastman, IEEE Elect. Dev. Lett. **EDL–4**, 125 (1983).

25. C. O. Bozler, and G. D. Alley, IEEE Electron Devices **ED–27**, 1128 (1980).

26. G. D. Alley, IEEE Electron Devices **ED–30**, 52 (1983).

27. T. K. Woodward, T. C. McGill, and R. D. Burnham, "Experimental Realization of a Resonant Tunneling Transistor," to be published.

Chapter 6

Growth Characterization of GaAs/$Al_xGa_{1-x}As$ Tunnel Structures Grown by Metalorganic Chemical Vapor Deposition

6.1 Introduction

In this chapter, measurements of current–voltage, I–V, characteristics, as well as first, (dI/dV)(V), and second, (d^2I/dV^2)(V), derivatives of the I–V curves are used to study the growth uniformity of some of the MOCVD grown samples discussed in this thesis. Because tunneling phenomena are strong functions of the doping densities and the thicknesses of the layers through which the charge carriers tunnel, electrical measurements constitute a method of choice for probing the growth uniformity of these heterostructures and detecting fluctuations in

doping concentrations and layer thicknesses.

Section 6.2 discusses the reproducibility and uniformity in the electrical characteristics of GaAs/AlAs single and double barrier tunnel structures. This is achieved by analyzing data obtained from large numbers of devices taken randomly across the wafers under test. The experimental results show evidence that these samples were grown with uniform layer thicknesses and doping concentrations.

In section 6.3, discrete fluctuations in layer thicknesses are reported in GaAs/ $Al_xGa_{1-x}As$ double barrier heterostructures. These fluctuations cause the width of the GaAs quantum well to vary by discrete steps and the resonant states in the well to form sets of quasi–stationary levels. Such effects are manifested by non–uniform experimental results and by sequences of negative differential resistances in the I–V characteristics of a number of devices. These observations suggest that islands may be formed during the growth of certain samples.

6.2 Uniformity in the Electrical Characteristics of GaAs/AlAs Tunnel Structures

Each of the heterostructures used in this study was grown by an MOCVD technique[1,2] on a GaAs substrate doped n–type with Si at 2–3 $\times 10^{18} cm^{-3}$. The first layer grown on the substrate was a 2–3 μm thick GaAs cladding layer, degenerately doped n–type with Se. It was followed either by one thin AlAs barrier layer, or by two AlAs tunnel barriers separated by a nominally undoped GaAs quantum well. Finally, a top GaAs cladding layer was grown, degenerately doped n–type with Se. The AlAs barriers were typically 50–150 Å thick. They were doped p–type with Mg[3,4] at 0.5–1 $\times 10^{18} cm^{-3}$. In the double barrier structures, the GaAs quantum well was on the order of 50 Å wide. Devices were prepared

on the samples by defining mesas on the epitaxial sample face using conventional photolithography and a GaAs etch (4:1:1, H_2SO_4:H_2O_2:H_2O). Ohmic contacts were made on the surface of the mesas and on the substrate by evaporating Au–Ge and Au, and annealing at 400–420°C for 15–20 s. Finally, the samples were either mounted on transistor headers and wire bonded, or probed with a whisker. The mesas were circular and 12–700 μm in diameter. For the purpose of this study, all the samples and devices were carefully prepared under similar conditions. Furthermore, in order to reduce the error introduced by undercutting during the etching process, the top GaAs cladding layer was preliminarily etched down to about 0.2 μm. Well defined mesas could then be obtained by etching less than 1 μm down from the surface.

Starting from wafers which were about 2 cm^2, at least 5 small pieces, approximately 4 mm^2 each, were chosen as far apart from each other as possible, and cleaved. A large number of mesas were then defined on each one of these pieces and, depending on their sizes, about 10 to 80 devices were taken randomly and systematically tested. Although this procedure was repeated for sets of devices having diameters between 12 and 700 μm, a more complete study was performed for mesas close to 50 and 80 μm in diameter. Current–voltage curves, as well as their first and second derivatives, were measured at temperatures ranging from 4.2 to 300 K. The I–V characteristics were taken with a Tektronix 577 curve tracer. Point–by–point measurements using a dc power supply were also made. First and second derivative curves were obtained using modulation techniques, with typical modulation voltages of 1–5 mV peak–to–peak.[5]

Some of the measurements performed are the following. For single barrier samples, in which elastic and inelastic tunneling occur, we studied (*i*) the zero–bias resistance at different temperatures, and (*ii*) the uniformity and reproducibility of the I–V curves as well as their first and second derivatives. In double

barrier structures, resonant tunneling takes place, and the I–V curves feature negative differential resistances. For these samples, we performed a careful study of (*i*) the zero–bias resistance at different temperatures, (*ii*) the voltages and currents at the peaks and valleys of the negative differential resistance regions, and (*iii*) the uniformity and reproducibility of the features displayed in the derivative spectra. Only a few of these properties are discussed below. Furthermore, experimental data are presented for only two samples. Other heterostructures led to similar results and conclusions.

Fig.6.1 is a logarithmic plot of the zero–bias resistance as a function of device diameter for a single barrier sample, (H160), in which the GaAs cladding layers are doped at $3 \times 10^{18} cm^{-3}$ and the AlAs barrier layer is 54 Å thick. The error bars correspond to averages over more than 20 measurements performed on different devices having the same size and taken randomly across the wafer. The crosses correspond to single measurements. The curve passing through the experimental data is a straight line. Its slope is almost exactly (–2). This indicates that the zero–bias resistance does scale with area. Furthermore, the zero–bias resistance, which depends on the transmission rate through the quantum barrier, is a strong function of the thickness of the AlAs layer through which the electrons actually tunnel. In particular, keeping all other parameters the same, a 7 Å change in barrier width makes the zero–bias resistance vary by more than an order of magnitude.[5] Since the tunneling electrons always tend to pass through the thinnest part of a barrier, variations in the values of the zero–bias resistance are directly related to fluctuations in the barrier thickness. The zero–bias resistance is also a function of the doping concentrations, which define the actual position of the Fermi level in the GaAs electrodes. It should also depend on the contacts. However, in all the samples studied, contact resistances were found to be negligible compared to the resistances of the tunnel barriers themselves. As a

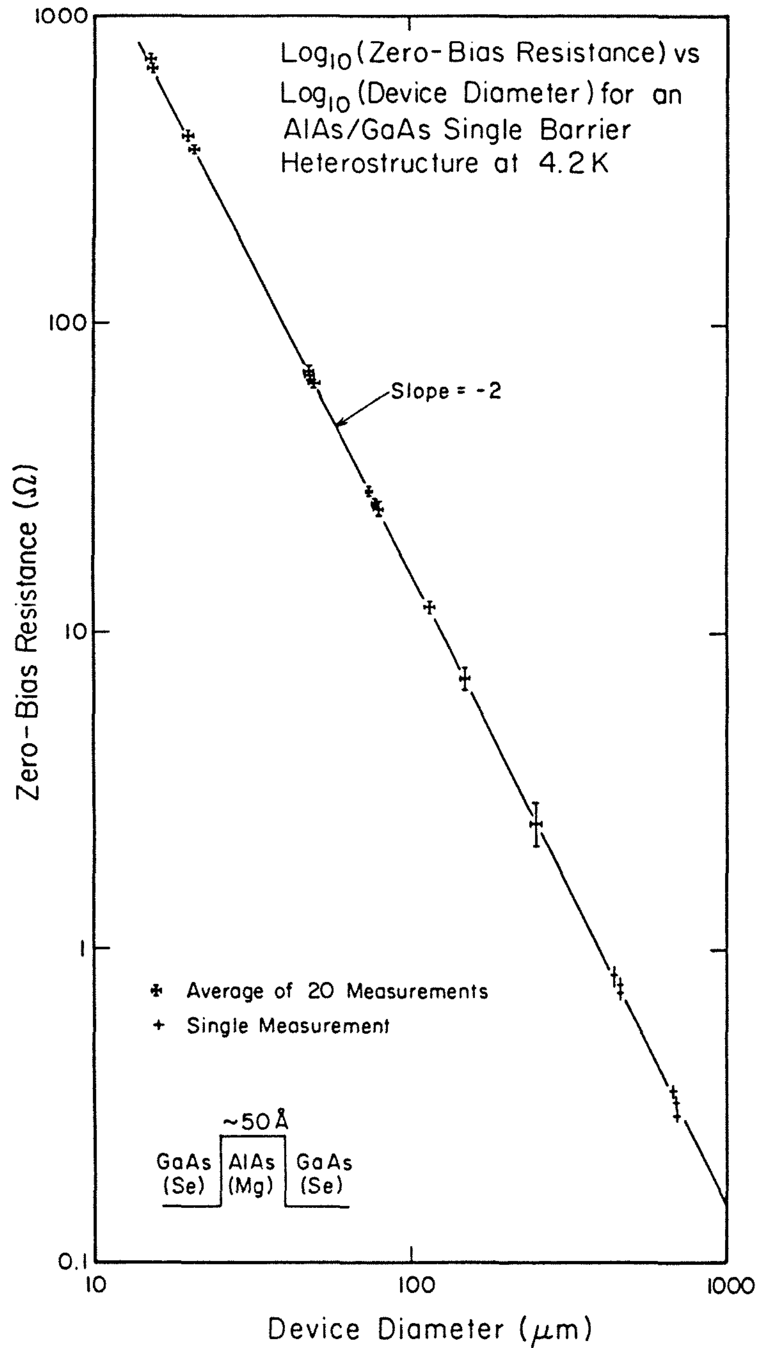

Figure 6.1: Log_{10}(Zero–bias Resistance) versus Log_{10}(Device Diameter) for a single barrier sample in which the GaAs cladding layers are doped at $3 \times 10^{18} cm^{-3}$ and the AlAs tunnel barrier is 54 Å thick (H160).

result, they did not alter the tunneling currents significantly. It should be noted that the error bars in Fig.6.1, which represent the standard deviations of the results, are very small. This indicates that leakage and edge currents, as well as effects associated with the local fluctuations in the electrostatic potential due to the ionized dopants, were negligible compared to the tunneling currents. Fig.6.2 is the superposition of seven $(d^2I/dV^2)(\mathrm{V})$ curves at 4.2 K for seven different devices, 78 μm in diameter, taken randomly among 100 mesas of the same size prepared on sample H160. The fact that these spectra overlap exactly was a common feature of all the series of devices tested. Similar results were obtained from other heterostructures. The above observations make it possible to conclude that both the doping profiles and layer thicknesses in the samples under test are uniform across the entire wafers. They suggest further that the average fluctuations in the thicknesses of ultra–thin layers in single barrier structures can be as small as one atomic layer or less.

In double barrier heterostructures, series of more than 60 devices close to 20, 50 and 80 μm in diameter were tested. I–V curves, as well as first and second derivatives, were measured. In a given series, the curves would all coincide, except for an occasional one, which could be due to the preparation procedure, a bad contact, or an improper bond. Fig.6.3 shows experimental I–V curves at 300 and 77 K for 10 different devices, 78 μm in diameter, taken randomly across the wafer of a double barrier sample, (H408). The GaAs cladding layers are doped at $1.75\times10^{18}cm^{-3}$. The AlAs barrier layer closer to the substrate is 51 Å thick. The other barrier is 42 Å thick. The GaAs quantum well is 62 Å wide. The breaks in the low temperature I–V curves are due to the fact that the curve tracer used for these measurements could not reliably resolve negative differential resistance regions. Resonant tunneling currents depend critically upon layer thicknesses and doping concentrations. Consequently, the reproducibility and uniformity of the

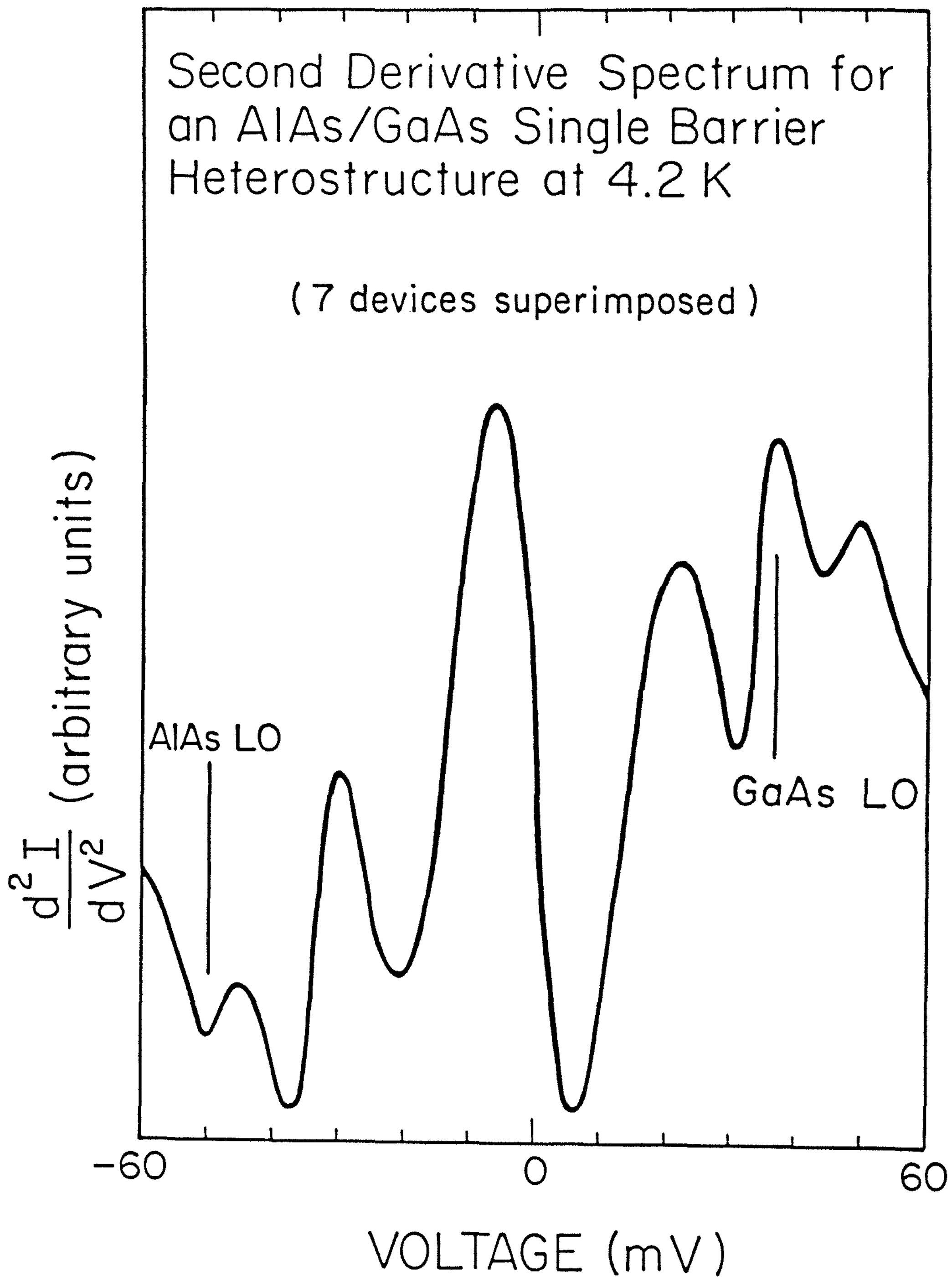

Figure 6.2: Second derivative spectra at 4.2 K for 7 devices, 78 μm in diameter, selected randomly among 100 of the same size. The structure is the same as in Fig.6.1 (sample H160).

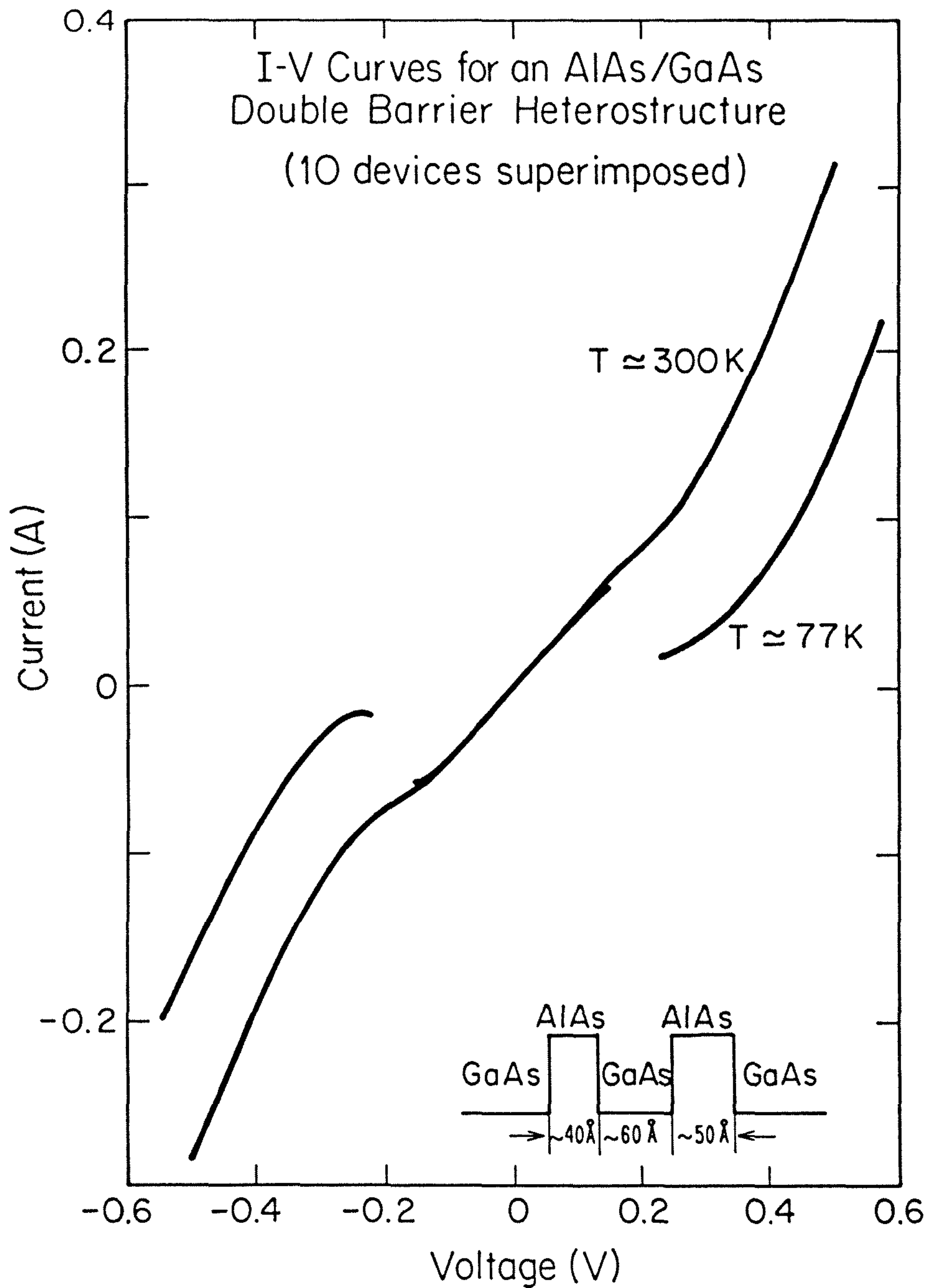

Figure 6.3: *I–V* curves measured on a double barrier sample, (H408), at 300 and 77 K for 10 devices, 78 μm in diameter. The GaAs cladding layers are doped at $1.75 \times 10^{18} cm^{-3}$. The AlAs barrier layer closer to the substrate is 51 Å thick. The other barrier is 42 Å thick. The GaAs quantum well is 62 Å wide.

experimental data are, again, a clear indication that the geometrical parameters and doping profiles are uniform across the entire sample.

In summary, we have studied the reproducibility and uniformity of I–V characteristics and their derivatives in MOCVD grown GaAs/AlAs tunnel structures. This was achieved by performing systematic measurements on large numbers of devices taken randomly across the wafers under test. The measured properties were strong functions of layer thicknesses and doping concentrations. The reproducibility and uniformity of the experimental results showed evidence that the doping profiles and the geometrical parameters of the structures were uniform across the wafers. In single barrier samples, they suggested further that the average fluctuations in the thicknesses of ultra–thin layers should be within one atomic layer.

6.3 Layer Thickness Fluctuations in GaAs/Al_x Ga_{1-x}As Double Barrier Heterostructures

As illustrated in section 6.2, several of the single and double barrier tunnel structures discussed in this thesis have reproducible and uniform electrical characteristics. However, this is not the case for all the samples. It is observed, in particular, that a number of devices prepared on certain GaAs/Al_xGa_{1-x}As resonant tunneling heterostructures display sequences of negative differential resistances in their I–V characteristics. Although the experimental results obtained from these structures are reproducible for any device taken individually, they are not uniform from device to device across the wafers. These phenomena show evidence of discrete fluctuations in layer thicknesses. Energy band diagram calculations indicate further that the thicknesses of the Al_xGa_{1-x}As tunnel barriers and the GaAs quantum well must fluctuate by integral numbers of monolayers.

Such phenomena are observed in samples H943 and H945 (see Tables 4.1 and 4.2 in Chapter 4). These effects may be related to the fact that the barrier layers are made of $Al_{0.35}Ga_{0.65}As$. The discreteness in layer thickness fluctuations revealed in these structures is illustrated below by discussing data obtained from sample H943 alone. H945 produces similar results. In H943, the GaAs cladding layers are doped n–type with Se at $1 \times 10^{18} cm^{-3}$. The p–type doping density in the $Al_{0.35}Ga_{0.65}As$ tunnel barriers is estimated to be $2 \times 10^{17} cm^{-3}$. The GaAs quantum well is nominally undoped. TEM measurements have determined that the thicknesses of the barrier layers vary between 59.5 and 62 Å (21–22 monolayers) and that the width of the GaAs quantum well fluctuates between 31 and 36.5 Å (11–13 monolayers).

The experimental I–V characteristics of the structure are found to depend strongly upon the area of the device under test. If the device is sufficiently small, its low temperature I–V curves display only one pronounced negative differential resistance in each bias direction. The peak–to–valley current ratios are on the order of 2.5 at 4.2 K. Fig.6.4 depicts an experimental I–V curve for a circular device, 50 μm in diameter. Because this curve is symmetric with respect to the origin, both $Al_{0.35}Ga_{0.65}As$ tunnel barriers must be identical over the whole area of the mesa. For other devices, the positions of the peaks in current differ in forward bias and in reverse bias. The two tunnel barriers must then have different thicknesses. Energy band diagram calculations have indicated that the observed negative differential resistances are due to resonant tunneling via E_1^Γ, the quasi–stationary level confined in the GaAs quantum well by the $Al_{0.35}Ga_{0.65}As$ Γ–point potential energy barriers. The results obtained in Fig.6.4 are consistent with 59.5 Å thick $Al_{0.35}Ga_{0.65}As$ barriers and a 34 Å wide GaAs well. E_1^Γ then lies 110 meV above the conduction band edge at the middle of the well in the unbiased structure.

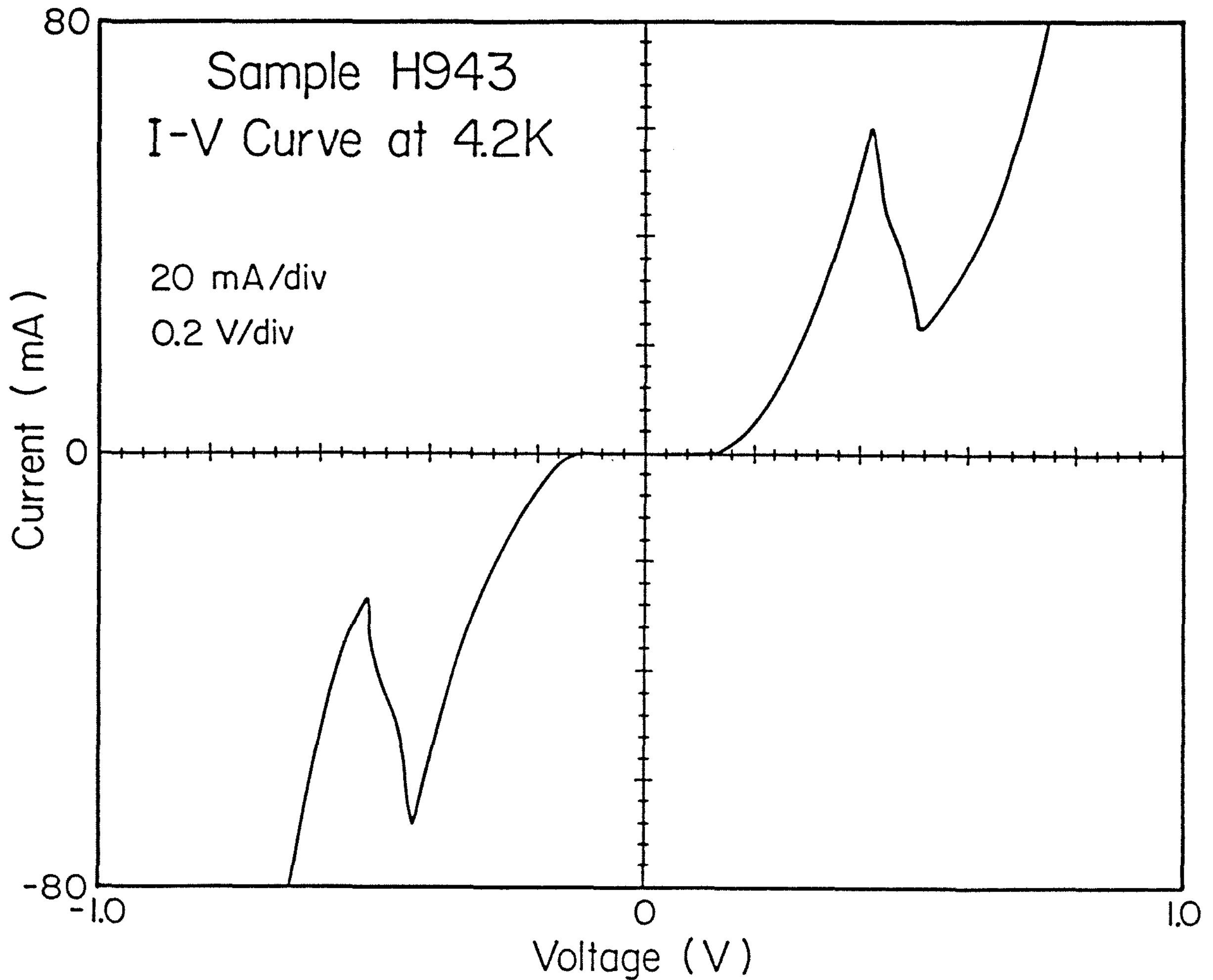

Figure 6.4: Experimental I–V characteristic at 4.2 K for a circular device, 50 μm in diameter, fabricated on sample H943. H943 is an MOCVD grown GaAs/$Al_{0.35}Ga_{0.65}As$ double barrier heterostructure. The GaAs electrodes are doped n–type with Se at $1 \times 10^{18} cm^{-3}$. The barrier layers are 59.5–62 Å thick. They are doped p–type with Mg at $2 \times 10^{17} cm^{-3}$. The nominally undoped GaAs quantum well is 31–36.5 Å wide.

The experimental I–V curves become less symmetric and uniform with increasing device areas. This confirms that fluctuations in layer thicknesses play a more important role as these areas are made larger. Fig.6.5 depicts an I–V characteristic at 4.2 K for a circular device having a diameter of 125 μm. This curve differs significantly from that shown in Fig.6.4 in that each of the pronounced negative differential resistances has been replaced by a sequence of three weak current peaks. In reverse bias, these occur at $V_1^R = -380$ mV, $V_2^R = -440$ mV, and $V_3^R = -530$ mV. In forward bias, the peaks in current are obtained at $V_1^F = 340$ mV, $V_2^F = 400$ mV, and $V_3^F = 450$ mV. Other devices only show two negative differential resistances in each bias direction, but some larger devices depict as many as four current peaks for each polarity of the applied voltage. This reveals that the resonant state in the GaAs quantum well has been replaced by a set of quasi–stationary levels arising from discrete fluctuations in well width. This is an indication that islands may be formed during sample growth, causing the tunnel barriers and the quantum well to consist of adjacent domains having different thicknesses. These thicknesses must only vary by discrete values, producing sets of resonant energy levels in the well when the device under test overlaps with several domains. When this occurs, sequences of negative differential resistances are observed in the experimental I–V characteristics. Because the resonant energy levels are close in energy, the peaks in current are small and close to one another. Their actual spacing may be related to fluctuations in layer thicknesses by calculating the energy band diagrams of the biased structures. In the case of sample H943, a variation in well width by one monolayer (2.83 Å) produces a variation of approximately 8 meV in E_1^Γ. This causes the corresponding current peaks to shift by about 30 mV. This shift is reduced to approximately 20 mV if either tunnel barrier varies in thickness by one monolayer. These values may be used to interpret the experimental results depicted

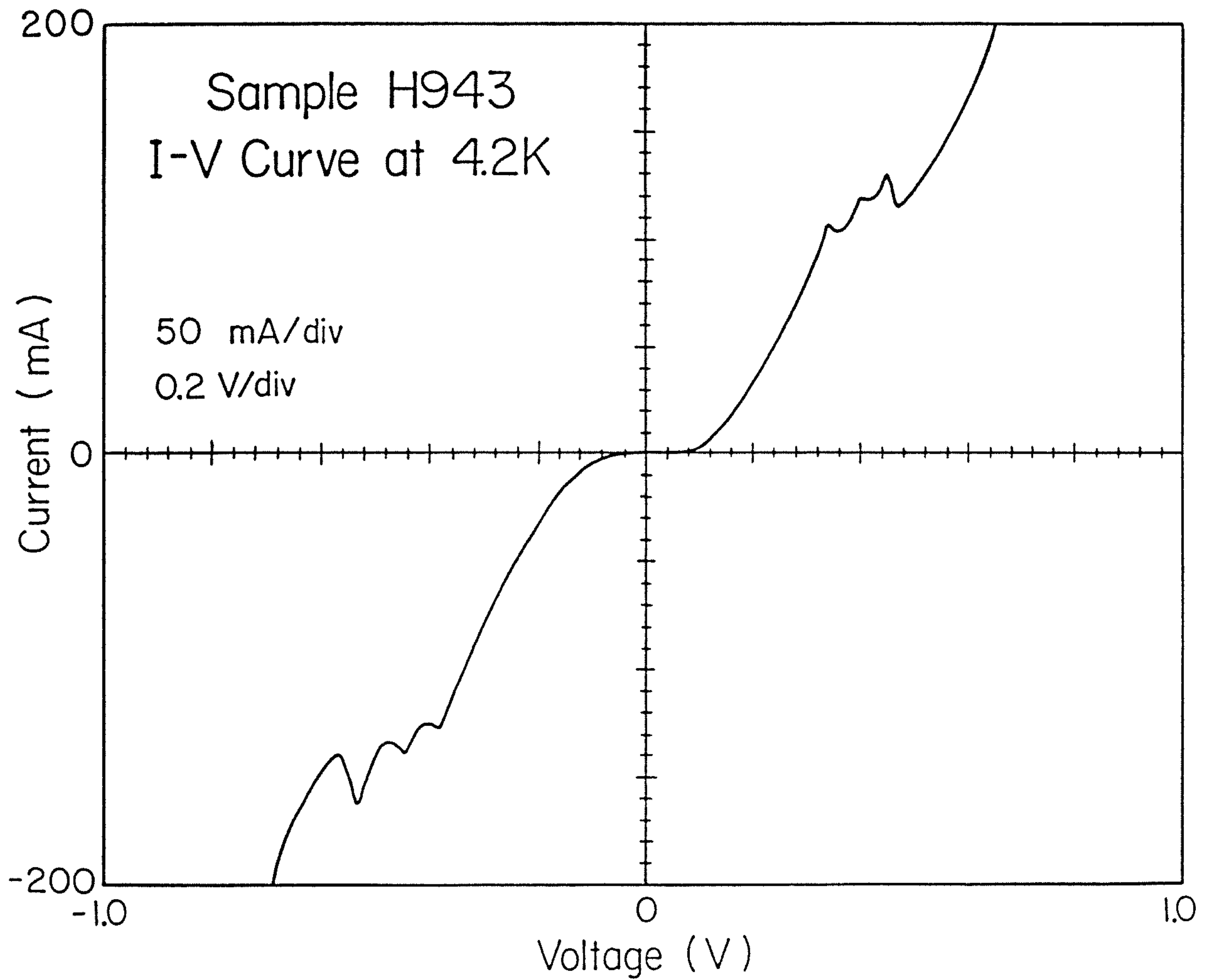

Figure 6.5: Experimental I–V characteristic at 4.2 K for a circular device, 125 μm in diameter, fabricated on sample H943. The sequences of negative differential resistances are due to discrete fluctuations in layer thicknesses.

in Fig.6.5. The negative differential resistances observed at $V_1^R = -380$ mV and $V_1^F = 340$ mV may be explained by making the quantum well thicker than in Fig.6.4 by two monolayers, but the barrier closer to the top electrode thinner by one monolayer. The peaks in current at $V_2^R = -440$ mV and $V_2^F = 400$ mV are consistent with a structure in which the GaAs well would be 34 Å wide, as in Fig.6.4, but the barrier closer to the top cladding layer would be thinner than the other barrier by one monolayer. Finally, the negative differential resistances at $V_3^R = -530$ mV and $V_3^F = 450$ mV may be explained by making the well thinner than in Fig.6.4 by two monolayers, and the barrier closer to the top electrode thinner than the other barrier by two monolayers. The *I–V* characteristics of other devices may be interpreted using the same approach. For example, the *I–V* curves of a device which is 78 μm in diameter reveal peaks in current at $V_1^R = -460$ mV, $V_2^R = -520$ mV, $V_1^F = 380$ mV, and $V_2^F = 520$ mV. V_1^R and V_1^F are consistent with a structure in which the barrier closer to the top electrode is thinner than the other barrier by two monolayers. The peaks at V_2^R and V_2^F may be explained by making the well thinner than in Fig.6.4 by three monolayers.

In summary, we have studied discrete fluctuations in layer thicknesses in MOCVD grown GaAs/$Al_xGa_{1-x}As$ double barrier heterostructures. As a result of these fluctuations, the width of the GaAs quantum well varies by discrete values and the resonant states in the well form sets of quasi–stationary levels. This causes the experimental results to be non–uniform and sequences of weak negative differential resistances to be obtained in the *I–V* characteristics of certain devices. However, single and pronounced current peaks are obtained when the devices are sufficiently small. Energy band diagrams may be used to correlate the spacings between the peaks in current observed in the *I–V* curves with the fluctuations in layer thicknesses. They indicate that the $Al_xGa_{1-x}As$ tunnel barriers and the GaAs quantum well fluctuate by integral numbers of monolay-

ers. These results reveal that islands are formed during the growth of certain samples. Fabricating such islands in a controlled manner may have potential applications. In particular, they could be used to produce multiple negative differential resistances with specific spacings and amplitudes.

References

1. H. M. Manasevit, Appl. Phys. Lett. **12**, 156 (1968).

2. R. D. Dupuis, and P. D. Dapkus, Appl. Phys. Lett. **31**, 466 (1977).

3. C. R. Lewis, W. T. Dietze, and M. J. Ludowise, Electron. Lett. **18**, 569 (1982).

4. R. D. Burnham, W. Streifer, D. R. Scifres, C. Lindstrom, T. L. Paoli, and N. Holonyak, Jr., Electron. Lett. **18**, 1095 (1982).

5. R. T. Collins, Ph.D. thesis, California Institute of Technology, 1985.